Ministry of Education and Science of the Russian Federation
Saint Petersburg National Research University of Information Technologies, Mechanics, and Optics

NANOSYSTEMS:
PHYSICS, CHEMISTRY, MATHEMATICS

2019, volume 10(5)

Наносистемы: физика, химия, математика

2019, том 10, № 5

NANOSYSTEMS:

PHYSICS, CHEMISTRY, MATHEMATICS

ADVISORY BOARD MEMBERS

Chairman: V.N. Vasiliev *(St. Petersburg, Russia),*
V.M. Buznik *(Moscow, Russia)*; V.M. Ievlev *(Voronezh, Russia),* P.S. Kop’ev*(St. Petersburg, Russia),* N.F. Morozov *(St. Petersburg, Russia),* V.N. Parmon *(Novosibirsk, Russia),* A.I. Rusanov *(St. Petersburg, Russia),*

EDITORIAL BOARD

Editor-in-Chief: I.Yu. Popov *(St. Petersburg, Russia)*

Section Co-Editors:
Physics – V.M. Uzdin *(St. Petersburg, Russia),*
Chemistry, material science –V.V. Gusarov *(St. Petersburg, Russia),*
Mathematics – I.Yu. Popov *(St. Petersburg, Russia).*

Editorial Board Members:
V.M. Adamyan *(Odessa, Ukraine)*; O.V. Al’myasheva *(St. Petersburg, Russia)*; A.P. Alodjants *(Vladimir, Russia)*; S. Bechta *(Stockholm, Sweden)*; J. Behrndt *(Graz, Austria)*; M.B. Belonenko *(Volgograd, Russia)*; A. Chatterjee (*Hyderabad, India)*; S.A. Chivilikhin *(St. Petersburg, Russia)*; A.V. Chizhov *(Dubna, Russia)*; A.N. Enyashin *(Ekaterinburg, Russia),* P.P. Fedorov *(Moscow, Russia)*; E.A. Gudilin *(Moscow, Russia)*; V.K. Ivanov *(Moscow, Russia),* H. Jónsson *(Reykjavik, Iceland)*; A.A. Kiselev *(Durham, USA)*; Yu.S. Kivshar *(Canberra, Australia)*; S.A. Kozlov *(St. Petersburg, Russia)*; P.A. Kurasov *(Stockholm, Sweden)*; A.V. Lukashin *(Moscow, Russia)*; I.V. Melikhov *(Moscow, Russia)*; G.P. Miroshnichenko *(St. Petersburg, Russia)*; I.Ya. Mittova *(Voronezh, Russia)*; V.V. Pankov *(Minsk, Belagus)*; K. Pankrashkin *(Orsay, France)*; A.V. Ragulya *(Kiev, Ukraine)*; V. Rajendran *(Tamil Nadu, India)*; A.A. Rempel *(Ekaterinburg, Russia)*; V.Ya. Rudyak *(Novosibirsk, Russia)*; D Shoikhet *(Karmiel, Israel)*; P Stovicek *(Prague, Czech Republic)*; V.M. Talanov *(Novocherkassk, Russia)*; A.Ya. Vul’ *(St. Petersburg, Russia)*; A.V. Yakimansky (*St. Petersburg, Russia*), V.A. Zagrebnov *(Marseille, France).*

Editors:
I.V. Blinova; A.I. Popov; A.I. Trifanov; E.S. Trifanova *(St. Petersburg, Russia),*
R. Simoneaux *(Philadelphia, Pennsylvania, USA).*

Address: University ITMO, Kronverkskiy pr., 49, St. Petersburg 197101, Russia.
Phone: +7(812)312-61-31, **Journal site:** http://nanojournal.ifmo.ru/,
E-mail: popov1955@gmail.com

AIM AND SCOPE

The scope of the journal includes all areas of nano-sciences. Papers devoted to basic problems of physics, chemistry, material science and mathematics inspired by nanosystems investigations are welcomed. Both theoretical and experimental works concerning the properties and behavior of nanosystems, problems of its creation and application, mathematical methods of nanosystem studies are considered.

The journal publishes scientific reviews (up to 30 journal pages), research papers (up to 15 pages) and letters (up to 5 pages). All manuscripts are peer-reviewed. Authors are informed about the referee opinion and the Editorial decision.

CONTENT

MATHEMATICS

PHYSICS

CHEMISTRY AND MATERIAL SCIENCE

NANOSYSTEMS: PHYSICS, CHEMISTRY, MATHEMATICS, 2019, 10 (5), P. 505–510

Transparent vertex boundary conditions for quantum graphs: Simplified approach

M. M. Aripov[1], K. K. Sabirov[2], J. R. Yusupov[3]

[1]National University of Uzbekistan, Vuzgorodok, Tashkent, Uzbekistan

[2]Tashkent University of Information Technologies, 108 Amir Temur Str., 100200, Tashkent, Uzbekistan

[3]Turin Polytechnic University in Tashkent, 17 Niyazov Str., 100095, Tashkent, Uzbekistan

jambul.yusupov@gmail.com

PACS 03.65.Aa, 02.60.Cb, 05.60.Gg **DOI 10.17586/2220-8054-2019-10-5-505-510**

We consider quantum graphs providing reflectionless wave transmission at the vertices. Imposing Kuska's version of so-called absorbing boundary conditions we derive the constraints, which make usual continuity and Kirchhoff conditions equivalent to transparent boundary conditions.

Keywords: quantum graph, transparent boundary conditions, ballistic transport, wave packet dynamics.

Received: 14 October 2019

Revised: 18 October 2019

1. Introduction

The problem of wave propagation in absorbing or transparent media is of importance for different practical applications in optics, acoustics, fluid dynamics and condensed matter physics. An effective way for modeling of wave dynamics in transparent media is describing them in terms of a wave equation, for which so-called transparent boundary conditions are imposed. The problem of wave equation with transparent boundary conditions has attracted much attention in mathematical physics (see, e.g., papers [1–10] for review). Such boundary conditions describe absorption or reflectionless motion of waves in their transmission from one domain to a different one. Therefore, one uses similar terminology for the boundary conditions of both types of processes, calling them absorbing or transparent boundary conditions. The problem of transparent boundary conditions (TBC) for linear partial differential equations (PDEs) was first introduced in the Refs. [1, 2] and has become a well developed topic in mathematical and theoretical physics now (see, e.g., [3–18] for review). For both (absorbing and transparent transmission) processes, the boundary conditions can be derived by factorization of the differential operator corresponding to a wave equation, which, in general, leads to complicated equations for the boundary conditions. Explicit form of such boundary conditions are much complicated than those of Dirichlet, Neumann and Robin conditions.

For transparent (absorbing) boundary conditions, the wave equation cannot be solved analytically and always requires using highly accurate numerical methods. In other words, numerical implementation of transparent boundary conditions is a complicated problem, which requires finding effective discretization schemes. Therefore, some authors proposed different simplifications of TBC for the linear Schrödinger equation. Shibata derived such TBC from dispersion relations for the linear Schrödinger equation [19]. Further simplification of TBC obtained by approximating such dispersion relations has been derived by Kuska [20]. Here, we use Kuska's approach for the derivation of simplified vertex boundary conditions for quantum graphs. The latter represent system of quantum wires connected to each other through some rule and are described in terms of the Schrödinger equation on metric graphs [21–25]. Strict mathematical derivation of TBC for quantum graphs has been presented recently in [26]. However, the explicit form of TBC derived in that paper are quite complicated for numerical implementation. Here, we derive a rather simplified version of TBC using the above mentioned Kuska's approach. The explicit form of boundary conditions obtained within such approach is much simpler than those derived in the Ref. [26].

2. Absorbing boundary conditions on interval

Following the Ref. [20], we briefly recall the derivation of the approximate transparent boundary conditions for the one-dimensional Schrödinger equation on a finite interval. Consider the one-dimensional time-dependent Schrödinger equation (in the units $m = \hbar = 1$):

$$i\frac{\partial\psi}{\partial t}(x,t) = -\frac{1}{2}\frac{\partial^2\psi}{\partial x^2}(x,t) + V(x)\psi(x,t), \tag{1}$$

which describes the motion of a quantum particle in the interval $x \in (-\infty, +\infty)$ under the influence of the space-dependent potential V. Taking a plane wave of the form

$$\psi(x,t) = \exp\big[-i(\omega t - kx)\big], \tag{2}$$

from Eqs.(1) and (2), one obtains the dispersion relation for the wave vector k, cf. [20]

$$k^2 = 2[\omega - V]. \tag{3}$$

This dispersion relation can be solved for k and yields

$$k = \pm\sqrt{2[\omega - V]}, \tag{4}$$

where the plus sign describes waves moving to $x = +\infty$ and the minus sign means waves moving to $x = -\infty$. The left boundary has to be transparent for left-propagating waves and the right boundary must be transparent for right propagating waves. The main idea used in the Refs. [19, 20] for the derivation of absorbing (transparent) boundary conditions was the requirement that plane wave should remain as plane on both sides of the boundary.

The square root function can be approximated using the rational function approximation method following [20]:

$$\sqrt{z} \approx \frac{1+3z}{3+z}. \tag{5}$$

With this approximation (5) for the square root in the dispersion relation (4), one obtains

$$k = \pm k_0\sqrt{\frac{2(\omega - V)}{k_0^2}} \approx \pm k_0\frac{1+3z}{3+z}, \quad \text{with} \quad z = \frac{2(\omega - V)}{k_0^2}. \tag{6}$$

Then, we write (6) as $k(3+z) \approx \pm k_0(1+3z)$ and inserting expression for z into this equation, one obtains:

$$k\left(3\frac{k_0^2}{2} + \omega - V\right) \approx \pm k_0\left(\frac{k_0^2}{2} + 3\omega - 3V\right).$$

Now by requiring that the boundaries of a given interval $-L < x < L$ should be transparent (i.e., the boundary does not break profile of the plane wave) and using the correspondence between quantities k and ω with their operator definitions

$$k \leftrightarrow -i\partial/\partial x \text{ and } \omega \leftrightarrow i\partial/\partial t$$

we obtain the TBC at the boundaries $x = \pm L$:

$$-i\left(3\frac{k_0^2}{2} - V\right)\frac{\partial\psi}{\partial x}(x,t)|_{x=\pm L} + \frac{\partial^2\psi(x,t)}{\partial x\partial t}|_{x=\pm L} =$$
$$= \pm\, k_0\left(\frac{k_0^2}{2} - 3V\right)\psi(x,t)|_{x=\pm L} \pm 3ik_0\frac{\partial\psi(x,t)}{\partial t}|_{x=\pm L}. \tag{7}$$

Plus and minus signs in Eq.(7) corresponds to the boundary conditions for the right and left walls, respectively. Eq.(1) together with the boundary condition (7) present the problem of absorbing boundary conditions for 1D box.

3. Absorbing boundary conditions for quantum graph

In this section, we extend the treatment of the previous section to the case of quantum graphs. To do so, we start from the simplest, star-shaped graph presented in Fig. 1. The Schrödinger equation on such graph can be written as

$$\frac{\partial\Psi_j}{\partial t}(x,t) = \left[-\frac{1}{2}\frac{d^2}{d^2x} + V_j\right]\Psi_j(x,t), \tag{8}$$

where $j = 1, 2, 3$ denotes the bond index, V_j is the external potential on jth bond. The coordinates are chosen as $-L_1 < x < 0$ for $j = 1$ and $0 < x < L_j$ for $j = 1, 2$. In order to solve Eq.(8), one needs to impose boundary conditions at the (internal) vertex and at the edges (external vertices) of each bond. In this work we focus on the internal vertex, therefore the choice of boundary conditions at external vertices are not essential. Here they are imposed as Dirichlet BC, while the vertex boundary conditions are imposed as continuity condition of the wave function weights at the graph vertex:

$$\alpha_1\Psi_1(x,t)|_{x=0} = \alpha_2\Psi_2(x,t)|_{x=0} = \alpha_3\Psi_3(x,t)|_{x=0}, \tag{9}$$

where α_j, $(j = 1, 2, 3)$ are the arbitrary constant, which will be determined below. The second boundary condition is imposed as the "current conservation" at the internal vertex

$$\frac{1}{\alpha_1}\frac{d\Psi_1(x,t)}{dx}\bigg|_{x=0} = \frac{1}{\alpha_2}\frac{d\Psi_2(x,t)}{dx}\bigg|_{x=0} + \frac{1}{\alpha_3}\frac{d\Psi_3(x,t)}{dx}\bigg|_{x=0}. \tag{10}$$

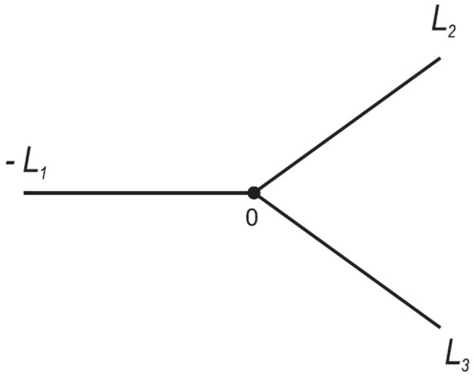

FIG. 1. Sketch of a metric star graph. L_j is the length of the jth bond with $j = 1, 2, 3$

Now we apply for such graph prescription for the derivation of absorbing BC used in the previous section. The dispersion relation for this case can be written as

$$k_j = \pm\sqrt{2[\omega_j - V_j]}. \tag{11}$$

Applying the Eqs.(5) and (11), we derive the absorbing vertex boundary conditions (AVBCs) for quantum graph:

$$-i\left(3\frac{k_{0j}^2}{2} - V_j\right)\frac{\partial\psi_j}{\partial x}(x,t)|_{x=0} + \frac{\partial^2\psi_j(x,t)}{\partial x\partial t}|_{x=0} =$$
$$- k_{0j}\left(\frac{k_{0j}^2}{2} - 3V_j\right)\psi_j(x,t)|_{x=0} - 3ik_{0j}\frac{\partial\psi_j(x,t)}{\partial t}|_{x=0}, \tag{12}$$

Under weak assumptions $k_{0j} = k_0$, $V_j = V_0$ =const, from (9) and (10), we get the following constraint

$$\frac{1}{\alpha_1^2} = \frac{1}{\alpha_2^2} + \frac{1}{\alpha_3^2}. \tag{13}$$

Eq.(13) is the condition that makes possible fulfilling the boundary conditions given by Eq.(12) with the plane wave solutions of Eq.(8).

It should be noted here that for other two choices, when the second or third bonds are incoming, such constraints can be derived analogously. Thus, for the incoming second bond and outgoing first and third bonds, the constraint is

$$\frac{1}{\alpha_2^2} = \frac{1}{\alpha_1^2} + \frac{1}{\alpha_3^2},$$

and for the incoming third bond and outgoing first and second bonds the constraint is

$$\frac{1}{\alpha_3^2} = \frac{1}{\alpha_1^2} + \frac{1}{\alpha_2^2}.$$

4. Numerical experiment

In this section, we show numerically that fulfilling the constraint (13) allows reflectionless transmission of the Gaussian wave packet (GWP) through the vertex (branching point) of a graph with boundary conditions in the form of (9) and (10). The configuration of the experimental set-up consists of star graph with three bonds (see Fig. 1) of lengths $L_1 = L_2 = L_3 = 10$. We consider the wave going from the first bond to the second and the third ones, i.e., the initial condition is compactly supported in the first bond. The initial state of the wave function is given by the following Gaussian function

$$\Psi^I(x) = (2\pi)^{-1/4}\exp(5ix - (x-5)^2/4). \tag{14}$$

To solve Eq.(8) numerically, we use Crank-Nicolson finite difference scheme with the space discretization $\Delta x = 0.016$ and the time step $\Delta t = 5 \cdot 10^{-5}$. We consider time interval $[0, 1.1]$, which is enough for complete splitting of GWP into the second and the third bonds.

Firstly, we simulate GWP dynamics in a quantum star graph with "natural" vertex boundary conditions, i.e. boundary conditions given by (9) and (10) with $\alpha_1 = \alpha_2 = \alpha_3 = 1$. For this case we have reflection of GWP with "mass" of fraction $N_1 = 1/9$ (see, Ref. [21]). Other $8/9$ part of mass is transmits through the vertex and splits into

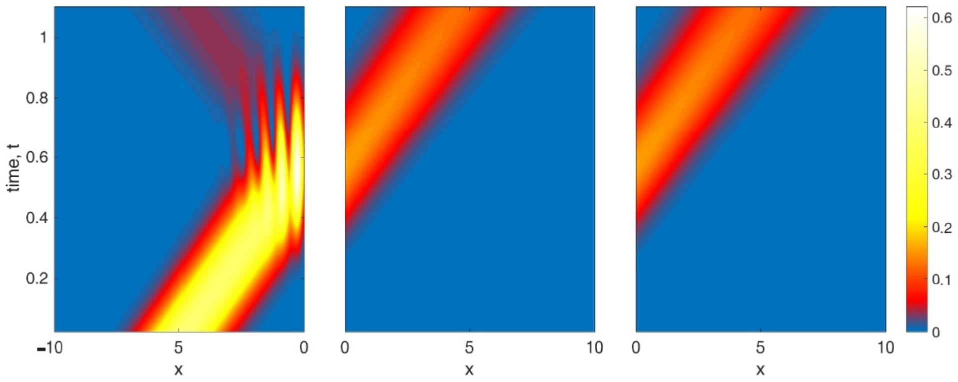

FIG. 2. Contour plot of the probability density for the GWP initially located on the first bond and given by (14). The imposed vertex boundary conditions are “natural” ones, i.e. $\alpha_1 = \alpha_2 = \alpha_3 = 1$. Each column corresponds to a bond, numbering from left to right

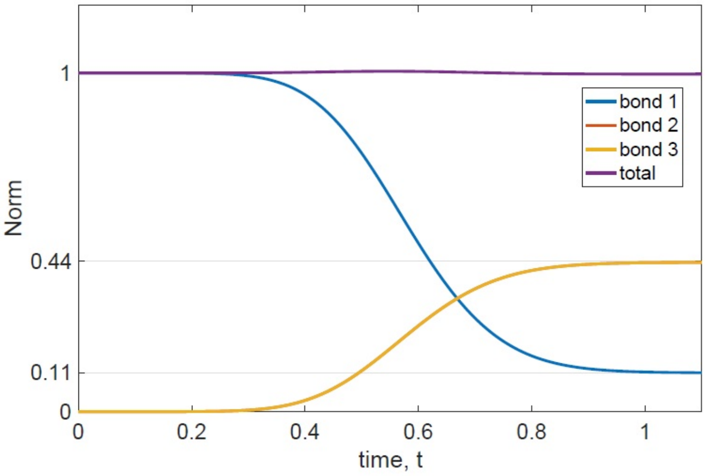

FIG. 3. Partial norms of GWP for the case shown in Fig. 2

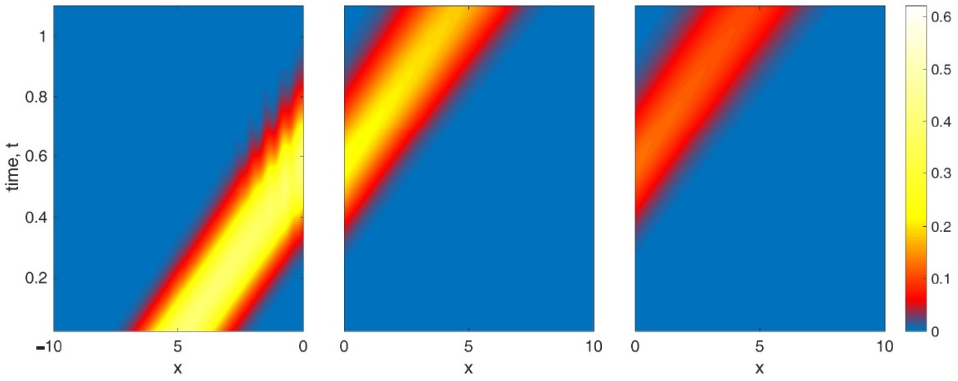

FIG. 4. Contour plot of the probability density for the GWP initially located on the first bond and given by (14). The imposed vertex boundary conditions are Kirchhoff-type ones with $\alpha_1 = 2.4$, $\alpha_2 = 3$ and $\alpha_3 = 4$. Each column corresponds to a bond, numbering from left to right

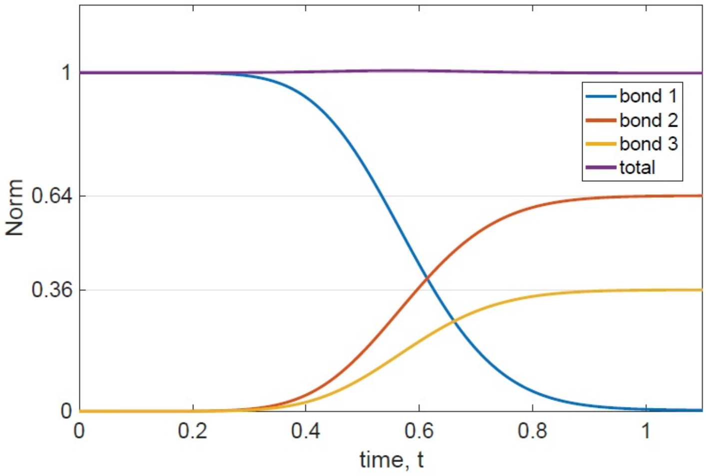

FIG. 5. Partial norms of the GWP for the case shown in Fig. 4. The masses of transmitted fractions are $N_2 = 0.64$ and $N_3 = 0.36$, which confirm $N_j = \alpha_j^2/(\alpha_2^2 + \alpha_3^2)$, $j = 1, 2$

two identical fractions. Fig. 2 demonstrates this dynamics and in the Fig. 3 one can see the time-dependence of partial norms.

Now, we choose parameters α_j so that they fulfill the constraint (13): $\alpha_1 = 2.4$, $\alpha_2 = 3$ and $\alpha_3 = 4$. The GWP dynamics for this set-up is shown in Fig. 4 and Fig. 5. Here we note that it is easy to show the possibility of controlling of the GWP transition through the vertex by choosing proper parameters $\alpha_{2,3}$ so that the "masses" of fractions will be $N_2 = \alpha_2^2/(\alpha_2^2 + \alpha_3^2)$ and $N_3 = \alpha_3^2/(\alpha_2^2 + \alpha_3^2)$, accordingly.

5. Conclusions

We have studied reflectionless wave transport in quantum graphs using simplified version of transparent boundary conditions concept (so-called Kuska's approach). It is shown that within such simplification, under certain constraints, usual continuity condition and Kirchhoff rules imposed at the graph vertex become equivalent to transparent boundary conditions. Reflectionless transmission of quantum particle through the graph branching point is shown by numerical solution of the time-dependent Schrödinger equation on a graph. Although the problem is solved for simple star graph, extension of the approach for other graph (branching) topologies is rather trivial.

References

[1] Engquist B., Majda A. Absorbing boundary conditions for the numerical simulation of waves. *Math. Comput.*, 1977, **31**, P. 629–651.

[2] Kosloff R., Kosloff D., Absorbing boundaries for wave propagation problems. *J. Comput. Phys.*, 1986, **63**(2), P. 363–376.

[3] Arnold A., Ehrhardt M. Discrete Transparent Boundary Conditions for Wide Angle Parabolic Equations in Underwater Acoustics. *J. Comput. Phys.*, 1998, **145**(2), P. 611–638.

[4] Ehrhardt M. Discrete Transparent Boundary Conditions for General Schrödinger-type Equations. *VLSI Design*, 1999, **9**(4), P. 325–338.

[5] Ehrhardt M., Arnold A. Discrete transparent boundary conditions for the Schrödinger equation. *Riv. di Math. Univ. di Parma*, 2001, **6**(4), P. 57–108.

[6] Ehrhardt M. Efficient Numerical Implementation of Discrete Transparent Boundary Conditions for Parabolic Equations in Underwater Acoustics. *Acta Acustica united with Acustica*, 2002, **88**, P. 711–713.

[7] Arnold A., Ehrhardt M. and Sofronov I. Discrete transparent boundary conditions for the Schrdinger equation: fast calculation, approximation, and stability. *Comm. Math. Sci.*, 2003, **1**(3), P. 501–556.

[8] Jiang S. and Greengard L. Fast evaluation of nonreflecting boundary conditions for the Schrödinger equation in one dimension. *Comput. Math. Appl.*, 2004, **47**, P. 955–966.

[9] Antoine X., Arnold A., Besse C., Ehrhardt M. and Schädle A., A Review of artificial boundary conditions for the Schrödinger equation. *Commun. Comput. Phys.*, 2008, **4**(4), P. 729–796.

[10] Ehrhardt M. Discrete transparent boundary conditions for Schrdinger-type equations for non-compactly supported initial data. *Appl. Numer. Math.*, 2008, **58**(5), P. 660–673.

[11] Šumichrast L. and Ehrhardt M. Comparison of the continuous, semi-discrete and fully-discrete transparent boundary conditions (TBC) for the parabolic wave equation: 1 theory. *J. Electr. Engineering*, 2009, **60**(6), P. 301–312.

[12] Antoine X., Besse C., Klein P. Absorbing boundary conditions for the one-dimensional Schrödinger equation with an exterior repulsive potential. *J. Comput. Phys.*, 2009, **228**(2), P. 312–335.

[13] Ehrhardt M. Absorbing Boundary Conditions for Hyperbolic Systems. *Numer. Math.: Theor. Meth. Appl.*, 2010, **3**(3), P. 295–337.

[14] Klein P., Antoine X., Besse C. and Ehrhardt M. Absorbing Boundary Conditions for Solving N-Dimensional Stationary Schrödinger Equations with Unbounded Potentials and Nonlinearities. *Commun. Comput. Phys.*, 2011, **10**(5), P. 1280–1304.

[15] Arnold A., Ehrhardt M., Schulte M. and Sofronov I. Discrete transparent boundary conditions for the Schrödinger equation on circular domains. *Commun. Math. Sci.*, 2012, **10**(3), P. 889–916.

[16] Feshchenko R.M. and Popov A.V. Exact transparent boundary condition for the three-dimensional Schrödinger equation in a rectangular cuboid computational domain. *Phys. Rev. E*, 2013, **88**, P. 053308.

[17] Antoine X. et al., Absorbing boundary conditions for relativistic quantum mechanics equations. *J. Comput. Phys.*, 2014, **277**, P. 268–304.

[18] Petrov P. and Ehrhardt M. Transparent boundary conditions for iterative high-order parabolic equations. *J. Comput. Phys.*, 2016, **313**, P. 144–158.

[19] Shibata T. Absorbing boundary conditions for the finite-difference time-domain calculation of the one-dimensional Schrödinger equation. *Phys. Rev. B*, 1991, **43**(8), P. 6760.

[20] Kuska J.-P. Absorbing boundary conditions for the Schrödinger equation on finite intervals. *Phys. Rev. B*, 1992, **46**(8), P. 5000.

[21] Kottos T. and Smilansky U. Periodic Orbit Theory and Spectral Statistics for Quantum Graphs. *Ann. Phys.*, 1999, **76**, P. 274.

[22] Gnutzmann S. and Smilansky U. Quantum graphs: Applications to quantum chaos and universal spectral statistics. *Adv. Phys.*, 2006, **55**, P. 527–625. .

[23] Gnutzmann S., Schanz H. and Smilansky U. Topological Resonances in Scattering on Networks (Graphs). *Phys. Rev. Lett.*, 2013, **110**, P. 094101.

[24] Gnutzmann S., Waltner D. Stationary waves on nonlinear quantum graphs: General framework and canonical perturbation theory. *Phys. Rev. E*, 2016, **93**, P. 032204.

[25] Gnutzmann S., Waltner D. Stationary waves on nonlinear quantum graphs. II. Application of canonical perturbation theory in basic graph structures. *Phys. Rev. E*, 2016, **94**, P. 062216.

[26] Yusupov J.R., Sabirov K.K., Ehrhardt M. and Matrasulov D.U. Transparent quantum graphs. *Phys. Lett. A*, 2019, **383**, P. 2382–2388.

[27] Crank J. and Nicolson P. A practical method for numerical evaluation of solutions of partial differential equations of the heat-conduction type. *Advances in Comput. Math.*, 1996, **6**(1), P. 207–226.

[28] Dubeibe F.L. Solving the time-dependent Schrödinger equation with absorbing boundary conditions and source terms in Mathematica 6.0. *Int. J. Mod. Phys. C*, 2010, **21**(11), P. 1391–1406.

[29] Jiang Sh. and Greengard L. Fast evaluation of nonreflecting boundary conditions for the Schrödinger equation in one dimension. *Computers & Mathematics with Applications*, 2004, **47**(6), P. 955–966.

[30] Neuhauser D. and Baer M. The time-dependent Schrödinger equation: Application of absorbing boundary conditions. *J. Chem. Phys.*, 1989, **90**(8), P. 4351–4355.

NANOSYSTEMS: PHYSICS, CHEMISTRY, MATHEMATICS, 2019, 10 (5), P. 511–519

Analytic description of the essential spectrum of a family of 3×3 operator matrices

T. H. Rasulov, N. A. Tosheva

Faculty of Physics and Mathematics, Bukhara State University M. Ikbol str. 11, 200100 Bukhara, Uzbekistan
rth@mail.ru, nargiza_n@mail.ru

DOI 10.17586/2220-8054-2019-10-5-511-519

We consider the family of 3×3 operator matrices $H(K)$, $K \in \mathbb{T}^{\mathrm{d}} := (-\pi;\pi]^{\mathrm{d}}$ arising in the spectral analysis of the energy operator of the spin-boson model of radioactive decay with two bosons on the torus $\mathbb{T}^{\mathrm{d}}$. We obtain an analog of the Faddeev equation for the eigenfunctions of $H(K)$. An analytic description of the essential spectrum of $H(K)$ is established. Further, it is shown that the essential spectrum of $H(K)$ consists the union of at most three bounded closed intervals.

Keywords: family of operator matrices, generalized Friedrichs model, bosonic Fock space, annihilation and creation operators, channel operator, decomposable operator, fiber operators, the Faddeev equation, essential spectrum, Weyl criterion.

Received: 6 October 2019

1. Introduction

In statistical physics [1], solid-state physics [2] and the theory of quantum fields [3], one considers systems, where the number of quasi-particles is not fixed. Their number can be unbounded, as in the case of full spin-boson models (infinite operator matrix) [4] or bounded, as in the case of "truncated" spin-boson models (finite operator matrix) [1, 5–8]. Often, the number of particles can be arbitrarily large as in cases involving photons, in other cases, such as scattering of spin waves on defects, scattering massive particles and chemical reactions, there are only participants at any given time, though their number can be changed.

Recall that the study of systems describing N particles in interaction, without conservation of the number of particles is reduced to the investigation of the spectral properties of self-adjoint operators, acting in the *cut subspace* $\mathcal{H}^{(N)}$ of Fock space, consisting of $n \leq N$ particles [1–3, 9].

The essential spectrum of the Hamiltonians (matrix operators) in the Fock space are the most actively studied objects in operator theory. One of the important problems in the spectral analysis of these operators is to describe the location of the essential spectrum. One of the well-known methods for the investigating the location of essential spectra of operator matrices are Weyl criterion and the Hunziker-van Winter-Zhislin (HWZ) theorem. Using these methods, in many works, the essential spectrum of the 3×3 and 4×4 lattice operator matrices are studied, see e.g., [10–13]. In particular, in [13] it is described the essential spectrum of 4×4 operator matrix by the spectrum of the corresponding channel operators and proved the HWZ theorem. In [9], geometric and commutator techniques have been developed in order to find the location of the spectrum and to prove absence of singular continuous spectrum for Hamiltonians without conservation of the particle number.

In the present paper, we consider the family of 3×3 operator matrices $H(K)$, $K \in \mathbb{T}^{\mathrm{d}}$ associated with the lattice systems describing two identical bosons and one particle, another nature in interactions, without conservation of the number of particles. This operator acts in the direct sum of zero-, one- and two-particle subspaces of the bosonic Fock space and it is a lattice analog of the spin-boson Hamiltonian [1]. In order to study the location of the essential spectrum of $H(K)$, we first introduce the notion of *channel operator* $H_{\mathrm{ch}}(K)$ corresponding to $H(K)$. Using the theorem on the spectrum of decomposable operators we describe the spectrum of $H_{\mathrm{ch}}(K)$ via the spectrum of a family of generalized Friedrichs models $h(K,k)$, $K, k \in \mathbb{T}^{\mathrm{d}}$. Then, we prove that the essential spectrum of $H(K)$ is coincide with the spectrum of $H_{\mathrm{ch}}(K)$ and show that the set $\sigma_{\mathrm{ess}}(H(K))$ consists the union of at most 3 bounded closed intervals. Further, we define the new so-called *two- and three-particle branches* of $\sigma_{\mathrm{ess}}(H(K))$.

We point out that the operator $H(K)$ has been considered before in [14, 15] for a fixed $K \in \mathbb{T}^{\mathrm{d}}$ and studied its essential and discrete spectrum. In this paper, we investigate the essential spectrum of $H(K)$ depending on $K \in \mathbb{T}^{\mathrm{d}}$. It is remarkable that, the essential spectrum and the number of the eigenvalues of a slightly simpler version of $H(K)$ were studied in [16] and the result for the location of the essential spectrum were announced without proof.

The present paper is organized as follows. Section 1 is an introduction to the whole work. In Section 2, the operator matrices $H(K)$, $K \in \mathbb{T}^{\mathrm{d}}$ are described as the family of bounded self-adjoint operators in the direct sum of zero-, one- and two-particle subspaces of the bosonic Fock space and the main aims of the paper are stated. The family of generalized Friedrichs model is introduced and its spectrum is established in Section 3. In Section 4, we determine the channel operator $H_{\mathrm{ch}}(K)$ corresponding to $H(K)$ and define its spectrum. The next Section is devoted to the derivation of the Faddeev equation for the eigenvectors of $H(K)$. In Section 6, we investigate the essential spectrum of $H(K)$ and its new branches.

Throughout this paper, we use the following notation. If A is a linear bounded self-adjoint operator from one Hilbert space to another, then $\sigma(A)$ denotes its spectrum, $\sigma_{\rm ess}(A)$ its essential spectrum and $\sigma_{\rm disc}(A)$ its discrete spectrum.

2. Family of 3×3 operator matrices and its relation with spin-boson models

Let us introduce some notations used in this work. Let $\mathbb{T}^{\rm d}$ be the d-dimensional torus, the cube $(-\pi,\pi]^{\rm d}$ with appropriately identified sides equipped with its Haar measure. Let $\mathcal{H}_0 := \mathbb{C}$ be the field of complex numbers (channel 1), $\mathcal{H}_1 := L^2(\mathbb{T}^{\rm d})$ be the Hilbert space of square integrable (complex) functions defined on $\mathbb{T}^{\rm d}$ (channel 2) and $\mathcal{H}_2 := L^2_{\rm sym}((\mathbb{T}^{\rm d})^2)$ stands for the subspace of $L^2((\mathbb{T}^{\rm d})^2)$ consisting of symmetric functions (with respect to the two variables) (channel 3). We denote by $\mathcal{H}$ the direct sum of spaces $\mathcal{H}_0$, $\mathcal{H}_1$ and $\mathcal{H}_2$, that is, $\mathcal{H} = \mathcal{H}_0 \oplus \mathcal{H}_1 \oplus \mathcal{H}_2$. The spaces $\mathcal{H}_0$, $\mathcal{H}_1$ and $\mathcal{H}_2$ are called zero-, one- and two-particle subspaces of a bosonic Fock space $\mathcal{F}_{\rm s}(L^2(\mathbb{T}^{\rm d}))$ over $L^2(\mathbb{T}^{\rm d})$, respectively, and the Hilbert space $\mathcal{H}$ is called the *truncated* Fock space or the *three-particle cut subspace* of the Fock space. We write elements f of the space $\mathcal{H}$ in the form, $f = (f_0, f_1, f_2)$, $f_i \in \mathcal{H}_i$, $i = 0, 1, 2$ and for any two elements $f = (f_0, f_1, f_2), g = (g_0, g_1, g_2) \in \mathcal{H}$ their scalar product is defined by:

$$(f,g) := f_0\overline{g_0} + \int\limits_{\mathbb{T}^{\rm d}} f_1(t)\overline{g_1(t)}dt + \int\limits_{(\mathbb{T}^{\rm d})^2} f_2(s,t)\overline{g_2(s,t)}dsdt.$$

In the present paper we study the essential spectrum of the family of 3 × 3 tridiagonal operator matrices:

$$H(K) := \begin{pmatrix} H_{00}(K) & H_{01} & 0 \\ H_{01}^* & H_{11}(K) & H_{12} \\ 0 & H_{12}^* & H_{22}(K) \end{pmatrix}, \quad K \in \mathbb{T}^{\rm d} \tag{2.1}$$

in the Hilbert space $\mathcal{H}$. The matrix entries $H_{ii}(K) : \mathcal{H}_i \to \mathcal{H}_i$, $i = 0, 1, 2$ and $H_{ij} : \mathcal{H}_j \to \mathcal{H}_i$, $i < j$, $i, j = 0, 1, 2$ are given by:

$$H_{00}(K)f_0 = w_0(K)f_0, \quad H_{01}f_1 = \int\limits_{\mathbb{T}^{\rm d}} v_0(t)f_1(t)dt,$$

$$(H_{11}(K)f_1)(p) = w_1(K;p)f_1(p), \quad (H_{12}f_2)(p) = \int\limits_{\mathbb{T}^{\rm d}} v_1(t)f_2(p,t)dt,$$

$$(H_{22}(K)f_2)(p,q) = w_2(K;p,q)f_2(p,q), \quad f_i \in \mathcal{H}_i, \quad i = 0, 1, 2.$$

Throughout the paper, we assume that the parameter functions $w_0(\cdot)$, $v_i(\cdot)$, $i = 0, 1$; $w_1(\cdot;\cdot)$ and $w_2(\cdot;\cdot,\cdot)$ are real-valued continuous functions on $\mathbb{T}^{\rm d}$; $(\mathbb{T}^{\rm d})^2$ and $(\mathbb{T}^{\rm d})^3$, respectively. In addition, for any fixed $K \in \mathbb{T}^{\rm d}$ the function $w_2(K;\cdot,\cdot)$ is a symmetric; that is, the equality $w_2(K;p,q) = w_2(K;q,p)$ holds for any $p, q \in \mathbb{T}^{\rm d}$.

Under these assumptions the operator $H(K)$ is bounded and self-adjoint.

We remark that the operators H_{01} and H_{12} resp. H_{01}^* and H_{12}^* are called annihilation resp. creation operators, respectively. A trivial verification shows that:

$$H_{01}^* : \mathcal{H}_0 \to \mathcal{H}_1, \quad (H_{01}^*f_0)(p) = v_0(p)f_0, \quad f_0 \in \mathcal{H}_0;$$

$$H_{12}^* : \mathcal{H}_1 \to \mathcal{H}_2, \quad (H_{12}^*f_1)(p,q) = \frac{1}{2}(v_1(p)f_1(q) + v_1(q)f_1(p)), \quad f_1 \in \mathcal{H}_1.$$

These operators have widespread applications in quantum mechanics, notably in the study of quantum harmonic oscillators and many-particle systems [17]. An annihilation operator lowers the number of particles in a given state by one. A creation operator increases the number of particles in a given state by one, and it is the adjoint of the annihilation operator. In many subfields of physics and chemistry, the use of these operators instead of wavefunctions is known as second quantization. In this paper we consider the case, where the number of annihilations and creations of the particles of the considering system is equal to 1. This means that $H_{ij} \equiv 0$ for all $|i - j| > 1$.

The family of operator matrices of this form plays a key role for the study of the energy operator of the spin-boson model with two bosons on the torus. In fact, the latter is a 6 × 6 operator matrix which is unitary equivalent to a 2 × 2 block diagonal operator with two copies of a particular case of $H(K)$ on the diagonal, see [6]. Consequently, the essential spectrum and finiteness of discrete eigenvalues of the spin-boson Hamiltonian are determined by the corresponding spectral information on the operator matrix $H(K)$ in (2.1).

Independently of whether the underlying domain is a torus or the whole space or the whole space $\mathbb{R}^{\rm d}$, the full spin-boson Hamiltonian is an infinite operator matrix in Fock space for which rigorous results are very hard to obtain. One line of attack is to consider the compression to the truncated Fock space with a finite N of bosons, and in fact, most of the existing literature concentrates on the case $N \leq 2$. For the case of $\mathbb{R}^{\mathrm{d}}$, there some exceptions, see e.g. [4,5] for arbitrary finite N and [8] for $N = 3$, where a rigorous scattering theory was developed for small coupling constants.

For the case when the underlying domain is a torus, the spectral properties $H(K)$ for a fixed K were investigated in [6, 10, 13–15], see also the references therein. The results obtained in this paper for all K will play important role when we study the problem of finding subset $\Lambda \subset \mathbb{T}^{\mathrm{d}}$, such that the operator matrices $H(K)$ have a finite number of or infinitely many eigenvalues for all $K \in \Lambda$.

It is well-known that the three-particle discrete Schrödinger operator $\widehat{H}$ in the momentum representation is the bounded self-adjoint operator on the Hilbert space $L_2((\mathbb{T}^{\mathrm{d}})^3)$. Introducing the total quasimomentum $K \in \mathbb{T}^{\mathrm{d}}$ of the system, it is easy to see that the operator $\widehat{H}$ can undergo decomposition to give the direct integral of the family $\{\widehat{H}(K),\ K \in \mathbb{T}^{\mathrm{d}}\}$ of self-adjoint operators [18, 19]:

$$\widehat{H} = \int\limits_{\mathbb{T}^{\mathrm{d}}} \oplus \widehat{H}(K) dK,$$

where the operator $\widehat{H}(K)$ acts on the Hilbert space $L_2(\Gamma_K)$ ($\Gamma_K \subset (\mathbb{T}^{\mathrm{d}})^2$ is some manifold).

Observe that $H(K)$ enjoys the main spectral properties of the three-particle discrete Schrödinger operator $\widehat{H}(K)$ (see [18, 19]), and the generalized Friedrichs model plays the role of the two-particle discrete Schrödinger operator. For this reason, the Hilbert space $\mathcal{H}$ is called the *three-particle cut subspace* of the Fock space, while the operator matrix $H(K)$ the Hamiltonian of the system with at most three particles on a lattice.

The main aims of the present paper are as follows:

(i) to investigate the spectrum of a family of generalized Friedrichs model;
(ii) to introduce the channel operator $H_{\mathrm{ch}}(K)$ corresponding to $H(K)$ and describe its spectrum;
(iii) to obtain an analog of the Faddeev equation for eigenvectors of $H(K)$;
(iv) to show that the essential spectrum of $H(K)$ is coincident with the spectrum of $H_{\mathrm{ch}}(K)$;
(v) to prove that the essential spectrum of $H(K)$ consists at most three bounded closed intervals;
(vi) to define the new branches of $\sigma_{\mathrm{ess}}(H(K))$.

The next sections are devoted to the discussion of these problems.

3. Family of generalized Friedrichs models and its spectrum

To study the spectral properties of the operator $H(K)$, we introduce a family of bounded self-adjoint operators (generalized Friedrichs models) $h(K, k)$, $K, k \in \mathbb{T}^{\mathrm{d}}$, which acts in the Hilbert space $\mathcal{H}_0 \oplus \mathcal{H}_1$ as 2×2 operator matrices:

$$h(K, k) := \begin{pmatrix} h_{00}(K, k) & h_{01} \\ h_{01}^* & h_{11}(K, k) \end{pmatrix}, \tag{3.1}$$

with matrix elements:

$$h_{00}(K, k) f_0 = w_1(K, k) f_0,\ \ h_{01} f_1 = \frac{1}{\sqrt{2}} \int\limits_{\mathbb{T}^{\mathrm{d}}} v_1(s) f_1(s) ds,$$

$$(h_{11}(K, k) f_1)(q) = w_2(K; k, q) f_1(q), \quad f_i \in \mathcal{H}_i, \quad i = 0, 1.$$

Here,

$$h_{01}^* : \mathcal{H}_0 \to \mathcal{H}_1, \quad (h_{01}^* f_0)(p) = v_1(p) f_0, \quad f_0 \in \mathcal{H}_0.$$

Next we study some spectral properties of the family $h(K, k)$, given by (3.1), which plays a crucial role in the study of the essential spectrum of $H(K)$. We notice that the spectrum, usual eigenvalues, threshold eigenvalues and virtual levels of the typical models for a fixed $K, k \in \mathbb{T}^{\mathrm{d}}$ have been studied in many works, see for example [14,15,20].

Let the operator $h_0(K, k)$, $K, k \in \mathbb{T}^{\mathrm{d}}$ acts in $\mathcal{H}_0 \oplus \mathcal{H}_1$ as:

$$h_0(K, k) := \begin{pmatrix} 0 & 0 \\ 0 & h_{11}(K, k) \end{pmatrix}.$$

The perturbation $h(K, k) - h_0(K, k)$ of the operator $h_0(K, k)$ is a self-adjoint operator of rank 2, and thus, according to the Weyl theorem, the essential spectrum of the operator $h(K, k)$ coincides with the essential spectrum of $h_0(K, k)$. It is evident that:

$$\sigma_{\mathrm{ess}}(h_0(K, k)) = [E_{\min}(K, k); E_{\max}(K, k)],$$

where the numbers $E_{\min}(K,k)$ and $E_{\max}(K,k)$ are defined by:

$$E_{\min}(K,k) := \min_{q\in\mathbb{T}^{\mathrm{d}}} w_2(K;k,q) \quad \text{and} \quad E_{\max}(K,k) := \max_{q\in\mathbb{T}^{\mathrm{d}}} w_2(K;k,q).$$

This yields $\sigma_{\mathrm{ess}}(h(K,k)) = [E_{\min}(K,k); E_{\max}(K,k)]$.

Remark 3.1. *We remark that for some $K,k \in \mathbb{T}^{\mathrm{d}}$ the essential spectrum of $h(K,k)$ may degenerate to the set consisting of the unique point $[E_{\min}(K,k); E_{\min}(K,k)]$ and hence we can not state that the essential spectrum of $h(K,k)$ is absolutely continuous for any $K,k \in \mathbb{T}^{\mathrm{d}}$. For example, this is the case if the function $w_2(\cdot;\cdot,\cdot)$ is of the form:*

$$w_2(K;k,q) = \varepsilon(k) + \varepsilon(q) + \varepsilon(K-k-q),$$

$K = \bar{0} := (0,\ldots,0)$, $k = \bar{\pi} := (\pi,\ldots,\pi) \in \mathbb{T}^{\mathrm{d}}$ and

$$\varepsilon(q) = \sum_{i=1}^{\mathrm{d}} (1-\cos q_i), \quad q = (q_1,\ldots,q_{\mathrm{d}}) \in \mathbb{T}^{\mathrm{d}}.$$

Then $\sigma_{\mathrm{ess}}(h(\bar{0},\bar{\pi})) = \{4\mathrm{d}\}$.

For any fixed $K,k \in \mathbb{T}^{\mathrm{d}}$ we define an analytic function $\Delta_K(k\,;\cdot)$ (the Fredholm determinant associated with the operator $h(K,k)$) in $\mathbb{C} \setminus [E_{\min}(K,k); E_{\max}(K,k)]$ by:

$$\Delta_K(k\,;z) := w_1(K;k) - z - \frac{1}{2} \int\limits_{\mathbb{T}^{\mathrm{d}}} \frac{v_1^2(t)dt}{w_2(K;k,t)-z}.$$

The following lemma [14] is a simple consequence of the Birman-Schwinger principle and the Fredholm theorem.

Lemma 3.2. *For any $K,k \in \mathbb{T}^{\mathrm{d}}$ the operator $h(K,k)$ has an eigenvalue $z(K,k) \in \mathbb{C} \setminus [E_{\min}(K,k); E_{\max}(K,k)]$ if and only if $\Delta_K(k\,;z(K,k)) = 0$.*

From Lemma 3.2 it follows that for the discrete spectrum of $h(K,k)$ the equality:

$$\sigma_{\mathrm{disc}}(h(K,k)) = \{z \in \mathbb{C} \setminus [E_{\min}(K,k); E_{\max}(K,k)] : \Delta_K(k\,;z) = 0\}$$

holds.

The following lemma describes the number and location of the eigenvalues of $h(K,k)$.

Lemma 3.3. *For any fixed $K,k \in \mathbb{T}^{\mathrm{d}}$ the operator $h(K,k)$ has no more than one simple eigenvalue lying on the l.h.s. (resp. r.h.s.) of $E_{\min}(K,k)$ (resp. $E_{\max}(K,k)$).*

The proof of Lemma 3.3 is an elementary and it follows from the fact that for any fixed $K,k \in \mathbb{T}^{\mathrm{d}}$ the function $\Delta_K(k\,;\cdot)$ is a monotonically decreasing on $(-\infty; E_{\min}(K,k))$ and $(E_{\max}(K,k);+\infty)$.

4. The spectrum of channel operator corresponding to $H(K)$

In this section, we define the channel operator $H_{\mathrm{ch}}(K)$ corresponding to $H(K)$ and describe its spectrum by the spectrum of the family of operators $h(K,k)$, $K,k \in \mathbb{T}^{\mathrm{d}}$, defined by (3.1).

We introduce so-called *channel operator* $H_{\mathrm{ch}}(K)$ acting in $L^2(\mathbb{T}^{\mathrm{d}}) \oplus L^2((\mathbb{T}^{\mathrm{d}})^2)$ as a family of 2×2 operator matrices:

$$H_{\mathrm{ch}}(K) := \begin{pmatrix} H_{11}(K) & \frac{1}{\sqrt{2}}H_{12} \\ \frac{1}{\sqrt{2}}H_{12}^* & H_{22}(K) \end{pmatrix}, \quad K \in \mathbb{T}^{\mathrm{d}}. \tag{4.1}$$

It is important that for this case the operator H_{12}^* is defined as follows:

$$H_{12}^* : L^2(\mathbb{T}^{\mathrm{d}}) \to L^2((\mathbb{T}^{\mathrm{d}})^2), \quad (H_{12}^* f_1)(p,q) = v_1(q) f_1(p), \quad f_1 \in L^2(\mathbb{T}^{\mathrm{d}}).$$

Under these assumptions the operator $H_{\mathrm{ch}}(K)$ is bounded and self-adjoint.

We set:

$$m_K := \min_{p,q\in\mathbb{T}^{\mathrm{d}}} w_2(K;p,q), \quad M_K := \max_{p,q\in\mathbb{T}^{\mathrm{d}}} w_2(K;p,q),$$

$$\Lambda_K := \bigcup_{k\in\mathbb{T}^{\mathrm{d}}} \sigma_{\mathrm{disc}}(h(K,k)), \quad \Sigma_K := [m_K; M_K] \cup \Lambda_K.$$

Here, by Lemma 3.2, we may define the set Λ_K as the set of all complex numbers $z \in \mathbb{C} \setminus [E_{\min}(K,k); E_{\max}(K,k)]$ such that the equality $\Delta_K(k\,;z) = 0$ holds for some $k \in \mathbb{T}^{\mathrm{d}}$.

The spectrum of the operator $H_{\mathrm{ch}}(K)$ can be precisely described by the spectrum of the family $h(K,k)$ of generalized Friedrichs models as well as in the following assertion.

Theorem 4.1. *The operator $H_{\mathrm{ch}}(K)$ has a purely essential spectrum and for its spectrum the equality $\sigma(H_{\mathrm{ch}}(K)) = \Sigma_K$ holds.*

Proof. It is clear that the operator $H_{\mathrm{ch}}(K)$ commutes with any multiplication operator U_α by the bounded function $\alpha(\cdot)$ on $\mathbb{T}^{\mathrm{d}}$:

$$U_\alpha \begin{pmatrix} g_1(p) \\ g_2(p,q) \end{pmatrix} = \begin{pmatrix} \alpha(p)g_1(p) \\ \alpha(p)g_2(p,q) \end{pmatrix}, \begin{pmatrix} g_1 \\ g_2 \end{pmatrix} \in L^2(\mathbb{T}^{\mathrm{d}}) \oplus L^2((\mathbb{T}^{\mathrm{d}})^2).$$

Therefore the decomposition of the space $L^2(\mathbb{T}^{\mathrm{d}}) \oplus L^2((\mathbb{T}^{\mathrm{d}})^2)$ into the direct integral:

$$L^2(\mathbb{T}^{\mathrm{d}}) \oplus L^2((\mathbb{T}^{\mathrm{d}})^2) = \int\limits_{\mathbb{T}^{\mathrm{d}}} \oplus (\mathcal{H}_0 \oplus \mathcal{H}_1) dk \tag{4.2}$$

yields the decomposition into the direct integral:

$$H_{\mathrm{ch}}(K) = \int\limits_{\mathbb{T}^{\mathrm{d}}} \oplus\, h(K,k) dk, \tag{4.3}$$

where the fiber operators (a family of the generalized Friedrichs models) $h(K,k)$ are defined by (3.1). We note that identical fibers appear in the direct integral in decomposition (4.2). Then the theorem on the spectrum of decomposable operators [21] gives the equality:

$$\sigma(H_{\mathrm{ch}}(K)) = \bigcup_{k \in \mathbb{T}^{\mathrm{d}}} \sigma(h(K,k)). \tag{4.4}$$

The definition of the set Λ_K and the equality:

$$\bigcup_{k \in \mathbb{T}^{\mathrm{d}}} [E_{\min}(K,k); E_{\max}(K,k)] = [m_K; M_K]$$

imply the equality:

$$\bigcup_{k \in \mathbb{T}^{\mathrm{d}}} \sigma(h(K,k)) = \Sigma_K. \tag{4.5}$$

Now, the equalities (4.4) and (4.5) complete the proof. □

5. The Faddeev equation and main property

In this section, we derive an analog of the Faddeev type system of integral equations for the eigenvectors corresponding to the discrete eigenvalues (isolated eigenvalues with finite multiplicity) of $H(K)$, which plays a crucial role in our analysis of the spectrum of $H(K)$.

For any fixed $K \in \mathbb{T}^{\mathrm{d}}$ and $z \in \mathbb{C} \setminus \Sigma_K$ we introduce a 2×2 block operator matrix $T(K,z)$ acting in $\mathcal{H}_0 \oplus \mathcal{H}_1$ as:

$$T(K,z) := \begin{pmatrix} T_{00}(K,z) & T_{01}(K,z) \\ T_{10}(K,z) & T_{11}(K,z) \end{pmatrix},$$

where the entries $T_{ij}(K,z) : \mathcal{H}_j \to \mathcal{H}_i$, $i,j = 0,1$ are defined by:

$$T_{00}(K,z)g_0 = (1 + w_0(K) - z)g_0, \quad T_{01}(K,z)g_1 = \int\limits_{\mathbb{T}^{\mathrm{d}}} v_0(t)g_1(t)dt;$$

$$(T_{10}(K,z)g_0)(p) = -\frac{v_0(p)g_0}{\Delta_K(p\,;z)}, \quad (T_{11}(K,z)g_1)(p) = \frac{v_1(p)}{2\Delta_K(p\,;z)} \int\limits_{\mathbb{T}^{\mathrm{d}}} \frac{v_1(t)g_1(t)dt}{w_2(K;p,t) - z}.$$

Here, $g_i \in \mathcal{H}_i$, $i = 0,1$. We note that for each $K \in \mathbb{T}^{\mathrm{d}}$ and $z \in \mathbb{C} \setminus \Sigma_K$ the entries $T_{00}(K,z)$, $T_{01}(K,z)$ and $T_{10}(K,z)$ are rank 1 operators, the integral operator $T_{11}(K,z)$ belongs to the Hilbert-Schmidt class and therefore, $T(K,z)$ is a compact operator.

The following theorem is an analog of the well-known Faddeev's result for the operator $H(K)$ and establishes a connection between eigenvalues of $H(K)$ and $T(K,z)$.

Theorem 5.1. *The number $z \in \mathbb{C} \setminus \Sigma_K$ is an eigenvalue of the operator $H(K)$ if and only if the number $\lambda = 1$ is an eigenvalue of the operator $T(K,z)$. Moreover the eigenvalues z and 1 have the same multiplicities.*

Proof. Let $z \in \mathbb{C} \setminus \sum_K$ be an eigenvalue of the operator $H(K)$ and $f = (f_0, f_1, f_2) \in \mathcal{H}$ be the corresponding eigenvector. Then f_0, f_1 and f_2 satisfy the system of equations:

$$\begin{aligned}
&(w_0(K) - z)f_0 + \int\limits_{\mathbb{T}^{\mathrm{d}}} v_0(t)f_1(t)dt = 0;\\
&v_0(p)f_0 + (w_1(K;p) - z)f_1(p) + \int\limits_{\mathbb{T}^{\mathrm{d}}} v_1(t)f_2(p,t)dt = 0; \qquad (5.1)\\
&\frac{1}{2}(v_1(p)f_1(q) + v_1(q)f_1(p)) + (w_2(K;p,q) - z)f_2(p,q) = 0.
\end{aligned}$$

The condition $z \notin [m_K, M_K]$ yields that the inequality $w_2(K;p,q) - z \neq 0$ holds for all $p, q \in \mathbb{T}^{\mathrm{d}}$. Then, from the third equation of the system (5.1) for f_2 we have:

$$f_2(p,q) = -\frac{v_1(q)f_1(p) + v_1(p)f_1(q)}{2(w_2(K;p,q) - z)}. \qquad (5.2)$$

Substituting the expression (5.2) for f_2 into the second equation of the system (5.1), we obtain that the system of equations:

$$\begin{aligned}
&(w_0(K) - z)f_0 + \int\limits_{\mathbb{T}^{\mathrm{d}}} v_0(t)f_1(t)dt = 0;\\
&v_0(p)f_0 + \Delta_K(p\,;z)f_1(p) - \frac{v_1(p)}{2}\int\limits_{\mathbb{T}^{\mathrm{d}}} \frac{v_1(t)f_1(t)dt}{w_2(K;p,t) - z} = 0 \qquad (5.3)
\end{aligned}$$

has a nontrivial solution and this system of equations has a nontrivial solution if and only if the system of equations (5.1) has a nontrivial solution.

By the definition of the set Λ_K the inequality $\Delta_K(p\,;z) \neq 0$ holds for all $z \notin \Lambda_K$ and $p \in \mathbb{T}^{\mathrm{d}}$. Therefore, the system of equations (5.3) has a nontrivial solution if and only if the following system of equations:

$$\begin{aligned}
&f_0 = (1 + w_0(K) - z)f_0 + \int\limits_{\mathbb{T}^{\mathrm{d}}} v_0(t)f_1(t)dt;\\
&f_1(p) = -\frac{v_0(p)f_0}{\Delta_K(p\,;z)} + \frac{v_1(p)}{2\Delta_K(p\,;z)}\int\limits_{\mathbb{T}^{\mathrm{d}}} \frac{v_1(t)f_1(t)dt}{w_2(K;p,t) - z}
\end{aligned}$$

or 2×2 matrix equation:

$$g = T(z)g, \quad g = (f_0, f_1) \in \mathcal{H}_0 \oplus \mathcal{H}_1 \qquad (5.4)$$

has a nontrivial solution and the linear subspaces of solutions of (5.1) and (5.4) have the same dimension. □

Remark 5.2. *We point out that the matrix equation 5.4 is an analog of the Faddeev type system of integral equations for eigenfunctions of the operator $H(K)$ and it is played crucial role in the analysis of the spectrum of $H(K)$.*

6. Essential spectrum and its new branches

In this section, applying the statements of Sections 3–5, the Weyl criterion [21] we investigate the essential spectrum of $H(K)$.

We denote by $\|\cdot\|$ and $(\cdot,\cdot)$ the norm and scalar product in the corresponding Hilbert spaces.

For the convenience of the reader we formulate Weyl's criterion for the essential spectrum of $H(K)$ as follows. First, a number λ is in the spectrum of $H(K)$ if and only if there exists a sequence $\{F_n(K)\}$ in the space $\mathcal{H}$ such that $||F_n(K)|| = 1$ and:

$$\lim_{n\to\infty} \|(H(K) - z_0(K)E)F_n(K)\| = 0. \qquad (6.1)$$

Here, E is an identity operator on $\mathcal{H}$. Furthermore, λ is in the essential spectrum if there is a sequence satisfying this condition, but such that it contains no convergent subsequence (this is the case if, for example $\{F_n(K)\}$ is an orthonormal sequence); such a sequence is called a singular sequence.

The following theorem describes the location of the essential spectrum of $H(K)$.

Theorem 6.1. *The essential spectrum of $H(K)$ is coincide with the spectrum of $H_{\mathrm{ch}}(K)$, that is, $\sigma_{\mathrm{ess}}(H(K)) = \sigma(H_{\mathrm{ch}}(K))$. Moreover the set $\sigma_{\mathrm{ess}}(H(K))$ consists no more than three bounded closed intervals.*

Proof. By the Theorem 4.1, we have $\sigma(H_{\mathrm{ch}}(K)) = \Sigma_K$. Therefore, we must to show that $\sigma_{\mathrm{ess}}(H(K)) = \Sigma_K$. We begin by proving $\Sigma_K \subset \sigma_{\mathrm{ess}}(H(K))$. Since, the set Σ_K has form $\Sigma_K = \Lambda_K \cup [m_K; M_K]$ first we show that $[m_K; M_K] \subset \sigma_{\mathrm{ess}}(H(K))$. Let $z_0(K) \in [m_K; M_K]$ be an arbitrary point. We prove that $z_0(K) \in \sigma_{\mathrm{ess}}(H(K))$. To this end it is suffices to construct a sequence of orthonormal vector-functions $\{F_n(K)\} \subset \mathcal{H}$ satisfying (6.1).

From continuity of the function $w_2(K;\cdot,\cdot)$ on the compact set $(\mathbb{T}^{\mathrm{d}})^2$ it follows that there exists some point $(p_0(K), q_0(K)) \in (\mathbb{T}^{\mathrm{d}})^2$ such that $z_0(K) = w_2(K; p_0(K), q_0(K))$.

For $n \in \mathbb{N}$ we consider the following vicinity of the point $(p_0(K), q_0(K)) \in (\mathbb{T}^{\mathrm{d}})^2$:

$$W_n(K) := V_n(p_0(K)) \times V_n(q_0(K)),$$

where:

$$V_n(p_0(K)) := \Big\{ p \in \mathbb{T}^{\mathrm{d}} : \frac{1}{n+n'+1} < |p - p_0(K)| < \frac{1}{n+n'} \Big\}$$

is the punctured neighborhood of the point $p_0(K) \in \mathbb{T}^{\mathrm{d}}$ and $n' \in \mathbb{N}$ is chosen in such way that $V_n(p_0(K)) \cap V_n(q_0(K)) = \emptyset$ for all $n \in \mathbb{N}$ (provided that $p_0(K) \neq q_0(K)$).

Let $\mu(\Omega)$ be the Lebesgue measure of the set Ω and $\chi_\Omega(\cdot)$ be the characteristic function of the set Ω. We choose the sequence of functions $\{F_n(K)\} \subset \mathcal{H}$ as follows:

$$F_n(K) := \frac{1}{\sqrt{2\mu(W_n(K))}} \begin{pmatrix} 0 \\ 0 \\ \chi_{W_n(K)}(p,q) + \chi_{W_n(K)}(q,p) \end{pmatrix}.$$

It is clear that $\{F_n(K)\}$ is an orthonormal sequence.

For any $n \in \mathbb{N}$ let us consider an element $(H(K) - z_0(K)E)F_n(K)$ and estimate its norm:

$$\|(H(K) - z_0(K)E)F_n(K)\|^2 \leq \sup_{(p,q)\in W_n(K)} |w_2(K;p,q) - z_0(K)|^2 + \mu(V_n(p_0(K))) \max_{p\in\mathbb{T}^{\mathrm{d}}} |v_1(p)|^2.$$

The construction of the set $V_n(p_0(K))$ and the continuity of the function $w_2(K;\cdot,\cdot)$ implies $\|(H(K) - z_0(K)E)F_n(K)\| \to 0$ as $n \to \infty$, i.e. $z_0(K) \in \sigma_{\mathrm{ess}}(H(K))$. Since the point $z_0(K)$ is an arbitrary we have $[m_K; M_K] \subset \sigma_{\mathrm{ess}}(H(K))$.

Now, let us prove that $\Lambda_K \subset \sigma_{\mathrm{ess}}(H(K))$. Taking an arbitrary point $z_1(K) \in \Lambda_K$ we show that $z_1(K) \in \sigma_{\mathrm{ess}}(H(K))$. Two cases are possible: $z_1(K) \in [m_K; M_K]$ or $z_1(K) \notin [m_K; M_K]$. If $z_1(K) \in [m_K; M_K]$, then it is already proven above that $z_1(K) \in \sigma_{\mathrm{ess}}(H(K))$. Let $z_1(K) \in \Lambda_K \setminus [m_K; M_K]$. Definition of the set Λ_K and Lemma 3.2 imply that there exists a point $p_1(K) \in \mathbb{T}^{\mathrm{d}}$ such that $\Delta_K(p_1(K)\,; z_1(K)) = 0$.

We choose a sequence of orthogonal vector-functions $\{\Phi_n(K)\}$ as

$$\Phi_n(K) := \begin{pmatrix} 0 \\ \phi_1^{(n)}(K;p) \\ \phi_2^{(n)}(K;p,q) \end{pmatrix}, \quad \text{where} \quad \phi_1^{(n)}(K;p) := \frac{c_n(K;p)\chi_{V_n(p_1(K))}(p)}{\sqrt{\mu(V_n(p_1(K)))}},$$

$$\phi_2^{(n)}(K;p,q) := -\frac{v_1(p)\phi_1^{(n)}(K;q) + v_1(q)\phi_1^{(n)}(K;p)}{2(w_2(K;p,q) - z_1(K))}.$$

Here, $c_n(K;p) \in L_2(\mathbb{T}^{\mathrm{d}})$ is chosen from the orthonormality condition for $\{\Phi_n(K)\}$, that is, from the condition:

$$(\Phi_n(K), \Phi_m(K)) = \frac{1}{2\sqrt{\mu(V_n(p_1(K)))}\sqrt{\mu(V_m(p_1(K)))}} \times \int\limits_{V_n(p_1(K))} \int\limits_{V_m(p_1(K))} \frac{v_1(p)v_1(q)c_n(K;p)c_m(K;q)}{(w_2(K;p,q) - z_1(K))^2} dpdq = 0 \tag{6.2}$$

for $n \neq m$. The existence of $\{c_n(K;\cdot)\}$ is a consequence of the following proposition.

Proposition 6.2. *There exists an orthonormal system* $\{c_n(K;\cdot)\} \subset L_2(\mathbb{T}^{\mathrm{d}})$ *satisfying the conditions* $\operatorname{supp} c_n(K;\cdot) \subset V_n(p_1(K))$ *and* (6.2).

Proof of Proposition 6.2. We construct the sequence $\{c_n(K;\cdot)\}$ by the induction method. Suppose that $c_1(K;p) := \chi_{V_1(p_1(K))}(p) \left(\sqrt{\mu(V_1(p_1(K)))}\right)^{-1}$. Now, we choose the function $\widetilde{c}_2(K;\cdot) \in L_2(V_2(p_1(K)))$ so that $\|\widetilde{c}_2(K;\cdot)\| = 1$ and $(\widetilde{c}_2(K;\cdot), \varepsilon_1^{(2)}(K;\cdot)) = 0$, where

$$\varepsilon_1^{(2)}(K;p) := v_1(p)\chi_{V_2(p_1(K))}(p) \int\limits_{\mathbb{T}^{\mathrm{d}}} \frac{v_1(q)c_1(K;q)dq}{(w_2(K;p,q) - z_1(K))^2}.$$

We set $c_2(K;p) := \widetilde{c}_2(K;p)\chi_{V_1(p_1(K))}(p)$. We continue this process. Suppose that $c_1(K;p), \ldots, c_n(K;p)$ are constructed. Then the function $\widetilde{c}_{n+1}(K;\cdot) \in L_2(V_{n+1}(p_1(K)))$ is chosen so that it is orthogonal to all functions:

$$\varepsilon_m^{(n+1)}(K;p) := v_1(p)\chi_{V_{n+1}(p_1(K))}(p) \int\limits_{\mathbb{T}^{\mathrm{d}}} \frac{v_1(q)c_m(K;q)dq}{(w_2(K;p,q)-z_1(K))^2}, \quad m = 1, \ldots, n$$

and $\|\widetilde{c}_{n+1}(K;\cdot)\| = 1$. Let $c_{n+1}(K;p) := \widetilde{c}_{n+1}(K;p)\chi_{V_{n+1}(p_1(K))}(p)$. Thus, we have constructed the orthonormal system of functions $\{c_n(K;\cdot)\}$ satisfying the assumptions of the proposition. Proposition 6.2 is proved. ☐

We continue the proof of Theorem 6.1. Now for $n \in \mathbb{N}$ we consider $(H(K) - z_1(K)E)\Phi_n(K)$ and estimate its norm as:

$$\begin{aligned} \|(H(K) - z_1(K)E)\Phi_n(K)\|^2 &\leq C(K) \max_{p \in \mathbb{T}^{\mathrm{d}}} v_1^2(p)\, \mu(V_n(p_1(K))) \\ &\quad + 2 \sup_{p \in V_n(p_1(K))} |\Delta_K(p;\, z_1(K))|^2 \end{aligned} \tag{6.3}$$

for some $C(K) > 0$.

Since $\mu(V_n(p_1(K))) \to 0$ and $\sup\limits_{p \in V_n(p_1(K))} |\Delta_K(p;\, z_1(K))|^2 \to 0$ as $n \to \infty$, from the (6.3) it follows that $\|(H(K) - z_1(K)E)\Phi_n(K)\| \to 0$ as $n \to \infty$. This implies $z_1(K) \in \sigma_{\mathrm{ess}}(H(K))$. Since the point $z_1(K)$ is an arbitrary, we have $\Lambda_K \subset \sigma_{\mathrm{ess}}(H(K))$. Therefore, we proved that $\Sigma_K \subset \sigma_{\mathrm{ess}}(H)$.

Now, we prove the inverse inclusion, i.e. $\sigma_{\mathrm{ess}}(H(K)) \subset \Sigma_K$. Since for each $z \in \mathbb{C} \setminus \Sigma_K$ the operator $T(K;z)$ is a compact-operator-valued function on $\mathbb{C}\backslash\Sigma_K$, from the self-adjointness of $H(K)$ and Theorem 5.1 it follows that the operator $(I - T(K,z))^{-1}$ exists if z is real and has a large absolute value. The analytic Fredholm theorem (see, e.g., Theorem VI.14 in [21]) implies that there is a discrete set $S_K \subset \mathbb{C} \setminus \Sigma_K$ such that the function $(I - T(K,z))^{-1}$ exists and is analytic on $\mathbb{C} \setminus (S_K \cup \Sigma_K)$ and is meromorphic on $\mathbb{C} \setminus \Sigma_K$ with finite-rank residues. This implies that the set $\sigma(H(K)) \setminus \Sigma_K$ consists of isolated points, and the only possible accumulation points of Σ_K can be on the boundary. Thus:

$$\sigma(H(K)) \setminus \Sigma_K \subset \sigma_{\mathrm{disc}}(H(K)) = \sigma(H(K)) \setminus \sigma_{\mathrm{ess}}(H(K)).$$

Therefore, the inclusion $\sigma_{\mathrm{ess}}(H(K)) \subset \Sigma_K$ holds. Finally we obtain the equality $\sigma_{\mathrm{ess}}(H(K)) = \Sigma_K$.

By Lemma 3.3 for any $K, k \in \mathbb{T}^{\mathrm{d}}$ the operator $h(K,k)$ has no more than one simple eigenvalue on the l.h.s. (resp. r.h.s) of $E_{\min}(K,k)$ (resp. $E_{\max}(K,k)$). Then, by the theorem on the spectrum of decomposable operators [21] and by the definition of the set Λ_K it follows that the set Λ_K consists of the union of no more than two bounded closed intervals. Therefore, the set Σ_K consists of the union of no more than three bounded closed intervals. Theorem 6.1 is completely proved. ☐

In the following we introduce the new subsets of the essential spectrum of $H(K)$.

Definition 6.3. *The sets Λ_K and $[m_K; M_K]$ are called two- and three-particle branches of the essential spectrum of $H(K)$, respectively.*

It is obvious that for a given $H(K)$, the operator $H_{\mathrm{ch}}(K)$ is uniquely selected by the property of decomposability into a direct integral.

According to Theorem 6.1, the operator $H_{\mathrm{ch}}(K)$ have the characteristic property of a channel operator of the corresponding discrete Schrödinger operator, see [18,19]. Therefore, we call this operator the channel operator associated with $H(K)$. We note that the channel operator $H_{\mathrm{ch}}(K)$ have a more simple structure than the operator $H(K)$, and hence, Theorem 6.1 plays an important role in the subsequent investigations of the essential spectrum of $H(K)$.

Since for any $K \in \mathbb{T}^{\mathrm{d}}$ and $z \in \mathbb{C} \setminus \Sigma_K$ the operators $T_{00}(K,z)$, $T_{01}(K,z)$ and $T_{10}(K,z)$ are one dimensional and the kernel of $T_{11}(K,z)$ is a continuous function on $(\mathbb{T}^{\mathrm{d}})^2$, the Fredholm determinant $\Omega_K(z)$ of the operator $I - T(K,z)$, where I is the identity operator in $\mathcal{H}_0 \oplus \mathcal{H}_1$, exists and is a real-analytic function on $\mathbb{C} \setminus \Sigma_K$.

According to Fredholm's theorem [21] and Theorem 5.1 the number $z \in \mathbb{C} \setminus \Sigma_K$ is an eigenvalue of $H(K)$ if and only if $\Omega_K(z) = 0$, that is:

$$\sigma_{\mathrm{disc}}(H(K)) = \{z \in \mathbb{C} \setminus \Sigma_K : \Omega_K(z) = 0\}.$$

References

[1] Minlos R.A., Spohn H. The three-body problem in radioactive decay: the case of one atom and at most two photons. *Topics in Statistical and Theoretical Physics. Amer. Math. Soc. Transl.*, Ser. 2, **177**, AMS, Providence, RI, 1996, P. 159–193.

[2] Mogilner A.I. Hamiltonians in solid state physics as multiparticle discrete Schrödinger operators: problems and results. *Advances in Sov. Math.*, 1991, **5**, P. 139–194.

[3] Friedrichs K.O. *Perturbation of spectra in Hilbert space*. Amer. Math. Soc. Providence, Rhole Island, 1965.

[4] Hübner M., Spohn H. Spectral properties of the spin-boson Hamiltonian. *Ann. Inst. H. Poincaré. Phys. Théor.*, 1995, **62**(3), P. 289–323.

[5] Hübner M., Spohn H. *Atom interacting with photons: an N-body Schrödinger problem*. Tech. rep., 1994.

[6] Muminov M., Neidhardt H., Rasulov T. On the spectrum of the lattice spin-boson Hamiltonian for any coupling: 1D case. *Journal of Mathematical Physics*, 2015, **56**, P. 053507.

[7] Rasulov T.Kh. Branches of the essential spectrum of the lattice spin-boson model with at most two photons. *Theoretical and Mathematical Physics*, 2016, **186**(2), P. 251–267.

[8] Zhukov Yu.V., Minlos R.A. The spectrum and scattering in the "spin-boson" model with at most three photons. *Theor. Math. Phys.*, 1995, **103**(1), P. 63–81.

[9] Sigal I.M., Soffer A., Zielinski L. On the spectral properties of Hamiltonians without conservation of the particle number. *J. Math. Phys.*, 2002, **42**(4), P. 1844–1855.

[10] Lakaev S.N., Rasulov T.Kh. A model in the theory of perturbations of the essential spectrum of multi-particle operators. *Math. Notes*, 2003, **73**(4), P. 521–528.

[11] Muminov M.I., Rasulov T.Kh. An eigenvalue multiplicity formula for the Schur complement of a 3×3 block operator matrix. *Siberian Math. J.*, 2015, **56**(4), P. 878-895.

[12] Rasulov T.H. Investigations of the essential spectrum of a Hamiltonian in Fock space. *Appl. Math. Inf. Sci.*, 2010, **4**(3), P. 395–412.

[13] Rasulov T.H., Muminov M.I., Hasanov M. On the spectrum of a model operator in Fock space. *Methods Funct. Anal. Topology*, 2009, **15**(4), P. 369–383.

[14] Albeverio S., Lakaev S.N., Rasulov T.H. On the spectrum of an Hamiltonian in Fock space. Discrete spectrum asymptotics. *J. Stat. Phys.*, 2007, **127**(2), P. 191–220.

[15] Albeverio S., Lakaev S.N., Rasulov T.H. The Efimov effect for a model operator associated with the Hamiltonian of a non conserved number of particles. *Methods Funct. Anal. Topology*, 2007, **13**(1), P. 1–16.

[16] Muminov M.I., Rasulov T.H. On the number of eigenvalues of the family of operator matrices. *Nanosystems: Physics, Chemistry, Mathematics*, 2014, **5**(5), P. 619–626.

[17] Feynman R.P. *Statistical Mechanics: A Set of Lectures* (2nd ed.). Reading, Massachusetts: Addison-Wesley, 1998.

[18] Lakaev S.N., Muminov M.É. Essential and discrete spectra of the three-particle Schrödinger operator on a lattices. *Theor. Math. Phys.*, 2003, **135**(3), P. 849–871.

[19] Albeverio S., Lakaev S.N., Muminov Z.I. On the structure of the essential spectrum for the three-particle Schrödinger operators on lattices. *Math. Nach.*, 2007, **280**, P. 699–716.

[20] Rasulov T.H., Dilmurodov E.B. Eigenvalues and virtual levels of a family of 2×2 operator matrices. *Methods Funct. Anal. Topology*, 2019, **25**(3), P. 273–281.

[21] Reed M., Simon B. *Methods of modern mathematical physics*. IV: Analysis of Operators. Academic Press, New York, 1979.

[22] Malishev V.A., Minlos R.A. *Linear infinite-particle operators*. Translations of Mathematical Monographs. 143, AMS, Providence, RI, 1995.

NANOSYSTEMS: PHYSICS, CHEMISTRY, MATHEMATICS, 2019, 10 (5), P. 520–529

Recombination radiation associated with A^+-centers in quantum dots in an external magnetic field

V. D. Krevchik[1], A. V. Razumov[1], P. S. Budyansky[1], M. B. Semenov[1], I. M. Moyko[1], N. N. Khvastunov[2]

[1]Penza State University, Krasnaya str., 40, Penza, 440026, Russia
[2]Mordovian State Pedagogical Institute named after M. E. Yevseviev,
Studend str., 11 “a”, Saransk, Mordovian Rep., 430007, Russia

physics@pnzgu.ru

PACS 73.40.Gk, 03.65.Xp **DOI 10.17586/2220-8054-2019-10-5-520-529**

The effect of an external magnetic field on the binding energy of a hole in an impurity complex $A^+ + e$ in a spherically symmetric quantum dot, as well as frequency dependence of the spectral intensity of recombination radiation of the quasi-zero-dimensional structure with impurity complexes $A^+ + e$ have been investigated. It is shown that in an external magnetic field there is a spatial anisotropy for the binding energy of A^+-state due to hybrid quantization in the quantum dot radial plane and dimensional quantization in the direction of an external magnetic field. It is shown that in an external magnetic field the spectral intensity curve of the recombination radiation shifts to the short-wavelength region of the spectrum and probability of the radiative transition of an electron to the level of A^+-center increases, which is caused by increase in the overlap integral of the envelope wave functions of a hole bound at the A^+-center and of an electron localized in the ground state of quantum dot.

Keywords: recombination radiation, quantum dots.

Received: 5 September 2019

Revised: 12 September 2019

1. Introduction

In recent years, interest in studying an external magnetic field’s influence on the photoluminescence (PL) of structures with quantum wells (QWs) and quantum dots (QDs) has not been weakened [1–15]. This is due, first of all, to modification of the optical spectrum of nanostructures, impurity and exciton states, which leads to new interesting effects in the photoluminescence and optical absorption spectra under application of external magnetic field conditions. For example, circular polarization of the PL peak associated with A^+-centers was first measured in the case of the QWs of GaAs/ AlGaAs, and analysis of which has made it possible to determine the fine, spin and energy structure of the A^+-center [1]. In [5], PL spectra were studied in an external magnetic field of an ensemble of QD-InAs grown by method of the molecular-beam epitaxy on a (001) GaAs substrate disoriented in the (010)-direction. It was established in [5] that in an external magnetic field, the capture of the photo-borne carriers in an array of QDs, which have been formed as a result of coalescence, is suppressed, and as a result, an increase in the PL intensity has been observed. A magnetic field also exerts an influence on the kinetics of the QD-photoluminescence. Thus, in [3], an acceleration of the photoluminescence kinetics of the QD-InAs in the AlAs matrix in an external 5 T – magnetic field has been observed. The obtained results are explained in the framework of a model that takes into account the exchange and Zeeman splitting of the QD exciton levels in an external magnetic field [3].

The present work is devoted to the theoretical study of an external magnetic field’s influence on the binding energy of a hole in an impurity complex $A^+ + e$ in a spherically symmetric QD, as well as on the frequency dependence of the recombination radiation spectral intensity (SIRI) of a quasi-zero-dimensional structure with impurity complexes $A^+ + e$.

2. Model

Let us consider the problem of the hole bound states in an impurity complex $A^+ + e$ of a semiconductor spherically symmetric QD in an external magnetic field. The potential of an infinitely deep spherically symmetric well has been used as a model of the QD confinement potential:

$$U(\rho) = \begin{cases} 0, & \text{if } \rho \leq R_0; \\ \infty, & \text{if } \rho \geq R_0, \end{cases} \tag{1}$$

where R_0 – the QD radius. Interaction of an electron in the ground state of QD with a hole localized at the A^0-center will be considered in the framework of the adiabatic approximation [4]. In this case, the electron potential, $V_{n,l,m}(r)$, acting on the hole, can be considered as averaged one over the electron motion [4]:

$$V_{n,l,m}(\vec{r}) = -\frac{e^2}{4\pi\varepsilon_0\varepsilon}\int\limits_0^{R_0}\frac{\left|\Psi_{n,l,m}(\vec{r}_e)\right|^2}{\left|\vec{r}-\vec{r}_e\right|}d\vec{r}_e, \tag{2}$$

Where e – the electron charge; ε – dielectric constant of the QD material; ε_0 – the electric constant; $\Psi_{n,l,m}(\vec{r})$ – the electron wave function in QD; $m = 0,\ \pm1,\ \pm2\ldots$ – the magnetic quantum number; $l = 0,\ 1,\ 2\ldots$ – the orbital quantum number.

In the first order of perturbation theory, for the ground state of an electron ($m = 0,\ l = 0$), potential (2) can be written in the next form:

$$V_{n,0,0}(\rho) = -\frac{e^2\beta_n}{4\pi\varepsilon_0\varepsilon R_0} + \frac{m_h^*}{2}\left(\omega_n^2 + \frac{\omega_B^2}{2}\right)\rho^2 + \frac{m_h^* z^2}{2}\omega_n^2, \tag{3}$$

where $\beta_n = \gamma_0 - \mathrm{Ci}(2\pi n) + \ln(2\pi n)$; $\hbar\omega_n = \left[\left(2\hbar^2\pi^2 n^2 e^2\right)/\left(3m_h^* R_0^3 4\pi\varepsilon_0\varepsilon\right)\right]^{1/2}$; ρ,φ,z – cylindrical coordinates; $\gamma_0 = 1.781$ – the Euler constant; $\mathrm{Ci}(x)$ – the integral cosine; n – the electron radial quantum number; m_h^* – the hole effective mass; $\omega_B = |e|\,B/m^*$ – the cyclotron frequency.

It can be shown that the wave function and energy spectrum corresponding to potential (3) have the next form:

$$\Psi_{n_1,m,n_2}(\rho,\varphi,z) = \frac{1}{a_1^2}\left(\frac{n_1!}{2^{n_2+1}\pi^{3/2}n_2!\,(n_1+|m|)!\,a_n}\right)^{1/2}\left(\frac{\rho^2}{2a_1^2}\right)^{|m|/2}\times$$
$$\exp\left[-\left(\frac{\rho^2}{4a_1^2}+\frac{z^2}{2a_n^2}\right)\right]H_{n_2}\left(\frac{z}{a_n}\right)L_{n_1}^{|m|}\left(\frac{\rho^2}{2a_1^2}\right)\exp(im\varphi), \tag{4}$$

where $n_1,\ n_2 = 0,\ 1,\ 2,\ldots$ – quantum numbers corresponding to Landau levels and to energy levels of an oscillating spherically symmetric well; $a_1^2 = a_n^2/\left(2\sqrt{1+a_n^4/\left(4a_B^4\right)}\right)$; $a_n = \sqrt{\hbar/\left(m_h^*\omega_n\right)}$ – the characteristic oscillator length; $a_B = \sqrt{\hbar/\left(m^*\omega_B\right)}$ – the magnetic length; $H_n(x)$, $L_n^c(x)$ – the Hermite and Lagger polynomials, respectively.

$$E_{n_1,m,n_2}^{n,0,0} = -\frac{e^2}{4\pi\varepsilon_0\varepsilon R_0}\beta_n + \hbar\omega_n\left(n_2+\frac{1}{2}\right) + \hbar\omega_n\left(2n_1+|m|+1\right)\sqrt{1+\frac{\omega_B^2}{8\omega_n^2}} + \frac{\hbar\omega_B m}{2}. \tag{5}$$

The short-range impurity potential is described in terms of the zero-radius potential model:

$$V_\delta(\rho,\varphi,z;\ \rho_a,\varphi_a,z_a) = \gamma\frac{\delta(\rho-\rho_a)}{\rho}\delta(\varphi-\varphi_a)\,\delta(z-z_a)\left[1+(\rho-\rho_a)\frac{\partial}{\partial\rho}+(z-z_a)\frac{\partial}{\partial z}\right], \tag{6}$$

where $\gamma = 2\pi\hbar^2/\left(\alpha m_h^*\right)$ – the zero radius potential power; α is determined by the bound state energy E_i of the same A^+-center in a bulk semiconductor; ρ_a, z_a – coordinates of the A^+-center in QD.

The one-hole Green function $G(\rho,\varphi,z,\ \rho_a,\varphi_a,z_a,\ E_{\lambda h})$ to the Schrödinger equation, corresponding to the source at the point $\vec{r}_1 = (\rho_1,\varphi_1,z_1)$ and to the energy $E_{\lambda h}$, can be written as

$$G(\rho,\varphi,z,\ \rho_a,\varphi_a,z_a,\ E_n) = -\sum_{n_1,m,n_2}\frac{\Psi_{n_1,m,n_2}^{(n)*}(\rho_1,\varphi_1,z_1)\,\Psi_{n_1,m,n_2}^{(n)}(\rho,\varphi,z)}{|E_{\lambda h}| + E_{n_1,m,n_2}^{n,0,0}}, \tag{7}$$

where $E_{\lambda h}$ – the hole binding energy, measured from the bottom of the electron adiabatic potential.

Using the expressions for the single-particle wave functions (4) and for the energy spectrum (5), for the Green function $G(\rho,\varphi,z,\ \rho_a,\varphi_a,z_a,\ E_n)$ in units of the effective Bohr energy $E_h = \hbar^2/\left(2m_h^* a_h^2\right)$ and the effective Bohr radius of the hole $a_h = 4\pi\varepsilon_0\varepsilon\hbar^2/\left(m_h^*\,|e|^2\right)$, we obtain

$$\begin{aligned}
G\left(\rho,\varphi,z,\,\rho_a,\varphi_a,z_a,\,E_{\lambda h}\right) &= \frac{-\beta_h}{2\pi^{3/2}a_n^3E_h}\exp\left[-\left(\frac{\rho^2+\rho_a^2}{4a_1^2}+\frac{z^2+z_a^2}{2a_n^2}\right)\right]\times \\
&\int\limits_0^{+\infty} dt\,\exp\left[-\left(\eta_{\lambda h}^2\beta_h-\beta_0+w+1\right)t\right]\sum_{n_2=0}^{\infty}\left(\frac{e^{-t}}{2}\right)^{n_2}\frac{H_{n_2}\left(\frac{z_a}{a_n}\right)H_{n_2}\left(\frac{z}{a_n}\right)}{n_2!}\times \\
&\sum_{m=-\infty}^{+\infty}\exp\left(-w\,|m|\,t\right)\left(\frac{\rho^2\rho_a^2}{2a_1^2}\right)^{|m|}\exp\left(im\left(\left(\varphi-\varphi_a\right)-\beta_h\left(a^*\right)^{-2}t\right)\right)\times \\
&\sum_{n_1=0}^{+\infty}\frac{n_1!}{\left(n_1+|m|\right)!}L_{n_1}^{|m|}\left(\frac{\rho^2}{2a_1^2}\right)L_{n_1}^{|m|}\left(\frac{\rho_a^2}{2a_1^2}\right)\exp\left[-2n_1wt\right],
\end{aligned}\tag{8}$$

here $\eta_{\lambda h}^2 = \left|E_{\lambda h}\right|/E_h$; $\beta_0 = \beta_n^s e^2/\left(4\pi\varepsilon_0\varepsilon R_0^* a_h E_h\right)$; $R_0^* = R_0/a_h$; $\beta_h = E_h/\hbar\omega_n$; $a^* = a_B/a_h$; $w = \sqrt{1+\beta_h^2\left(a^*\right)^{-4}}/2$.

Summation over a quantum number n_2 can be performed using the Mehler formula:

$$\sum_{n_2=0}^{\infty}\left(\frac{e^{-t}}{2}\right)^{n_2}\frac{H_{n_2}\left(\frac{z_a}{a_n}\right)H_{n_2}\left(\frac{z}{a_n}\right)}{n_2!} = \frac{1}{\sqrt{1-e^{-2t}}}\exp\left\{\frac{2z_az\,e^{-t}-\left(z_a^2+z^2\right)e^{-2t}}{a_n^2\left(1-e^{-2t}\right)}\right\}. \tag{9}$$

Using the Hille–Hardy formula for the bilinear generating function of the Laguerre polynomials, it is possible to sum the series over the quantum number n_1:

$$\begin{aligned}
&\sum_{n_1=0}^{\infty}\frac{n_1!}{\left(n_1+|m|\right)!}L_{n_1}^{|m|}\left(\frac{\rho_a^2}{2a_1^2}\right)L_{n_1}^{|m|}\left(\frac{\rho^2}{2a_1^2}\right)\exp\left(-2n_1wt\right) = \\
&\left(\frac{\rho_a\rho}{2a_1^2}\right)^{-|m|}\exp\left[|m|\,wt\right]\times\left(1-\exp\left(-2wt\right)\right)^{-1}\exp\left(-\exp\left(-2wt\right)\frac{\left(\rho_a^2+\rho^2\right)}{2a_n^2\left(1-\exp\left(-2wt\right)\right)}\right)\times \\
&I_{|m|}\left(\frac{\rho_a\rho\,\exp\left(-wt\right)}{2a_1^2\left(1-\exp\left(-2wt\right)\right)}\right).
\end{aligned}\tag{10}$$

Summation over the magnetic quantum number m gives:

$$\begin{aligned}
&\sum_{m=-\infty}^{+\infty}\exp\left[\left(i\left(\varphi-\varphi_a\right)-\beta_h\left(a^*\right)^{-2}t\right)m\right]I_{|m|}\left(\frac{\rho_a\rho\exp\left(-wt\right)}{2a_1^2\left(1-\exp\left(-2wt\right)\right)}\right) = \\
&\exp\left[\left(\exp\left[i\left(\varphi-\varphi_a\right)-\beta_h\left(a^*\right)^{-2}t\right]+\exp\left[-i\left(\varphi-\varphi_a\right)+\beta_h\left(a^*\right)^{-2}t\right]\right)\times\frac{\rho_a\rho\exp\left(-wt\right)}{2a_1^2\left(1-\exp\left(-2wt\right)\right)}\right].
\end{aligned}\tag{11}$$

Taking into account (9) – (11), after separation of the diverging part, we obtain:

$$G\left(\rho,\varphi,z,\,\rho_a,\varphi_a,z_a;E_{\lambda h}\right) =$$

$$
-\frac{1}{(2\pi)^{3/2}\sqrt{\beta_h}E_h a_h^3}\Bigg\{\exp\left[-\frac{\left(\rho_a^2+\rho^2\right)w+z_a^2+z^2}{4\beta_h a_h^2}\right]\times
\int\limits_0^{+\infty} dt\,\exp\left[-\left(\beta_h\eta_{\lambda h}^2-\beta_0+w+1/2\right)t\right]\times
$$

$$
\left[w\left(1-e^{-2t}\right)^{-1/2}\left(1-\exp\left[-2wt\right]\right)\times\exp\left\{\frac{2z_a z\,e^{-t}-\left(z_a^2+z^2\right)\,e^{-2t}}{2\beta_h a_h^2\left(1-e^{-2t}\right)}\right\}\times\right.
$$

$$
\exp\left[-\exp\left(-2wt\right)\frac{\left(\rho_a^2+\rho^2\right)w}{2\beta_h a_h^2\left(1-\exp\left[-2wt\right]\right)}\right]\times
$$

$$
\exp\left[\frac{1}{2}\left(\exp\left[i\left(\varphi-\varphi_a\right)-\beta_h\left(a^*\right)^{-2}t\right]+\exp\left[-i\left(\varphi-\varphi_a\right)+\beta_h\left(a^*\right)^{-2}t\right]\right)\times\frac{w\rho_a\rho\,\exp\left(-wt\right)}{\beta_h a_h^2\left(1-\exp\left(-2wt\right)\right)}\right]-
$$

$$
\left.t^{-3/2}\exp\left[-\frac{\left(\rho-\rho_a\right)^2w+\left(z-z_a\right)^2}{4\beta_h a_h^2 t}\right]\right]+2\sqrt{\pi\beta_h}a_h\frac{\exp\left[-\sqrt{\frac{\left(2\beta_h\eta_{\lambda h}^2-2\beta_0+2w+1\right)\left(\left(\rho-\rho_a\right)^2w+\left(z-z_a\right)^2\right)}{2\beta_h a_h^2}}\right]}{\sqrt{\left(\rho-\rho_a\right)^2w+\left(z-z_a\right)^2}}\Bigg\}. \quad (12)
$$

The bound state energy of a hole in the total field (including the zero radius well located at a point $\vec{R}_a=(\vec{\rho}_a,\,z_a)$) is the pole of the Green's function, i.e. the equation solution:

$$
\alpha=\frac{2\pi\hbar^2}{m^*}\left(\mathbf{T}G\right)\left(\rho_a,\varphi_a,z_a,\rho_a,\varphi_a,z_a;E_{\lambda h}\right), \quad (13)
$$

where

$$
\left(\mathbf{T}G\right)\left(\rho_a,\varphi_a,z_a,\rho_a,\varphi_a,z_a;E_{\lambda h}\right)=\lim_{\substack{\rho\to\rho_a\\ \varphi\to\varphi_a\\ z\to z_a}}\left[1+\left(\rho-\rho_a\right)\partial/\partial\rho+\left(z-z_a\right)\partial/\partial z\right]\times G\left(\rho,\varphi,z,\rho_a,\varphi_a,z_a;E_{\lambda h}\right).
$$

Substituting (12) into (13), we obtain the dispersion equation for a hole, localized at the QD A^+-center in a magnetic field:

$$
\sqrt{\eta_{\lambda h}^2-\beta_0\beta_h^{-1}+\left(2\beta_h\right)^{-1}+w\beta_h^{-1}}=\eta_i-\sqrt{\frac{2}{\pi\beta_h}}\int\limits_0^{+\infty} dt\;\exp\left[-\left(\beta_h\eta_{\lambda h}^2-\beta_0+w+1/2\right)t\right]\times
$$

$$
\left[\frac{1}{2t\sqrt{2t}}-w\left(1-e^{-2t}\right)^{-1/2}\left(1-\exp\left(-2wt\right)\right)^{-1}\exp\left[-\frac{\left(z_a^*\right)^2}{2\beta_h}\cot\left(\frac{t}{2}\right)\right]\times\right.
$$

$$
\left.\exp\left[-\frac{w\left(\rho_a^*\right)^2}{2\beta_h\left(1-\exp\left(-2wt\right)\right)}\left(1+\exp\left(-2wt\right)-2\exp\left(-wt\right)\cosh\left(\beta_h\left(a^*\right)^{-2}t\right)\right)\right]\right], \quad (14)
$$

where $\eta_i^2=\left|E_i\right|/E_h$; E_i – the bound state energy of a hole localized at the same A^+-center in a bulk semiconductor; $z_a^*=z_a/a_h$; $\rho_a^*=\rho_a/a_h$.

Let us consider the process of the radiative transition of an excited electron to the A^+-center level. To calculate the frequency dependence of the recombination radiation spectral intensity (SIRR), it is necessary to obtain an expression for the wave function of an electron localized in the ground state of a spherically symmetric QD in a magnetic field. In the second order of perturbation theory, the energy spectrum of an electron in an external magnetic field can be written as

$$
E=E^{(0)}+V_{n,l,m;\,n,l,m}+\sum_{n'\,l'\,m'}\frac{\left(R_0^*\right)^2\left|V_{n,l,m;\,n',l',m'}\right|^2}{\pi^2-\tilde{X}_{n',l'}^2}, \quad (15)
$$

here $\tilde{X}_{n',l'}$ – the root of the Bessel function of a half-integer order $l+1/2$, $E^{(0)}=\tilde{X}_{n,l}^2E_h/\left(R_0^*\right)^2$ – zero approach to electron energy in the size-quantized band, $V_{n,l,m;\,n',l',m'}$ – matrix element of the perturbation operator, which in spherical coordinates has the form:

$$
\hat{V}_{n,l,m;\,n',l',m'}=-\frac{i\hbar\omega_B}{2}\frac{\partial}{\partial\varphi}+\frac{m_h^*\omega_B^2}{2}r^2\sin^2\theta. \quad (16)
$$

In the second order of perturbation theory, the electron wave function is given by an expression of the form:

$$\Psi_{n,l,m}\left(r,\theta,\varphi\right)=\Psi^{(0)}_{n,l,m}\left(r,\theta,\varphi\right)+\sum_{n'l'm'}\frac{\left(R_0^*\right)^2 V_{n,l,m;\,n',l',m'}}{\pi^2-\tilde{X}^2_{n',l'}}\Psi^{(0)}_{n',l',m'}\left(r,\theta,\varphi\right), \tag{17}$$

where $\Psi^{(0)}_{n,l,m}\left(r,\theta,\varphi\right)$ – the zero approximation wave function:

$$\Psi^{(0)}_{n,l,m}\left(r,\theta,\varphi\right)=Y_{l,m}\left(\theta,\varphi\right)\frac{J_{l+3/2}\left(\frac{\tilde{X}_{n,l}}{R_0^*}r^*\right)}{a_h^{3/2}\sqrt{2\pi}R_0^*\sqrt{r^*}J_{l+3/2}\left(\tilde{X}_{n,l}\right)}. \tag{18}$$

The matrix element $V_{n,l,m;\,n',l',m'}$ of the perturbation operator, taking into account (18), can be written as:

$$V_{n,l,m;\,n',l',m'}=\frac{\int\limits_0^{R_0^*}\int\limits_0^{\pi}\int\limits_0^{2\pi}Y^*_{l,m}\left(\theta,\varphi\right)J_{l+3/2}\left(\frac{\tilde{X}_{n,l}}{R_0^*}r^*\right)\hat{V}_{n,l,m;\,n',l',m'}Y_{l',m'}\left(\theta,\varphi\right)J_{l'+3/2}\left(\frac{\tilde{X}_{n',l'}}{R_0^*}r^*\right)r^*dr^*d\theta d\varphi}{2\pi R_0^*J_{l+3/2}\left(\tilde{X}_{n,l}\right)J_{l'+3/2}\left(\tilde{X}_{n',l'}\right)}. \tag{19}$$

Using the recurrence relations between the spherical functions and the properties of their orthogonality, the integrals over the variables θ and φ can be written as

$$\int\limits_0^{\pi}\int\limits_0^{2\pi}Y^*_{l,m}\left(\theta,\varphi\right)Y_{l',m'}\left(\theta,\varphi\right)\sin\theta d\theta d\varphi=\delta_{ll'}\delta_{mm'}, \tag{20}$$

$$\begin{aligned}\int\limits_0^{\pi}\int\limits_0^{2\pi}&Y^*_{l,m}\left(\theta,\varphi\right)Y_{l',m'}\left(\theta,\varphi\right)\sin^3\theta d\theta d\varphi=\\&\sqrt{\frac{\left(l-m+4\right)\left(l-m+3\right)\left(l-m+2\right)\left(l-m+1\right)}{\left(2l+1\right)\left(2l-1\right)^2\left(2l-3\right)}}\delta_{l,l'+2}\delta_{m,m'-2}\quad-\\&\frac{2}{\left(2l+3\right)\left(2l-1\right)}\sqrt{\left(l-m\right)\left(l-m-1\right)\left(l+m+2\right)\left(l+m+1\right)}\delta_{ll'}\delta_{m,m'-2}\quad+\\&\sqrt{\frac{\left(l+m+4\right)\left(l+m+3\right)\left(l+m+2\right)\left(l+m+1\right)}{\left(2l+5\right)\left(2l+3\right)^2\left(2l+1\right)}}\delta_{l,l'-2}\delta_{m,m'-2}.\end{aligned} \tag{21}$$

Integration over a variable r^* gives

$$\begin{aligned}\int\limits_0^{R_0^*}&J_{l+3/2}\left(\frac{\tilde{X}_{n,l}}{R_0^*}r^*\right)J_{l'+3/2}\left(\frac{\tilde{X}_{n',l'}}{R_0^*}r^*\right)r^*dr^*=\frac{R_0^*}{\left(\tilde{X}^2_{n,l}-\tilde{X}^2_{n',l}\right)}\times\\&\left[R_0^*\tilde{X}_{n',l}J_{l+1/2}\left(R_0^*\tilde{X}_{n',l}\right)J_{l+3/2}\left(R_0^*\tilde{X}_{n,l}\right)-R_0^*\tilde{X}_{n,l}J_{l+1/2}\left(R_0^*\tilde{X}_{n,l}\right)J_{l+3/2}\left(R_0^*\tilde{X}_{n',l}\right)\right]\end{aligned} \tag{22}$$

and

$$\begin{aligned}\int\limits_0^{R_0^*}&J_{l+3/2}\left(\frac{\tilde{X}_{n,l}}{R_0^*}r^*\right)J_{l'+3/2}\left(\frac{\tilde{X}_{n',l'}}{R_0^*}r^*\right)r^{*3}dr^*=\\&\frac{\tilde{X}^{l+3/2}_{n,l}\tilde{X}^{l'+3/2}_{n',l'}}{2^{l+l'+3}\Gamma\left(l'+5/2\right)}\sum_{k=0}^{\infty}\frac{\left(-1\right)^k}{k!\Gamma\left(l+k+5/2\right)}\left(\frac{\tilde{X}^{l+3/2}_{n,l}}{2R_0^*}\right)^{2k}\frac{F\left(-k,-l-k-3/2,l+5/2,\frac{\tilde{X}^2_{n',l'}}{\tilde{X}^2_{n,l}}\right)}{l+l'+2k+4},\end{aligned} \tag{23}$$

where $F\left(\alpha,\beta,x\right)$ – the degenerate hypergeometric function.

Taking into account (20) – (23), the matrix element of the considered optical transition can be represented as

$$V_{n,l,m;\,n',l',m'} = \\ \sum_{n'=0}^{\infty}\left\{\frac{\hbar\omega_B m}{4\pi\left(\tilde{X}_{n,l}^2-\tilde{X}_{n',l}^2\right)J_{l+3/2}\left(\tilde{X}_{n,l}\right)J_{l+3/2}\left(\tilde{X}_{n',l}\right)}\left[R_0^*\tilde{X}_{n',l}J_{l+1/2}\left(R_0^*\tilde{X}_{n',l}\right)\ J_{l+3/2}\left(R_0^*\tilde{X}_{n,l}\right)-\right.\right. \\ \left. R_0^*\tilde{X}_{n',l}J_{l+1/2}\left(R_0^*\tilde{X}_{n,l}\right)\ J_{l+3/2}\left(R_0^*\tilde{X}_{n',l}\right)\right]+\sum_{k=0}^{\infty}\frac{(-1)^k\,m_h^*\omega_B^2R_0^*\left(\tilde{X}_{n,l}^{l+3/2}\right)^{2k+1}}{k!\Gamma\left(l+k+5/2\right)2^{l+4+2k}}\times \\ \left[\sqrt{\frac{(l-m+4)(l-m+3)(l-m+2)(l-m+1)}{(2l+1)(2l-1)^2(2l-3)}}\,\frac{F\left(-k,-l-k-3/2,l+5/2,\frac{\tilde{X}_{n',l-2}^2}{\tilde{X}_{n,l}^2}\right)}{(2l+2k+2)\Gamma\left(l+1/2\right)}-\right. \\ \frac{2F\left(-k,-l-k-3/2,l+5/2,\frac{\tilde{X}_{n',l}^2}{\tilde{X}_{n,l}^2}\right)}{(2l+3)(2l-1)(2l+2k+4)}\sqrt{(l-m)(l-m-1)(l+m+2)(l+m+1)}+ \\ \left.\left.\frac{F\left(-k,-l-k-3/2,l+5/2,\frac{\tilde{X}_{n',l+2}^2}{\tilde{X}_{n,l}^2}\right)}{2l+2k+6}\sqrt{\frac{(l+m+4)(l+m+3)(l+m+2)(l+m+1)}{(2l+5)(2l+3)^2(2l+1)}}\right]\right\}. \quad (24)$$

SIRR, taking into account the QD size dispersion, is determined by the expression of the next form:

$$\Phi(\omega) = \\ \frac{4\omega^2\sqrt{\varepsilon}e^2}{c^3V}\left|\frac{\mathbf{P}_{eh}\mathbf{e}_0}{m_0}\right|\int\sum_n\left|\int\Psi_{n,l,m}^*(\rho,\varphi,z)\,\Psi_\lambda(\rho,\varphi,z)\,d\rho d\varphi dz\right|^2\times\ P(u)\,\delta\left(E_i-E_f-\hbar\omega\right)\,du, \quad (25)$$

where m_0 – the free electron mass; $\mathbf{P}_{eh}$ – matrix element of the momentum operator on the band carriers Bloch amplitudes; ω – frequency of radiated electromagnetic wave with polarization $\mathbf{e}_0$; V – the QD volume; $P(u)$ – the Lifshitz–Slezov function.

The wave function of the A^+-state, as is known, differs only by a constant factor from the one-particle Green function:

$$\Psi_{\lambda h}(\rho,\varphi,z) = C\exp\left(-\frac{w\rho^2+z^2}{4\beta_h a_h^2}\right)\times \\ \int_0^{\infty}dt\ \exp\left[-\left(\beta_h\eta_{\lambda h}^2-\beta_0+w+\frac{1}{2}\right)t\right]\left(1-e^{-2t}\right)^{-\frac{1}{2}}\left(1-\exp\left[-2wt\right]\right)^{-1}\times \\ \exp\left\{-\frac{z^2\exp\left[-2t\right]}{2\beta_h a_h^2\left(1-\exp\left[-2t\right]\right)}\right\}\exp\left[-\exp\left[-2wt\right]\frac{w\rho^2}{4\beta_h a_h^2\left(1-\exp\left[-2wt\right]\right)}\right], \quad (26)$$

where C – the normalization factor determined by an expression of the next form:

$$C = \left[-2^{-1/2}\pi^{-3/2}\beta_h^{3/2}a_h^3w\Gamma\left(\frac{1}{2}-w\right)\frac{\Gamma\left(\frac{\beta_h\eta_{h\lambda}^2+w}{2}+\frac{5}{4}\right)}{\left(\frac{\beta_h\eta_{h\lambda}^2+w}{2}+\frac{1}{4}\right)^2\Gamma\left(\frac{\beta_h\eta_{h\lambda}^2-w}{2}+\frac{3}{4}\right)}\times\right. \\ \left.\left[\left(\frac{\beta_h\eta_{h\lambda}^2+w}{2}+\frac{1}{4}\right)\left[\Psi\left(\frac{\beta_h\eta_{h\lambda}^2+w}{2}+\frac{5}{4}\right)-\Psi\left(\frac{\beta_h\eta_{h\lambda}^2-w}{2}+\frac{3}{4}\right)\right]-1\right]\right]^{-1/2}. \quad (27)$$

Taking into account (18), (24) and (26), the matrix element of the radiative recombination transition of an electron from the ground state of the size-quantized band to the level of the QD A^+-center in a magnetic field can be written as:

$$M_{1,\lambda} = \frac{C\left(2\beta_h\right)^{5/4} a_h^2}{2\pi R_0^{*2} J_{3/2}\left(\tilde{X}_{n,1}\right)} \int\limits_0^{+\infty} \int\limits_{-\infty}^{+\infty} \int\limits_0^{2\pi} \rho^* d\rho^* dz^* d\varphi \times$$
$$\int\limits_0^{+\infty} dt \exp\left[-\left(\beta_h \eta_{\lambda h}^2 - \beta_0 + w + \frac{1}{2}\right) t\right] \left(1 - e^{-2t}\right)^{-1/2} \left(1 - \exp\left[-2wt\right]\right)^{-1} \times$$
$$\exp\left[-\left(\frac{z^{*2}\left(1 + \exp\left[-2t\right]\right)}{2\beta_h\left(1 - \exp\left[-2t\right]\right)} + \frac{p^{*2} w\left(1 + \exp\left[-2wt\right]\right)}{2\beta_h\left(1 - \exp\left[-2wt\right]\right)}\right)\right] \times$$
$$\frac{\rho^*}{\left(\rho^{*2} + z^{*2}\right)^{3/4}} \left[\frac{J_{5/2}\left(\frac{\tilde{X}_{n,1}}{R_0^*}\sqrt{\rho^{*2} + z^{*2}}\right)}{J_{5/2}\left(\tilde{X}_{n,1}\right)} + \sum_{n'=1}^{\infty} \frac{R_0^{*2} V_{n,1,-1;n',1,-1} J_{5/2}\left(\frac{\tilde{X}_{n',1}}{R_0^*}\sqrt{\rho^{*2} + z^{*2}}\right)}{\left(\pi^2 - \tilde{X}_{n',1}^2\right) J_{5/2}\left(\tilde{X}_{n',1}\right)}\right], \quad (28)$$

where $R_0^* = R_0/a_h^2$.

Performing integration in (28), we obtain

$$M_{1,\lambda} = \frac{C\left(2\beta_h\right)^{5/4} a_h^2}{2\pi R_0^{*2} J_{3/2}\left(\tilde{X}_{n,1}\right)} \int\limits_0^{+\infty} dt \exp\left[-\left(\beta_h \eta_{\lambda h}^2 - \beta_0 + w + \frac{1}{2}\right) t\right] \left(1 - e^{-2t}\right)^{-1/2} \times$$
$$\left(1 - \exp\left[-2wt\right]\right)^{-1} \sum_{j=0}^{\infty} (-1)^j \left(\frac{1 - \exp\left[-2wt\right]}{1 + \exp\left[-2wt\right]}\right)^{2j+5/2} \times$$
$$\left[\frac{\sqrt{\pi}}{2} \Gamma\left(2j + \frac{5}{2}\right) \left(\frac{\tilde{X}_{n,1}\sqrt{2\beta_h}}{2R_0^*}\right)^{2j+3/2} \left(\frac{1 + \exp\left[-2t\right]}{1 - \exp\left[-2t\right]} - \frac{1 + \exp\left[-2wt\right]}{1 - \exp\left[-2wt\right]}\right)^{-1/2} - \right.$$
$$R_0^{*2} \sum_{n'=0}^{\infty} \frac{(-1)^{n'} (2j+3)!}{2n!\left(2j + \frac{5}{2} + n'\right)} \left(\frac{\tilde{X}_{n',1}\sqrt{2\beta_h}}{2R_0^*}\right)^{2j+3/2} \times$$
$$\left.\frac{V_{n,1,-1;n',1,-1}}{\pi^2 - \tilde{X}_{n',1}^2} \left(\frac{1 + \exp\left[-2wt\right]}{1 - \exp\left[-2wt\right]}\right)^{2j+5/2+n'} \left(\frac{1 + \exp\left[-2t\right]}{1 - \exp\left[-2t\right]} - \frac{1 + \exp\left[-2wt\right]}{1 - \exp\left[-2wt\right]}\right)^{-2j-3}\right]. \quad (29)$$

After integration in (29), we finally obtain:

$$\Phi\left(X\right) = \Phi_0 \frac{X^2 \bar{\beta}_h^4 u_1 \bar{w}}{\left(J_{3/2}\left(\tilde{X}_{n,0}\right)\right)^2 \bar{R}_0^{*5}} \times \frac{\Gamma\left(\frac{1}{2} - \bar{w}\right) \Gamma\left(\Delta + 1\right)}{\Delta^2 \Gamma\left(\Delta - \bar{w} + \frac{1}{2}\right)} \times$$
$$\left[\Delta\left[\Psi\left(\Delta + 1\right) - \Psi\left(\Delta - \bar{w} + \frac{1}{2}\right)\right] - 1\right] P\left(u_1\right) \times$$
$$\left|\int\limits_0^{\infty} dt \exp\left[-\left(\bar{\beta}_h \eta_{\lambda h}^2 u_1^{3/2} - \bar{\beta}_0 u_1^{-1} + \bar{w} + \frac{1}{2}\right) t\right] \left(1 - e^{-2t}\right)^{-1/2} \left(1 - \exp\left[-2\bar{w}t\right]\right)^{-1} \times\right.$$
$$\sum_{j=0}^{\infty} (-1)^j \left(\frac{1 - \exp\left[-2\bar{w}t\right]}{1 + \exp\left[-2\bar{w}t\right]}\right)^{2j+5/2} \times$$
$$\left[\frac{\sqrt{\pi}}{2} \Gamma\left(2j + \frac{5}{2}\right) \left(\frac{\tilde{X}_{n,1}\sqrt{2\beta_h}}{2\bar{R}_0^*}\right)^{2j+3/2} \left(\frac{1 + \exp\left[-2t\right]}{1 - \exp\left[-2t\right]} - \frac{1 + \exp\left[-2wt\right]}{1 - \exp\left[-2wt\right]}\right)^{-1/2} - \right.$$
$$\bar{R}_0^{*2} \sum_{n'=0}^{\infty} \frac{(-1)^{n'} (2j+3)!}{2n'!\left(2j + \frac{5}{2} + n'\right)} \left(\frac{\tilde{X}_{n',1}\sqrt{2\beta_h}}{2\bar{R}_0^*}\right)^{2j+3/2} \times$$
$$\left.\left.\frac{V_{n,1,-1;n',1,-1}}{\pi^2 - \tilde{X}_{n',1}^2} \left(\frac{1 + \exp\left[-2wt\right]}{1 - \exp\left[-2wt\right]}\right)^{2j+5/2+n'} \left(\frac{1 + \exp\left[-2t\right]}{1 - \exp\left[-2t\right]} - \frac{1 + \exp\left[-2wt\right]}{1 - \exp\left[-2wt\right]}\right)^{-2j-3}\right]\right|^2, \quad (30)$$

where $\Phi_0 = 6\sqrt{\varepsilon}e^2 2^2 a_h^3 \pi^{-3/2} \left|\mathbf{P}_{eh}\mathbf{e}_0\right| / \pi^2 c^3 m_0$; $\Delta = \left(\bar{\beta}_h \eta_{h\lambda}^2 u^{3/2} + \bar{w}\right)/2 + 1/4$; $\bar{w} = \sqrt{1 + \bar{\beta}_h^2 u^3 a^{*-4}/2}$; $\bar{\beta}_0 = \beta_n e^2/4\pi\varepsilon_0\varepsilon a_h \bar{R}_0^*$; $\bar{\beta}_h = \left(3E_h a_h \bar{R}_0^{*3}\pi\varepsilon_0\varepsilon\right)^{1/2} / \left(\pi^2 e^2\right)^{1/2}$; $X = \hbar\omega/E_d$; u – is the root of a transcendental equation of the form:

$$\pi^2/R_0^{*2}u + \sum_{nn'=1}^{\infty} R_0^{*2}u\left(V_{1n'}(u)\right)^2 / \left(\pi^2 - X_{n',1}^2\right) = \eta_{\lambda h}^2 + X.$$

3. Dependence of the spectral intensity of recombination radiation on the energy of emitted photon and on the magnitude of an external magnetic field

Figure 1 shows the frequency dependence of the spectral intensity of recombination radiation, as well as its dependence on the magnitude of an external magnetic field. The spectral intensity of recombination radiation in an external magnetic field increases, which is associated with an increase in the overlap integral of the envelope wave functions of a hole bound at the A^+-center and of an electron localized in the ground state of quantum dot. Fig. 2(a,b) shows the coordinate dependence of the wave function modulus square, for the A^+-state and for the electronic wave function of the ground state, respectively, for different values of the magnitude of an external magnetic field "B". It can be seen that as the value of B increases, the degree of localization both as for the hole (see Fig. 2a) and as for the electron wave functions increases, and accordingly the overlap integral increases.

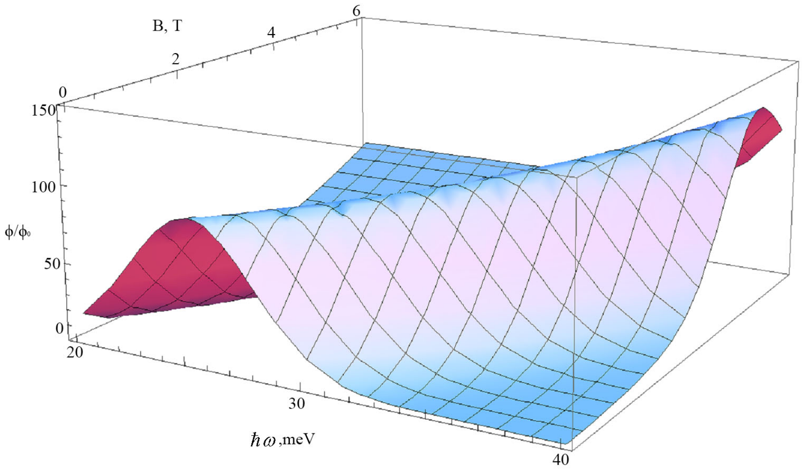

FIG. 1. Dependence of the spectral intensity of recombination radiation (in relative units) on the emitted photon energy and on the magnitude of an external magnetic field B, for the quasi-zero-dimensional structure of InSb–QD at $R_0 = 55$ nm

4. Conclusions

Dependence of the binding energy of a hole in the $A^+ + e$ complex on the magnitude of an external magnetic field has been investigated by the zero-range potential method in the adiabatic approximation. It is shown that in an external magnetic field there is a spatial anisotropy of the binding energy for A^+-state due to hybrid quantization in the QD radial plane and due to dimensional quantization in the direction of an external magnetic field. In the dipole approximation, the frequency dependence calculation of the spectral intensity of recombination radiation for a quasi-zero-dimensional structure in an external magnetic field has been performed, taking into account dispersion of the QDs radius. It is shown that in an external magnetic field the spectral intensity of recombination radiation curve shifts to the short-wave region of the spectrum and probability of the electron radiative transition to the A^+-center level increases, which is associated with an increase in the overlap integral of the envelope wave functions of a hole bound at the A^+-center and of an electron localized in the ground state of quantum dot. The obtained results can be used in the development of IR sources or terahertz radiation (depending on the QD radius), on the basis of quasi-zero-dimensional structures with impurity complexes, with parameters controlled in an external magnetic field.

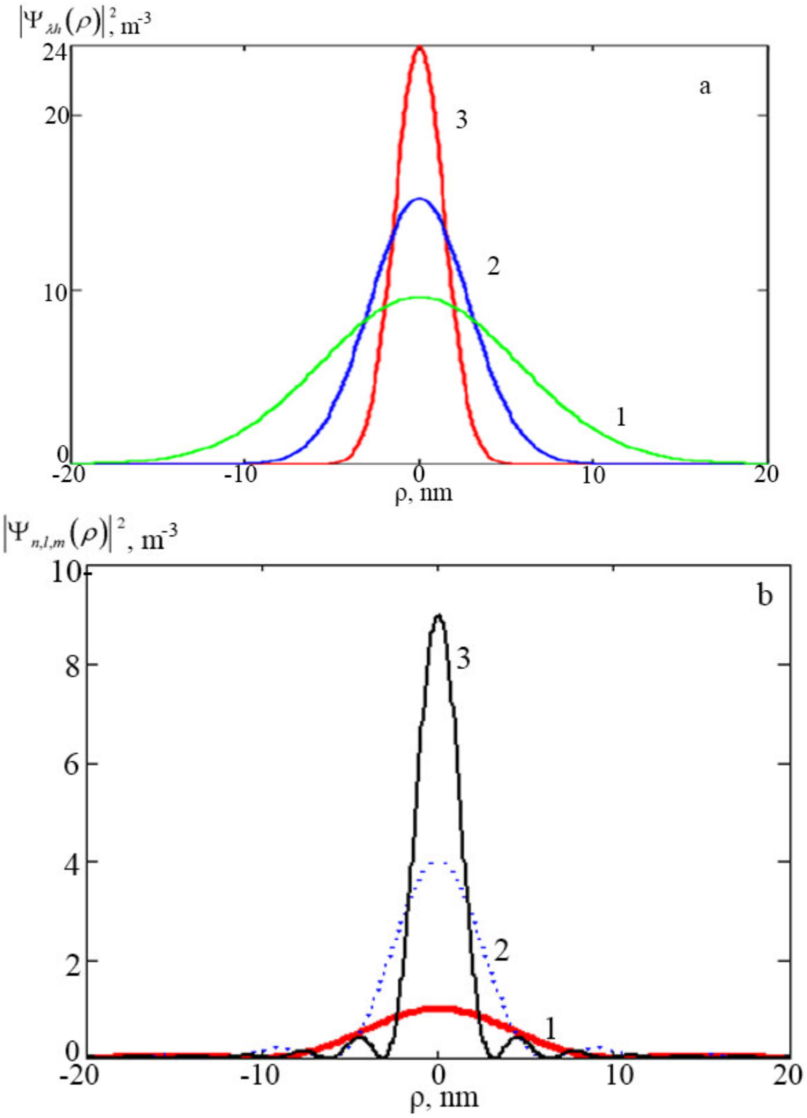

FIG. 2. The coordinate dependence of the wave function modulus square: (a) for A^+-state and (b) for the electronic wave function for various values of the magnetic field intensity B. 1: $B = 0$; 2: $B = 2T$; 3: $B = 5T$, at $R_0 = 20$ nm

Acknowledgements

This work was supported by the Ministry of Education and Science of the Russian Federation (project No. 3.6321.2017/8.9 and 2019-0940).

References

[1] Zaytsev S.A., Knyr V.A. Reaction of the atoms double photoionization in the J-matrix approach. *Bulletin of the Pacific State University*, 2010, **1** (16), 13.

[2] Petrov P.V., Ivanov Yu.L., Averkiev N.S. Circular polarization of photoluminescence for the two-dimensional system of A^+-centers in an external magnetic field. *Physics and technology of semiconductors* , 2011, **45** (27), 794.

[3] Shamirzayev T.S., Timensky A.M., et al. Long-term kinetics of photoluminescence for InAs/AlAs-quantum dots in an external magnetic field. *Physics and technology of semiconductors*, 2005, **33** (1), 35.

[4] Ekimov A.I., Onuschenko A.A., Efros Al.L. Quantization of the holes energy spectrum in the electron adiabatic potential. *JETP Letters*, 1986, **43** (6), 292.

[5] Astakhov G.V., Kochereshko V.P., et al. Photoluminescence of the InAs-quantum dots grown on the disoriented GaAs-substrates. *Physics and technology of semiconductors*, 1999, **33**, 1084.

[6] Krevchik V.D., Grunin A.B., Zaitsev R.V. Anisotropy of the magneto-optical absorption for complexes “quantum dot-impurity center”. *Physics and technology of semiconductors*, 2002, **36** (10), 1225.

[7] Zhu J.L. Exact Solutions for hydrogenic donor states in a spherically rectangular quantum well. *Physical Review B*, 1989, **39** (12), 8780(R).

[8] Galiev V.I., Poluanov A.F. Spectra of energy and optical absorption of shallow impurities in the semiconductor quantum dot. *Physics and technology of semiconductors*, 1993, **27** (7), 1202.

[9] Krevchik V.D., Zaitsev R.V. The light impurity absorption in structures with quantum dots. *Physics and technology of semiconductors*, 2001, **43** (23), 504.

[10] Pakhomov A.A., Khalipov K.V., Yassievich I.N. Local electronic states in semiconductor quantum wells. *Physics and technology of semiconductors*, 1996, **30** (8), 1387.

[11] Mikhailov A.I., Mikhailov I.A. Double photoionization and ionization with excitation under the Compton scattering of high-energy photons on metastable states of the helium-like ions. *JETP*, 1999, **116** (6), 1889.

[12] Grinberg A.A., Belorusets E.D. On the energy spectrum of multiply charged impurity centers in semiconductors. *Solid State Physics*, 1978, **20**, P. 1970–1978.

[13] Huant S., Najda S.P., Etienne B. Two-dimensional D^--centers. *Physical Review Letters*, 1990, **65**, 1486.

[14] Durnev M.V. Zeeman splitting of the lightweight hole states in quantum wells: comparison of theory and experiment. *Solid State Physics*, 2014, **56** (7), 1364.

[15] Krevchik V.D., Zaitsev R.V., Evstifeev V.V. To the photoionization theory for the deep impurity centers in a parabolic quantum well. *Physics and technology of semiconductors*, 2000, **34** (10), 1244.

NANOSYSTEMS: PHYSICS, CHEMISTRY, MATHEMATICS, 2019, 10 (5), P. 530–535

The heat capacity of a semiconductor quantum dot in magnetic fields

Ayham Shaer, Mohammad K. Elsaid*, Eshtiaq Hjaz

Physics Department, Faculty of Science, An-Najah National University, Nablus, West Bank, Palestine

*mkelsaid@najah.edu

PACS 73.21.La, 65.80.-g **DOI 10.17586/2220-8054-2019-10-5-530-535**

The heat capacity of two interacting electrons confined in a quantum dot presented in a magnetic field has been calculated by solving the Hamiltonian using the exact diagonalization method. The statistical average energies for confined and interacting electrons have been computed for various values of magnetic fields, confining frequency and temperature. We had investigated the dependence of the heat capacity on quantum dot Hamiltonian's parameters and temperature. The singlettriplet transitions in the ground state of the quantum dot spectra and the corresponding jumps in the heat capacity curves had been shown. The comparisons show that our results are in very good agreement with theoretical reported works.

Keywords: quantum dot, magnetic field, exact diagonalization, heat capacity.

Received: 14 September 2019

Revised: 16 October 2019

1. Introduction

Semiconductor quantum dots (QDs) have been the subject of interest and hot research area due to their physical properties and significant electronic device applications such as quantum dot lasers, quantum memories, solar cells, single electron transistors, light emitting diodes, biological markers and quantum computers [1–5] The application of a magnetic field perpendicular to the dot plane will introduce an additional structure on the energy levels and correlation effects, of the interacting electrons confined in a quantum dot.

Many authors have used different numerical methods and computational techniques to solve the two electrons QD Hamiltonian, including the effect of an applied magnetic field, and obtain the eigenenergies [6–12]. The energy levels of the interacting electrons show transitions in the angular momentum of the ground states. Computed energies have been used to calculate the statistical average energies of the QD and then, to investigate theoretically the magneto-thermodynamic properties of the two-interacting electron in a quantum dot [13–25].

In this work, we had calculated the heat capacity as a thermodynamic quantity for a quantum dot helium atom in which both the magnetic field and the electron-electron interaction are fully taken into account. Since, the eigenvalues of the electrons in the QD are the starting point to calculate the physical properties of the QD system, we had, first, applied the exact diagonalization method to solve the QD Hamiltonian and obtain the eigenenergies. Second, we had used the computed eigenenergies spectra to display theoretically the heat capacity behavior of the QD as a function of magnetic field strength, confining frequency and temperature.

The rest of this paper is organized as follows: the Hamiltonian formalism, computation exact diagonalization technique and how to calculate the heat capacity from the mean energy expression are presented in Section 2. The final section will be devoted for numerical results and conclusions.

2. Theory

In this section we will describe in detail the main three parts which consist the theory, namely: quantum dot Hamiltonian, exact diagonalization method and the heat capacity.

2.1. Quantum dot Hamiltonian

The effective mass Hamiltonian for two interacting electrons confined in a QD by a parabolic potential in a uniform magnetic field of strength B, applied along z direction is given by:

$$\widehat{H} = \sum_{j=1}^{2} \left(\frac{1}{2m^*}(\vec{p}(\vec{r}_j) + \frac{e}{c}\vec{A}(\vec{r}_j))^2 + \frac{1}{2}m^*\omega_0^2 r_j^2\right) + \frac{e^2}{\epsilon\,|\vec{r_1} - \vec{r_2}|} \tag{1}$$

where m^* is the effective mass of electron, e is the electron charge, c is the speed of light, ω_0 and ϵ are defined as the confining frequency and the dielectric constant for the GaAs medium, respectively. Here, r_1 and r_2 describe the positions of the first and second electron in the xy plane; ω_c is the cyclotron frequency and the symmetric gauge

$A = \frac{1}{2}B \times r$ has been used for the vector potential. The complete two electron QD Hamiltonian can be separated into center of mass Hamiltonian H_{CM} and relative Hamiltonian part H, as shown below:

$$H = H_{CM} + H_r \tag{2}$$

$$H_{CM} = \frac{1}{2M}(\overrightarrow{P}_R + \frac{Q}{c}\vec{A}(R))^2 + \frac{1}{2}M\omega_0^2 R^2 \tag{3}$$

$$H_r = \frac{1}{2\mu}(\overrightarrow{p}_r + \frac{q}{c}\vec{A}(r))^2 + \frac{1}{2}\mu\omega_0^2 r^2 + \frac{e^2}{\epsilon\,|r|} \tag{4}$$

where M is the total mass $2m^*$, Q is the total charge$=2e$, μ is reduce mass$=\frac{m^*}{2}$, and q is the reduce charge $=\frac{e}{2}$.

The corresponding energy of this Hamiltonian equation (1) is

$$E_{total} = E_{CM} + E_r \tag{5}$$

The center of mass Hamiltonian given by equation (3) is a harmonic oscillator type with well-known eigenenergies:

$$E_{CM} = (2n_{CM} + |m_{CM}| + 1)\hbar\sqrt{\frac{\omega_c^2}{4} + \omega_0^2} + m_{CM}\frac{\hbar\omega_c}{2} \tag{6}$$

where n_{CM}, m_{CM} are the radial and angular quantum numbers, respectively.

However, the relative motion Hamiltonian part (H_r), given by equation (4) does not have an analytical solution for all ranges of ω_0 and ω_c. In this work, an exact diagonalization method will be applied to solve the relative part of the Hamiltonian and obtain the corresponding eigenenergies, E_r.

2.2. Exact diagonalization method

For non-interacting case the relative Hamiltonian in equation (4) can be reduced to a single particle problem with eigenstates $|n_r, m_r\rangle$ known as Fock-Darwin states [9] given by the following form:

$$|n_r, m_r\rangle = N_{n_r,m_r}\frac{e^{im_r\varphi}}{\sqrt{2\pi}}(\alpha r)^{|m_r|}e^{-\alpha^2 r^2/2}L_{n_r}^{|m_r|}(\alpha^2 r^2) \tag{7}$$

where the functions $L_{n_r}^{|m_r|}(\alpha^2 r^2)$ are the standard associated Laguerre polynomials. The normalization constant N_{n_r,m_r} can be calculated from the normalization condition of the basis, $\langle n_r, m_r\ |n_r, m_r\rangle = 1$, to give:

$$N_{n_r,m_r} = \sqrt{\frac{2n_r!\alpha^2}{(n_r + |m_r|)!}} \tag{8}$$

$\alpha = \sqrt{\frac{m\omega}{h}}$, is a constant which has the dimensionality of an inverse length.

The eigenenergies of the QD Hamiltonian which are given by equation (5), consist of the sum of the energies for the center of mass Hamiltonian, and the eigenenergies obtained by direct diagonalization to the relative Hamiltonian part. For the interacting case, we shall apply exact diagonalization method to solve equation (4) and find the corresponding exact eigenenergies for arbitrary values of ω_0 and ω_c.

The matrix element of the relative Hamiltonian part using the basis can be expressed as:

$$h_{nn'} = \langle n_r, m_r\ |H_r|n_r, m_r\rangle = \langle n_r, m_r| -\frac{\hbar^2}{2\mu}\nabla^2 + \frac{1}{2}\mu\omega^2 r^2\ |n_r, m_r\rangle + \langle n_r, m_r|\ \frac{e^2}{\epsilon r}\ |n_r, m_r\rangle \tag{9}$$

The corresponding relative dimensionless energies are:

$$\frac{E_r}{\hbar\omega_0} = \frac{h_{nn'}}{\hbar\omega_0} = ((2n + |m_z| + 1)\sqrt{1 + \frac{\gamma^2}{4}} - \frac{\gamma}{2}\,|m_z|)\delta_{nn'} + \frac{\lambda}{\sqrt{2}}\sqrt{\frac{n'!n!}{(n' + |m_z|)!(n + |m_z|)!}} \times I_{nn'}\,|m_z| \tag{10}$$

where $\gamma = \frac{\omega_c}{\omega_0}$, $\lambda = \frac{e^2\alpha}{\hbar\omega_0}$ are dimensionless parameters and $\omega^2 = \frac{\omega_c^2}{4} + \omega_0^2$ is the effective confining frequency. $I_{nn'}$ is the coulomb energy matrix element that can be evaluated in a closed form by using the following Laguerre relation [17]:

$$\int_0^\infty t^{\alpha-1}e^{-pt}L_m^{\lambda}(at)L_n^{\beta}(bt)dt = \frac{\Gamma(\alpha)(\lambda+1)_m(\beta+1)_n p^{-\alpha}}{m!n!}\sum_{j=0}^{m}\frac{(-m)_j(\alpha)_j}{(\lambda+1)_j j!}\left(\frac{a}{p}\right)^j\sum_{k=0}^{n}\frac{(-n)_k(\alpha+j)_k}{(\beta+1)_k k!}\left(\frac{b}{p}\right)^k. \tag{11}$$

This closed form result of the coulomb energy reduces greatly the computation time needed in the diagonalization process.

In our calculation, we had used the basis, $|n_r, m_r\rangle$ defined by equation (16) to diagonalize the relative QD Hamiltonian and obtained its corresponding eigenenergies E_r.

2.3. Heat Capacity

The heat capacity C_v of the QD system is evaluated as the temperature derivative of the mean energy of the QD:

$$C_v(T, \omega_c, \omega_0) = \frac{\partial \langle E(T, \omega_c, \omega_0)\rangle}{\partial T} \tag{12}$$

where the statistical average energy is calculated as:

$$\langle E(T, \omega_c, \omega_0)\rangle = \frac{\sum\limits_{\alpha=1}^{N} E_\alpha e^{-E_\alpha/K_B T}}{\sum\limits_{\alpha=1}^{N} e^{-E_\alpha/K_B T}} \tag{13}$$

and the sum is taken over energy levels of the QD.

The dependence of the computed heat capacity C_v on the magnetic field ω_c, confining frequency ω_0 and temperature are displayed in the next section.

3. Results and conclusions

Our computed results for two interacting electrons in a quantum dot made from GaAs material ($R^* = 5.825$ meV) are presented in Fig. 1 to 4 and Table 1. We tested the calculated energy against different works. In Table 1, we listed the calculated energy results by the exact diagonalization method for different number of single particle basis s_p against Ciftja's work [9]. The comparison clearly shows excellent agreement between both works. In Fig. 1 we plotted the computed energy results of this work against the strength of the magnetic field for $\omega_0 = \frac{2}{3}R^*$. The present results also show very good agreement compared with Dyblaski [18], where the authors had used the variational method.

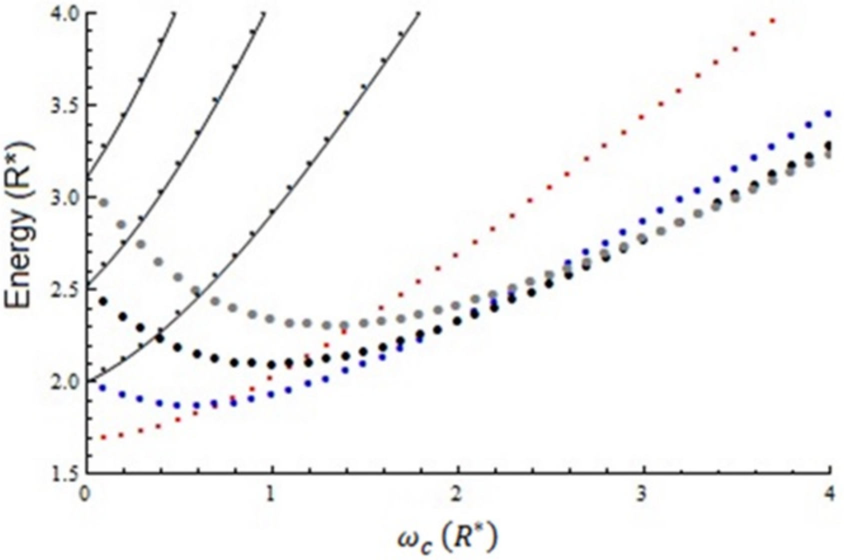

FIG. 1. The computed eigenenergy spectra of two electron quantum dot against the strength of the magnetic field for $\omega_0 = \frac{2}{3}R^*$, and angular momentum $m_r = 0, \pm1, \pm2, \pm3$

Fig. 1 shows clearly the transition in the angular momentum of the ground state of the QD system as the magnetic field increases. The origin of these transitions is due to the effect of coulomb interaction energy in the QD Hamiltonian. These transitions in the angular momentum of the QD system correspond to the (S-T) transitions are expected to manifest themselves as cusps in the heat capacity curve of the QD.

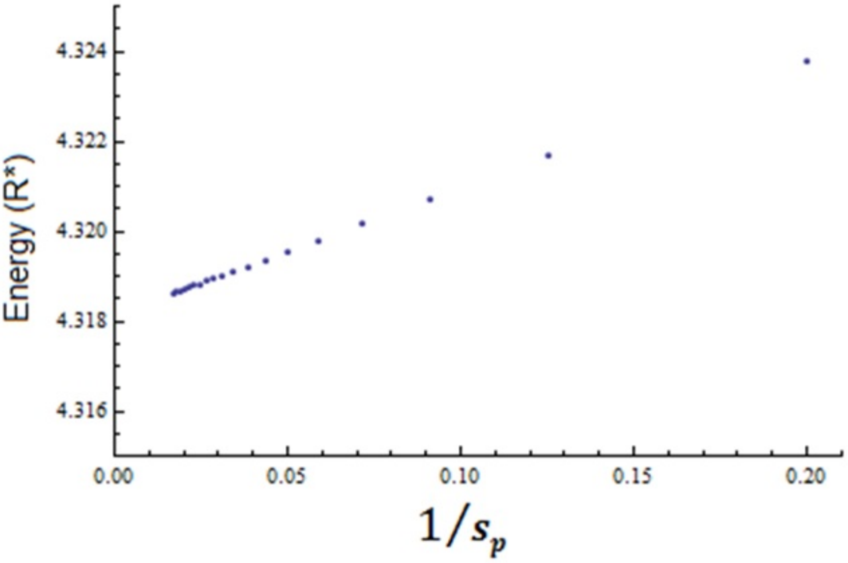

FIG. 2. The computed ground state energy of a two-electron quantum dot in zero magnetic field and $\lambda = 3$, against the inverse of the number of basis taken in diagonalization process

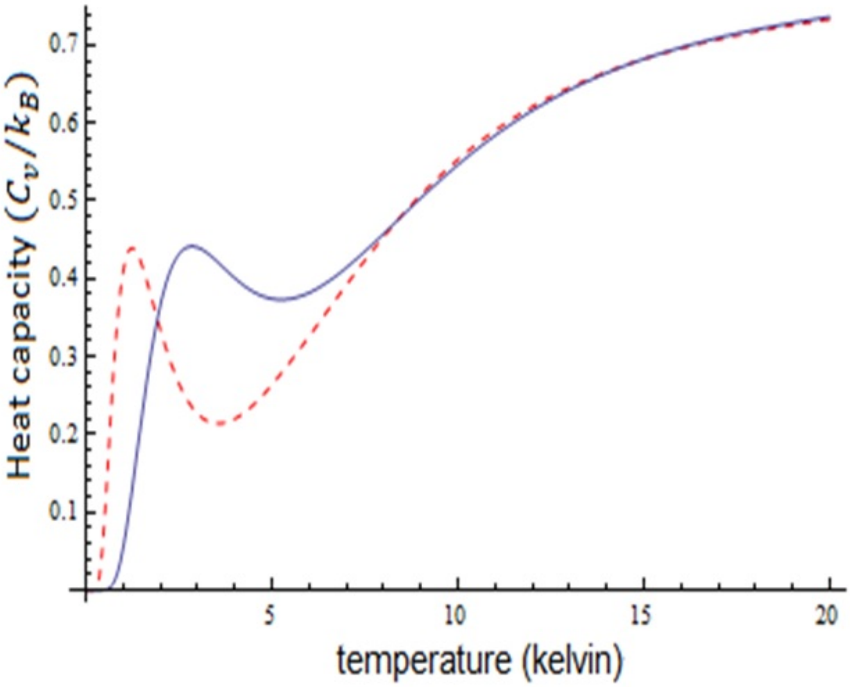

FIG. 3. The dependence of the heat capacity on the temperature for fixed value of magnetic field and various confinement frequencies: $\omega_0 = 0.5R^*$ and $\omega_0 = 0.67R^*$

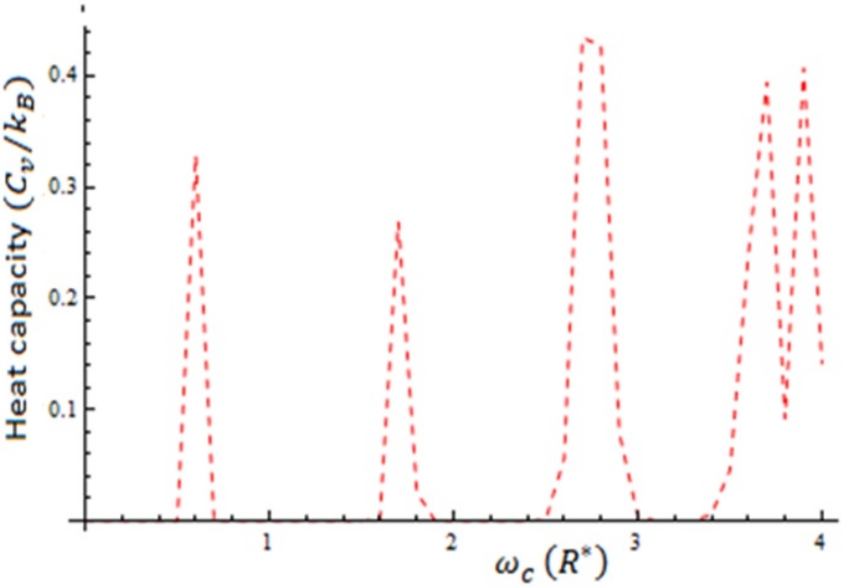

FIG. 4. The heat capacity as function of magnetic field strength for fixed value of temperature (0.01 K) and confinement frequency ($\omega_0 = \frac{2}{3}R^*$)

TABLE 1. Ground state energies in units of $\hbar\omega_0$ of exact diagonalization method at zero magnetic field for different values of dimensionless parameter $\lambda = \frac{e^2\alpha}{\hbar\omega_0}$. The computed results are shown for various number of basis (s_p) against the result which are taken from [9]

λ	Energy $\hbar\omega_0$			
	Ref. [9]	Present work		
		$s_p = 5$	$s_p = 50$	$s_p = 60$
0	2.00000	2.00000	2.00000	2.00000
1	3.00097	3.00122	3.00097	3.00080
2	3.72143	3.72166	3.72143	3.72128
3	4.31872	4.31885	4.31872	4.31863
4	4.84780	4.84787	4.84780	4.84775
5	5.33224	5.33227	5.33224	5.33222
6	5.78429	5.78431	5.78429	5.78428
7	6.21129	6.21129	6.21129	6.21128
8	6.61804	6.61805	6.61804	6.61804
9	7.00795	7.00795	7.00795	7.00795
10	7.38351	7.38351	7.38351	7.38351

In all steps of calculations, we had ensured the issue of convergence. For example, the ground state energy is plotted in Fig. 2 against the inverse of number of basis $\left(\frac{1}{s_p}\right)$, which clearly shows the numerical stability of the ground state energy as the number of basis increased. The diagonalization scheme was found to be very efficient in reproducing the exact energies of the QD system. For example, at $\lambda = 10$, we had found that only five bases are sufficient to reproduce the exact energy value, $\frac{E}{\hbar\omega_0} = 7.38351$ as shown in the table.

In Fig. 3 we showed the behavior of the heat capacity C_v against the temperature for different values of the confining frequency ω_0, while keeping ω_c unchanged. For particular confining frequency, the heat capacity curve shows a peak value at low temperature, while keeping ω_c unchanged. For particular confining frequency, the heat capacity curve shows a peak value at low temperature, while at high temperature, the heat capacity saturate. These peaks are attributed to the Schottky anomaly. This behavior for the heat capacity is in agreement with the findings of [19, 20]. As the confining frequency increases, the peak of the heat capacity shifts to a higher temperature.

In Fig. 4 we had shown the dependence of the heat capacity on the magnetic field strength for fixed values of the confining frequency and temperature. The heat capacity shows a peak structure which is a result of the transition in the angular momentum of the ground state energy as shown and discussed previously in Fig. 1. For example, the first peak corresponds to the transition in the angular momentum of the ground state from $m_r = 0$ to $m_r = 1$.

In conclusion, we have applied the exact diagonalization method as a theoretical approach to solve the Hamiltonian for interacting electrons confined parabolically in a quantum dot subjected to a magnetic field. We had used the Fock Darwin states as bases to evaluate the coulomb matrix element and to give the result in a closed form. In addition, we had shown the angular momentum transitions in the ground state of GaAs quantum dot spectra. These level crossings cause oscillations in the heat capacity curve of the quantum dot. The results of both, the eigenenergies and the heat capacity, calculated by exact diagonalization method show very good agreement comparable with other recent works.

References

[1] Ashoori R.C., Stormer H.L., Weiner J.S., Pfeiffer L.N., Baldwin K.W., West K.W. N-electron ground state energies of a quantum dot in magnetic field. *Physical review letters*, 1993, **71**(4), P. 613–616.

[2] Ciftja O. Understanding electronic systems in semiconductor quantum dots. *Physica Scripta*, 2013, **88**(5), P. 058302.

[3] Kastner M.A. The single-electron transistor. *Reviews of modern physics*, 1992, **64**(3), P. 849–858.

[4] Loss D., DiVincenzo D.P. Quantum computation with quantum dots. *Physical Review A*, 1998, **57**(1), P. 120–126.

[5] Burkard G., Loss D. and DiVincenzo D.P. Coupled quantum dots as quantum gates. *Physical Review B*, 1999, **59**(3), P. 2070–2078.

[6] Maksym P.A. and Chakraborty T. Quantum dots in a magnetic field: Role of electron-electron interactions. *Physical Review Letters*, 1990, **65**(1), P. 108–111.

[7] Wagner M., Merkt U. and Chaplik A.V. Spin-singlet–spin-triplet oscillations in quantum dots. *Physical Review B*, 1992, **45**(4), P. 1951–1954.

[8] Taut M. Two electrons in a homogeneous magnetic field: particular analytical solutions. *Journal of Physics A: Mathematical and General*, 1994, **27**(3), P. 1045–1055.

[9] Ciftja O. and Kumar A.A. Ground state of two-dimensional quantum-dot helium in zero magnetic field: Perturbation, diagonalization, and variational theory. *Physical Review B*, 2004, **70**(20), P. 205326.

[10] Ciftja O. and Faruk M.G. Two-dimensional quantum-dot helium in a magnetic field: Variational theory. *Physical Review B*, 2005, **72**(20), P. 205334.

[11] Kandemir B.S. Variational study of two-electron quantum dots. *Physical Review B*, 2005, **72**(16), P. 165350.

[12] El-Said M. Spectroscopic structure of two interacting electrons in a quantum dot by the shifted 1/N expansion method. *Physical Review B*, 2000, **61**(19), P. 13026–13031.

[13] De Groote J.J.S., Hornos J.E.M. and Chaplik A.V. Thermodynamic properties of quantum dots in a magnetic field. *Physical Review B*, 1992, **46**(19), P. 12773–12776.

[14] Nguyen N.T. and Peeters F.M. Magnetic field dependence of the many-electron states in a magnetic quantum dot: The ferromagnetic-antiferromagnetic transition. *Physical Review B*, 2008, **78**(4), P. 045321.

[15] Boyacioglu B. and Chatterjee A. Heat capacity and entropy of a GaAs quantum dot with Gaussian confinement. *Journal of applied physics*, 2012, **112**(4), P. 083514.

[16] Helle M., Harju A. and Nieminen, R.M. Two-electron lateral quantum-dot molecules in a magnetic field. *Physical Review B*, 2005, **72**(20), P. 205329.

[17] Nguyen N.T. and Sarma S.D. Impurity effects on semiconductor quantum bits in coupled quantum dots. *Physical Review B*,2011, **83**(23), P. 235322.

[18] Dybalski W. and Hawrylak P. Two electrons in a strongly coupled double quantum dot: From an artificial helium atom to a hydrogen molecule. *Physical Review B*, 2005, **72**(20), P. 205432.

[19] Mikhailov S.A. Quantum-dot lithium in zero magnetic field: Electronic properties, thermodynamics, and Fermi liquid–Wigner solid crossover in the ground state. *Physical Review B*, 2002, **65**(7), P. 115312.

[20] Müller, H.M. and Koonin, S.E. Phase transitions in quantum dots. *Physical Review B*, 1996, **54**(20), P. 14532.

[21] Sharma H.K., Boda A., Boyacioglu B. and Chatterjee A. Electronic and magnetic properties of a two-electron Gaussian GaAs quantum dot with spin-Zeeman term: A study by numerical diagonalization. *Journal of Magnetism and Magnetic Materials*, 2019, **469**, P. 171–177.

[22] Shaer A., Elsaid M.K. and Elhasan M. Variational calculations of the heat capacity of a semiconductor quantum dot in magnetic fields. *Chinese journal of physics*, 2016, **54**(3), P. 391–397.

[23] Al Shorman M.M., Nammas F.S., Haddad H. and Shukri A.A. Heat capacity and entropy of two electrons quantum dot in a magnetic field with parabolic interaction. *Chinese journal of physics* 2018, **56**(3), P. 1057–1063.

[24] Nammas F.S. Thermodynamic properties of two electrons quantum dot with harmonic interaction. *Physica A: Statistical Mechanics and its Applications*, 2018, **508**, P. 187–198.

[25] Shaer A., Elsaid M.K. and Elhasan M. Magnetization of GaAs parabolic quantum dot by variation method. *J. Phys. Sci. Appl* 2016, **6**(2), P. 39–46.

NANOSYSTEMS: PHYSICS, CHEMISTRY, MATHEMATICS, 2019, 10 (5), P. 536–539

Magnetic properties of the electrons in a phosphorene monolayer

V. V. Karpunin, N. N. Khvastunov

Evseviev Mordovia State Pedagogical Institute, Studencheskaya 11 A, Saransk, 340007, Russia
karpuninvv@mail.ru, khvastunovnn@mail.ru

PACS 07.55.Jg, 13.40.Em **DOI 10.17586/2220-8054-2019-10-5-536-539**

The magnetic moment of a phosphorene monolayer is calculated in the presence of a perpendicular magnetic field **B**. Landau levels are strongly anisotropic with different anisotropic effective masses. The oscillatory character of the magnetic moment dependences on the magnetic field is investigated.

Keywords: Magnetic moment, phosphorene monolayer.

Received: 24 September 2019

Revised: 28 September 2019

1. Introduction

In recent years, monolayers of black phosphorus (phosphorene) have been intensively studied. In [1], the Landau levels (LLs) and magneto-transport (MT) properties of phosphorene under a perpendicular magnetic field were studied. Owing to the anisotropic energy dispersions, i.e., the effective masses, the Landau splittings of conduction and valence band are different for a fixed magnetic field, and the wavefunctions corresponding to the LLs show strong anisotropic behavior.

In [2], the magneto-optical transport properties of a phosphorene monolayer subjected to an external perpendicular magnetic field were studied, the magneto-optical Hall and longitudinal optical conductivities as functions of temperature, a magnetic field, and Fermi energy were evaluated, and it was shown that they were strongly influenced by the magnetic field.

In [3], continuum descriptions of single layer and bilayer black phosphorus, starting from a tight binding model that reproduces the results of first-principles calculations, have been presented; also, the spectra of electrons and holes in the vicinity of the Fermi level at the Γ point were obtained and the Landau-level spectra for both systems were calculated.

In [4], the electronic properties of 2D electron gas in black phosphorus multilayers due to the presence of a perpendicular magnetic field have been examined. Authors found that resonant structures in the ac conductivity exhibit a redshift with increasing doping due to interband coupling,suggesting possible electric modulation of light absorption and Faraday rotation.

In [5], the linear, the third-order nonlinear, and the total magneto-optical absorption coefficients have been studied, as well as the relative refractive index changes in monolayer phosphorene in the presence of an external perpendicular magnetic field.

In [6], the authors review recent experimental and theoretical work addressing the quantum oscillatory magnetization $M(B)$ in 2DESs subject to SOI. They first introduce a theoretical model that describes $M(B)$ by numerically solving the Hamiltonian including Rashba-SOI and Dresselhaus-SOI and the Zeeman term in an arbitrarily tilted magnetic field. Both $E_F(B)$ and $M(B)$ show pronounced beating patterns in low magnetic fields. This pattern is a consequence of the nonlinear LL dispersion induced by the SOI, leading to an uneven spacing of levels at E_F.

In [7], the authors investigated the optical responses of monolayer phosphorene subjected to a circular electromagnetic wave. Band structures for the monolayer phosphorene in the absence and presence of perpendicular electric field were plotted. With the aid of the tight-binding model and Kubo formalism implemented in the linear response theory, the anisotropic optical conductivity of phosphorene is being calculated. They have evaluated the reflected, transmitted and absorbed waves as a function of the electric field at optical frequencies beneath, near and above the band gap.

The microscopic mechanism of magnetization and polarization resulting from strong spin-orbital coupling of the electron gas in multiferroics was examined in [8]. Explicit analytic expressions were obtained for the magnetization and polarization of the electron gas in multiferroics.

The magnetic response of a quantum wire of elliptical cross section was investigated in [9]. An explicit analytic expression was found for the spectrum and wave functions of an electron in the wire. Using an approach based on classical partition function finding, an expression was obtained for the magnetic response of the electron gas in the wire. The dependence of the response on the magnitude and direction of the magnetic field was found.

The magnetic moment of single layer graphene rings is investigated in [10]. An analytical expression for the magnetic moment as a function of the magnetic field flux through the one-dimensional quantum rings was obtained. This expression has the oscillation character. The oscillation period is equal to one flux quanta.

The absorption coefficient of the electromagnetic radiation in a phosphorene single layer placed in a magnetic field was found in [11]. A degenerate and nondegenerate electron gas is being considered. The resonant dependences of the absorptance on the radiation frequency and applied magnetic field were found.

Let us consider a quasi-one-dimensional electron gas in a phosphorene monolayer. An analytical expression for the LLs in low energy regime is obtained via solving the decoupled Hamiltonian, which agrees well with the numerical calculations [1,2]. The Hamiltonian of such a system is defined by the expression [1,2]:

$$H = \begin{pmatrix} E_c + (\alpha'\Pi_x^2 + \beta\Pi_y^2)/2 & 0 \\ 0 & E_v - (\lambda'\Pi_x^2 - \eta\Pi_y^2)/2 \end{pmatrix}, \tag{1}$$

where E_c corresponds to the boundary of the conduction band, E_v corresponds to the boundary of the valence band, $\alpha' = \alpha + \gamma^2/E_g$, $\lambda' = \lambda + \gamma^2/E_g$, $\gamma = 8.5 \cdot 10^5 m/s$, $\alpha = 1/m_{cx}$, $\beta = 1/m_{cy}$, $\lambda = 1/m_{vx}$, $\eta = 1/m_{vy}$, $m_{cx} = 0.793 m_e$, $m_{cy} = 0.848 m_e$, $m_{vx} = 0.1.363 m_e$, $m_{vy} = 1.142 m_e$, m_e is the free electron mass, $E_g = E_c - E_v = 1.52$ eV, $\mathbf{\Pi} = \mathbf{p} + \frac{e}{c}\mathbf{A}$ is a generalized momentum operator.

The energy spectrum of the eigenstates of electrons in a magnetic field can be written as follows [1,2]:

$$E_{n,s} = E_s + s\left(n + \frac{1}{2}\right)\hbar\omega_s, \tag{2}$$

where $s \pm 1$ corresponds to the boundary of the conduction and valence band, formula universally describes the Landau levels of the conduction band and the valence band, $E_s = E_+ = E_c$ for conduction band, $n = 0, 1, 2, 3....$, $\omega_+ = \omega_c' = eB/(m_{cx}' m_{cy})^{1/2} c = 2.657\omega_e$ is modified cyclotron frequency,$m_{cx}' = 0.167 m_e$, $\omega_e = eB/m_e c$.

The article is organized as follows: The magnetic moment is being calculated by two methods and the results are being discussed.

2. Magnetic moment

The classical expression of the thermodynamic potential has the form [13]:

$$\Omega = -T\sum_{n=0}^{\infty} \ln\left(1 + \exp\left(\frac{\mu - E_{n,+}}{T}\right)\right), \tag{3}$$

here μ_B is the Bohr magneton, μ is chemical potential. Then for the magnetic moment we get:

$$-M = \sum_{n=0}^{\infty} \frac{dE_{n,+}}{dB}\left(1 + \exp\left(\frac{E_{n,+} - \mu}{T}\right)\right)^{-1}, \tag{4}$$

where

$$\frac{dE_{n,+}}{dB} = a\left(n + \frac{1}{2}\right)\mu_B, \tag{5}$$

where $a = 5.314$. Finally we can obtain:

$$-\frac{M(T)|_{T\neq 0}}{\mu_B} = \sum_{n=0}^{\infty} a\left(n + \frac{1}{2}\right)\frac{1}{1 + \exp(E_{n,+} - \mu)/T}. \tag{6}$$

In the second method thermodynamic potential Ω can be obtained from the dependence $\Omega(Z)$ [8,10]. This method is applied in [12] for three-dimensional electron gas Then we obtain:

$$\Omega = \frac{E_+}{2\pi i}\int_{\alpha - i\infty}^{\alpha + i\infty} \frac{Z(\xi)d\xi}{\xi^2}\int_0^{\infty} \exp(E\xi)\frac{\partial f_0}{\partial E}dE, \tag{7}$$

where $f_0(E)$ is the Fermi distribution function and $\alpha \leq 1/T$.

The statistical sum has the form:

$$Z(\xi) = \sum_{n=0}^{\infty} \exp(-\xi\varepsilon_n), \quad \xi = E_+/T. \tag{8}$$

We use the approach [8, 10] in order to find Ω. Let us introduce the notation $z(\varepsilon_F)$:

$$z(\varepsilon) = \frac{1}{2\pi i} \int\limits_{\alpha - i\infty}^{\alpha + i\infty} \frac{\exp(\varepsilon\xi) Z(\xi) d\xi}{\xi^2}. \tag{9}$$

As is clear from (7) $\Omega_0 = \Omega(T = 0) = -z(\varepsilon_F)E_0$, where $\varepsilon_F = E_F/E_+$ and E_F is Fermi energy. We can represent (9) in the form:

$$z(\varepsilon_F) = \frac{1}{2\pi i} \int\limits_{\alpha - i\infty}^{\alpha + i\infty} \sum_{n=0}^{\infty} \exp[(\varepsilon_F - \varepsilon_n)\xi] \frac{d\xi}{\xi^2}. \tag{10}$$

We rewrite magnetic moment of the phosphorene monolayer $\mathbf{M} = -\partial\Omega/\partial\mathbf{B}$ in the convenient form:

$$M = -\frac{\partial\omega_+}{\partial B} \frac{\partial\Omega}{\partial\omega_+} = -2.657 \frac{e}{m_0 c} \frac{\partial\Omega}{\partial\omega_+}. \tag{11}$$

It should be noted that from the formula (9) one must get the expression for $\partial z/\partial\omega_+$:

$$\frac{dz(\varepsilon)}{d\omega_+} = \frac{1}{2\pi i} \int\limits_{\alpha - i\infty}^{\alpha + i\infty} \exp(\varepsilon\xi) \frac{1}{\xi^2} \frac{dZ}{d\omega_+} d\xi, \tag{12}$$

where

$$\frac{dZ}{d\omega_+} = -\xi \sum_{n=0}^{\infty} \exp(-\varepsilon_n \xi) \frac{\hbar(n + 1/2)}{E_+}. \tag{13}$$

As it follows from (13),(12) $dz/d\omega_+$ has the form:

$$\frac{dz(\varepsilon)}{d\omega_+} = -\frac{1}{2\pi i} \int\limits_{\alpha - i\infty}^{\alpha + i\infty} \sum_{n=0}^{\infty} \frac{\exp((\varepsilon - \varepsilon_n)\xi)}{\xi} \frac{\hbar(n + 1/2)}{E_+} d\xi. \tag{14}$$

To take the integral in (14), we need to use [14]:

$$\frac{1}{2\pi i} \int\limits_{\alpha - i\infty}^{\alpha + i\infty} z^{\gamma - 1} e^{-pz} dz = \begin{cases} 0, & p > 0; \\ \dfrac{1}{(-p)^\gamma \Gamma(1 - \gamma)}, & p < 0. \end{cases} \tag{15}$$

In the case $T \neq 0$ we obtain from (11):

$$-\frac{M(T)|_{T\neq 0}}{\mu_B} = \sum_{n=0}^{\infty} a \left(n + \frac{1}{2}\right) \frac{1}{1 + \exp(E_{n,+} - \mu)/T}, \tag{16}$$

here μ_B is the Bohr magneton, μ is chemical potential , m_0 is the free electron mass, $a = 5.314$.

3. Conclusion

The expression of the magnetic moment of phosphorus electrons was obtained by two methods. The first method is to calculate the classical expression of the thermodynamic potential and then obtain the magnetic moment; the second method is to calculate the thermodynamic potential through the contour integral and then obtain the magnetic moment. Both methods leads to the same expression for the magnetic moment. Note that the second method also makes it easy to go to the $T \to 0$ case. The derivative of the Fermi distribution function is equal to the Dirac delta function. This makes it easy to take the second integral in (7).

Figure 1 shows the oscillatory dependence of the magnetic moment on the inverse magnetic field. Oscillation peaks are smoothed by temperature. The effect should be observed at high magnetic fields, oscillation attenuation occurs in weak fields. This corresponds to de Haas van Alphen oscillations. It should be noted that similar oscillations were also observed in other low-dimensional structures [15].

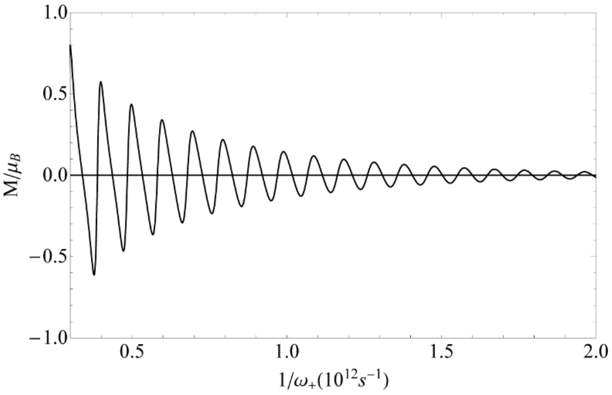

FIG. 1. Dependence of the magnetic moment on the reverse magnetic field, $\mu/T = 1000$, $s = +1$

References

[1] Zhou X.Y., Zhang R., et al. Landau levels and magneto-transport property of monolayer phosphorene. *Sci. Rep.*, 2015, **5**, 12295.
[2] Tahir M., Vasilopoulos P., Peeters F.M. Magneto-optical transport properties of monolayer phosphorene. *Phys. Rev. B*, 2015, **92**, 045420.
[3] Pereira J.M.Jr., Katsnelson M.I. Landau levels of single-layer and bilayer phosphorene. *Phys. Rev. B*, 2015, **92**, 075437.
[4] Jiang Y., Roldan R., Guinea F., Low T. Magnetoelectronic properties of multilayer black phosphorus. *Phys. Rev. B*, 2015, **92**, 085408.
[5] Nguyen C.V., Hieu N.N., et al. Linear and nonlinear magneto-optical properties of monolayer phosphorene. *J. Appl. Phys.*, 2017, **121**, 045107.
[6] Wilde M.A., Rupprecht B., et al. Spinorbit interaction in the magnetization of two-dimensional electron systems. *Phys. Status Solidi B*, 2014, **251**, P. 1710–1724 .
[7] Lea P.T.T., Yarmohammadi M. Perpendicular electric field effects on the propagation of electromagnetic waves through the monolayer phosphorene. *J. Magn. Magn. Mater.*, 2019, **491**, 165629.
[8] Margulis V.A. Magnetization and polarization of the electron gas in multiferroics. *Low Temp. Phys.*, 2014 **40**, P. 363–366.
[9] Margulis V.A., Karpunin V.V., Mironova K.I. Magnetic response of a quantum wire of elliptical cross-section in a magnetic field perpendicular to the axis of the wire. *Nanosystems: Phys. Chem. Math.*, 2018, **9** (2), P. 244–251.
[10] Margulis V.A., Karpunin V.V., Mironova K.I. Magnetic moment of single layer graphene rings. *Sol. St. Commun.*, 2018, **269**, P. 108–111.
[11] Margulis V.A., Karpunin V.V. Resonance Absorption of Electromagnetic Radiation in a Phosphorene Single Layer. *Semiconductors*, 2019, **53**, P. 458–464.
[12] Rumer Yu.B. On the theory of electron gas magnetism. *Zh. Eksp. Teor. Fiz.*, 1948, **18**, P. 1081–1095.
[13] Landau L.D., Lifshitz E.M. *Statistical Physics*, Part 1, 3rd ed., Pergamon Press, Oxford, 1980, 544 p.
[14] Prudnikov A.P., Brychkov Yu.A., Marichev O.I. *Integrals and series, Elementary Functions*, N. Y.: Gordon and Breach, 1986, 808 p.
[15] Zhang S., Ma N., Zhang E. The modulation of the de Haasvan Alphen effect in graphene by electric field. *J. Phys.: Condens. Matter*, 2010, **22**, 115302.

NANOSYSTEMS: PHYSICS, CHEMISTRY, MATHEMATICS, 2019, 10 (5), P. 540–548

Feaftures of the double photoionization spectra of two-electron impurity centers in quasi-zero-dimensional structures

V. D. Krevchik, A. V. Razumov, P. S. Budyansky, M. B. Semenov, I. M. Moyko

Penza State University, Krasnaya str., 40, Penza, 440026, Russia

physics@pnzgu.ru

PACS 73.40.Gk, 03.65.Xp **DOI 10.17586/2220-8054-2019-10-5-540-548**

The zero-range potential method has been generalized to the case of two-electron impurity centers with an effective nuclear charge equal to zero in a spherically symmetric quantum dot (QD), and on the basis of this method the first ionization potential has been calculated by variational method. It is shown that as the radius of QD decreases, the threshold value of the second ionization potential also decreases, beginning with which the existence of the two-electron bound state is possible due to an increase in the size-quantization energy accompanied by suppression of mutual electron repulsion. The light impurity absorption coefficient has been calculated using the dipole approximation for double ionization of the two-electron impurity center by a single photon in a quasi-zero-dimensional structure, which is the transparent dielectric matrix with semiconductor QDs synthesized in it. It is shown that characteristic feature of the double photoionization spectrum is a two-humped profile of the spectral curve due to electron correlations.

Keywords: double photoionization spectra, two-electron impurity centers, quasi-zero-dimensional structures.

Received: 5 September 2019

Revised: 18 September 2019

1. Introduction

A large number of impurities in semiconductors in the bound state can possess not only one, but also two electrons, i.e. these impurities are the helium-like impurity centers [1–14]. Difficulties in the theoretical study of the two-electron impurity states are due to the complex character of the interaction between electrons from the outer shell of the impurity center with valence electrons of the nearest lattice atoms [1]. As a result, it turns out to be impossible to predict not only the position of the multiply charged centers levels, but also their possible charge states. In [1], a variational method has been used to calculate the ground state of the two-electron impurity center. Simulation of the two-electron impurity was based on generalization to the case of two electrons for the Lukovsky model [2]. As is known within the framework of this model, it is assumed that there is a short-range potential of zero radius which determines the ionization energy of a singly ionized impurity, i.e. the second ionization potential, E_2. The authors [1] succeeded in calculating of the first ionization potential E_1 as a function of the nucleus charge Z for the impurity center, with the second ionization potential being taken as the empirical parameter. The process of double photoionization for two-electron impurity centers by a single photon is of special interest. This reaction is one of the fundamental reactions involving several particles. The present paper is devoted to calculation of the first ionization potential for the two-electron impurity center in QD by the variational method, as well as the theoretical study of features of the double photoionization spectra of two-electron impurity centers in a quasi-zero-dimensional structure.

2. Relationship between the first and second ionization potentials of the two-electron impurity center in quantum dot. Comparison with the bulk semiconductor case

We use the semi-empirical model of two-electron impurity centers developed in [1]. The short-range potential in this model is approximated by a potential well of depth V_0, radius of d which is much smaller than the radius of the localized state. As an empirical parameter, we take the energy of a doubly ionized impurity, i.e. the second ionization potential E_2.

Thus, the task is to calculate the first ionization potential E_1. The value E_1 can be found by the variational method with wave functions taken in the form of the product of one-electron wave functions $\Psi\left(\rho_i\right)$ with a variational parameter η, which is associated with the variable energy of the one-electron state.

As units of length and energy, we choose, respectively $a_d = \varepsilon\hbar^2/\left(m^* e^2\right)$ – the effective Bohr radius and $E_d = \hbar^2/\left(2m^* a_d^2\right)$ – the effective Bohr energy. In this case, we take into account that the power of the short-range potential $V_0 d^2$ at $d \to 0$ remains finite. The two-electron wave function satisfies the Schrödinger equation:

$$\mathbf{H}\left(\rho_1, \rho_2\right)\, \Psi\left(\rho_1, \rho_2\right) = E\,\Psi\left(\rho_1, \rho_2\right), \tag{1}$$

where

$$\mathbf{H}(\rho_1,\rho_2)=\mathbf{H}(\rho_1)+\mathbf{H}(\rho_2)+\hbar^2/\left(m^*a_d^2\left|\vec{\rho}_1-\vec{\rho}_2\right|\right),$$

$$\mathbf{H}(\rho_i)=-\hbar^2\Delta_i/\left(2m^*a_d^2\right)-\hbar^2V(\rho_i)/\left(2m^*a_d^2\right),$$

$$\rho_d=d/a_d,\quad V(\rho_i)=\begin{cases}V_0^*, & \rho_i\le\rho_d;\\ 0, & \rho_i>\rho_d,\end{cases},\quad V_0^*=V_0/E_d,\quad \rho_i=r_i/a_d,$$

r_i – electron coordinates at $i=1,2$, m^* – effective electron mass.

Usually, the simplest form of a two-electron wave function $\Psi(\rho_1,\rho_2)$ leading to a satisfactory approximation in problems of helium-like centers is the product of one-electron wave functions:

$$\Psi(\rho_1,\rho_2)=\Psi(\rho_1)\Psi(\rho_2). \tag{2}$$

Using the results of [5], where in the framework of the spherically symmetric potential well model (the "hard wall" model), an expression is obtained for the wave function of an electron localized at a short-range potential in a quantum dot, and for the one-electron wave function $\Psi(\rho_i)$ we have:

$$\Psi(\rho_i)=\frac{B}{\rho_i}\begin{cases}\dfrac{\sinh\left(R_0^*\eta^{-1}-\rho_d\eta^{-1}\right)}{\sinh\left(R_0^*\eta^{-1}\right)}\dfrac{\sin(\chi_0\rho_i)}{\sin(\chi_0\rho_d)}, & \rho_i\le\rho_d;\\ \dfrac{\sinh\left(R_0^*\eta^{-1}-\rho_i\eta^{-1}\right)}{\sinh\left(R_0^*\eta^{-1}\right)}, & \rho_i\ge\rho_d,\end{cases} \tag{3}$$

here, $\chi_0=\sqrt{V_0^*-\eta^{-2}}$, $V_0^*=V_0/E_d$, $\eta=\sqrt{E_d/|E_2|}$, $R_0^*=R_0/a_d$, R_0 – the QD radius,

$$B=\sqrt{\frac{2\eta^{-1}}{\tanh\left(R_0^*\eta^{-1}\right)-R_0^*\eta^{-1}\csc\left(R_0^*\eta^{-1}\right)}}.$$

Taking into account (3), the test two-electron wave function is written in the next form:

$$\Psi(\rho_1,\rho_2)=\frac{B^2}{\rho_1\rho_2}\begin{cases}\dfrac{\sinh^2\left(R_0^*\eta^{-1}-\rho_d\eta^{-1}\right)}{\sinh^2\left(R_0^*\eta^{-1}\right)}\dfrac{\sin(\chi_0\rho_1)\sin(\chi_0\rho_2)}{\sin^2(\chi_0\rho_d)}, & \rho_i\le\rho_d;\\ \dfrac{\sinh\left(R_0^*\eta^{-1}-\rho_1\eta^{-1}\right)\sinh\left(R_0^*\eta^{-1}-\rho_2\eta^{-1}\right)}{\sinh^2\left(R_0^*\eta^{-1}\right)}, & \rho_i\ge\rho_d.\end{cases} \tag{4}$$

The energy of a two-electron impurity center $\varepsilon(R_0^*,\eta)$ is determined by the minimum of the average value of the Hamiltonian:

$$\frac{\varepsilon(R_0^*,\eta)}{E_d}=\frac{\left\langle\Psi(\rho_1,\rho_2)\left|\mathbf{H}(\rho_1,\rho_2)\right|\Psi(\rho_1,\rho_2)\right\rangle}{\left\langle\left|\Psi(\rho_1,\rho_2)\right|^2\right\rangle}. \tag{5}$$

Expression (5), taking into account (4), can be represented in the form:

$$
\begin{aligned}
&\frac{\varepsilon\left(R_0^*,\eta\right)}{E_d} = \\
&-\frac{2^6\eta^{-2}\pi^2}{\sinh^4\left(R_0^*\eta^{-1}\right)\left(\tanh\left(R_0^*\eta^{-1}\right)-R_0^*\eta^{-1}\csc\left(R_0^*\eta^{-1}\right)\right)^2}\Bigg\{\frac{\sinh^4\left(R_0^*\eta^{-1}-\rho_d\eta^{-1}\right)}{\sin^4\left(\chi_0\rho_d\right)}\times \\
&\Bigg[\frac{\eta^{-2}}{16\chi_0^2}\Big(\sin\left(2\chi_0\rho_d\right)-2\chi_0\rho_d\Big)^2-\frac{\left(4\chi_0\rho_d-2\sin\left(2\chi_0\rho_d\right)-2\,\mathrm{Si}\left(2\chi_0\rho_d\right)+\mathrm{Si}\left(4\chi_0\rho_d\right)\right)^2}{4\chi_0}\Bigg]+ \\
&2^{-4}\Big(2\eta^{-1}\left(R_0^*-\rho_d\right)-\sinh\left(2\eta^{-1}\left(R_0^*-\rho_2\right)\right)\Big)^2- \\
&\frac{\eta}{2^3}\Bigg\{4\eta^{-1}\left(R_0^*-\rho_d\right)-4\eta^{-1}\rho_d\ln\left(\frac{R_0^*}{\rho_d}\right)-\sinh\left(4R_0^*\eta^{-1}\right)\Big[\mathrm{Chi}\left(4R_0^*\eta^{-1}\right)-\mathrm{Chi}\left(4\rho_d\eta^{-1}\right)\Big]- \\
&\sinh\left(4\eta^{-1}\left(R_0^*-\rho_d\right)\right)-2\sinh\left(4\eta^{-1}\left(R_0^*-\rho_d\right)\right)\ln\left(\frac{R_0^*}{\rho_d}\right)+2\Big[\mathrm{Chi}\left(4\eta^{-1}R_0^*\right)-\mathrm{Chi}\left(4\eta^{-1}\rho_d\right)\Big]\times \\
&\Big[\sinh\left(2\eta^{-1}R_0^*\right)+\cosh\left(2\eta^{-1}R_0^*\right)\Big(2\eta^{-1}\rho_d+\sinh\left(2\eta^{-1}\left(R_0^*-\rho_d\right)\right)\Big)\Big]- \\
&\cosh\left(2\eta^{-1}R_0^*\right)\Big[\mathrm{Shi}\left(2\eta^{-1}R_0^*\right)-\mathrm{Shi}\left(2\eta^{-1}\rho_d\right)\Big]+\cosh\left(2\eta^{-1}\rho_d\right)\times \\
&\Big[\mathrm{Shi}\left(2\eta^{-1}R_0^*\right)-\mathrm{Shi}\left(2\eta^{-1}\rho_d\right)\Big]-\cosh\left(2\eta^{-1}\left(2R_0^*-\rho_d\right)\right)\Big[\mathrm{Shi}\left(2\eta^{-1}R_0^*\right)-\mathrm{Shi}\left(2\eta^{-1}\rho_d\right)\Big]- \\
&4\eta^{-1}\rho_d\ \sinh\left(2\eta^{-1}R_0^*\right)\Big[\mathrm{Shi}\left(2\eta^{-1}R_0^*\right)-\mathrm{Shi}\left(2\eta^{-1}\rho_d\right)\Big]+ \\
&\cosh\left(4\eta^{-1}R_0^*\right)\times\Big[\mathrm{Shi}\left(4\eta^{-1}R_0^*\right)-\mathrm{Shi}\left(4\eta^{-1}\rho_d\right)\Big]\Bigg\}\Bigg\},
\end{aligned}
\tag{6}
$$

where $\mathrm{Chi}\,(x)$ and $\mathrm{Shi}\,(x)$ – integral hyperbolic cosine and sine, respectively.

To perform transition to the limit, it is necessary to study the behavior of the short-range potential power $\gamma = \rho_d^2\chi_0^2$ at $d \to 0$. For this purpose, we use the continuity of the derivative of the one-electron wave function (3) at $\rho_i = \rho_d$. Elementary calculations lead to the following:

$$\cos\left(\rho_d\chi_0\right) = 0. \tag{7}$$

In the limit $d \to 0$, we have:

$$\gamma = \left(\rho_d^2\chi_0^2\right)_{d\to 0} = \left[\frac{\pi}{2}\left(2n+1\right)\right]^2, \quad n = 0, 1, 2\ldots. \tag{8}$$

Thus, the value γ can take only discrete values defined by the expression (8).

Condition (8) allows one to obtain the limiting values of some trigonometric and integral functions that are necessary for the transition to the limit:

$$
\begin{gathered}
\sin\left(\chi_0\rho_d\right) = 0, \quad \sin\left(2\chi_0\rho_d\right) = 0, \quad \mathrm{Si}\left(2\chi_0\rho_d\right) = 0, \\
\mathrm{Si}\left(4\chi_0\rho_d\right) = 0, \quad \mathrm{Chi}\left(4\rho_d\eta^{-1}\right) = 1, \quad \mathrm{Shi}\left(2\eta^{-1}\rho_d\right) = 0.
\end{gathered}
\tag{9}
$$

Having made the transition to the limit ($d \to 0$) in (6), taking into account (9), for $\varepsilon\left(R_0^*,\eta\right)/E_d$ we obtain:

$$
\begin{aligned}
&\frac{\varepsilon\left(R_0^*,\eta\right)}{E_d} = \\
&-2^3\eta^{-2}\pi^2\sinh^{-4}\left(R_0^*\eta^{-1}\right)\Big(\tanh\left(R_0^*\eta^{-1}\right)-R_0^*\eta^{-1}\csc\left(R_0^*\eta^{-1}\right)\Big)^{-2}\times \\
&\Bigg\{2^{-1}\left(2\eta^{-1}R_0^*-\sinh\left(2\eta^{-1}R_0^*\right)\right)^2+\eta\Bigg[-4\eta^{-1}R_0^*-8\cosh^3\left(\eta^{-1}R_0^*\right)\sinh\left(\eta^{-1}R_0^*\right)\mathrm{Chi}\left(2\eta^{-1}R_0^*\right)+ \\
&2\eta^{-1}R_0^*+2\ln\left(2\exp\left(1+C\right)\eta^{-1}R_0^*\right)\sinh\left(2\eta^{-1}R_0^*\right)+\left(\mathrm{Chi}\left(4\eta^{-1}R_0^*\right)-\ln 2\right)\sinh\left(4\eta^{-1}R_0^*\right)- \\
&\mathrm{Shi}\left(2\eta^{-1}R_0^*\right)\left(1-2\cosh\left(2\eta^{-1}R_0^*\right)-\cosh\left(4\eta^{-1}R_0^*\right)\right)+\cosh\left(4\eta^{-1}R_0^*\right)\mathrm{Shi}\left(4\eta^{-1}R_0^*\right)\Bigg]\Bigg\},
\end{aligned}
\tag{10}
$$

here, $C = 0.577$ – the Euler constant.

Minimization with respect to the parameter η leads to a transcendental equation for finding the extreme value $\tilde{\eta}$:

$$\frac{\partial\varepsilon\left(R_0^*,\eta\right)}{\partial\eta}=0. \tag{11}$$

The explicit expression for (11) has the following:

$$\begin{gathered}
\Bigg\{\frac{2^7\pi^2\tilde{\eta}^{-2}}{\sinh^4\left(R_0^*\tilde{\eta}^{-1}\right)\left(\tanh\left(R_0^*\tilde{\eta}^{-1}\right)-R_0^*\tilde{\eta}^{-1}\operatorname{csc}\left(R_0^*\tilde{\eta}^{-1}\right)\right)^3}\times\\
\Big[R_0^*\tilde{\eta}^{-2}\operatorname{csc}\left(2\eta^{-1}R_0^*\right)-R_0^*\tilde{\eta}^{-3}\cot\left(2\tilde{\eta}^{-1}R_0^*\right)\operatorname{csc}\left(2\tilde{\eta}^{-1}R_0^*\right)-R_0^*\tilde{\eta}^{-2}\operatorname{sech}\left(2\tilde{\eta}^{-1}R_0^*\right)\Big]+\\
\frac{2^7\pi^2\tilde{\eta}^{-3}-2^8\pi^2\tilde{\eta}^{-4}\coth\left(R_0^*\tilde{\eta}^{-1}\right)}{\sinh^4\left(R_0^*\tilde{\eta}^{-1}\right)\left(\tanh\left(R_0^*\tilde{\eta}^{-1}\right)-R_0^*\tilde{\eta}^{-1}\operatorname{csc}\left(R_0^*\tilde{\eta}^{-1}\right)\right)^2}\Bigg\}\times\\
\Bigg\{\frac{1}{16}\left(2R_0^*\tilde{\eta}^{-1}-\sinh\left(2\tilde{\eta}^{-1}R_0^*\right)\right)^2+\frac{1}{8}\tilde{\eta}\Bigg[-4R_0^*\tilde{\eta}^{-1}-8\cosh^3\left(2\tilde{\eta}^{-1}R_0^*\right)\operatorname{Ci}\left(2\tilde{\eta}^{-1}R_0^*\right)\sinh\left(\tilde{\eta}^{-1}R_0^*\right)+\\
2\ln\left(\tilde{\eta}^{-1}R_0^*e^{1+\gamma}\right)\sinh\left(2\tilde{\eta}^{-1}R_0^*\right)+\left(\operatorname{Ci}\left(4\tilde{\eta}^{-1}R_0^*\right)-\ln 2\right)\sinh\left(4\tilde{\eta}^{-1}R_0^*\right)-\operatorname{Si}\left(2\tilde{\eta}^{-1}R_0^*\right)\times\\
\Big(1-2\cosh\left(2\tilde{\eta}^{-1}R_0^*\right)-\cosh\left(4\tilde{\eta}^{-1}R_0^*\right)\Big)-\operatorname{Si}\left(4\tilde{\eta}^{-1}R_0^*\right)+\cosh\left(4\tilde{\eta}^{-1}R_0^*\right)\operatorname{Si}\left(4\tilde{\eta}^{-1}R_0^*\right)\Bigg]\Bigg\}-\\
\frac{2^6\pi^2\tilde{\eta}^{-2}}{\sinh^4\left(R_0^*\tilde{\eta}^{-1}\right)\left(\tanh\left(R_0^*\tilde{\eta}^{-1}\right)-R_0^*\tilde{\eta}^{-1}\operatorname{csc}\left(R_0^*\tilde{\eta}^{-1}\right)\right)^2}\times\\
\Bigg\{\Bigg[\frac{1}{8}\Big(2R_0^*\tilde{\eta}^{-2}-2\tilde{\eta}^{-2}\cosh\left(2\tilde{\eta}^{-1}R_0^*\right)\Big)^2\Big(2R_0^*\tilde{\eta}^{-1}-\sinh\left(2\tilde{\eta}^{-1}R_0^*\right)\Big)+\\
\frac{\tilde{\eta}}{8}\Bigg[4R_0^*\tilde{\eta}^{-2}+8\tilde{\eta}^{-2}R_0^*\cosh^4\left(\tilde{\eta}^{-1}R_0^*\right)\operatorname{Ci}\left(2\tilde{\eta}^{-1}R_0^*\right)+4\tilde{\eta}^{-2}R_0^*\cosh^4\left(4\tilde{\eta}^{-1}R_0^*\right)+\\
2\ln\left(\tilde{\eta}^{-1}R_0^*e^{1+\gamma}\right)\sinh\left(2\tilde{\eta}^{-1}R_0^*\right)+\left(\operatorname{Ci}\left(4\tilde{\eta}^{-1}R_0^*\right)-\ln 2\right)\sinh\left(4\tilde{\eta}^{-1}R_0^*\right)-\operatorname{Si}\left(2\tilde{\eta}^{-1}R_0^*\right)\times\\
\Big(1-2\cosh\left(2\tilde{\eta}^{-1}R_0^*\right)-\cosh\left(4\tilde{\eta}^{-1}R_0^*\right)\Big)-\operatorname{Si}\left(4\tilde{\eta}^{-1}R_0^*\right)+\cosh\left(4\tilde{\eta}^{-1}R_0^*\right)\operatorname{Si}\left(4\tilde{\eta}^{-1}R_0^*\right)\Bigg]\Bigg]+\\
\frac{1}{8}\Bigg[-4R_0^*\tilde{\eta}^{-1}-8\cosh^3\left(2\tilde{\eta}^{-1}R_0^*\right)\operatorname{Ci}\left(2\tilde{\eta}^{-1}R_0^*\right)\sinh\left(\tilde{\eta}^{-1}R_0^*\right)\times\\
\Big(\operatorname{Ci}\left(2\tilde{\eta}^{-1}R_0^*\right)-\ln 2\Big)-4\tilde{\eta}^{-2}R_0^*\ln\left(\tilde{\eta}^{-1}R_0^*e^{1+\gamma}\right)\cosh\left(2\tilde{\eta}^{-1}R_0^*\right)+8\tilde{\eta}^{-1}\cosh^3\left(\tilde{\eta}^{-1}R_0^*\right)\times\\
\cosh\left(2\tilde{\eta}^{-1}R_0^*\right)\sinh\left(\tilde{\eta}^{-1}R_0^*\right)+24\tilde{\eta}^{-1}R_0^*\cosh^2\left(\tilde{\eta}^{-1}R_0^*\right)\operatorname{Ci}\left(2\tilde{\eta}^{-1}R_0^*\right)\sinh^2\left(\tilde{\eta}^{-1}R_0^*\right)-\\
2\tilde{\eta}^{-1}\sinh\left(2\tilde{\eta}^{-1}R_0^*\right)-\tilde{\eta}^{-1}\sinh\left(2\tilde{\eta}^{-1}R_0^*\right)\left(1-2\cosh\left(2\tilde{\eta}^{-1}R_0^*\right)-\cosh\left(4\tilde{\eta}^{-1}R_0^*\right)\right)+\\
\tilde{\eta}^{-1}\sinh\left(4\tilde{\eta}^{-1}R_0^*\right)-2\tilde{\eta}^{-1}\cosh\left(4\tilde{\eta}^{-1}R_0^*\right)\sinh\left(4\tilde{\eta}^{-1}R_0^*\right)-4\tilde{\eta}^{-1}R_0^*\operatorname{Si}\left(2\tilde{\eta}^{-1}R_0^*\right)\times\\
\Big(\sinh\left(4\tilde{\eta}^{-1}R_0^*\right)+\sinh\left(4\tilde{\eta}^{-1}R_0^*\right)\Big)-4\tilde{\eta}^{-1}R_0^*\sinh\left(4\tilde{\eta}^{-1}R_0^*\right)\operatorname{Si}\left(4\tilde{\eta}^{-1}R_0^*\right)\Bigg]\Bigg\}=0.
\end{gathered} \tag{12}$$

Taking into account that the minimum value of the functional $\varepsilon\left(R_0^*,\eta\right)/E_d$ achieved with the extreme value of the parameter $\eta=\tilde{\eta}$ is the sum:

$$\frac{\varepsilon\left(R_0^*,\eta\right)}{E_d}=-\frac{E_1}{E_d}-\frac{E_2}{E_d}, \tag{13}$$

one can find the first ionization potential E_1 as a function of the second ionization potential E_2 taken from the experiment:

$$\frac{E_1}{E_d}=-\frac{\varepsilon\left(R_0^*,\eta\right)}{E_d}-\frac{E_2}{E_d}. \tag{14}$$

Figure 1 shows relationship between the first and second ionization potentials of the two-electron impurity center with the nucleus zero charge ($Z=0$) in a semiconductor QD in the Bohr energy units, obtained by numerical calculations (curves 1, 2, 3), and also in the bulk semiconductor case (curves 4, 5, 6) [1].

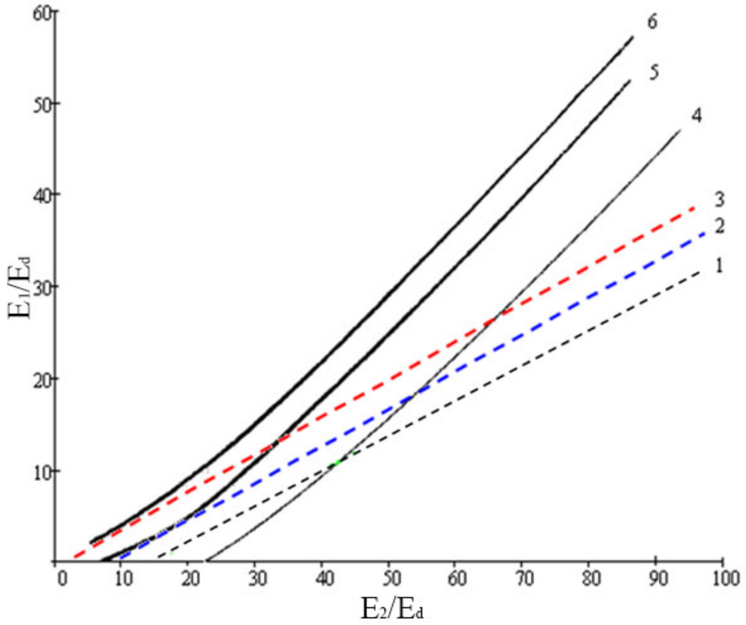

FIG. 1. Connection between the first and second ionization potentials of the two-electron impurity center with the nucleus zero charge ($Z = 0$) (curves 1, 2, 3) in a semiconductor QD and for the bulk semiconductor case [1] (curves 4, 5, 6), for different values of R_0^*:
1: $R_0^* = 0.5$; 2: $R_0^* = 1$; 3: $R_0^* = 3$ and for different values of the nucleus charges Z for the two-electron impurity center: 4: $Z = 1$; 5: $Z = 2$; 6: $Z = 3$

It can be seen that as the QD radius R_0^* increases, the threshold energy E_2/E_d, beginning with which the existence of the two-electron bound state is possible, also increases. This is due to the fact that energy of the electrons' mutual repulsion is not compensated for by the corresponding Coulomb attraction to the nucleus, since $Z = 0$. Indeed, the action of the short-range potential is sharply attenuated due to an increase in the electrons' localization effective radius because of their repulsion. With decreasing R_0^*, the size quantization energy increases, which is accompanied by a suppression of the electrons' mutual repulsion and accordingly by decrease in the threshold value of E_2/E_d. Thus, in QD with $R_0^* \leq 1$, the condition for emergence of the two-electron bound state is much more favorable in comparison with the bulk semiconductor case (compare curves 3 and 4 in Fig. 1).

3. Coefficient of the light absorption under photoionization of the two-electron impurity centers in a quasi-zero-dimensional structure

Atoms of helium and helium-like ions in the ground state are the simplest systems in which double photoionization by a single photon can be observed. The double photoionization process under consideration is an optical transition of two electrons from bound states to the dimensionally – quantized QD states due to absorption of a photon by an impurity atom. The fundamental role of this process consists in the possibility of the theoretical study of an electron's correlations in the double photoionization spectra. Study of such reaction in semiconductive nanostructures is of particular interest in connection with the new physical situation due to dimensional quantization. In this section, the photoionization process of the two-electron impurity center, located in the semiconductive QD ground state, has been considered [5].

In this section, we consider the process of photoionization of a two-electron impurity center in the ground state in a semiconductor QD [5]:

$$\Psi(\rho_1, \rho_2) = \frac{2^2\eta^{-2}}{\left(\tanh\left(R_0^*\eta^{-1}\right) - R_0^*\eta^{-1}\csc\left(R_0^*\eta^{-1}\right)\right)^2} \frac{\sinh\left(R_0^*\eta^{-1} - \rho_1\eta^{-1}\right)\sinh\left(R_0^*\eta^{-1} - \rho_2\eta^{-1}\right)}{\rho_1\rho_2\sinh^2\left(R_0^*\eta^{-1}\right)}. \tag{15}$$

The wave function of the final state will be determined by the product of the wave functions of electrons in a spherical QD:

$$\Phi(\rho_1, \rho_2) = \Psi_{n,l,m}(\rho_1, \phi_1, \theta_1)\,\Psi_{n,l,m}(\rho_2, \phi_2, \theta_2), \tag{16}$$

where

$$\Psi_{n,l,m}\left(\rho_i,\phi_i,\theta_i\right)=\frac{\sqrt{2}}{R_0\sqrt{\rho_i}}\frac{J_{l+1/2}\left(k_{nl}\rho_i\right)}{J_{l+3/2}\left(\xi_{nl}\right)}Y_{lm}\left(\phi_i,\theta_i\right), \tag{17}$$

here $i=1,2$; $Y_{l,m}$ – normalized ball functions; l, m – orbital and magnetic quantum numbers; $J_\nu(x)$ – the first-kind Bessel function of the ν-th order; $k_{nl}=\xi_{nl}/R_0$; ξ_{nl} – n-th root of the Bessel function with l-th order.

The energy of one-electron states, unperturbed by impurities in a spherical QD, will have the form:

$$E_{n,l}=\frac{\hbar^2\xi_{nl}^2}{2m^*R_0^2}. \tag{18}$$

The effective interaction Hamiltonian with the light wave field with a unit polarization vector $\mathbf{e}_\lambda$ and a wave vector $\mathbf{q}$ is determined by the expression

$$\mathbf{H}_{int}=-i\lambda_0\hbar\left(\frac{2\pi\hbar^2\alpha^*}{\varepsilon\omega m^{*2}}I_0\right)^{1/2}\exp\left(i\mathbf{q}\mathbf{r}\right)\left(\mathbf{e}_\lambda\nabla_{\mathbf{r}}\right), \tag{19}$$

where λ_0 – the local field coefficient taking into account the difference between the amplitudes of the local and average macroscopic fields; I_0 – the light intensity; ω – the absorbed light frequency; ϵ – the static dielectric permeability of the QD material; α^* – the fine structure constant taking into account dielectric permeability.

The matrix element that determines the magnitude of the oscillator strength for the dipole optical transitions of electrons from the ground state of the two-electron impurity center (15) to the states $\Psi_{n,l,m}\left(\rho,\phi,\theta\right)$ of the discrete spectrum of quantum dots, is written as follows:

$$\begin{aligned}M=i\lambda_0\sqrt{\frac{2\pi\alpha^*}{\omega}I_0}\Bigg[&\left(E_{n,l,m}-E_1\right)\left\langle\Psi^*_{n,l,m}\left(\rho_1,\theta_1,\phi_1\right)\psi^*\left(\rho_2\right)\left|\mathbf{e}_\lambda,\mathbf{r}_1\right|\Psi\left(\rho_1,\rho_2\right)\right\rangle+\\ &\left(E_{n,l,m}-E_2\right)\left\langle\Psi^*_{n,l,m}\left(\rho_1,\theta_1,\phi_1\right)\psi^*\left(\rho_2\right)\left|\mathbf{e}_\lambda,\mathbf{r}_2\right|\Psi\left(\rho_1,\rho_2\right)\right\rangle\Bigg].\end{aligned} \tag{20}$$

Taking into account (15) – (18), the expression (20) for the square of the matrix element can be written as:

$$\begin{aligned}|M|^2=&\\ &\lambda_0^2\frac{2\pi\alpha^*}{\omega}I_0\frac{E_d^2}{\sinh^6\left(R_0^*\eta^{-1}\right)}\frac{2}{a_d^2R_0^{*2}\left|J_{l+3/2}\left(\xi_{nl}\right)\right|^2}\frac{2^3\eta^{-3}}{\left(\tanh\left(R_0^*\eta^{-1}\right)-R_0^*\eta^{-1}\csc\left(R_0^*\eta^{-1}\right)\right)^3}\times\\ &\left(2\xi_{nl}^2\left(R_0^*\right)^{-2}+\frac{|E_1|}{E_d}+\frac{|E_2|}{E_d}\right)^2k_{nl}^{-3}\left(k_{nl}^2+\eta^{-2}\right)^{-2}\times\\ &\Bigg|\Bigg[\sqrt{k_{nl}+i\eta^{-1}}\left(k_{nl}-i2\eta^{-1}\right)\cosh\left(R_0^*\eta^{-1}\right)\;S\left(\sqrt{\frac{2}{\pi}R_0^*\left(k_{nl}-i\eta^{-1}\right)}\right)+\\ &i\sqrt{k_{nl}-i\eta^{-1}}\left(k_{nl}+i2\eta^{-1}\right)\;\cosh\left(R_0^*\eta^{-1}\right)\mathrm{Si}\left(\sqrt{\frac{2}{\pi}R_0^*\left(k_{nl}+i\eta^{-1}\right)}\right)+\\ &\sqrt{k_{nl}+i\eta^{-1}}\left(k_{nl}-i2\eta^{-1}\right)\sinh\left(R_0^*\eta^{-1}\right)\mathrm{Ci}\left(\sqrt{\frac{2}{\pi}R_0^*\left(k_{nl}-i\eta^{-1}\right)}\right)+\\ &\sqrt{k_{nl}-i\eta^{-1}}\left(k_{nl}+i2\eta^{-1}\right)\sinh\left(R_0^*\eta^{-1}\right)\mathrm{Ci}\left(\sqrt{\frac{2}{\pi}R_0^*\left(k_{nl}+i\eta^{-1}\right)}\right)\Bigg]\Bigg|^2\times\\ &\frac{2}{\pi k_{nl}}\left(\eta^{-2}+k_{nl}^2\right)^{-4}\Bigg|\Bigg\{\eta^{-1}\Big[\left(\eta^{-2}+k_{nl}^2\right)R_0^*\cos\left(k_{nl}R_0^*\right)-\left(\eta^{-2}+2k_{nl}+k_{nl}^2\right)R_0^*\sin\left(k_{nl}R_0^*\right)\Big]+\\ &\left(\eta^{-2}\left(k_{nl}-1\right)+k_{nl}^2\left(k_{nl}+1\right)\right)\sinh\left(R_0^*\eta^{-1}\right)\Bigg\}\Bigg|^2,\end{aligned} \tag{21}$$

here $\mathrm{Ci}(x)$ and $\mathrm{Si}(x)$ – integral cosine and sine, respectively.

We assume that the size dispersion of QDs u arises during the phase decay of a supersaturated solid solution and is satisfactorily described by the Lifshitz–Slezov formula:

$$P\left(u\right)=\begin{cases}\dfrac{3^4 e u^2\exp\left[-1/\left(1-2u/3\right)\right]}{2^{5/3}\left(u+3\right)^{7/3}\left(3/2-u\right)^{11/3}}, & u<3/2;\\ 0, & u>3/2,\end{cases}\tag{22}$$

where $u=R_0/\bar{R}_0$, R_0 and $\bar{R}_0$ – the QD radius and its mean value, correspondingly; e – base of the natural logarithm.

The light impurity absorption coefficient $K(\omega)$, taking into account dispersion of the QD size, is determined by the expression:

$$K\left(\omega\right)=\frac{2\pi N_0}{\hbar I_0}\sum_n\int\limits_0^{3/2}du\,P\left(u\right)\left|M\right|^2\delta\left(E_{n,0,1}+\left|E_1\right|+\left|E_2\right|-\hbar\omega\right),\tag{23}$$

where N_0 – the QD concentration in dielectric matrix; $\delta(x)$ – the Dirac Delta function.

Taking into account (21) and performing integration in (23), the light impurity absorption coefficient $K\left(\omega\right)$ can be written in the next form:

$$\begin{aligned}
&K\left(X\right)=\\
&\sum_{n=1}^{N}P\left(u_n\right)\frac{2^3\lambda_0^2\pi\alpha^*}{X}\times\frac{E_d\left(\eta^{-2}+\xi_{nl}^2\left(\bar{R}_0^*\right)^{-2}u_n^{-2}\right)^{-6}}{a_d^2\left(\bar{R}_0^*\right)^2u_n^2\,\sinh^6\left(\bar{R}_0^*u_n\eta^{-1}\right)\pi\xi_{nl}\left(\bar{R}_0^*\right)^{-1}u_n^{-1}\left|J_{l+3/2}\left(\xi_{nl}\right)\right|^2}\times\\
&\frac{2^3\eta^{-3}}{\left(\tanh\left(\bar{R}_0^*u_n\eta^{-1}\right)-\bar{R}_0^*u_n\eta^{-1}\operatorname{csc}\left(-\bar{R}_0^*u_n\eta^{-1}\right)\right)^3}\left(2\xi_{nl}^2\left(\bar{R}_0^*\right)^{-2}u_n^{-2}+\left|E_1\right|/E_d+\left|E_2\right|/E_d\right)^2\xi_{nl}^3\left(\bar{R}_0^*\right)^{-3}u_n^{-3}\times\\
&\Bigg|\sqrt{\xi_{nl}\bar{R}_0^*+i\eta^{-1}}\left(\xi_{nl}\bar{R}_0^*-i2\eta^{-1}\right)\cosh\left(\bar{R}_0^*u_n\eta^{-1}\right)\operatorname{Si}\left(\sqrt{\frac{2}{\pi}\bar{R}_0^*u_n\left(\xi_{nl}\left(\bar{R}_0^*\right)^{-1}u_n^{-1}-i\eta^{-1}\right)}\right)+\\
&i\sqrt{\xi_{nl}\left(\bar{R}_0^*\right)^{-1}u_n^{-1}-i\eta^{-1}}\left(\xi_{nl}\left(\bar{R}_0^*\right)^{-1}u_n^{-1}+i2\eta^{-1}\right)\cosh\left(\bar{R}_0^*u_n\eta^{-1}\right)\times\\
&\operatorname{Si}\left(\sqrt{\frac{2}{\pi}\bar{R}_0^*u_n\left(\xi_{nl}\left(\bar{R}_0^*\right)^{-1}u_n^{-1}+i\eta^{-1}\right)}\right)+\\
&\sqrt{\xi_{nl}\left(\bar{R}_0^*\right)^{-1}u_n^{-1}-i\eta^{-1}}\left(\xi_{nl}\left(\bar{R}_0^*\right)^{-1}u_n^{-1}-i2\eta^{-1}\right)\sinh\left(\bar{R}_0^*u_n\eta^{-1}\right)\times\\
&\operatorname{Ci}\left(\sqrt{\frac{2}{\pi}\bar{R}_0^*u_n\left(\xi_{nl}\left(\bar{R}_0^*\right)^{-1}u_n^{-1}-i\eta^{-1}\right)}\right)+\\
&\sqrt{\xi_{nl}\left(\bar{R}_0^*\right)^{-1}u_n^{-1}-i\eta^{-1}}\left(\xi_{nl}\left(\bar{R}_0^*\right)^{-1}u_n^{-1}+i2\eta^{-1}\right)\sinh\left(\bar{R}_0^*u_n\eta^{-1}\right)\times\\
&\operatorname{Ci}\left(\sqrt{\frac{2}{\pi}\bar{R}_0^*u_n\left(\xi_{nl}\left(\bar{R}_0^*\right)^{-1}u_n^{-1}+i\eta^{-1}\right)}\right)\Bigg|^2\times\\
&\Bigg|\eta^{-1}\Bigg[\left(\eta^{-2}+\xi_{nl}^2\left(\bar{R}_0^*\right)^{-2}u_n^{-2}\right)\bar{R}_0^*u_n\cos\left(\xi_{nl}\right)-\bar{R}_0^*u_n\sin\left(\xi_{nl}\right)\left(\eta^{-2}+2\xi_{nl}\left(\bar{R}_0^*\right)^{-1}u_n^{-1}+\xi_{nl}^2\left(\bar{R}_0^*\right)^{-2}u_n^{-2}\right)\Bigg]+\\
&\left(\eta^{-2}\left(\xi_{nl}\left(\bar{R}_0^*\right)^{-1}u_n^{-1}-1\right)+k_{nl}^2\left(\xi_{nl}\left(\bar{R}_0^*\right)^{-1}u_n^{-1}+1\right)\right)\sinh\left(\bar{R}_0^*u_n\eta^{-1}\right)\Bigg|^2,
\end{aligned}\tag{24}$$

where $u_n=\xi_{nl}^2/\left(\left(\bar{R}_0^*\right)^2\left(X-\left|E_1\right|/E_d-\left|E_2\right|/E_d\right)\right)$; $N=[n]$ – is an integral part of the solution for a transcendental equation of the form: $\xi_{nl}^2=3\left(\bar{R}_0^*\right)^2\left(X-\left|E_1\right|/E_d-\left|E_2\right|/E_d\right)/2$.

Figures 2(a and b) show the calculated double photoionization spectra, the characteristic feature of which (see curve 1 in Fig. 2(a) and curves 1 – 3 in Fig. 2(b)) is the two-humped profile due to electron correlations. Distance between the spectral curve maxima is determined by modulus of the difference between the first and second ionization potentials of the two-electron impurity center. Fig. 2(a) shows that as the second ionization potential increases, the impurity absorption edge shifts to the spectrum short-wavelength region and the right-hand peak transforms at first to the step (curve 2 in Fig. 2(a)), and then completely disappears on the spectral curve (see curve 3 in Fig. 2(a)). Fig. 2(b)

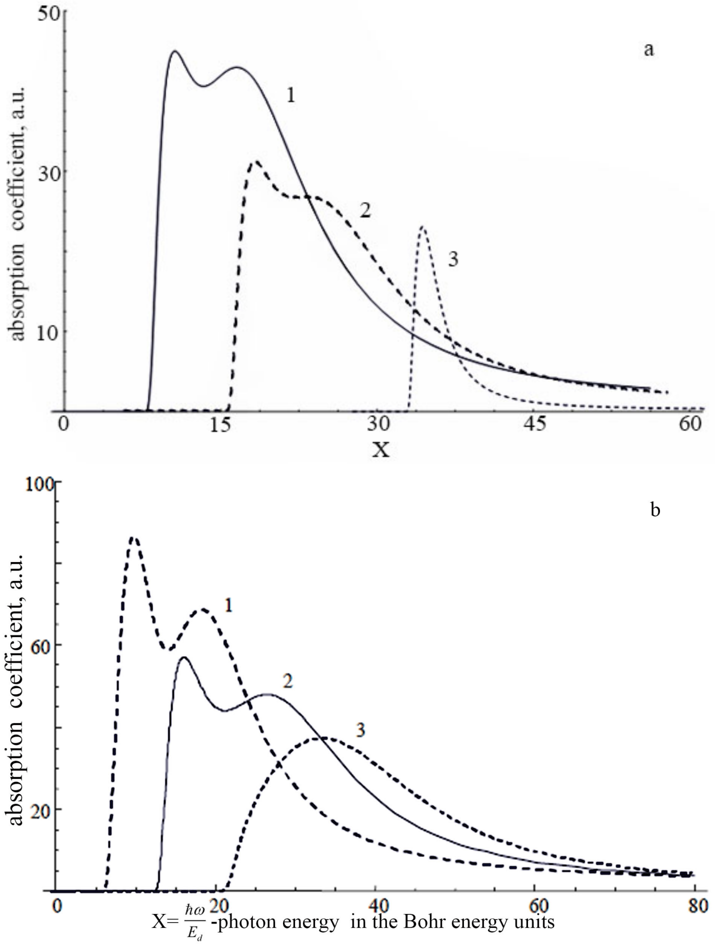

FIG. 2. Spectral dependence of the light absorption coefficient for double photoionization of the two-electron impurity centers in a quasi-zero-dimensional structure: a) for different values of the second ionization potential E_2:
1: $E_2 = 0.04$ eV; 2: $E_2 = 0.05$ eV; 3: $E_2 = 0.08$ eV;
b) for different values of R_0^*: 1 – 3; 2 – 1; 3 – 0.5, with $E_2 = 0.04$ eV

shows transformation of the right peak on the spectral curve with a decrease in the QD mean radius $\bar{R}_0^*$, as a result we can see, that this peak disappears. This is due to the fact that the dimensionally – quantization energy increases with decreasing of $\bar{R}_0^*$, as a result of which the electronic correlation is suppressed.

4. Conclusions

Generalization of the zero-range potential method to the case of two-electron impurity centers in a QD has been carried out. The first ionization potential has been calculated by the variational method, within the semiempirical model of a two-electron impurity center in the spherically symmetric QD. It is shown, that, unlike the case of a bulk semiconductor in QD, formation of the two-electron bound states is possible at sufficiently low ionization potential values, as well as for the nucleus zero charge of an impurity center. Diamagnetic susceptibility of the two-electron and one-electron impurity centers has been calculated for the semiconductive QD. It is shown that an increase in the QD radius leads to an increase in the diamagnetic susceptibility value, which is associated with an increase in the localized state radius. A comparison of the diamagnetic susceptibility for quasi-zero-dimensional two-electron impurity centers and for D^--centers shows that in case of the two-electron impurity centers, the diamagnetic susceptibility is several times larger. In the dipole approximation, in the framework of the effective-mass method, the light impurity absorption coefficient has been calculated for a double ionization of the two-electron impurity center by a single photon. It is shown that a characteristic feature of the double photoionization spectrum is the spectral curve's "two-humped" profile. The distance between the spectral curve maxima is determined by the difference between the first and second ionization potentials of the two-electron impurity center.

Acknowledgements

This work was supported by the Ministry of Education and Science of the Russian Federation (projects No. 3.6321.2017/8.9 and 2019-0940).

References

[1] Grinberg A.A., Belorusets E.D. On the energy spectrum of multiply charged impurity centers in semiconductors. *Solid State Physics*, 1978, **20**, P. 1970–1978.

[2] Lucovsky G. On the photoionization of deep impurity centers in semiconductors. *Solid State Communications*, 1965, **3**,299.

[3] Belorusets E.D., Imamov E.Z., Mamatkulov B.R. Diamagnetism of two-electron deep impurity centers in semiconductors. *Physics and technology of semiconductors*, 1982, **16** (1),89.

[4] Imamov E.Z., Krevchik V.D. On Diamagnetism of Deep Impurities in Quantized Semiconductor Film. *Phys. St. Sol.(b)*, 1982, **114**,201.

[5] Krevchik V.D., Levashov A.V. Energy spectrum and optical properties of the complex "quantum dot – impurity center". *Physics and technology of semiconductors*, 2002, **36** (2),216.

[6] Pakhomov A.A., Khalipov K.V., Yassievich I.N. Local electronic states in semiconductor quantum wells. *Physics and technology of semiconductors*, 1996, **30** (8), 1387.

[7] Mikhailov A.I., Mikhailov I.A. Double photoionization and ionization with excitation under the Compton scattering of high-energy photons on metastable states of the helium-like ions. *JETP*, 1999, **116** (6), 1889.

[8] Eseev M.K., Matveev V.I. Investigation of the analytic wave functions for two-electron systems under dynamic interactions with the multiply charged ions and with the ultrashort pulses of an electromagnetic field. *Journal of technical physics*, 2008, **78** (8),28.

[9] Zaytsev S.A., Knyr V.A., Popov Yu.V., Lahmam-Bennani A. Application of the J-matrix method to Faddeev–Merkuriev equations for (e,2e) reactions: Beyond pseudo-states. *Physical Review A*, 2007, **75** (2),022718.

[10] Pandey R.K., Harbola Manoj K., Singh Vijay A. Helium-like donors in semiconductor quantum dots. *J. Phys.: Condens. Matter*, 2004, **16**,1769.

[11] Castro Arata P.A. Two-electron impurity centers as a tool for the chalcogenide glassy semiconductors studying (St. Petersburg: Publishing House of the Russian State Pedagogical University named by A. I. Herzen), 2006.

[12] Boyarkina N.I., Vasil'ev A.V. Participation of the crystal electronic subsystem in reactions between multiply charged centers in semiconductors. *Physics and technology of semiconductors*, 2000, **34** (2), 172.

[13] Petrov P.V., Ivanov Yu.L., Averkiev N.S. The photoluminescence circular polarization of the two-dimensional system with A^{+}-centers in an external magnetic field. *Physics and technology of semiconductors*, 2011, **45** (27), 794.

[14] Huant S., Mandray A., et al. Well-width dependence of D-cyclotron resonance in quantum wells. *Physical Review B*, 1993, **48**,2370.

NANOSYSTEMS: PHYSICS, CHEMISTRY, MATHEMATICS, 2019, 10 (5), P. 549–563

Approaches to determining the kinetics for the formation of a nano-dispersed substance from the experimental distribution functions of its nanoparticle properties

S. Z. Adzhiev[1], I. V. Melikhov[1], V. V. Vedenyapin[2]
[1]Lomonosov Moscow State University, Moscow, Russia
[2]Keldysh Institute of Applied Mathematics of Russian Academy of Sciences; RUDN-University, Moscow, Russia
sergeyadzhiev@yandex.ru, vicveden@yahoo.com, melikhov@radio.chem.msu.ru

DOI 10.17586/2220-8054-2019-10-5-549-563

In the present paper, we discuss the kinetic equations for the evolution of particles of a nanodispersed substance, distinguishing by properties (sizes, velocities, positions, etc.). The aim of the present investigation is to determine the coefficients for the equations by the distribution functions, which are obtained experimentally. The experiment is characterized by the time interval, which is needed for the measurement of the distribution function. However, the nanodispersed substance is obtained from a highly supersaturated solution or vapor and this time interval is large, thus, one is able to measure distribution functions only when the processes of the integration and the fragmentation of the particles become rather slow. So it is advisable to reconstruct the kinetics for the formation of a nanodispersed substance by the experimental distribution functions measured when the processes are rather slow. The first problem that arises is the obtaining of correct equations, and, hence, the derivation of the equations from each other. From the discrete system of equations for the evolution of discrete distribution functions of particles of a nanodispersed substance, we obtain the continuum equation of the Fokker-Planck type, or of the Einstein-Kolmogorov type, or of the diffuse approximation on the distribution function of nanoparticles distinguishing by the numbers of molecules forming them. We consider the distribution functions, which approximate the experimental data. We determine the coefficients for the equation of the Fokker-Planck type by the stationary and non-stationary distribution functions of a nanodispersed substance. Due to unity of the kinetic approach, the present work may be useful for specialists of various areas, who study the evolution of structures (not only with nanosize) with differing properties.

Keywords: nanodispersed substance, nanoparticles, distribution function of particles by properties, emerging and growth of nanoparticles, aggregation and agglomeration, the Fokker-Planck equation, the Smoluchowski system of equations, the Becker-Döring equations.

Received: 8 September 2019

Revised: 5 October 2019

1. Statement of the problem

The problem, which is solved, is the mathematical description of the kinetics of the emerging, growth and aggregation of nanoparticles by their experimental distribution functions by properties.

The nanodispersed substance is obtained from a highly supersaturated solution or vapor. Significant supersaturation is required to ensure that during formation the particles do not have time to grow to sizes larger than nanometers, the nanoparticles have emerged in sufficient quantity so that the stage of their aggregation becomes dominant. In this case, we obtain aggregates of nanoparticles, i.e. a nanodispersed substance.

The experiment is characterized by the time interval, which is needed for the measurement of the distribution function. It is possible to obtain it only if the variation of the distribution function during this time interval is negligible. So, we are able to measure distribution functions only when the processes of the integration and the fragmentation of the particles are rather slow. In the beginning of the process of the forming of a nanodispersed substance the supersaturation is large and we are not able to measure the distribution function. So we need to reconstruct the kinetics for the formation of a nanodispersed substance by the experimental distribution functions measured, when the process become rather slow. One measurement is not sufficient, we should make the set of experiments varying the parameters of system's condition: the concentration of initial particles (molecules) and the temperature, in order to obtain the coefficients for the equations depending on these parameters.

The main idea for mathematical description of the experimental results of, which determines the structure of the article, is as follows: first, the statement of the problem arises: the parameters of the distribution function are determined. At this stage, the experimenters suggest which parameters they can measure, i.e. which parameters to choose for the model. Then, the first step in mathematical modeling is to create an a priori model containing unknown functions as parameters, which should be determined later. The a priori model consists of writing the correct equations containing unknown parameters. The model should answer the following questions: what are the conditions of the experiment, how and in what range they should be varied and what should be determined in the experiment in order to obtain these unknown functions of the a priori model. On the basis of experiments, these unknown functions are determined, and the a posteriori model arises. Thus, the mathematical description of the experiments is obtained. After that, the investigation is supposed to be repeated, expanding the list and the intervals of variation of the conditions taken into account. The goal is to predict how to synthesize materials.

In the frameworks of a priori models in the papers of J. C. Maxwell [1], L. Boltzmann [2] and etc. the time dependent distribution function by velocities and coordinates appears. Now, there is a multi-parameter description, which is due to the fact that it becomes available for experimental observation. Currently, several methods have been developed for measuring the size distribution of nanoparticles: electron microscopy, the method of dynamic light scattering, e.g. [3, 4]. The problem is to write the equations for the distribution function of particles (bodies) by these many parameters.

In the present paper, we continue the line of works [5–8] and others, devoted to mathematical modeling of emerging and growth of hierarchical structures of a dispersed substance, using the kinetic approach.

In [6], a model was proposed for nanostructure creation of as a result of growth of particles in a supersaturated medium with their multistage modification. The multistage modification was done in order to give particles the desired properties. The aggregation of nanoparticles in agglomerates and the integration of aggregates with each other was considered and the discrete and continuum balance equations for the number of particles and aggregates, taking into account the possibility of their growth and fragmentation, were formulated. The continuum equation has yielded to the evolutionary equation of the Fokker–Planck type, containing frequency functions. They describe the process of aggregate self-organization by the selection of more stable forms. Moreover, each stage of modification is characterized by its own frequency functions. They are subject to independent determination. Frequency functions for all types of impacts used for the creation of nanostructures can form the basis of a methodology for their optimal synthesis.

Typically, a nanostructure is a hierarchical structure. Molecules coalesce and give the original aggregates of molecules (clusters). Coalescences of original agglomerates are secondary aggregates. They also may coalesce with separate molecules. Similarly, the coalescence of secondary aggregates with each other give the tertiary agglomerates, etc. A particle of given generation (or type, kind) is the body in which the constituent elements of all lower generations can be identified. Types of bodies distinguishing by the levels of hierarchical structure (generation numbers) will be denoted by the parameter k: the particles of each k-th generation become larger by attaching particles of all kinds with the parameter $j < k$, and the acts of coalescences randomly alternate with the acts of fragmentations. As a result, the growth process of the particles forms bodies of a dispersed substance, which have a hierarchical structure.

For description of particle formation, it is advisable to distinguish several essential stages of the process: first, original aggregates emerge and grow, and then the stage of aggregation or the formation of agglomerates of the original clusters as a result of their collisions with each other comes, and then the formation of their aggregates occurs. Although all these processes proceed at the same time, but under some conditions, first the process of formation of original particles dominates, then the process of formation of their aggregates (i.e. secondary agglomerates) prevails, then the process of formation of aggregates of secondary agglomerates (i.e. tertiary aggregates) is main, etc.

Under such conditions, the formation of dispersed substance occurs incrementally, and each stage contributes to the nanostructure of the substance.

In order to create a nanostructure (and, generally speaking, some kind of structure) with the desired properties, the phenomena of the emerging and the disruption of the original subnanoparticles, the growth and the dissolution, the appearance and the elimination of growth defects, the capture and the release of the captured impurities, the coalescence and the destruction of agglomerates, recrystallization and the topochemical reactions of sintering and the ceramization are used [5–9]. For describing these phenomena we take into account the properties $\mathbf{X} \equiv \{\mathbf{X}_1, \mathbf{X}_2\}$ of each particle: $\mathbf{X}_1 \equiv \{x_1, x_2, ..., x_i, \ldots, x_r\}$ are external properties, and $\mathbf{X}_2 \equiv \{x_{r+1}, x_{r+2}, ..., x_i, \ldots, x_s\}$ are internal ones. The external parameters of state of a particle characterize its material and energy interaction with the medium, and the internal ones characterize the redistribution of the matter and the energy inside the particle [9].

The state of each particle of any level of the hierarchical structure of a nanodispersed substance is characterized by many parameters. The state of each molecule is characterized by the following external parameters: mass (the volume), the coordinate and the velocity of its center of mass. In the case of aggregates of the first generation, it is supplemented by the next external parameters: parameters of the shape, the surface topography and the volume, which can be more than the sum of the volumes of molecules constituting the given aggregate (the porosity is possible). In the case of secondary agglomerates, it is complemented by the following internal parameters: the positions of the center of mass (relative to center of mass of the considered secondary aggregate) of each of the original aggregates and of the remaining individual molecules constituting it as well as the parameters which define the orientation of the original clusters composing the given secondary agglomerate.

At all stages of the process, the considered system is heterogeneous, and there are the molecules, aggregates of molecules, growing by joining molecules, aggregates of second generation, etc. at its every area. As a first approximation it is appropriate to accept that the mixer provides homogeneity for the medium and the substance forming the phase. In the continuum approximation, each part of the system is characterized by its distribution function of particles by properties: $\Psi\left(\mathbf{X},t\right)=\sum_k\Psi_k\left(\mathbf{X},t\right)$, $N_{k,\mathbf{X}}=\int_{\mathbf{X}_0}^{\mathbf{X}}\Psi_k\left(\mathbf{X}',t\right)d\mathbf{X}'$. Here, $\Psi_k\left(\mathbf{X},t\right)$ is a distribution function of particles of the generation k, $N_{k,\mathbf{X}}$ is a number of particles of the type k in the system, for which the state parameters are smaller than the corresponding component of the vector **X**, $\mathbf{X}_0$ is the minimum possible value of property **X**. **X** does not include the spatial coordinates of the particle, which are identified with the coordinates of the area of the system. The distribution functions by these properties **X** depends upon the properties of the medium enveloping the particles.

The main parameter of the distribution function of particles of each of k kinds is defined as the first parameter in the decomposition below, and it is advisable to take the number of molecules n constituting the particle as the main parameter: $x_1=n$, and then:

$$\Psi_k\left(\mathbf{X},t\right)=\psi_k\left(n,t\right)\cdot f_{k,2}\left(x_2|\,n;t\right)\cdot\ldots\cdot f_{k,s}\left(x_s|\,n,x_2,\ldots,x_{s-1};t\right), \tag{1.1}$$

where $\psi_k\left(n,t\right)$ is the distribution function of particles by the number of molecules which constitute the particle, $f_{k,i}\left(x_i|\,n,x_2,\ldots,x_{i-1};t\right)$, where $i=2,\ldots,s$, are the densities of distributions of particles by the property x_i under the condition that the parameters, which are written after , are fixed: $\int f_{k,i}\left(x_i|\,n,x_2,...,x_{i-1};t\right)dx_i=1$.

The formula (1.1) is sufficient to prove for the case of two variables. Then it is proved by induction.

Lemma. Let a function $f\left(x_1,x_2,...,x_s\right)>0$ is such, that $\int f\left(x_1,...,x_s\right)dx_{s-k}...dx_s$ $(k=0,...,s-2)$ is finite. Then the function f may be represented in the unique way as follows:

$$f\left(x_1,x_2,\ldots,x_s\right)=g_1\left(x_1\right)g_2\left(x_1,x_2\right)\times\ldots\times g_s\left(x_1,x_2,\ldots,x_s\right), \tag{1.2}$$

where

$$\int g_i\left(x_1,x_2,\ldots x_i\right)dx_i=1. \tag{1.3}$$

The proof. According to the method of mathematical induction, this formula is sufficient to prove for the case of two variables. Functions $g_1\left(x_1\right)\equiv\int f\left(x_1,x_2\right)dx_2$, $g_2\left(x_1,x_2\right)\equiv\dfrac{f\left(x_1,x_2\right)}{g_1\left(x_1\right)}$ satisfy equality (1.2): $f\left(x_1,x_2\right)=g_1\left(x_1\right)g_2\left(x_1,x_2\right)$, with condition (1.3): $\int g_2\left(x_1,x_2\right)dx_2=1$.

This representation leads to the description of the probability theory for the second variable x_2 as a random variable: $g_2\left(x_1,x_2\right)$, which is a distribution function of the x_2 under the condition x_1, and is written in probability theory as $g_2\left(x_2|\,x_1\right)$.

The following formula in probability theory called Bayes formula [10], and the kinetic theory makes sense of the reduced description, as noted in [5].

Example 1 [1,2]. If a variable **v** is considered as a probabilistic one, and the description is reduced as a result of collisions to the locally Maxwell distribution:

$$f\left(\mathbf{x},\mathbf{v},t\right)=n\left(\mathbf{x},t\right)\left(\frac{M}{2\pi\kappa_BT\left(x,t\right)}\right)^{3/2}\exp\left(-\frac{M\left(\mathbf{v}-\mathbf{V}\left(\mathbf{x},t\right)\right)^2}{2\kappa_BT\left(\mathbf{x},t\right)}\right), \tag{1.4}$$

where $f\left(\mathbf{x},\mathbf{v},t\right)$ is a distribution functions of molecules with mass M by space $\mathbf{x}\in R^3$, velocities $\mathbf{v}\in R^3$ at a time t. Here, $n\left(\mathbf{x},t\right)\equiv\psi_1\left(\mathbf{x},t\right)$ is a concentration of such particles with mass M, $T\left(\mathbf{x},t\right)$ is the temperature, κ_B is the Boltzmann constant, $\mathbf{V}\left(\mathbf{x},t\right)$ is the value of the average velocity of particles with mass M.

The example 1 we consider as a classical one. Let us consider another example of distribution (1.1) from [11].

Example 2. [1,2,11]. An example of distribution (1.1) is given by the Maxwell distribution function of particles with mass $M_n=nM_0$, where M_0 is the mass of one molecule of a substance forming the solid phase, n is a number of molecules constituting the particle [11]:

$$\Psi_1(n,\mathbf{x},\mathbf{p},t)=\psi_1\left(n,\mathbf{x},t\right)\times\frac{1}{\left(2\pi\,M_n\kappa_BT\left(\mathbf{x},t\right)\right)^{3/2}}\exp\left(-\frac{\left(\mathbf{p}-M_n\mathbf{V}\left(\mathbf{x},t\right)\right)^2}{2M_n\kappa_BT\left(\mathbf{x},t\right)}\right), \tag{1.5}$$

where **p** is a momentum of a the particle with the mass M_n.

More strictly, mass M_n in (1.5) should be presented as

$$M_n=nM_0+n_LM_L, \tag{1.6}$$

where M_0 and M_L are the masses of single molecules of the substance forming the solid phase and of the medium of the system, n_L is a number of medium molecules trapped in the volume and on the surface of the particle.

Then:

$$n=\frac{v-n_Lv_{0L}}{v_0}, \tag{1.7}$$

where v is a volume of a particle, v_0 and v_{0L} are volumes occupied by single molecules of the substance forming the solid phase and of the medium of the system inside the particle. Within the framework of the evaluation model, it is advisable to assume that the volume v and surface area s of each particle can be represented as functions of the effective size l: when

$$v >> n_L v_{0L}, \tag{1.8}$$

we have:

$$l_M = \gamma_1 l, \quad s = \gamma_2 l^2, \quad v = \gamma_3 l^3, \tag{1.9}$$

where γ_1, γ_2 and γ_3 are shape factors, l_M is maximum distance between points on the particle surface. A number of regularities in the behavior of a particle can be revealed by assuming that its shape is close to a sphere ($\gamma_1 = 1$, $\gamma_2 = \pi$, $\gamma_3 = \frac{\pi}{6}$) or a cube ($\gamma_1 = \sqrt{3}$, $\gamma_2 = 6$, $\gamma_3 = 1$). For more accurate modeling, it is necessary to use experimentally determined shape factors.

If the particle has a plate shape, then it is advisable to assume that its volume is equal to $v = hs$, where h is an effective thickness of the particle. If the particle is a chain of molecules, then $v = h^2 l_M$. Therefore, in the general case, taking into account (1.7), (1.8) and (1.9), we have:

$$n = \frac{\gamma_\delta h^{3-\delta} l^\delta}{v_0}, \tag{1.10}$$

where v_0 is the volume of one molecule, $\delta = 1$ for chains of molecules, $\delta = 2$ for plates, $\delta = 3$ for spheres or cubes. We also assume that the shape parameters γ_δ doesn't depend on l.

The number of molecules n constituting the particle is the main parameter, and so, it is of interest in the first turn the distribution functions of a dispersed substance by it. In the experiment, we obtain the integral distribution function depending on the particle's size l, for which a discrete set of values at points are measured. We denote the integral distribution function of aggregates of generation k simulating (approximating) the experimental discrete distribution as $\theta_k(l)$ and the corresponding differential distribution function as $\phi_k(l)$.

We consider the two-component system which consists of the solvent or the carrier gas and the substance forming the solid phase. The system is restricted by the inert walls, which have the desired properties and transfer impacts from the system's surroundings. The number of molecules of the reagent and the number of molecules of the system medium are fixed: they are constant or vary in a specific manner. The system is considered as a set of homogeneous areas. The system is characterized by its volume, temperature, concentration of component at each point, pressure of the gas or of the liquid matter on the walls, and energies of various types is supplied in it. The laws of reflection of gas from the walls can be found in [12]. The dynamics of an elastic collision of two bodies has been studied by J. C. Maxwell [13].

The growth process of the aggregates of the type k is determined by the frequency of collisions with particles of smaller generation than k. The reason for the growth of the particles is a long-ranged attraction between them: because of this, during the acts of the collision, they coalesce. The repulsion is short-ranged. The fragmentation has two causes – due to the excited state of the particle itself and because of external collisions with the carrier gas.

The elementary act of the formation of aggregates can be considered as the collision of two particles of any kind with their subsequent stay in contact for a sufficiently long time. The frequency of such acts can be represented as:

$$\alpha = \alpha_{12} N_1 N_2 \exp \frac{-\varepsilon_A}{kT},$$

where α_{12} is a frequency function associated with the probability of particles approaching until the contact, N_1 and N_2 are particle concentrations, ε_A is an activation energy required to overcome the attraction of particles to the molecules of their environment. The termination of particle contact can be considered as an act of fragmentation of the aggregate. The fragmentation of aggregates is expediently described by the Arrhenius equation [11, 14, 15], introducing into consideration the activation energy of fragmentation ε_F.

The frequency functions of particles, which are volumes of molecules, can be proportional to $n^{1/3}$, $n^{2/3}$, or be independent on n. The first case means that the active centers are one-dimensional structure, in the second one the number of active centers is proportional to the square of the surface, and in the last case the number of active centers is a fixed number.

The question about the formation and about the size of the particles, starting from which the particle begins to grow rapidly, is a separate problem. The experiments demonstrate the existence of such size, and the problem is to construct a mathematical model which evaluates this size. At a certain particle size, the molecules in it are arranged due to the mutual attraction, and the probability of the fragmentation decreases. This particle has low porosity and obtains the certain shape. In the mathematical modeling, as the maximum of simplification, it is necessary to consider three forms of the particles which are the one-dimensional, two-dimensional and three-dimensional configurations.

Based on the consideration of the three configurations, we can estimate their stability, which depends on the binding energy between molecules in the particle.

We'll consider only two parameters characterizing the particle of a nanodispersed substance: its mass and its potential energy, which we will account in the equations of the model.

The aim of our investigation is to determine the coefficients of the equations for the distribution function from ones, which are obtained in experiments. Thus, the first problem is to obtain this equations, the second one is to consider the classes of distribution functions of particles of a nanodispersed substance, reasonably approximating the experimental data obtained, and the third is to obtain relationships between the parameters of such functions and the coefficients of the equations.

The first problem that arises is the obtaining of correct equations describing the kinetic of a nanodispersed substance, and, hence, the derivation of the equations from each other: the consideration of the connection between the discrete and continuum equations, the transition from a description with multiple parameters to a reduced one. For instance, the derivation of equations on the particle size distribution function from the generalized Boltzmann-type equations for the distribution function of bodies by sizes and velocities of their centers of mass. The second problem was preliminarily considered in [11]. In the next paragraph, we begin to discuss the first one. A discrete distribution function is considered, and the equations for it is obtained. For particles consisting of less than 10^2–10^3 molecules, the introduction of the continuum description is not advisable.

In Section 2 it is shown how from the discrete description the continuum equations of the Fokker–Planck type are obtained. In probability theory, the Fokker–Planck equation is called the differential Einstein–Kolmogorov equation [16]. Due to the parabolic nature of the obtained equation, it is also called the diffuse approximation.

In Section 3, we determine the coefficients of the considered kinetic equations of a nanodispersed substance by their stationary solution. However, in experiments, we obtain distribution functions which can't be the stationary solutions of the considered equations. They will continue disperse in the space of particles' sizes. We discuss such functions in the following paragraphs.

In Sections 4 and 5, we discuss the parameters and the classes of distribution functions of particles of a dispersed substance, approximating well the data obtained in the experiments.

In Section 6, we consider the exact solution of the diffuse approximation, which coincides with the proposed new approximating distribution function of particles of a dispersed substance at each moment of time and obtain the relationships between the parameters of approximating functions and the coefficients of the equations describing the kinetic of a dispersed substance.

2. The Becker-Doring case and the continuum description of the kinetics of a dispersed substance

Let us write the simplest kinetic equations for the evolution of the distribution function of particles of a dispersed substance: first, the discrete ones, and then the continuous ones (the equations of the Fokker–Planck type).

The equations for the coalescence of particles were first derived and studied for solutions by Smoluchowski [17] (without the fragmentation – the Smoluchowski case). If only one molecule can attach to or separate from another particle, then we have the Becker–Döring system of equations [18]. It describes the first stage of the aggregation process. During the formation of first generation aggregates, it can be assumed that their number is quite small, and therefore the formation of the secondary aggregates consisting of them can be neglected. Becker and Döring [18] have written an infinite system, but in the real physical problem numbers, n is always bounded above: $n \leq m$, where m is some natural number, whose value is determined by the properties of the system. The most rough estimate of m obviously gives that $m \leq N_0$, where N_0 is the number of all molecules of the forming the phase substance in the system. In this case for the homogeneous system, we have the following system of equations for the evolution of the discrete distribution function of aggregates for the case $k = 1$ and for single molecules $N(1,t)$ [18] (we'll skip the index $k = 1$ in the following equations):

$$\frac{dN(1,t)}{dt} = -2\Big(\alpha(1)\,N(1,t)^2 - \beta(1)\,N(2,t)\Big) - \sum_{i=2}^{m-1}\left(\alpha(i)\,N(1,t)\,N(i,t) - \beta(i+1)\,N(i+1,t)\right), \quad (2.1)$$

$$\begin{gathered}\frac{dN(n,t)}{dt} = \left[\left(\alpha(n-1)\,N(1,t)\,N(n-1,t) - \beta(n)\,N(n,t)\right) + \right.\\ \left. + \left(\beta(n+1)\,N(n+1,t) - \alpha(n)\,N(1,t)\,N(n,t)\right)\right],\ n = 2,3,...,m-1,\end{gathered} \quad (2.2)$$

$$\frac{dN(m,t)}{dt} = \alpha(m-1)\,N(1,t)\,N(m-1,t) - \beta(m)\,N(m,t), \quad (2.3)$$

where $N(n,t)$ is a concentration (or a number) of the aggregates of the first generation consisting of n molecules for $n = 2,3,...,m$, $N(1,t)$ is a concentration (or a number) of single molecules, $\alpha(n)$ is a frequency function (a cross section) of the coalescence of an original aggregate consisting of n molecules with the single molecule, and $\beta(n)$ is a frequency of disintegration of a cluster consisting of n molecules into the particle consisting of $(n-1)$ molecules and the single molecule.

But experiments and calculations on a computer require the discrete equations with time step, Δt, so we must write $\dfrac{\Delta N(n,t)}{\Delta t}$ instead of $\dfrac{dN(n,t)}{dt}$. $\Delta N(n,t)$ is a variation of $N(n,t)$ during time interval Δt. We must give definition of it through $N(n,t)$. If $\Delta N(n,t) \equiv N(n,t+\Delta t) - N(n,t)$, then we have the explicit time discretization of the system (2.1)–(2.3). For the system of equation (2.1)–(2.3) the H-theorem is fulfilled, but for the system with the explicit time discretization the H-theorem is not valid: it is proved in [19, 20] that the H-theorem is not fulfilled for the case of this system when only single molecules and dimers are considered. Also, it is valid for the implicit time discretization: when $\Delta N(n,t) \equiv N(n,t) - N(n,t-\Delta t)$ [20, 21], and thus, we can't use the explicit time discretization for the computer simulations.

Instead the equation (2.1) one can write the conservation law of the number of all molecules of the forming the phase substance in the system N_0:

$$\sum_{n=1}^{m} nN(n,t) \equiv N_0, \tag{2.4}$$

where N_0 is constant.

Here, we have considered the discrete distribution function, which is the ordered set of numbers $N(n,t)$, $n = 1, 2, ..., m$. The equations (2.1), (2.3) are the boundary conditions for equations (2.2).

In the previous section we discuss a more general situation than one which is described by these systems, but in this case we have equations of the same form:

$$\begin{gathered}\Delta N_k(n,t) = \\ = \Delta t \Big[\textstyle\sum_{p=1}^{k-1} \Big(\sum_{c \ge n_{p,0}} \alpha_{k,p}(n-c,c) N_p(c,t) N_k(n-c,t) - \sum_{d \ge n_{p,0}} \beta_{k,p}(n,d) N_k(n,t)\Big) + \\ + \textstyle\sum_{p=1}^{k-1} \Big(\sum_{d \ge n_{p,0}} \beta_{k,p}(n+d,d) N_k(n+d,t) - \sum_{c \ge n_{p,0}} \alpha_{k,p}(n,c) N_p(c,t) N_k(n,t)\Big) + W\Big]\end{gathered} \tag{2.5}$$

for $n \ge n_{k,0}$, where $n_{p,0}$ is a minimum number of molecules in a particle of type p, $\Delta N_k(n,t)$ is as before a variation of the number of particles $N_k(n,t)$ of the type k consisting of n molecules during time interval Δt, $\alpha_{k,p}(n,c)$ is a frequency function (a section) of the coalescence of the particle of the generation k consisting of n molecules with the particle of the type p consisting of c molecules, $\beta_{k,p}(n,d)$ is a frequency of fragmentation of the particle of the kind k consisting of n molecules into the particle of the same kind consisting of $(n-d)$ ones and the particle of the generation p consisting of d molecules. Term W in (2.5) takes into consideration that the number of particles of the kind k can varies also due to the coalescence of two particles of generation $k-1$, because of a result of the reverse process, due to the coalescence of the particle of the type k with particles of generation more or equal to k and due to the fragmentation the particle of the kind k from particles of generation more or equal to k.

The histograms, which get the experimenters, as a rule, are replaced by continuous functions. So it is necessary to use a continuum description. You can transit from a discrete distribution function and the system of equation (2.1)–(2.3) to the continuum model by the introduction of the continuum distribution functions of particles of a nanodispersed substance $\psi_k(n,t)$, for which the accordance to the discrete distribution of particles of a nanodispersed substance is valid:

$$\sum_{i=n_{k,0}}^{n} N_k(i,t) = \int\limits_{n_{k,0}}^{n} \psi_k(\tilde{n},t)\, d\tilde{n}.$$

Further, we'll only consider the case $k = 1$, so we'll skip the index $k = 1$. The continuum problem is considered on the interval $[n_1, n_2]$. Here, n_1 and n_2 are the minimum and maximum number of molecules in the cluster, the growth of which can be considered as a continuous process. The minimum possible value is $n_1 \approx 10^2$ [5], and $n_2 \le m$. The simple continuum analogy of (2.2) has the form:

$$\frac{\partial\psi(n,t)}{\partial t} = (\alpha(n-1) N(1,t) \psi(n-1,t) - \beta(n) \psi(n,t)) + (\beta(n+1) \psi(n+1,t) - \alpha(n) N(1,t) \psi(n,t)), \tag{2.6}$$

where now $\alpha(n)$ and $\beta(n)$ are continuum functions.

The conservation law of the number of all molecules of the forming the phase substance in the system (2.4) is rewritten in the form:

$$\sum_{n=1}^{n_1-1} nN(n,t) + \int\limits_{n_1}^{n_2} n\psi(n,t)\, dn + \sum_{n=n_2+1}^{m} nN(n,t) = N_0. \tag{2.7}$$

The equations (2.6), (2.7) is proved by that the substitution the sum of the δ-functions: $\psi(n,t) = \sum_{i=1}^{n_M} N(i,t) \cdot \delta(n-i)$, gives (2.2), (2.3). Indeed, the transition from (2.7) to (2.4) is obvious. Substituting in (2.6) the sum of the δ-functions and integrating for each positive integer $n \in [n_1, n_2]$ the both parts of the obtained equation on the interval containing only one integer value of n, we obtain (2.2), (2.3) for this n.

Let us decompose the increments of the functions in (2.6) $\alpha(n) N(1,t) \psi(n,t)$ and $\beta(n) \psi(n,t)$ in the Taylor series and consider only two terms of the decomposition in the Taylor series. Then we obtain the equation of the Fokker–Planck type for the function $\psi = \psi(n,t)$, which has the form:

$$\frac{\partial \psi}{\partial t} = -\frac{\partial}{\partial n} J[N(1,t), \psi] = -\frac{\partial}{\partial n}(G(n,t)\psi) + \frac{\partial^2}{\partial n^2}(D(n,t)\psi), \tag{2.8}$$

where $J[N(1,t), \psi] \equiv G(n,t)\psi - \dfrac{\partial}{\partial n}(D(n,t)\psi)$, $G(n,t) \equiv \alpha(n,t) N(1,t) - \beta(n,t)$, $D(n,t) \equiv \dfrac{\alpha(n,t) N(1,t) + \beta(n,t)}{2}$. So, $D(n,t) > 0$.

Thus, α and β are determined by the functions:

$$\alpha(n,t) = \frac{G(n,t) + 2D(n,t)}{2N(1,t)}, \qquad \beta(n,t) = \frac{2D(n,t) - G(n,t)}{2}. \tag{2.9}$$

The problem (2.8) is solved on the interval $[n_1, n_2]$, and it is supplemented by the equations (2.2) for $2 \le n \le n_1 - 1$ and for $n_2 + 1 \le n \le m$ (if $n_2 < m$), by the conservation law of the number of all molecules of the forming the phase substance in the system (2.7) and by the boundary conditions.

The boundary conditions will be the relationship of the equality of flows of the continuum distribution function: $J[N(1,t), \psi(n,t)]$, and of the discrete one on the left and right bounds of the continuum distribution:

$$J[N(1,t), \psi(n,t)]|_{n=n_1} = \alpha(n_1 - 1, t) N(1,t) N(n_1 - 1, t) - \beta(n_1, t) N(n_1, t), \tag{2.10}$$

$$J[N(1,t), \psi(n,t)]|_{n=n_2} = \alpha(n_2, t) N(1,t) N(n_2, t) - \beta(n_2 + 1, t) N(n_2 + 1, t), \tag{2.11}$$

where $N(n_1,t) \equiv \psi(n_1,t)$, $N(n_2,t) \equiv \psi(n_2,t)$, if $n_2 < m$, and

$$J[N(1,t), \psi(n,t)]|_{n=n_2} = 0, \tag{2.12}$$

if $n_2 = m$.

If n is not restricted from above $m \to +\infty$, then we have the boundary condition at the infinity:

$$\lim_{n \to +\infty} \left(n^{\lambda} \left(\alpha(n,t) N(1,t) N(n,t) - \beta(n+1,t) N(n+1,t) \right) \right) \to 0, \tag{2.13}$$

for some $\lambda > 1$. In this case the sum in the right side of (2.1) is finite, when $m \to +\infty$. If $n_2 = m \to +\infty$, we have:

$$n^{\lambda} J[N(1,t), \psi(n,t)]|_{n \to +\infty} \to 0, \tag{2.14}$$

The following system of equations is also considered (e.g., [8]): $N(n,t) = 0$ for $2 \le n \le n_0 - 1$ ($n_0 > 2$). It accords to the simple assumption that besides the single molecules the particles, consisting of smaller than n_0 molecules, don't exist. The particles consisting from n_0 molecules give n_0 molecules, when they fragmentize. Let for simplicity $n_1 = n_0$, $n_2 = m \to +\infty$. n_0 may depend on time t. Then we have the equation (2.8) on the interval $[n_0, +\infty)$ and the conservation law of the number of all molecules of the forming the phase substance in the system, which has the form:

$$N(1,t) + \int_{n_0(t)}^{+\infty} n\psi(n,t)\, dn = N_0. \tag{2.15}$$

In this case, we have the boundary conditions for the equation (2.8) on the right bound (2.14) and one on the left bound, which is obtained from (2.15).

In (2.1)–(2.3) the coalescence of particles due to pair collisions is assumed. This supposition is valid only for rarified gases. The experiments are described by the system of equations, which is more general, than (2.1)–(2.3): instead of terns $\alpha(n) N(1,t)$ we must write some unknown function $\tilde{\alpha}(n, N(1,t))$, which is a linear function: $\tilde{\alpha}(n, N(1,t)) = \alpha(n) N(1,t)$, only for rarified gases. The equation of the Fokker–Planck type is obtained similarly. It has the form (2.8), where:

$$G(n,t) \equiv \tilde{\alpha}(n, N(1,t)) - \beta(n), \quad D(n,t) \equiv \frac{\tilde{\alpha}(n, N(1,t)) + \beta(n)}{2}. \tag{2.16}$$

So, $D(n,t) > 0$, $\tilde{\alpha}$ and β are determined by the functions:

$$\tilde{\alpha} = G(n,t) + 2D(n,t), \quad \beta = 2D(n,t) - G(n,t). \tag{2.17}$$

The boundary conditions (2.14) and the conservation law of all molecules of the forming the phase substance in the system are the same.

Our further aim is to determine the coefficients of the equations by the stationary and non-stationary distribution functions of particles of a dispersed substance.

3. The determination of coefficients of the kinetic equations of a dispersed substance by their stationary solution

Let the frequency functions be nonzero.

It is obvious, that the stationary solution of (2.1)–(2.3): $N(n,t) = N_{eq}(n)$ (“eq” from “equilibrium”), $n = 1,2,...,m$, satisfies the relationships:

$$\alpha(n)\,N_{eq}(1)\,N_{eq}(n) = \beta(n+1)\,N_{eq}(n+1), \tag{3.1}$$

for $n = 1,2,3,...,m-1$, and the conservation law (2.7). In (3.1) for the stationary solution $N_{eq}(n)$ the rate of the forward process (of the coalescence) equals the rate of reverse one (which is fragmentation) for each of such processes. For the physico-chemical kinetic equations such relationships are called the condition of detailed balance. From (3.1) and $N_{eq}(n+1) - N_{eq}(n) \equiv \Delta N_1(n)$ we have:

$$\left(\alpha(n)\,N_{eq}(1) - \beta(n+1)\right)N_{eq}(n) = \beta(n+1)\,\Delta N_1(n). \tag{3.2}$$

From (3.1) we also obtain:

$$N_{eq}(n) = \frac{N_{eq}^{n}(1)\prod_{j=1}^{n-1}\alpha(j)}{\prod_{j=2}^{n}\beta(j)} \qquad \text{for} \quad n = 2,3,...,m. \tag{3.3}$$

This relation indicates that $\alpha(n)$ and $\beta(n)$ is sufficient to determine the function $N_{eq}(n)$. Indeed, substituting (3.3) in the conservation law (2.4) we obtain the equation for calculation of $N_{eq}(1)$.

Also, we can solve the reverse problem: due to (3.1) we are able to find the ratios of coefficients $\dfrac{\beta(n+1)}{\alpha(n)}$, where $n = 2,3,...,m$, by the stationary solution. Thus, according to (3.1), for the system of equations (2.1)–(2.3), we can find the frequency function $\alpha(n)$ or $\beta(n)$ by the stationary solution, if we know another frequency function: $\beta(n)$ or $\alpha(n)$.

Let us consider the same issue for hybrid (discrete and continuous) problem: the equation (2.11) on the interval $[n_1, n_2]$, which is supplemented by the system of equations (2.2)–(2.3) for $n = 2,...,n_1-1$ and for $n = n_2+1,...,m$ (if $n_2 < m$), by the conservation law of the number of all molecules of the forming the phase substance in the system (2.7) and by the boundary conditions (2.10), (2.11) for $n_2 < m$ or (2.10), (2.12) for $n_2 = m$.

Let us denote the stationary solution of this problem as $N_{eq}(n)$ for $n = 1,2,...,n_1-1, n_2+1,...,n_M$ and $\psi_{eq}(n)$ for $n \in [n_1, n_2]$.

From equations (2.2), (2.3) for $n = n_2+1,...,m$ (if $n_2 < m$) we obtain that the stationary solution satisfies the relationships of detailed balance (3.1) for $n = n_2,...,m-1$. According to this and (2.11), for $n_2 < m$ or due to (2.15) for $n_2 = m$:

$$J\left[N_{eq}(1), \psi_{eq}(n)\right]\Big|_{n=n_2} = 0. \tag{3.4}$$

A stationary solution of (2.8) is determined by the equation $J\left[N_{eq}(1), \psi_{eq}(n)\right] = C(t)$ for $n \in [n_1, n_2]$. According to (3.4) $C(t) \equiv 0$, and we have:

$$J\left[N_{eq}(1), \psi_{eq}(n)\right] \equiv \left(\alpha(n)\,N_{eq}(1) - \beta(n)\right)\psi_{eq}(n) - \frac{d}{dn}\left(\left(\alpha(n)\,N_{eq}(1) + \beta(n)\right)\psi_{eq}(n)\right) = 0 \tag{3.5}$$

for $n \in [n_1, n_2]$. (2.10) gives that $\alpha(n_1-1)\,N_{eq}(1)\,N_{eq}(n_1-1) - \beta(n_1)\,N_{eq}(n_1) = 0$, and, therefore, from the equations (2.2) for $n = 2,\ldots,n_1-1$ (if $n_1 > 2$) we obtain that the stationary solution satisfies the relationships of detailed balance (3.1) for $n = 1,\ldots,n_1-2$.

Thus, the stationary solution satisfies the following hybrid system of equations: the relationships of detailed balance (3.1) for $n = 1,2,3,...,n_1-1, n_2,...,m-1$, the equation (3.5) and the conservation law of the number of all molecules of the forming the phase substance in the system (2.7).

As before, we subsequently find the values of $N_{eq}(n)$ for $n = 2,...,n_1$ through the value of $N_{eq}(1)$: the formula (3.3). Then we solve the equation (3.5) with initial data $N_{eq}(n_1) = \dfrac{N_{eq}^{n}(1)\prod_{j=1}^{n_1-1}\alpha(j)}{\prod_{j=2}^{n_1}\beta(j)}$ and find $N_{eq}(n)$ for $n \in [n_1, n_2]$ through the value of $N_{eq}(1)$. So, in particular, now we know $N_{eq}(n_2) \equiv \psi_{eq}(n_2)$ through the value of $N_{eq}(1)$. Then, we again use the relationships of detailed balance (3.1) for $n = n_2,\ldots,m-1$ and calculate the remaining values of $N_{eq}(n)$. Finally, we substitute all these values in (2.10) and find $N_{eq}(1)$. Thus, we find the stationary solution by the frequency functions.

Also we can solve the reverse problem. So, the following theorem is valid.

Theorem. For the system of equations (2.7), (2.8) and (2.2), (2.3) for $n = 2, \ldots, n_1 - 1$ and for $n = n_2 + 1, ..., m$ (if $n_2 < m$) with the boundary conditions (2.10), (2.11) for $n_2 < m$ or (2.10), (2.12) for $n_2 = m$ the frequency function $\alpha(n)$ or $\beta(n)$ for $n = 1, 2, ..., n_1 - 1, n_2 + 1, ..., n_M - 1$ and for $n \in [n_1, n_2]$ can be calculated by the stationary solution, if we know another frequency function.

The proof. The frequency function is determined by the relationships of detailed balance (3.1) for $n = 1, 2, 3, ...,$ $n_1 - 1, n_2, ..., n_M - 1$, and the equation (3.5) for $n \in [n_1, n_2]$. According to the condition of detailed balance we solve (3.5) with initial data $\beta(n_1) = \dfrac{\alpha(n_1 - 1) N_{eq}(1) N_{eq}(n_1 - 1)}{N_{eq}(n_1)}$, if we calculate $\beta(n)$, and with $\alpha(n_2) = \dfrac{\beta(n_2 + 1) N_{eq}(n_2 + 1)}{(N_{eq}(1) N_{eq}(n_2))}$, if we calculate $\alpha(n)$.

4. The parameters of modeling distribution functions of particles of a nanodispersed substance

A distribution function by sizes $\phi(l)$ is usually used. It is such function, that $\int_{l_0}^{l} \phi(l')\, dl'$ gives the number of particles with sizes which are less than l and more than l_0, where l_0 is the smallest particle's size. In equations, we consider the distribution function by the number of molecules constituting the particle $\psi(n)$ instead of $\phi(l)$, considering that these functions are related to the fact that $\int_{l_0}^{l} \phi(l', t)\, dl' = \int_{n_0}^{n(l)} \psi(n, t)\, dn$, where $n(l)$ is a number of molecules constituting a particle with size l. The total number of particles is $N(t) \equiv \int_{l_0}^{l_M} \phi(l', t)\, dl' = \int_{n_0}^{n_M} \psi(n, t)\, dn$, where l_M is the biggest particle's size, n_M is the largest number of molecules constituting a particle. The integral distribution functions $\theta(l)$ are also considered: $\theta(l) \equiv \dfrac{1}{N(t)} \int_{l_0}^{l} \phi(l', t)\, dl'$. They are normalized to the total number of particles $N(t)$. Thus, they take values from zero to one.

In order to describe the particle size distribution of powders, basically, four formulas are used in practice [22]: the Gorden–Andreev [22, 23], the Rozin–Rammlar–Bennett [24], [22], the normal [25–29] or lognormal [25–28, 30–48] distributions. In other research [27, 36, 37], it is considered the issue that distributions with only two parameters are insufficient. Using of normal and lognormal distribution with $l_0 = 0$ and $l_M \to +\infty$ is inadvisable.

The Gorden–Andreev formula is the function with only two parameters:

$$\theta(l) = A l^q, \tag{4.1}$$

which, generally speaking, is not an integral distribution function, as it tends to infinity when $l \to +\infty$, and integral distribution functions should to take values from zero to one. It is applied for small l.

The Rozin–Rammlar–Bennett formula is also the distribution function with only two parameters:

$$\theta(l) = 1 - \exp(-A l^q), \tag{4.2}$$

and is the prototype of the functions with tree and four parameters, which we'll consider further.

Let us note that the formula (4.1) is obtained as the first two terms of the decomposition in the Maclaurin series of the function (4.2). This indicates its applicability for small l.

Let $\theta_e(l)$ ("e" from "experiment") is the integral distribution function measured in the experiment for a discrete set of sizes of particles. $\theta_e(l) = \dfrac{N_e(l)}{N_e}$, where $N_e(l)$ is a number of measured particles with size less than l, N_e is a total number of measured particles. We'll call such set of parameters for modeling functions, in which the minimum of the deviation of the function $\theta_e(l)$ from $\theta_e(l)$ is achieved, as the optimal set of parameters.

The parameters of the distribution function are the smallest particle's size l_0 (it corresponds to the minimum number of molecules in the cluster: $n = n_0$): $\theta(l_0) = 0$, the median value l_R (it corresponds to $n = n_R$):

$$\theta(l_R) = \frac{1}{N(t)} \int\limits_{l_0}^{l_R} \phi(l', t)\, dl' = \frac{1}{N(t)} \int\limits_{n_0}^{n_R} \phi(n', t)\, dn' = \frac{1}{2},$$

and the maximum particle size l_M: $\theta(l_M) = 1$. The value l_0 is from the interval $(0, l_1)$. And it is required that $\dfrac{l_0}{l_1} \approx 1$, because in the experiment particles with size smaller, than l_1, aren't registered.

5. The classes of modeling integral distribution functions of particles of a nanodispersed substance

We considered the following classes of modeling integral distribution functions of particles of a nanodispersed substance:

$$\theta\left(l\right)=1-\exp\left(-\omega\left(l\right)\right), \tag{5.1}$$

where we took the following functions $\omega\left(l\right)$, containing the power parameter (q):

$$\omega\left(l\right)=\omega_1\left(l\right)=a_0\left(Z_1\left(l\right)\right)^q, \quad \text{where} \quad a_0=\ln 2, \quad Z_1\left(l\right)\equiv\frac{l-l_0}{l_R-l_0}, \tag{5.2}$$

and

$$\omega\left(l\right)=\omega_2\left(l\right)=a\left(Z_2\left(l\right)\right)^q, \quad \text{where} \quad Z_2\left(l\right)\equiv\frac{l-l_0}{l_M-l}. \tag{5.3}$$

The optimal values of the parameter q were fractional mainly in the range from one to three.

It is advisable to use the following class of functions:

$$\theta\left(s\right)=1-\exp\left(-a_1Z_3\left(s\right)\left(1+a_2Z_3\left(s\right)\right)\right), \quad \text{where} \quad Z_3\left(s\right)\equiv\frac{s}{s_0-1}. \tag{5.4}$$

Here, a_1, a_2, s_0 are parameters of the distribution function, $s=\gamma_s l^2$ is a square of a particle of a nanodispersed substance, $s_0=\gamma_s l_0^2$. (In the one-dimensional case (in the case of chains of molecules) the square of the image of the particle is proportional to l.) Equation (5.4) reasonably approximates the distribution functions of particles, which are surfaces of initial particles. In this case, $\delta=2$ in (1.10), and we can rewrite (5.4) in the following form:

$$\theta\left(n\right)=1-\exp\left(-a_1\left(\frac{n}{n_0}-1\right)\left(1+a_2\left(\frac{n}{n_0}-1\right)\right)\right). \tag{5.5}$$

So, according (1.2) we have the classes of functions:

$$\theta\left(l\right)=1-\exp\left(-a_1\left(\frac{l^\delta}{l_0^\delta}-1\right)\left(1+a_2\left(\frac{l^\delta}{l_0^\delta}-1\right)\right)\right), \tag{5.6}$$

where $\delta=1,2,3$ respectively for chains, surfaces and volumes of initial particles.

We checked by calculations on the computer that the considered approximating functions describe well the experimental distribution functions of particles of nanodispersed substances [49–52].

6. The relationships between parameters of approximating distribution functions of particles of a dispersed substance and the coefficients of the equation of the Fokker-Planck type describing their kinetics

Now we try to connect the simple phenomenological formulas of Section 5 with the equations of the Fokker–Planck type from Section 2.

The equation of the Fokker–Planck type has the form (2.8). The equation (2.8) is considered in the region $n\in[n_0,+\infty)$, $t\in[t_0,+\infty)$. When $n<n_0$, the distribution function is equal to zero. If the functions G and D depend only on time – it is the case of fixed number of active aggregation centers on the surface of the particle, then (2.8) has the form:

$$\frac{\partial\psi}{\partial t}=-\frac{\partial}{\partial n}J\left[N_1,\psi\right]=-G\left(t\right)\frac{\partial\psi}{\partial n}+D\left(t\right)\frac{\partial^2\psi}{\partial n^2}, \tag{6.1}$$

here, $J\left[N_1,\psi\right]\equiv-G\left(t\right)\psi+D\left(t\right)\dfrac{\partial\psi}{\partial n}$. For Equation (6.1) after the substitution [53 (p. 309)]:

$$\tau=\tau\left(t\right)=\int\limits_{t_0}^{t}D\left(x\right)dx+A, \quad z=z\left(n,t\right)=n-\int\limits_{t_0}^{t}G\left(x\right)dx+B, \tag{6.2}$$

where A and B are constants, gives the equation for the function $\tilde{\psi}\left(z,\tau\right)\equiv\psi\left(n,t\right)$:

$$\frac{\partial\tilde{\psi}}{\partial\tau}=\frac{\partial^2\tilde{\psi}}{\partial z^2}. \tag{6.3}$$

Let us consider in the following exact solution of (6.3) (see, e.g., [53 (p. 233)]):

$$\tilde{\psi}\left(z,\tau\right)=C\frac{z}{\tau^{3/2}}\exp\left(-\frac{z^2}{4\tau}\right). \tag{6.4}$$

In order, $\tau > 0$, due to (6.2) the value of A should be positive (here we use that $D(t) > 0$). The function (6.4) is nonnegative, if and only if $z \geq 0$. So, according to (6.2) for any $t \in [t_0, +\infty)$:

$$B \geq \int\limits_{t_0}^{t} G(x)\, dx - n_0. \tag{6.5}$$

The condition of normalization gives the total number of all particles $N(t)$ at any fixed moment of time t, and due to (6.4) has the form:

$$N(t) = \int\limits_{n_0}^{+\infty} \psi(n,t)\, dn = \int\limits_{z(n_0,t)}^{+\infty} \tilde{\psi}(z,\tau)\, dz = \frac{2C}{\sqrt{\tau}} \exp\left(-\frac{(z(n_0,t))^2}{4\tau}\right). \tag{6.6}$$

From (6.4) and (6.6), we have:

$$\theta = \frac{1}{N(t)} \int\limits_{n_0}^{n} \psi(n,t)\, dn = \frac{1}{N(t)} \int\limits_{z(n_0,t)}^{z(n,t)} \tilde{\psi}(z',\tau)\, dz' = 1 - \exp\left(\frac{(z(n_0,t))^2}{4\tau}\right) \exp\left(-\frac{(z(n,t))^2}{4\tau}\right). \tag{6.7}$$

Let us rewrite (5.5) in the form:

$$\theta(n) = 1 - \exp\left(\frac{(n_0 - b_1)^2}{4b_2}\right) \exp\left(-\frac{(n - b_1)^2}{4b_2}\right), \tag{6.8}$$

where $b_1 = n_0 \left(1 - \frac{1}{2a_2}\right)$, $b_2 = \frac{n_0^2}{4a_1 a_2}$.

So, due to (6.2) we have the same function in (6.8) as in (6.7), if

$$b_1(t) = n - z(n,t) = \int\limits_{t_0}^{t} G(x)\, dx - B, \quad b_2(t) = \tau(t) = \int\limits_{t_0}^{t} D(x)\, dx + A, \tag{6.9}$$

We can check by the substitution, that the functions from the class (6.8) are solutions of (6.1), if and only if the relationships (6.9) are valid.

The conditions (6.5) and $\tau > 0$ are fulfilled, if for any $t \in [t_0, +\infty)$ $b_1(t) \leq n_0(t)$, $b_2(t) > 0$. So, $a_1(t)$ and $a_2(t)$ should be positive.

We'll now strive to express the frequency functions G and D through the parameters of the simple phenomenological formulas of Section 5. From (6.9), we obtain $b_1(t_0) = -B$, $b_2(t_0) = A$, and:

$$\int\limits_{t_0}^{t} G(x)\, dx = b_1(t) - b_1(t_0), \quad \int\limits_{t_0}^{t} D(x)\, dx = b_2(t) - b_2(t_0),$$

or:

$$G(t) = \frac{db_1(t)}{dt}, \quad D(t) = \frac{db_2(t)}{dt} \tag{6.10}$$

According to the definition (2.16) of $G(t)$ and $D(t)$, they depend upon t only through the temperature $T(t)$ and the concentration of single molecules $N(1,t)$: $G(t) = g(T(t), N(1,t))$, $D(t) = d(T(t), N(1,t))$. If $T(t)$ and $N(1,t)$ are constant or their variations during time interval $[t, t+\Delta t]$ are negligible, then according to (6.10) by two measurements in the moments of time t and $t + \Delta t$ we can find the values of $G = g(T, N_1)$ and $D = d(T, N_1)$ for the given temperature T and the concentration of single molecules $N(1)$:

$$\begin{gathered} G = \frac{b_1(t+\Delta t) - b_1(t)}{\Delta t} = \left(n_0(t+\Delta t)\left(1 - \frac{1}{2a_2(t+\Delta t)}\right) - n_0(t)\left(1 - \frac{1}{2a_2(t)}\right)\right) \Big/ \Delta t, \\ D = \frac{b_2(t+\Delta t) - b_2(t)}{\Delta t} = \frac{1}{4}\left(\frac{n_0^2(t+\Delta t)}{a_1(t+\Delta t)\, a_2(t+\Delta t)} - \frac{n_0^2(t)}{a_1(t)\, a_2(t)}\right) \Big/ \Delta t. \end{gathered} \tag{6.11}$$

Varying system's condition (considering different values of T and $N(1,t)$) and calculating in each case values of $G = g(T, N(1))$ and $D = d(T, N(1))$ according to (6.11) we can find functions $g(T, N(1))$ and $d(T, N(1))$.

These formulas (6.11) connect the phenomenology of Section 5 with the Fokker–Planck type equation of Section 2.

Let us note, that we vary the value of $N\left(1\right)$ in order to find the function $\tilde{\alpha}\left(N\left(1\right)\right)$ in (2.17). If we have a rarified gas, then we can assume the pair interaction. In this case, we can calculate α and β according (2.9), where $N\left(1\right)$ is calculated according (2.15). In this case, we need not vary $N\left(1\right)$, and we can even calculate the frequency function without the condition that $N\left(1,t\right)$ is constant during time interval $[t,t+\Delta t]$.

We can consider other approximating functions instead of (5.5). For example, we can obtain the relationships between the parameters of normal distributions by n with $n\in[n_0,+\infty)$ and the coefficients of the equation of the Fokker–Planck type (6.1) (the case, when G and D depend only on time). The choice of which approximating class of functions (or which solution of the equation of the Fokker–Planck type) is realized depends upon the law of varying of the number of particles with minimum size n_0, which determines the initial data and the boundary condition on the left bound of the continuum distribution.

We have two one-dimensional functions in the coefficients of (6.1): $G\left(t\right)$ and $D\left(t\right)$. In order to determine these, we need at least two independent parameters in modeling class of functions depending upon time. The further development of the solving of this problem is to consider the case, when G and D depend upon n with the number of parameters depending upon time more or equal to the number of one-dimensional functions in the coefficients of (2.8).

Thus, by two measurements of the distribution function of particles of a nanodispersed substance, we have learned to find the frequency functions, in the case when the temperature T and the concentration of single molecules of the forming the phase substance $N\left(1\right)$ are constant or their relative variations is negligible. Varying system's condition, we can find frequency functions in dependence on T and $N\left(1\right)$.

7. Discussion of the results

In the present paper, we considered the connection between the discrete equations describing the kinetics of particles of a dispersed substance and the continuum one, in the case when only single molecules integrate with or fragmentize from the particles, i.e. in the Becker–Döring case: equations (2.1)–(2.3). We obtained hybrid systems of equations, which have both discrete and continuum parts.

We considered the basic known simulating (approximating) distribution functions (formulas (4.1)–(4.6)) and new ones and their parameters. The exact solutions of the equation of the Fokker–Planck type, which gives distribution functions of particles of a nanodispersed substance, are found, and we learned to find frequency functions by the parameters of the modeling distribution functions.

Let us note that the consideration of the *H*-theorem for nonlinear systems with discrete time, in particular, even for the Becker–Döring system of equations, becomes an extremely important problem as the computer simulation has a significance in the solution of fundamental problem of the creating of new materials. In the linear case, the transition from continuous time to discrete gives the transition from a Markov process to a Markov chain and the *H*-theorem is valid and studied (see [54] and references in it, [55]). In the nonlinear case, for explicit time discretization it is fulfilled in rare cases [19, 20] and for the implicit one, it is investigated in [20, 21]. The diffuse approximation is widely used for the modeling of crystallization processes of a dispersed substance [5–8]. Therefore, the consideration of the *H*-theorem for it is of interest.

The equation of the Fokker–Planck type allows one to understand, to explain and even, if the initial information is enough, to predict the behaviors of the experimental distribution functions by properties of particles of a dispersed substance.

All approximating distribution functions considered in the present paper were single humped. But, of course, it is required not only such functions for practical problems: for example, with more than one extremum [56, 57].

We have considered the distribution function of particles of a dispersed substance by the number of constituting of them molecules, because it is the basic parameter. Sometimes other parameters may be also very essential in a counterbalance to the distribution by sizes. The simplest distribution function by this parameter is such, when we take into account only monomers and dimers. It may be used for some practical problems. The state of each particle is characterized by many parameters. Even dimers are such, and one can consider the distribution function by these parameters [58]. And, of cause, very often, it is needed to investigate the distribution function by sizes and other parameters with its value, which is not only number or concentration of particles [29]. In these cases the distribution functions can have interesting plots [29]. And certainly, distribution functions of single initial particles (molecules, atoms, etc.) or nucleation centers are also considered [59].

It turned out that three-parameter functions of the type (5.6), which are more informative than the commonly used normal and log-normal distributions, and also the distributions (4.1), (4.2), have become available for determining. The availability of three-parameter distribution functions is indicated, in particular, by the data published in [52] about variations in the properties of nano-vesicles – niosomes, when they are heated to different temperatures.

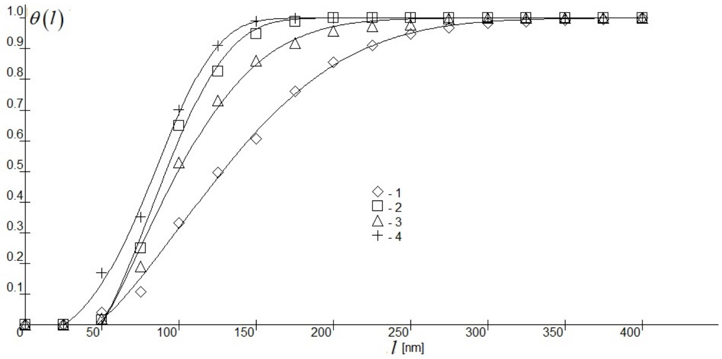

FIG. 1. Integral distribution functions of particle size in niosomal dispersions after heating at 303 K (1), 313 K (2), 323 K (3) and 333 K (4)

TABLE 1. Distribution parameters of distribution functions (7.1) of particle size in niosomal dispersions after heating to temperatures of 303 K (1), 313 K (2), 323 K (3) and 333 K (4)

Temperature	303 K (1)	313 K (2)	323 K (3)	333 K (4)
l_0, ± 0.1 nm	46.6	49.7	50	25.1
a_1, ± 0.01	0.105	0.24	0.234	0.04
a_2, ± 0.001	0,001	0,087	0,001	0,058

Processing of these data showed that the studied niosomes had size distributions (Fig. 1) in accordance with the distribution function of the type (5.6), namely:

$$\theta(l) = 1 - \exp\left(-a_1 Z(l)\left(1 + a_2 Z(l)\right)\right), \tag{7.1}$$

where $Z(l) \equiv \dfrac{l^2}{l_0^2} - 1$, a_1, a_2, l_0 are distribution parameters.

When heated, niosomes were compressed while retaining the three-parameter function $\theta(l)$, and it cannot be ruled out that when heated at $T = 333$ K, they were transformed into a heat-resistant state characterized by a parameter $l_0 = 25$ nm. It is also possible that additional information on the kinetics of such a transition can be extracted from the functions $a_1(T)$ and $a_2(T)$.

The distribution functions retain their informative value when the system transitions to an equilibrium state, as indicated by equations (3.1), containing parameters $\alpha(n)$ and $\beta(n)$. According to these relations, particles of different sizes can be present in the equilibrium system. The theorem of Section 3 indicates that it is possible to use data on the equilibrium distribution function to determine the kinetics for the formation and fragmentation of aggregates.

Relations (3.1) and (7.1) characterize the morphological diversity of dispersed systems, the distribution of particles by properties of which preserves information about the kinetics of the processes occurring in the systems.

Acknowledgment

This research was financially supported by the Ministry of Education and Science of the Russian Federation on the program to improve the competitiveness of Peoples' Friendship University of Russia (RUDN-University) "5-100" among the world's leading research and educational centers in 2016–2020.

References

[1] Maxwell J.C. On the Dynamical Theory of Gases. *Philosophical Magazine*, 1868, 4 ser, **35**(235), P. 141–144.

[2] Boltzmann L. Weitere Studien über das Wärmegleichgewicht unter Gasmolekülen. Wien. Ber., 1872, **66**, P. 275–370; Wissenschaftliche Abhandlungen, Barth, Leipzig, 1909, **1**, P. 316–402.

[3] Konyakhin S.V, Sharonova. L.V., Eidelman. E.D. Labeling detonation nanodiamond suspensions using the optical methods. *Tech. Phys. Lett.*, 2013, **39**(3), P. 244–247.

[4] Aleksenskii A.E., Shvidchenko A.V., Eidel'man E.D. The applicability of dynamic light scattering to determination of nanoparticle dimensions in sols. *Tech Phys Lett.*, 2012, **38**(12), P. 1049–1052.

[5] Melikhov I.V. *Physico-chemical evolution of solids*. Binom, Moscow, 2006 (in Russian).

[6] Melikhov I.V. Evolutional approach to creation of nanostructures. *Nanosystems: Physics, Chemistry, Mathematics*, 2010, **1**(1), P. 148–155 (in Russian).

[7] Melikhov I.V., Mikheev N.B., Kulyukhin S.A., and Kozlovskaya E.D. Morphological Memory of Dispersed Solid Phases. *Colloid Journal*, 2001, **63**(6), P. 738–745.

[8] Melikhov I.V., Rudin V.N., Kozlovskaya E.D., Adzhiev S.Z., Alekseeva O.V. Morphological memory of polymers and their use in developing new materials technology. *Theoretical Foundations of Chemical Engineering*, 2016, **50**(3), P. 260–269.

[9] Eliseev A.A., Lukashin A.V. *Functional nanomaterials*. Under the editorship of Yu.D. Tretyakov. Fizmatlit, Moscow, 2010 (in Russian).

[10] Bayes Thomas, Price Thomas. An Essay towards solving a Problem in the Doctrine of Chance, By the late Rev. Mr. Bayes communicated by Mr. Price, in a letter to John Canton, M.A. and F.R.S. Phylocophical Transactions of the Royal Society of London, 1963, **53**, P. 370–418.

[11] Adzhiev S.Z., Vedenyapin V.V., Volkov Yu.A., Melikhov I.V. Generalized Boltzmann-Type Equations for Aggregation in Gases. *Computational Mathematics and Mathematical Physics*, 2017, **57**(12), P. 2017–2029.

[12] Batishcheva J.G. On the motion of solid in gas reacting with its surface. Derivation of the dynamical system. Keldysh Institute preprints, 2003, **18**, 21 p. (in Russian).

[13] Maxwell J.C. Illustration of the Dynamical Theory of Gases. *Philosophical Magazine*, 1860, **1**, P. 377–409.

[14] Arrhenius S. Über die Reaktionsgeschwindigkeit bei der Inversion von Rohrzucker durch Säuren. *Z. physik. Chemie* (Leipzig), 1889, **4**, P. 226–248.

[15] Stiller W. Arrhenius Equation and Non-Equilibrium Kinetics, 100 Years Arrhenius Equation. BSB B. S. Teubner Verlagsgesellschaft, Leipzig, 1989.

[16] Kolmogorov A.N. On the analytic methods in probability theory. *Russian Mathematical Surveys*, 1938, **5**, P. 5–41 (in Russian).

[17] Smoluchowski M. Versuch einer mathematischen Theorie der Koagulationskinetik kolloider Losungen. *Z. Phys. Chem.*, 1917, **92**, P. 129–168.

[18] Becker R., Döring W. Kinetische Behandlung der Keimbildung in ubersattingten Dampfer. *Ann. Phys.*, 1935, **24**, P. 719–752.

[19] Adzhiev S.Z., Melikhov I.V., Vedenyapin V.V. The H-theorem for the physico-chemical kinetic equations with explicit time discretization. *Physica A: Statistical Mechanics and its Applications*, 2017, **481**, P. 60–69.

[20] Adzhiev S., Melikhov I., Vedenyapin V. The H-theorem for the chemical kinetic equations with discrete time and for their generalizations. *Journal of Physics: Conference Series*, 2017, **788**(1), P. 012001.

[21] Adzhiev S.Z., Melikhov I.V., Vedenyapin V.V. The H-theorem for the physico-chemical kinetic equations with discrete time and for their generalizations. *Physica A: Statistical Mechanics and its Applications*, 2017, **480**, P. 39–50.

[22] Kousov P.A. *The foundations of the analysis of disperse composition of industrial dusts and crushed materials*. Chemistry, Leningrad, 1987 (in Russian).

[23] Andreev S.E. On the formulas of mean diameter. *Mining journal*, 1951, **11**, P. 32–36 (in Russian).

[24] Rozin P., Rammlar E. Die Kornzusammensetzung des Mahlgutes im Lichte der Wahrscheinlichkeitslehre. *Kolloid Zeitschrift*, 1964, **67**(1), P. 16–26.

[25] Fannin P.C., Charles S.W. AC susceptibility measurements in the investigation of aggregation in magnetic fluids. *Physica Polonica A*, 2000, **97**(3), P. 591–594.

[26] Dahi S.R., Clelland R., Hrenya C.M. The effects of continuous size distributions on the rapid flow of inelastic particles. *Physics of Fluids*, 2002, **14**(6), 1972.

[27] Vargas-Ubera J., Aguilar J.F., Gale D.M. Reconstruction of particle-size distributions from light-scattering patterns using three inversion methods. *Applied Optics*, 2007, **46**(1), P. 124–132.

[28] Nosov V.V. Remote technique for simultaneous measurement of the particles' velocity and size distribution function. Atmospheric and oceanic optics, 1996, **9**(1), P. 56–59.

[29] Bachina A., Ivanov V.A., Popkov V.I. Peculiarities of $LaFeO_3$ nanocrystals formation via glycine-nitrate combustion. *Nanosystems: Physics, Chemistry, Mathematics*, 2017, **8**(5), P. 647–653.

[30] Kolmogorov A.N. On the logarithmically normal distribution law of particle sizes under fragmentation. *Dokl. Akad. Nauk SSSR*, 1941, **31**(2), P. 99–101 (in Russian).

[31] Aitchison J., Brown J.A.C. *The Lognormal Distribution*. Cambridge Univ. Press, 1963.

[32] Dacey M.F., Krumbein W.C. Models of breakage and selection for particle size distributions. *Journal of the International Association for Mathematical Geology*, 1979, **11**(2), P. 193–222.

[33] Cooper D.W. On the products of lognormal and cumulative lognormal particle size distributions. *Journal of Aerosol Sciences*, 1982, **13**(2), P. 111–120.

[34] Melik D.H., Fogler H.S. Turbidimetric determination of particle size distributions of colloidal systems. *Journal of Colloid and Interface Science*, 1983, **92**(1), P. 161–180.

[35] LeBlanc S.E., Fogler H.S. Dissolution of powdered minerals: the effect of polydispersity. *AIChE Journal*, 1989, **35**(5), P. 865–868.

[36] Buchan G.D., Grewal K.S., and Robson A.B. Improved models of particle-size distribution: an illustration of model comparison techniques. *Soil Sci. Soc. Am. J.*, 1993, **57**, P. 901–908.

[37] Wagner L.E., Ding D. Representing aggregate size distributions as modified lognormal distributions. *Transactions of the ASAE*, 1994, **37**(3), P. 815–821.

[38] Chen Yongcheng, Zhang Yuanhui, Barber E.M. A new mathematical model of particle size distribution. *Prairie Swine Centre Annual Research Report*, 1994, P. 76–79.

[39] Chaiken J., Goodisman J. Application of fractals and kinetic equation in modelling cluster and ultrafine particle size distributions. *NanoStructured Materials*, 1995, **5**(2), P. 225–231.

[40] Jonasz M., Fournier G. Approximation of the size distribution of marine particles by a sum of log-normal functions. *Limnol. Oceanogr.*, 1996, **41**(4), P. 744–754.

[41] Kiss L.B., Söderlund J., Niklasson G.A., Granqvist C.G. New approach to the origin of lognormal size distributions of nanoparticles. *Nanotechnology*, 1999, **10**(1), P. 25–28.

[42] Selivanov V.N., Smyslov E.F. X-ray determination of the particle-size lognormal distribution in nanocrystalline materials. *Industrial Laboratory*, 2000, **66**(11), P. 718–725.

[43] Popa N.C., Balzar D. An analytical approximation for a size-broadened profile given by the lognormal and gamma distributions. *Journal of Applied Crystallography*, 2002, **35**, P. 338–346.

[44] Ždímal V., Brabec M., Wagner Zd. Comparison of two approaches to modeling atmospheric aerosol particle size distributions. *Aerosol and Air Quality Research*, 2008, **8**(4), P. 392–410.

[45] Rajesh T.A. Software Package for Aerosol Size Distribution. *International Journal of Scientific Engineering and Technology*, 2013, **2**(4), P. 249–255.

[46] Hossain M.A., Mori Sh. Determination of particle size distribution of used black tea leaves by scanning electron microscope. *Dhaka Univ. J. Sci.*, 2013, **61**(1), P. 111–115.

[47] Desmond K.W. and Weeks E.R. Influence of particle size distribution on random close packing of spheres. *Physical Review E*, 2014, **90**, P. 022204.

[48] Gao M., Xia Q., Akwe A.W. et al. Self-preserving lognormal volume-size distributions of starch granules in developing sweetpotatoes and modulation of their scale parameters by a starch synthase II (SSII). *Acta Physiologiae Plantarum*, 2016, **38**(11), Article: 259.

[49] Qiao Yongsheng, Shen Yongsheng Lashes, Wu Meixia, Guo Yong, Meng Shuangming. A novel chemical synthesis of bowl-shaped polypyrrole particles. *Materials Letters*, 2014, **126**, P. 185–188.

[50] Azmeera Venkanna, Rastogi Pankaj Kumar, Adhikary Pubali, Ganesan Vellaichamy, Krishnamoorthi S. Synthesis, characterization and cyclic voltammetric study of copper(II) and nickel(II) polymer chelates. *Carbohydrate Polymers*, 2014, **110**, P. 388–395.

[51] Liu Junli, Ma Jianzhong, Bao Yan, Wang John, Zhu Zhenfeng, Tang Huiru, Zhang Limin. Nanoparticle morphology and film-forming behavior of polyacrylate/ZnO nanocomposite. *Composites Science and Technology*, 2014, **98**, P. 64–71.

[52] Diskaeva E.I., Vecher O.V., Bazikov I.A., Vakalov D.S. Particle size analysis of niosomes as a function of temperature. *Nanosystems: Physics, Chemistry, Mathematics*, 2018, **9**(2), P. 290–294.

[53] Polyanin A.D., Zaitsev V.F. *Handbook on the differential equations with partial derivatives*. Exact solutions. Intern. education program, Moscow, 1996 (in Russian).

[54] Adzhiev S.Z., Vedenyapin V.V. Time averages and Boltzmann extremals for Markov chains, discrete Liouville equations, and the Kac circular model. *Comput. Math. Math. Phys.*, 2011, **51**(11), P. 1942–1952.

[55] Vedenyapin V.V., Adzhiev, S.Z. Entropy in the sense of Boltzmann and Poincaré, *Russian Math. Surveys*, 2014, **69**(6), P. 995–1029.

[56] Almjasheva O.V., Gusarov V.V. Metastable clusters and aggregative nucleation mechanism. *Nanosystems: Physics, Chemistry, Mathematics*, 2014, **5**(3), P. 405–416.

[57] Kuni F.M., Rusanov A.I. Statistical theory of aggregative equilibrium. *Theoretical and Mathematical Physic*, 1970, **2**(2), P. 192–206.

[58] Moliver S.S. Modeling chemisorption of carbon dimer at (8,0) nanotube. *Nanosystems: Physics, Chemistry, Mathematics*, 2017, **8**(5), P. 641–646.

[59] Durnev M.A., Eidelman E.D. Distribution of supercritical nucleation centers during the crystallization process in the presence of a flow as illustrated by the example of boron carbide-reinforced aluminum. *Nanosystems: Physics, Chemistry, Mathematics*, 2017, **8**(3), P. 360–364.

NANOSYSTEMS: PHYSICS, CHEMISTRY, MATHEMATICS, 2019, 10 (5), P. 564–572

Cerium oxide nanoparticles provide radioprotective effects upon X-ray irradiation by modulation of gene expression

N. R. Popova[1], T. O. Shekunova[2], A. L. Popov[1], I. I. Selezneva[1], V. K. Ivanov[2]

[1]Institute of Theoretical and Experimental Biophysics, Russian Academy of Sciences,
Pushchino, Moscow region, 142290, Russia
[2]Kurnakov Institute of General and Inorganic Chemistry, Russian Academy of Sciences,
Moscow, 119991, Russia

nellipopovaran@gmail.com, taisia.shekunova@yandex.ru, antonpopovleonid@gmail.com,
selezneva_i@mail.ru, van@igic.ras.ru

PACS 68.65.k, 81.20.n, 82.70.Dd, 87.80.-y **DOI 10.17586/2220-8054-2019-10-5-564-572**

Nanocrystalline cerium dioxide is known as a unique redox active nanomaterial. Cerium dioxide is considered as the basis for future biomedical preparations, including radioprotectors. In the framework of this study, we synthesized citrate-stabilized CeO_2 nanoparticles and carried out a comprehensive *in vitro* assessment of their radioprotective properties on a NCTC L929 murine fibroblast culture. It was shown that CeO_2 nanoparticles ensure the survival of murine fibroblasts, even after high-dose X-ray irradiation, reducing the number of dead cells in the culture and modulating the mRNA level of the key antioxidant enzymes – superoxide dismutase 1 (SOD1) and superoxide dismutase 2 (SOD2). The results obtained confirm the potential for studying the properties of CeO_2 nanoparticles as basic materials for designing new efficient and safe preparations for protection against ionizing radiation.

Keywords: cerium oxide nanoparticles, radioprotection, cytotoxicity, X-ray, ionizing radiation, fibroblasts.

Received: 22 June 2019

Revised: 4 October 2019

1. Introduction

Nanocrystalline cerium dioxide is a synthetic nanomaterial that is widely used in modern high-tech industries [1]. In recent years, cerium dioxide nanoparticles have been considered as one of the most promising nanobiomaterials [2]. It was shown that, due to their unique antioxidant activity, CeO_2 nanoparticles are able to inactivate a wide range of free radicals and reactive oxygen species (ROS) in various models of oxidative stress, including exposure to ionizing radiation [3]. It was established that unique properties of nanodispersed cerium dioxide allow this material to exhibit enzyme-like activity, for example, as a synthetic analogue of superoxide dismutase, peroxidase, haloperoxidase, phosphatase, esterase, etc. [4]. The low toxicity and high biocompatibility of nanodisperse CeO_2 ensure the comparative safety of its application *in vivo*, which allows one to consider this material as a promising component of drugs and medicinal preparations. We have previously found [5] that CeO_2 nanoparticles are able to prevent the development of oxidative stress induced by ionizing radiation not only by direct inactivation of free radicals, but also indirectly, by modulating the expression of a number of genes involved in key intracellular enzyme cascades. The unique physicochemical characteristics of cerium dioxide nanoparticles and their biological activity make it possible to consider this nanomaterial as a promising radioprotector with a complex mechanism of protective action.

Caputo et al. have demonstrated on a HaCat keratinocyte culture that CeO_2 nanoparticles reduce the number of DNA breaks caused by exposure to X-ray radiation, weakening mutagenesis [6]. Wason et al. showed that activation of c-Jun terminal kinase (JNK), a key driver of radiation-induced apoptosis, was significantly enhanced by the combined action of CeO_2 nanoparticles and ionizing radiation in pancreatic cancer cells *in vitro*, as well as in pancreatic tumors of naked mice *in vivo* as compared to using CeO_2 nanoparticles or radiation therapy alone. These data demonstrate the important role of CeO_2 nanoparticles in the selective destruction of cancer cells and show new prospects for the use of CeO_2 as a radiosensitizer [7].

Xu et al. [8] showed that the intraperitoneal administration of CeO_2 nanoparticles to CBA/J mice exposed to radiation at a dose of 15 Gy resulted in a significant increase in their survival. In the corresponding experiments, CeO_2 nanoparticles were administered to mice intraperitoneally twice a week for 4 weeks. At 160 days after irradiation, 90 % of mice which received 10 μM CeO_2 nanoparticles injection survived, compared with 10 % survival rate for mice that did not receive the nanoparticles and 30 % survival rate for mice which received a lower dose of CeO_2 nanoparticles (100 nM). Zal et al. showed that CeO_2 nanoparticles reduced to 73 % the number of cytogenetic incidences induced in lymphocytes by irradiation at a dose of 1.5 Gy, in comparison with the control group. The introduction of CeO_2 nanoparticles significantly reduced the number of apoptotic and necrotic cells in the culture of human lymphocytes [9].

Colon et al. have demonstrated the radioprotective efficacy of cerium dioxide nanoparticles (10 nM) on a culture of normal human lung fibroblasts. Cells were irradiated at a dose of 20 Gy, and after 48 hours, their viability was assessed, which correlated with the concentration of CeO_2 nanoparticles. At the same time, CeO_2 nanoparticles did not protect cancer cells of the A549 line. It is worth noting that nanocrystalline cerium dioxide was found to be superior to Amifostin – a clinically used radioprotector [10], in a series of model *in vivo* experiments performed for nude athymic mice. The radioprotective properties of nanodisperse cerium dioxide in the culture of gastrointestinal epithelium were studied [11]. The pretreatment of the culture with cerium dioxide nanoparticles provided a dose-dependent protection against radiation damage by reducing the production of ROS and increasing the expression of SOD2. It was shown [12] that the use of nanosized cerium dioxide can reduce xerostomia and dermatitis after exposure to ionizing radiation. Using two types of cell culture as examples (MCF-7 cancer cells and normal CRL-8798 cells), the selective cytotoxicity of cerium dioxide nanoparticles was revealed [13]. It was additionally shown, by the example of radiation-resistant 9L gliosarcoma cells, that the radioprotective effect of cerium dioxide nanoparticles is a function of the irradiation energy [14]. The radioprotective properties of cerium dioxide were manifested when cells treated with cerium dioxide nanoparticles were exposed to high-energy X-ray radiation. On the other hand, low-intensity radiation promoted the formation of Auger electrons by interaction with the surface of cerium dioxide nanoparticles, which significantly reduce cell viability.

The synthetic method used for CeO_2 nanoparticles determines their physicochemical characteristics, which in turn dictate their biological activity [15, 16]. In the framework of this study, we synthesized citrate-stabilized CeO_2 nanoparticles and carried out a comprehensive assessment of their radioprotective properties *in vitro* for a NCTC L929 murine fibroblast culture line.

1.1. Materials and methods

1.2. Preparation and analysis of physicochemical properties of CeO_2 nanoparticles

The aqueous sol of nanocrystalline cerium oxide stabilized by citrate ions was used in the present work. It was obtained by dissolving 0.24 g of citric acid in 25 ml of 0.05 M aqueous solution of cerium (III) nitrate, which was then rapidly added with stirring to 100 ml of a 3 M ammonia solution and then kept for 2 hours [17]. Transmission electron microscopy testified that the sol consisted of weakly aggregated nearly isotropic 2 – 3 nm CeO_2 particles. The concentration of CeO_2 nanoparticles in the sol was 0.01 M. The pH value of the sol was in the range of 7.2 – 7.4. Just before biological experiments, CeO_2 nanoparticles were precipitated by acidifying the sol with 10 % hydrochloric acid to pH = 3, followed by centrifugation at 20 °C, at 11200 g for 10 minutes. The precipitated nanoparticles were resuspended in distilled water and re-centrifuged under the same conditions. The resulting precipitate was resuspended in the culture medium DMEM/F12 + 10 % fetal bovine serum (Gibco).

1.3. Cell culture

The NCTC L929 murine fibroblasts were cultured in DMEM/F12 (1:1) medium with the addition of 10 % fetal bovine serum and 100 U/ml penicillin/streptomycin under 5 % CO_2 at 37 °C.

1.4. MTT assay

The determination of mitochondrial and cytoplasmic dehydrogenases activity in living cells was carried out using a MTT assay based on the reduction of the colorless tetrazolium salt (3-[4.5-dimethylthiazol-2-yl]-2.5-diphenyltetrazolium bromide, MTT). After 24 hours of cell incubation with different concentrations of CeO_2 nanoparticles, 0.5 mg/ml of MTT reagent was introduced into the wells by replacing the culture media, followed by a standard MTT assay.

1.5. Live/Dead assay

Assessment of the viability of the cells cultured in the presence of CeO_2 nanoparticles was performed on a Carl Zeiss Axiovert 200 microscope. An L-7007 LIVE/DEAD BacLight Bacterial Viability Kit (Invitrogen) was used for the assay, which included a SYTO 9 fluorescent dye (absorption – 420 nm, emission – 580 nm) and a propidium iodide (PI) dye (absorption – 488 nm, emission – 640 nm). The dyes were added to the medium (1 μg/ml) and the plate was placed in a CO_2 incubator for 15 min. Microphotographs were taken after washing the cells with a phosphate-buffered saline.

1.6. Confocal and scanning electron microscopy

The cells were seeded on the surface of glass slides in Petri dishes (Ibidi, Germany) at a density of 10^3 per cm^2. After cell seeding for 24 h, 10^{-5} M of CeO_2 nanoparticles was added to the culture medium. After incubation (24 h) the medium in the plates was replaced with HBSS containing DNA-tropic fluorescent dye Hoechst-33342 (excitation at 345 nm, emission at 487 nm). The morphology analysis of the cells was carried out using an upright confocal microscope LSM-510 with multiphoton excitation of fluorescence and an image analysis system.

After a 24 h cultivation period, the cells on the cover slips were washed with a 0.1 M phosphate buffer (pH 7.2) and fixed with a 2.5 % solution of glutaraldehyde in the same buffer for 2 h at room temperature to prepare the samples for scanning electron microscopy (SEM) analysis. After the samples were dehydrated in ethanol solutions (50 – 100 %) at 4 °C, ethanol was replaced with hexamethyldisilazane. The resulting preparations were studied on a Carl Zeiss NVision 40 workstation at an accelerating voltage of 0.5 kV.

1.7. X-ray irradiation

X-ray irradiation was conducted using an X-ray therapeutic machine RTM-15 (Mosrentgen, Russia) with a dose of 15 Gy for cell culture at a dose rate of 1 Gy min^{-1}, 200 kV voltage, 37.5 cm focal length and 20 mA current.

1.8. Real-time PCR

Total RNA from the sample cells was isolated using an RNA extraction kit (SINTOL, Russia). Reverse transcription reaction was carried out using a kit for RT (SINTOL, Russia). Real-time PCR amplification was performed using a thermocycler ANK-32 (SINTOL, Russia). Primers used for estimation of transcription level for the analyzed gene and glyceraldehyde-3-phosphate dehydrogenase (GAPDH) (reference gene) were supplied by SINTOL. A kit (SINTOL, Russia) containing SYBR Green I intercalating dye was used for real-time PCR. Then the threshold cycle values obtained in the result of PCR were determined (Table 1).

TABLE 1. The primers (sequence) of analyzed genes

Name of gene	**Gene primers**
IL-6	F: cttccatccagttgccttcttg R: ttgggagtggtatcctctgtga
CuZnSOD	F: gtaccagtgcaggacctcatttt R: gtctccaacatgcctctcttcat
GAPDH	F: atgtgtccgtcgtggatctga R: cctgcttcaccaccttcttga
MnSOD	F: ccacacattaacgcgcagat R: ggtggcgttgagattgttca
Gpx-1	F: ccaccgtgtatgccttct R: gagacgcgacattctcaatga
GSR	F:aaagaagaccccatcgggctcgg R:agagaggcaatcgacatccggaa

1.9. Statistical analysis

The experiments were carried out in 3 – 4 replicates and analytical determinations for each sample were performed in duplicate. The results were compared with the control experiment. Methods of variation statistics were applied to estimate the reliability of the results. To assess the statistical significance, the Mann-Whitney U test was used ($p \leq 0.05$). The obtained data were processed using Microsoft Excel 2007 software.

2. Results and discussion

Cerium oxide nanoparticles were synthesized by a facile precipitation method using citric acid as a stabilizer. TEM images (Fig. 1(a)) of CeO_2 nanoparticles confirmed their ultra-small dimensions (2 – 3 nm). They have a quasispherical shape and are sufficiently monodisperse. Maximum optical absorbance of citrate-stabilized nanoparticles is at 320 nm (Fig. 1(b)). Dynamic light scattering allowed to determine the mean hydrodynamic radius of cerium

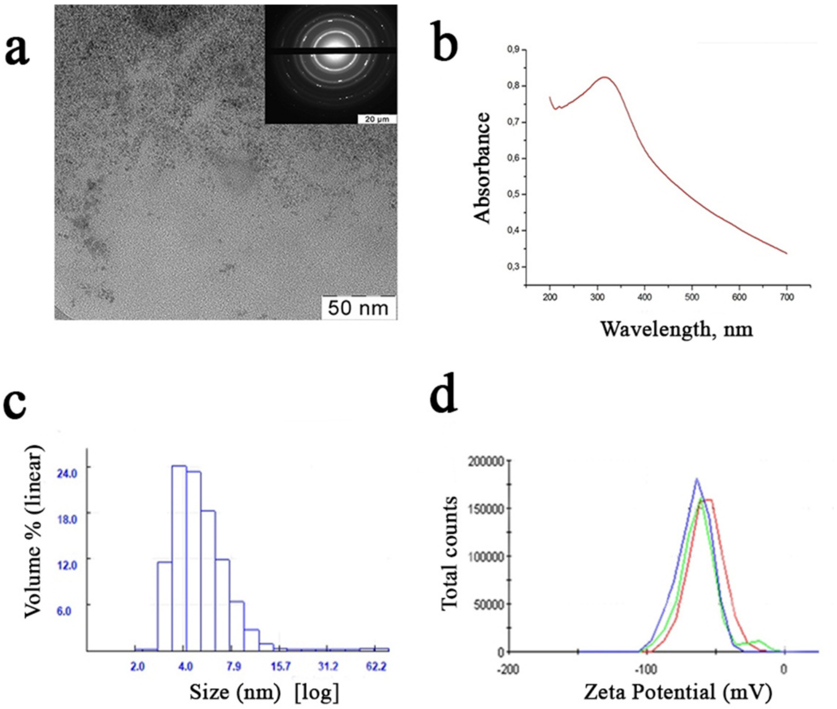

FIG. 1. image of citrate-stabilized cerium oxide nanoparticles (a), UV-vis absorption spectrum (b), hydrodynamic radii distribution of citrate-stabilized cerium oxide nanoparticles (c), potential of citrate-stabilized cerium oxide nanoparticles (d)

oxide nanoparticles diluted in DMEM/F12 + 10 % FBS culture medium, which amounted about 5 – 7 nm (Fig. 1(c)). Negative zeta potential (~ -65 mV) of CeO_2 nanoparticles is provided by the citrate ions on their surface (Fig. 1(d)).

It is known that the UV-vis spectra of cerium dioxide sols can contain two absorption bands due to the presence of cerium in different valence states (+3 and +4) [18]. In the nonstoichiometric (reduced) state, CeO_2 nanoparticles exhibit luminescence of Ce(III) ions at 390 nm [19]. To that end, with a decrease in CeO_2 particle size, a bathochromic shift of the luminescence maximum and an increase in its intensity are observed [20]. Given these spectral characteristics of CeO_2 nanoparticles, we investigated their intracellular localization by confocal microscopy. The intracellular localization of nanoparticles was confirmed (Fig. 2). CeO_2 nanoparticles are distributed over the entire cytoplasm of the cell, which is shown by a characteristic green glow (Fig. 2(b)), while in the control group (without CeO_2 nanoparticles) the green glow is not observed (Fig. 2(a)).

An *in vitro* study of the radioprotective effect of cerium dioxide nanoparticles was carried out using NCTC L929 murine fibroblast culture. To optimize the radiation dose, we performed preliminary studies that showed that X-rays at doses of 5 and 10 Gy do not cause damage, which are reliably detected at the cellular level after 24, 48 or 72 hours. However, a dose of 15 Gy reveals significant violations of cell structures and metabolism (40 % decrease in dehydrogenase activity according to the MTT test, morphological changes and the presence of dead cells) in a fibroblast culture within 72 hours after irradiation. It was found that preliminary incubation of NCTC L929 cell lines with CeO_2 nanoparticles increases their viability (up to control values) (Fig. 3). It should be noted that all the tested concentrations of CeO_2 nanoparticles (10^{-5} – 10^{-9} M) increased the cell viability after irradiation in a dose-dependent manner.

A comparative analysis of cell viability using the LIVE/DEAD fluorescence test (Fig. 4) showed that preliminary treatment of cells with CeO_2 nanoparticles at the concentration of 10^{-5} M significantly reduces the number of dead (stained with propidium iodide) cells protecting the cell culture from the negative effects of ionizing radiation. The data obtained indicate that CeO_2 nanoparticles prevent the development of oxidative stress after exposure to X-ray radiation.

The radiolysis of water that occurs in the cytoplasm of cells under the action of ionizing radiation leads to the generation of a large number of free radicals and reactive oxygen species, which damage the cellular structures, ultimately leading to its death [21]. We have previously shown that the main contribution to the radioprotective effect of CeO_2 nanoparticles is precisely the decrease of intracellular ROS concentration due to chemical inactivation of water radiolysis products on the surface of nanoparticles [5]. At the same time, we revealed a complex mechanism

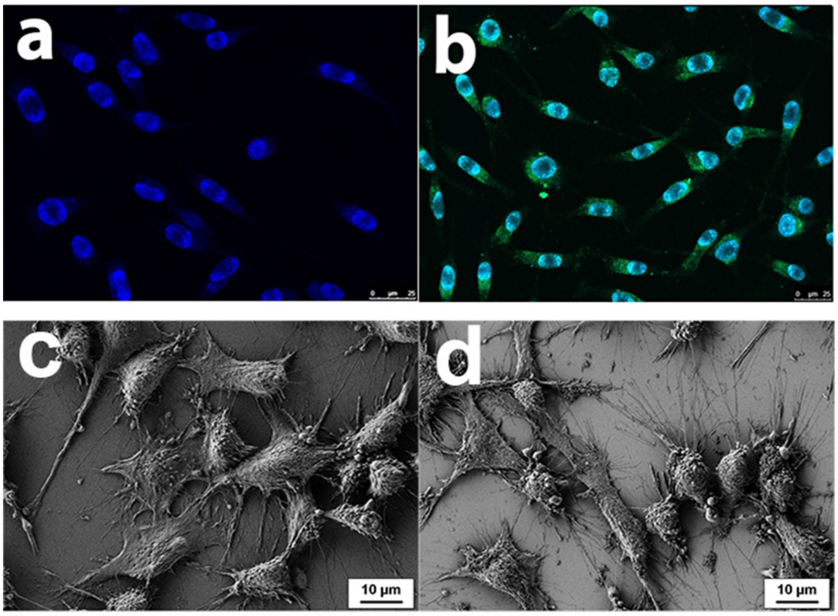

FIG. 2. Confocal images of NCTC L929 fibroblasts after 24 h exposure with cerium oxide nanoparticles (a – control, b – CeO_2 nanoparticles, 10^{-4}). DAPI dye was used for nuclear staining. Morphological analysis of NCTC L929 fibroblasts after 24 h incubation with cerium oxide nanoparticles (c – control, d – CeO_2 nanoparticles, 10^{-4})

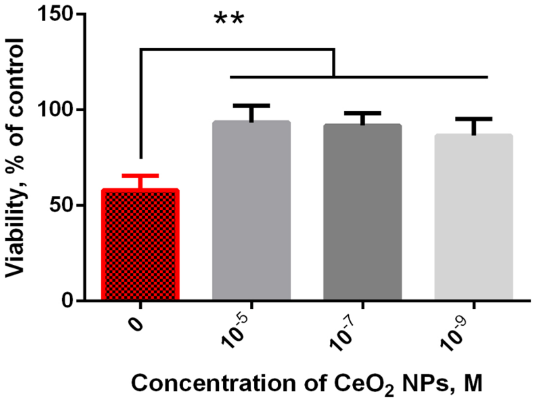

FIG. 3. Dehydrogenase activity of NCTC L929 fibroblasts after treatment with CeO_2 nanoparticles 72 h after exposure to X-rays at a dose of 15 Gy, as assessed by MTT-test. Control – 15 Gy without CeO_2 nanoparticles. * – Significant differences estimated by the U Mann–Whitney test, $p < 0.005$

for the radioprotective action of nanocrystalline cerium dioxide, which, in addition to chemical protection, involved physical and biological protection. The physical protection is realized through the absorption of ionizing radiation by CeO_2 nanoparticles and biological protection – through the activation of genes expression responsible for the development of oxidative stress in the cell.

The expression of four key antioxidant enzymes (SOD1, SOD2, glutathione peroxidase-1 and glutathione reductase) was further studied by real-time polymerase chain reaction (PCR) upon exposure of the cells to X-rays in the presence of CeO_2 nanoparticles (Figs. 5, 6). The glutathione reductase/glutathione peroxidase (GR/GP) system is an essential component of the body's antioxidant defence, which maintains the intensity of free radical oxidation at a stationary level [22]. Due to the GR/GP system functioning in mammalian cells, the inactivation of hydroperoxides and peroxides is achieved, which are the main source of the hydroxyl radical formed in the Fenton reaction in the presence of Fe^{2+} ions [23]. Glutathione reductase (GR) is a common flavin enzyme that catalyzes the reversible NADPH-dependent reduction of oxidized glutathione (GSSG) [24]. The biological role of GR is to maintain a high intracellular concentration of reduced glutathione (GSH) without increasing its production.

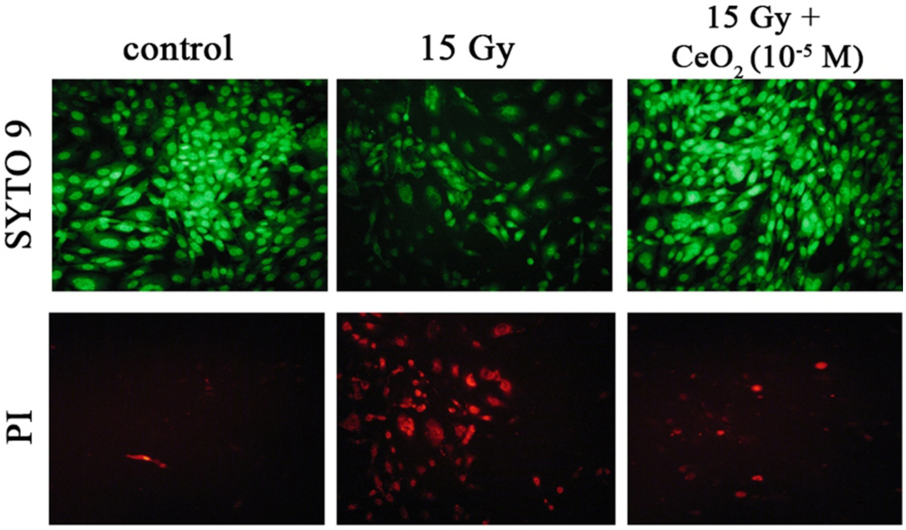

FIG. 4. Viability of murine fibroblasts (NCTC L929 cell line) treated with CeO_2 nanoparticles 72 h after exposure to X-rays at a dose of 15 Gy, as assessed by Live/DEAD assay. Control – cells without CeO_2 nanoparticles

It was shown that exposure to X-rays at a dose of 10 Gy leads to an increase in the expression of glutathione peroxidase-1 by a factor of 25 in comparison to the unirradiated control (Fig. 5). Pre-treatment of L929 cells with CeO_2 nanoparticles reduces the expression level of this enzyme by 2.5-fold. It can be assumed that a large number of radicals formed upon exposure to X-ray radiation are directly inactivated by CeO_2 nanoparticles, which exhibit activity similar to natural antioxidant enzymes of the cell including glutathione peroxidase-1. At the same time, the level of glutathione reductase transcripts remains close to the control of the treated cells, which, apparently, is associated with the need to maintain a high level of reduced glutathione after exposure to X-ray radiation. The change in the expression of Mn-superoxide dismutase (MnSOD) occurs upon incubation with cerium dioxide nanoparticles even without exposure to ionizing radiation.

Literature data [25–28] confirm the dominant role of MnSOD in protecting cells from oxidative stress induced by ionizing radiation. It was also previously shown that preincubation of colon cells [29] with CeO_2 nanoparticles leads to overexpression of MnSOD. There is much evidence that some forms of ROS act as signaling molecules, suggesting a much more complex role for ROS in genome expression and post-translational protein modification than it was assumed previously. For example, two transcription factors (NF-kB and AP1) are involved in intracellular redox signaling, which controls the induction of pro-inflammatory cytokines, as well as the control of the expression of MnSOD and similar antioxidants. Recent studies showed that nanocrystalline cerium dioxide is able to modulate cellular oxidative signaling pathways that are closely associated with inflammation through activation of JNK kinase, mitogen-activated protein kinase, and p38 protein [7, 30].

Using the www.genemania.org resource, we built a map of signaling pathways that involves the studied genes (Fig. 6). We conducted a study of the interleukin-6 expression – the cytokine involved in pro-inflammatory reaction. The results provide evidence that almost triple increase of expression occurs after exposure to ionizing radiation. Cerium dioxide nanoparticles do not cause an increase in the expression of the proinflammatory cytokine, and provide its reduction to the control level when exposed to ionizing radiation (Fig. 5).

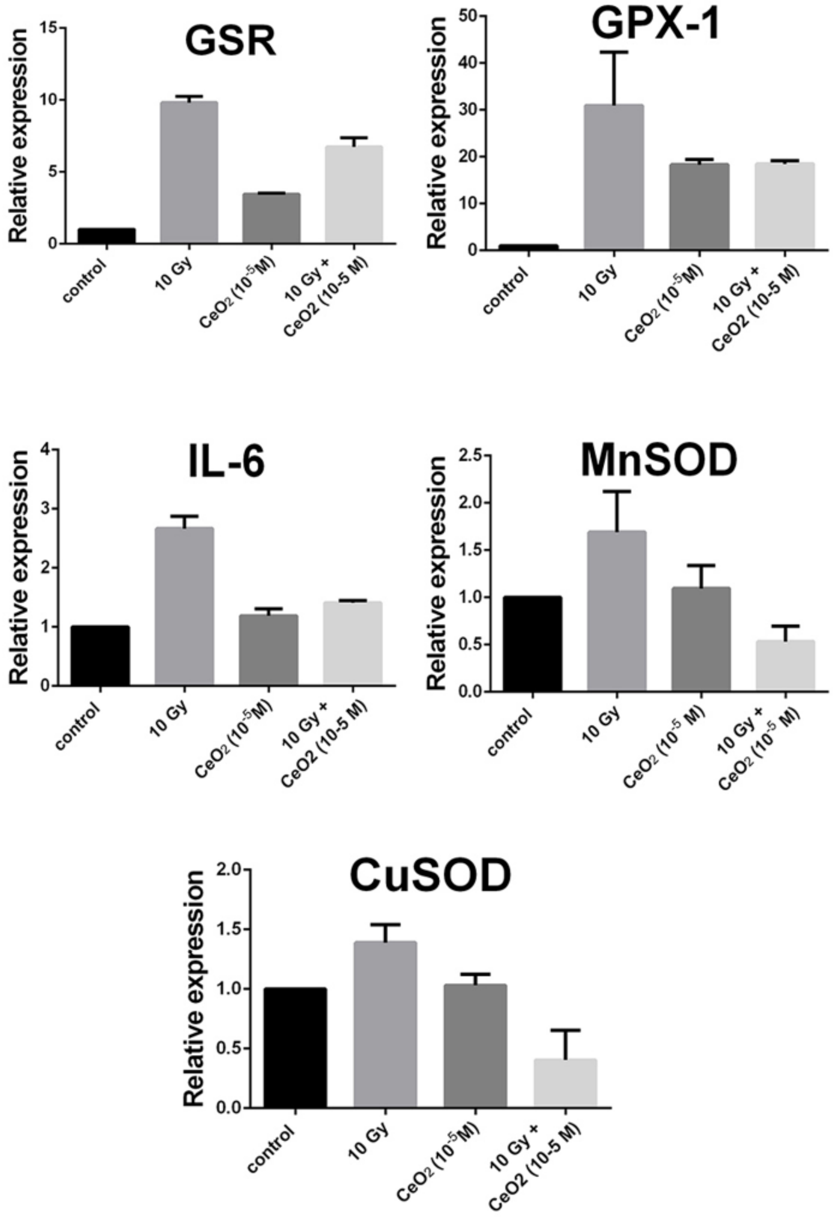

FIG. 5. Gene expression of SOD1, SOD2, GPX-1, GSR and IL-6 in murine fibroblast cell line NCTC L929 24 h after incubation with CeO_2 nanoparticles (10^{-5}) and X-ray irradiation at a dose of 10 Gy

3. Conclusions

The data obtained indicate that cerium dioxide nanoparticles are able to modulate the expression level of key cellular antioxidant enzymes, providing a radioprotective effect upon exposure to high doses of X-rays.

Acknowledgements

This research has been supported by the Russian Science Foundation (project 19-13-00416). Irradiation experiments were performed using the equipment of the Center of Shared Facilities of ICB RAS “Sources of ionizing radiations”.

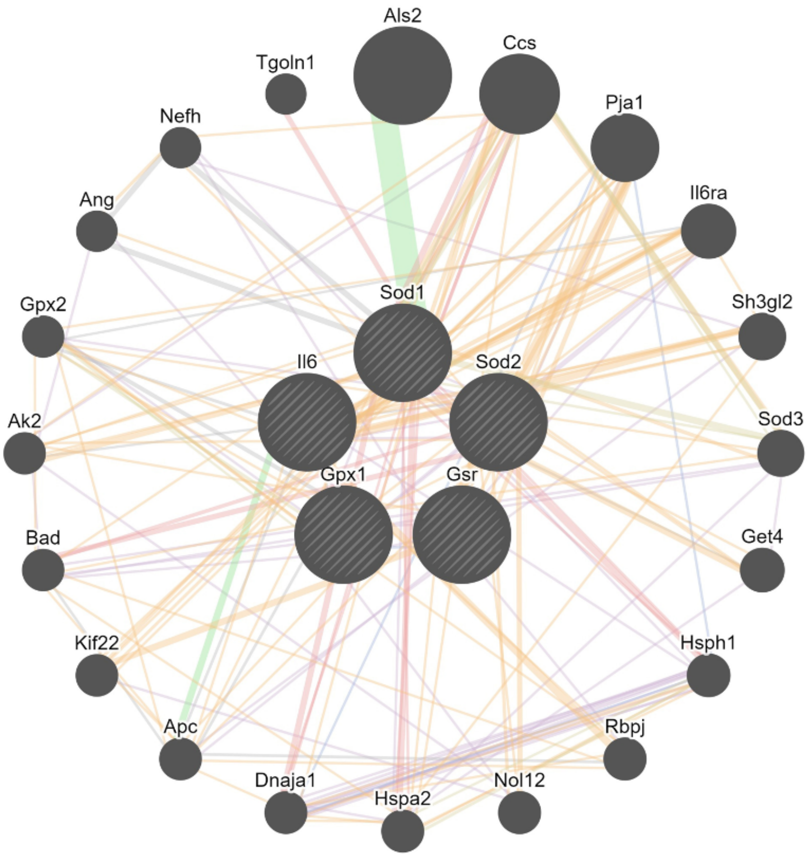

FIG. 6. Gene map of signaling pathways involved in SOD1, SOD2, GPX-1, GSR and IL-6 action

References

[1] Younis A., Chu D., Li S. Cerium Oxide Nanostructures and their Applications. *Intech. Open*, 2016, **3**, P. 53–68.

[2] Shcherbakov A.B., Zholobak N., Ivanov V.K. Biological, biomedical and pharmaceutical applications of cerium oxide. In: *Metal Oxides Series: Cerium Oxide (CeO$_2$): Synthesis, Properties and Applications*. Publisher: Elsevier, Amsterdam, 2019, P. 279–358.

[3] Zholobak N.M., Ivanov V.K., et al. UV-shielding property, photocatalytic activity and photocytotoxicity of ceria colloid solutions. *J. Photochem. Photobiolog. B: Biology*, 2011, **102**, P. 32–38.

[4] Popov A.L., Shcherbakov A.B., et al. Cerium dioxide nanoparticles as third-generation enzymes (Nanozymes). *Nanosystems: Physics, Chemistry, Mathematics*, 2017, **8** (6), P. 760–781.

[5] Popov A.L., Zaichkina S.I., et al. Radioprotective effects of ultra-small citrate-stabilized cerium oxide nanoparticles in vitro and in vivo. *RSC Adv.*, 2016, **6**, P. 106141–106149.

[6] Caputo F., Giovannetti A., et al. Cerium oxide nanoparticles re-establish cell integrity checkpoints and apoptosis competence in irradiated HaCat cells via novel redox-independent activity. *Front Pharmacol.*, 2018, **9**, 1183.

[7] Wason M.S., Lu H., et al. Cerium oxide nanoparticles sensitize pancreatic cancer to radiation therapy through oxidative activation of the JNK apoptotic pathway. *Cancers (Basel)*, 2018, **10** (9), 303.

[8] Xu P-T., Maidment B.W., et al. Cerium oxide nanoparticles: A potential medical countermeasure to mitigate radiation-induced lung injury in CBA/J Mice. *Radiat. Res.*, 2016, **185**, P. 516–526.

[9] Zal Z., Ghasemi A., et al. Radioprotective effect of cerium oxide nanoparticles against genotoxicity induced by ionizing radiation on human lymphocytes. *Curr. Radiopharm.*, 2018, **11** (2), P. 109–115.

[10] Colon J., Herrera L., et al. Protection from radiation-induced pneumonitis using cerium oxide nanoparticles. *Nanomedicine*, 2009, **5** (2), P. 225–231.

[11] Colon J., Hsieh N., et al. Cerium oxide nanoparticles protect gastrointestinal epithelium from radiation-induced damage by reduction of reactive oxygen species and upregulation of superoxide dismutase 2. *Nanomedicine*, 2010, **6** (5), P. 698–705.

[12] Madero-Visbal R.A., Alvarado B.E., et al. Harnessing nanoparticles to improve toxicity after head and neck radiation. *Nanomedicine*, 2012, **8** (7), P. 1223–1231.

[13] Tarnuzzer R.W., Colon J., Patil S., Seal S. Vacancy engineered ceria nanostructures for protection from radiation-induced cellular damage. *Nano Lett.*, 2005, **5** (12), P. 2573–2577.

[14] Briggs A., Corde S., et al. Cerium oxide nanoparticles: influence of the high-Z component revealed on radioresistant 9L cell survival under X-ray irradiation. *Nanomedicine*, 2013, **9** (7), P. 1098–1105.

[15] Ivanov V.K., Polezhaeva O.S., et al. Synthesis and thermal stability of nanocrystalline ceria sols stabilized by citric and polyacrylic acids. *Russ. J. Inorg. Chem.*, 2010, **55** (3), P. 328–332.

[16] Zholobak N.M., Shcherbakov A.B., et al. Panthenol-stabilized cerium dioxide nanoparticles for cosmeceutic formulations against ROS-induced and UV-induced damage. *J. Photochem. Photobiol. B*, 2014, **130**, P. 102–108.

[17] Ivanova O.S., Shekunova T.O., et al. One-stage synthesis of ceria colloid solutions for biomedical use. *Dokl. Chem.*, 2011, **437** (2), P. 103–106.

[18] Stoianov O.O., Ivanov V.K., et al. Determination of cerium(III) and cerium(IV) in nanodisperse ceria by chemical methods. *Russ. J. Inorg. Chem.*, 2014, **59** (2), P. 15–23.

[19] Maksimchuk P.O., Masalov A.A., Malyukin Yu.V. Spectroscopically detected formation of oxygen vacancies in nanocrystalline CeO_{2x}. *Journal of nano- and electronic physics*, 2013, **5** (1), 01004.

[20] Maksimchuk P., Masalov A.A. Optically detected effect of size on the oxygen vacancies concentration in cerium oxide nanocrystals. *Proceedings of the International Conference Nanomaterials: Applications and Properties*, Alushta, 2014, **3** (2), 02NAESF05.

[21] Le Caër S. Water Radiolysis: Influence of Oxide Surfaces on H_2 Production under Ionizing Radiation. *Water*, 2011, **3**, P. 235–253.

[22] Espinosa-Diez C., Miguel V., et al. Antioxidant responses and cellular adjustments to oxidative stress. *Redox Biol.*, 2015, **6**, P. 183–197.

[23] Zhao Y., Seefeldt T., et al. Effects of glutathione reductase inhibition on cellular thiol redox state and related systems. *Arch. Biochem. Biophys.*, 2009, **485** (1), P. 56–62.

[24] Couto N., Wood J., Barber J. The role of glutathione reductase and related enzymes on cellular redox homoeostasis network. *Free Radic. Biol. Med.*, 2016, **95**, P. 27–42.

[25] Murley J.S., Kataoka Y., et al. Delayed cytoprotection after enhancement of SOD2 (MnSOD) gene expression in SA-NH mouse sarcoma cells exposed to WR-1065, the active metabolite of amifostine. *Radiat. Res.*, 2002, **158**, P. 101–109.

[26] Wong G.H. Protective roles of cytokines against radiation: induction of mitochondrial MnSOD. *Biochim. Biophys. Acta*, 1995, **1271**, P. 205–209.

[27] Hirose K., Longo D.L., Oppenheim J.J., Matsushima K. Overexpression of mitochondrial manganese superoxide dismutase promotes the survival of tumor cells exposed to interlukin-1, tumor necrosis factor, selected anticancer drugs, and ionizing radiation. *FASEB J.*, 1993, **7**, P. 361–368.

[28] Sun J., Chen Y., Li M., Ge Z. Role of antioxidant enzymes on ionizing radiation resistance. *Free Radic. Biol. Med.*, 1998, **24**, P. 586–593.

[29] Motoori S., Majima H.J., et al. Overexpression of mitochondrial manganese superoxide dismutase protects against radiation-induced cell death in the human hepatocellular carcinoma cell. *Cancer Research*, 2001, **61**, P. 5382–5388.

[30] Selvaraj V., Nepal N., et al. Inhibition of MAP kinase/NF-kB mediated signaling and attenuation of lipopolysaccharide induced severe sepsis by cerium oxide nanoparticles. *Biomaterials*, 2015, **59**, P. 160–171.

NANOSYSTEMS: PHYSICS, CHEMISTRY, MATHEMATICS, 2019, 10 (5), P. 573–578

Successive ionic layer deposition of Co-doped $Cu(OH)_2$ nanorods as electrode material for electrocatalytic reforming of ethanol

I. A. Kodintsev[1*], K. D. Martinson[1], A. A. Lobinsky[2], V. I. Popkov[1]

[1]Ioffe Institute, 194021 Saint Petersburg, Russia
[2]Saint Petersburg State University, Peterhof, 198504 Saint Petersburg, Russia

*i.a.kod@mail.ru

PACS 73.61.r, 81.15.z, 82.65.+r **DOI 10.17586/2220-8054-2019-10-5-573-578**

In this work, a facile and cost-effective layer by layer method was proposed to synthesize novel high stable and effective electrode material based on the Co-doped $Cu(OH)_2$ nanocrystals. The crystals have orthorhombic structure and a rod-like morphology with a 23±2 nm in width and 43±4 nm in length. The composition of the nanocrystals corresponds to the 1 % Co-doped $Cu(OH)_2$ by EDX with no noticeable impurities as it was found by FTIR spectroscopy. It was shown that nickel electrode modified with nanorods is characterized by an overvoltage value of -347 mV at 10 mA/cm^2, which is 250 mV lower than that of an initial pure nickel electrode. The value of Tafel slope that reaches 138 mV/dec, high stability of the Co-doped $Cu(OH)_2$ nanorods in chronopotentiometric (10 hours) and cyclic volamperometric (500 cycles) tests allows us to consider them as a prospective basis of electrode materials for the hydrogen evolution from renewable water-alcohol sources.

Keywords: copper hydroxide, nanocrystals, successive ionic layer deposition, hydrogen evolution, electrocatalytic reforming.

Received: 13 June 2019

Revised: 18 September 2019

1. Introduction

The interest in the development of a clean and renewable energy source has been increased over the last few decades due to increased energy needs, the depletion of fossil fuel reserves and environmental pollution. Hydrogen is most often considered as such energy source [1]. There are various methods of hydrogen production, such as steam reforming [2], water electrolysis [3, 4], biological processes [5] and photoelectrolysis [6, 7]. In recent years, a method of hydrogen production from water-alcohol mixtures (or, as it is called electrochemical reforming or ECR) is being developed as an alternative technique to the water electrolysis because of the lower energy requirements [8]. However, the wide application of this method is limited because of the scarcity and high cost of Pt electrodes. Thus, the alternative electrode materials are the main research objective in this area.

Various cost-efficient nanomaterials have been developed for hydrogen evolution reactions, including oxides [9, 10] sulfides [11–13], phosphides [14–16], carbides [17], nitrides of d-elements [18], and composites with other materials [19–21]. However, among them, Cu-based materials are much less explored for hydrogen evolution, due to the instability and low catalytic efficiency, despite the fact that such materials have much higher electrical conductivity [22]. Those Cu-based materials seem to be promising electrode materials, basic for the ECR process, in the cases of solving the problem of their effective production and increasing of their functional characteristics.

There are two main strategies for improving the hydrogen evolution performance of Cu-based materials: the first one is to form nanocomposites by heteroatom doping; and the second is to construct nanostructures with specific morphologies with high surface area, such as nanowires, nanotubes, and nanosheets [23–25]. Both of strategies, as it will be shown below, can be attained by using successive ionic layer deposition (SILD) which is a kind of layer-by-layer methods [26, 27].

The layer-by-layer method is one technique that allows the synthesis of the nanocomposites mentioned above [28–30]. It is based on the sequential absorption of precursors on the substrate surface, followed by the removal of excess reagents. The result is a film of the synthesized substance, the thickness of which increases with repetition of adsorption reactions in proportion to the number of processing cycles [31]. This approach allows one to synthesize nanoparticles with non-isometric morphology and to finely vary their composition by changing the composition of the reaction solutions. So, the aim of this work is to investigate the structure and electrochemical properties of Co-doped $Cu(OH)_2$ non-isometric nanoparticles, synthesized via the SILD method, and the possible use of this nanocomposite as a suitable material for hydrogen evolution via electrochemical reforming of the water-ethanol solution.

2. Experimental

Monocrystalline silicon plates with the orientation of [100] and nickel foam plates (JSC ECAT, 90 PPI) with the size of 5×20 mm were used as substrates for nanocomposite synthesis. Before synthesis, these plates were treated in acetone for 10 minutes in an ultrasonic bath. Then, silicon plates were etched with concentrated HF for 15 minutes and nickel foam plates were treated with 6 M HCl solution for 15 minutes. After that, the silicon plates were treated for 20 minutes in dilute aq. KOH solution with pH = 9.0. Finally, all wafers were washed with deionized water and air-dried at 80° for 30 minutes.

The nanocomposite was synthesized on the substrates using a layer-by-layer technique. During the synthesis, the wafers were immersed for 30 seconds into the solution containing 0.1 M $Cu(CH_3COO)_2$ and 0.01 M $Co(CH_3COO)_2$, distilled water, solution of NaOH with pH = 9 and again distilled water. This treatment considered as one layer-by-layer cycle.

The elemental analysis and morphology of the synthesized sample were studied by energy dispersive X-ray analysis (EDX) and scanning electron microscopy (SEM) using Tescan Vega 3 SBH scanning electron microscope equipped with an Oxford INCA x-act X-ray microanalysis device. X-ray phase analysis was performed on a RigakuSmartLab 3 X-ray powder diffractometer, phase analysis of the composition was performed using ICDD PDF-2 powder database. The average crystallite size (coherent-scattering regions) was calculated from the broadening of X-ray diffraction lines using the Scherrer formula. FTIR spectra were obtained using Shimadzu IRTracer-100 FTIR spectrometer in the spectral range from 350 cm^{-1} to 4000 cm^{-1} with a spectral resolution 2 cm^{-1}.

Electrochemical properties of obtained electrodes for electrochemical reforming were investigated using potentiostat Elins P-45X and a three-electrode cell. Nickel foam plate with nanocomposite film deposited via the layer-by-layer method was used as a working electrode, the Ag/AgCl electrode was used as reference electrode and a platinum foil was used as a counter electrode. All measurements have been carried out at atmospheric pressure and room temperature in aq. 1 M KOH solution with 10 % (by volume) ethanol as the electrolyte. The voltammogram was made at 5 mV/s sweep rate with IR compensation (1.3Ω). Chronopotentiogram was made at a current density of -10 mA/cm^2.

3. Results and discussions

According to the XRD pattern (Fig. 1), the only phase in the sample is copper (II) hydroxide $Cu(OH)_2$ with the orthorhombic structure (JCPDS 13-420) with *Cmcm* space group.

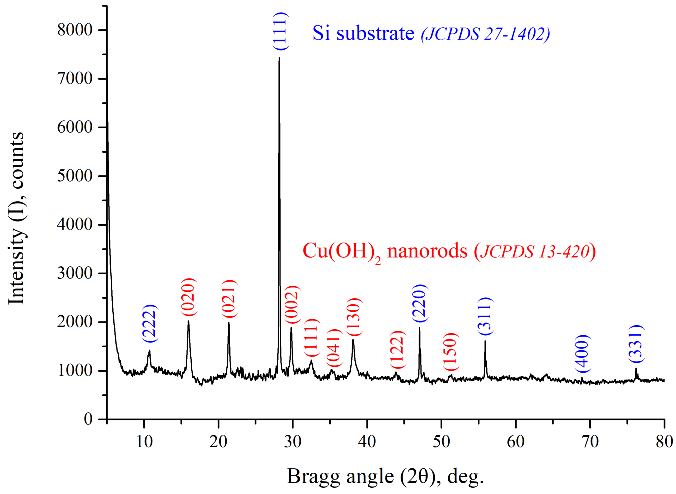

FIG. 1. XRD pattern of Co-doped $Cu(OH)_2$ nanorods on a silicon wafer

Refining of the unit cell parameters of this sample using Rietveld method yielded the following results: $a = 2.9489$ Å, $b = 11.1141$ Å, $c = 6.2414$ Å, $\alpha = \beta = \gamma = 90°$, $R_{wp} = 5.41$ %. A significant difference in the broadening of the X-ray diffraction lines in individual crystallographic directions indicates the anisotropic shape of the $Cu(OH)_2$ crystallites. Analysis of these data using the Scherrer formula allowed us to establish the size of coherent scattering region: in the [111] direction – 23±2 nm, in the [002] direction – 43±4 nm. Thus, taking into account the exact arrangement of these crystallographic planes in crystals with an orthorhombic structure [32], it could be concluded that the obtained nanocrystals have a morphology of nanorods, which is also confirmed by scanning electron microscopy (Fig. 2(b,c,d)).

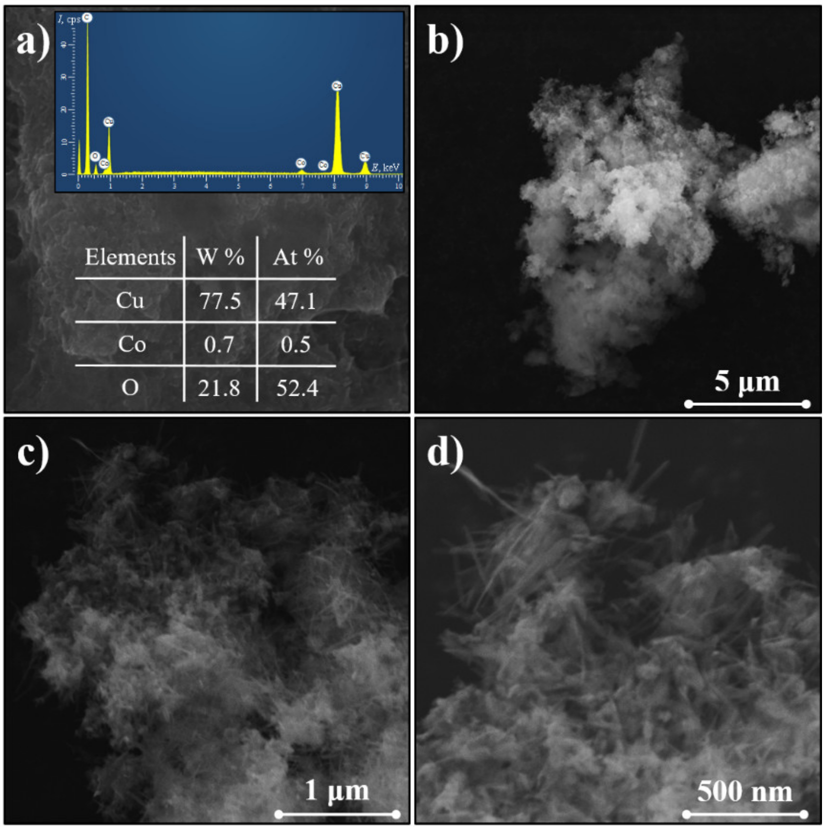

Elements	W %	At %
Cu	77.5	47.1
Co	0.7	0.5
O	21.8	52.4

FIG. 2. a – EDX spectrum; b,c,d – SEM images of Co-doped Cu(OH)$_2$ nanorods on a silicon wafer

The results of scanning electron microscopy indicate that the synthesized nanocrystals of Co-doped Cu(OH)$_2$ are in the sample in the form of agglomerates with micron sizes (Fig. 2(a)). Only at a higher magnification, it becomes noticeable that each agglomerate consists of a large number of copper hydroxide nanorods. However, the nanorods observed on SEM images have a submicron length, which differs from the crystallite lengths, about 40 nm, estimated on the base of X-ray diffractometry data. Thus, these submicron nanorods are non-oriented intergrown nanocrystals of Co-doped Cu(OH)$_2$. The similar structure of micron and submicron rods based on intergrown nanocrystals was observed earlier in work [33]. The EDX analysis shows that synthesized nanocrystals include cobalt atoms with Cu/Co ratio equal to 99.0 %: 1.0 %. Thus, 1 % Co-doped Cu(OH)$_2$ nanorods were synthesized as a result of the successive ionic layer deposition.

Figure 3 shows the FT-IR spectra of the obtained nanocomposite. The strong and broad absorption band at around 3300 cm^{-1} and a sharp peak at 3571 cm^{-1} is attributed to the stretching mode of –OH groups, which indicates the presence of hydroxyls in the free water and in the copper hydroxides, correspondently. The bands at 913, 1358, and 1561 cm^{-1} are attributed to the bending mode of H_2O and CO_2 coordinated to metal ions [34] that is the result of adsorption of these substances by the developed surface of the hydroxide obtained. Three intense bands at 683, 610, and 512 cm^{-1} are attributed to Cu–O vibrations and additionally confirm the presence of copper hydroxide. No absorption bands were detected, associated with the presence of cobalt and only a subtle shift in the absorption bands of the Cu–O bonds was observed with respect to pure copper hydroxide [26].

The electrochemical investigations show that the synthesized nanocomposite could be successfully used in electrochemical reforming of ethanol. Electrocatalytic properties were characterized by cyclic voltammetry and chronopotentiometry shown in Fig. 4.

The overpotential of hydrogen evolution for the initial sample and the sample after 500 cycles of charge-discharge was determined from the polarization curves obtained at 5 mV/s scanning rate. The initial sample shows overpotential about -347 mV at current density 10 mA/cm^2. For the original nickel electrode, the overpotential value at this current

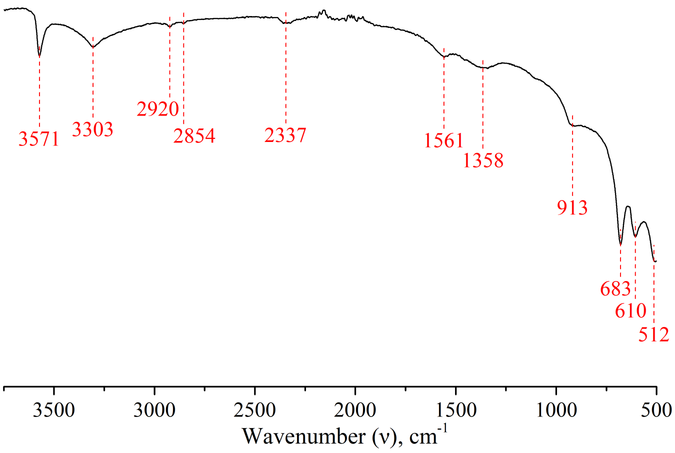

FIG. 3. FTIR spectrum of Co-doped Cu(OH)$_2$ nanorods

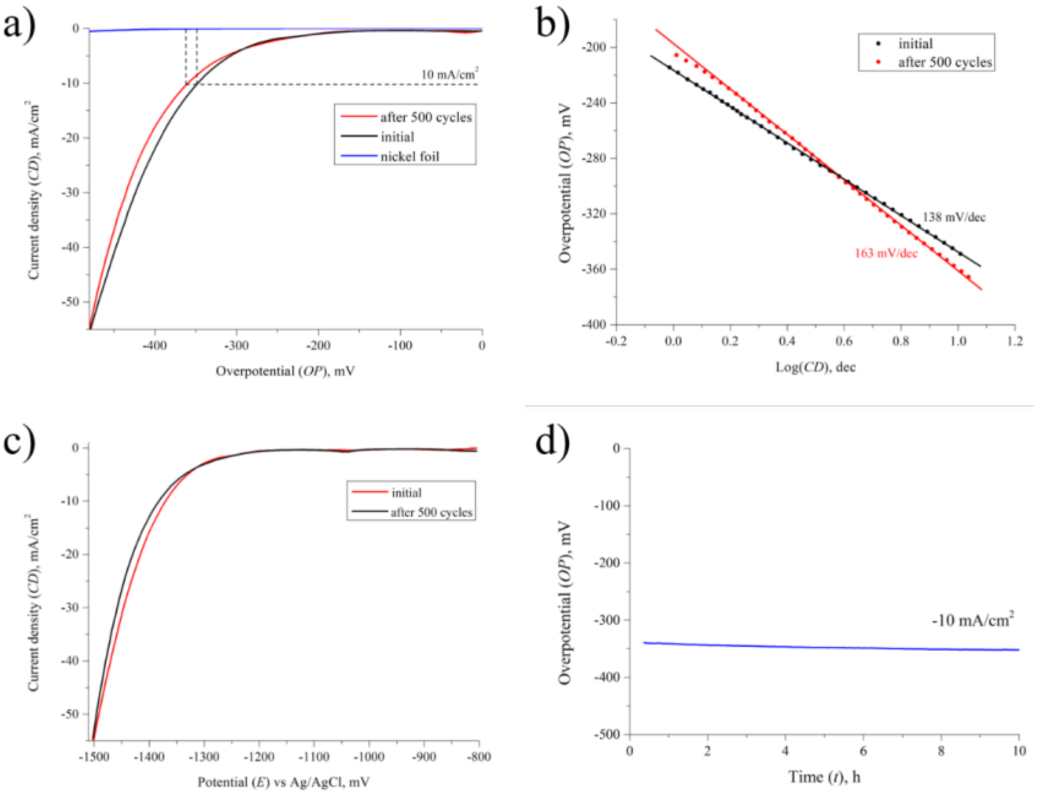

FIG. 4. a – polarization curves, b – Tafel slop, c – cyclic stability and d – chronoamperogramm of Co-doped Cu(OH)$_2$ nanorods

density is about -600 mV, thus the overvoltage on the cobalt-doped copper hydroxide electrode improved by 250 mV and approached the advanced electrode materials based on d-elements oxides [3, 4, 20]. A slight difference in the change of overpotential after 500 charge-discharge cycles indicates good electrochemical stability and low degradation of the obtained material.

The microkinetic characteristics of the samples were determined from the Tafel slope. The value of the Tafel slope was calculated using formula $\eta = a \cdot \log(i)$, where η – overpotential of HER reaction, i – current density, a – Tafel slope, from the linear part of the overpotential and it reaches 138 mV/dec and 163 mV/dec after 500 charge-discharge cycles (Fig. 4(b)). The obtained value of the Tafel slope is characteristic for electrocatalyst based on transition metal oxides and hydroxides during the HER reactions in an alkaline aqueous medium, as was previously noted [35]. It should be noted that after 500 charge-discharge cycles, the Tafel slope increases significantly (by 25 mV/dec), which indicates a change in the mechanism of hydrogen evolution from the catalyst surface. In our opinion, the observed effect may occur due to a change of surface morphology during cycling, at the same time the overvoltage changes insignificantly. The chronopotentiometry was used to characterize the stability of the material in a stationary mode at a given current density of 10 mA/cm^2. The measurements show that this nanocomposite is effective through all 10 hours of work and 500 cycles of voltammetry. Thus the results of electrocatalytic studies confirm that the Co-doped Cu(OH)$_2$ synthesized via successive ionic layer deposition can be considered as an effective and high stable material for hydrogen production by electrocatalytic reforming of water-ethanol solutions.

4. Conclusion

In this work, a successive ionic layer deposition method was used to synthesize Co-doped Cu(OH)$_2$ nanocrystals with rod-like morphology. As it was shown by XRD and SEM, nanocrystals of Co-doped Cu(OH)$_2$ have 23±2 nm in width (for [111] crystallographic direction) and 43±4 nm in length (for [002] crystallographic direction) and form agglomerates of the same width and micron-submicron length. The results of EDX, XRD and FTIR investigations confirmed the high purity of the synthesized Co-doped Cu(OH)$_2$ nanocrystals with Co content of 1 at. % in relation to Cu. Electrochemical investigation of the electrode with Co-doped Cu(OH)$_2$ shows overpotential values of 347 mV at a current density of 10 mA/cm^2 and Tafel slope values of 138 mV/dec for hydrogen evolution from water-ethanol solution (10 % v/v). In addition, it was found that the resulting electrode material has high stability in both chronoamperometry mode and in voltammetric cycling mode. On the base of this results, Co-doped Cu(OH)$_2$ nanorods synthesized via layer by layer approach, could be considered as a prospective basis of electrode materials for electrocatalytic reforming of ethanol.

References

[1] Ma T.Y., Dai S., Qiao S.Z. Self-supported electrocatalysts for advanced energy conversion processes. *Materials Today*, 2016, **19**, P. 265–273.

[2] Angeli S.D., Monteleone G., Giaconia A., Lemonidou A.A. State-of-the-art catalysts for CH$_4$ steam reforming at low temperature. *Int. J. Hydrogen Energy*, 2014, **39**, P. 1979–1997.

[3] Kelly N.A. *Hydrogen production by water electrolysis. Advances in Hydrogen Production, Storage and Distribution*. Woodhead Publishing, 2014, P. 159–185.

[4] Eftekhari A. Electrocatalysts for hydrogen evolution reaction. *Int. J. Hydrogen Energy*, 2017, **42**, P. 11053–11077.

[5] Das D., Veziroglu T.N. Hydrogen production by biological processes: a survey of literature. *Int. J. Hydrogen Energy*, 2001, **26**, P. 13–28.

[6] Huang Q., Li Q., Xiao X. Hydrogen evolution from Pt nanoparticles covered p-Type CdS: Cu photocathode in scavenger-free electrolyte. *J. Phys. Chem. C*, 2014, **118**, P. 2306–2311.

[7] Moha. Feroz Hossen, Abu Bakar Md. Ismail. Investigation on Fe$_2$O$_3$/por-Si photocatalyst for low-bias water-splitting. *J. Mater. Sci.: Mater. Electron.*, 2018, **29**, P. 15480–15485.

[8] Gutiérrez-Guerra N., Jiménez-Vázquez M., et al. Electrochemical reforming vs. catalytic reforming of ethanol: a process energy analysis for hydrogen production. *Chem. Eng. Process*, 2015, **95**, P. 9–16.

[9] Sun Z., Liao T., et al. Generalized self-assembly of scalable two-dimensional transition metal oxide nanosheets. *Nat. Commun.*, 2015, **5**, P. 3813.

[10] Lobinsky A.A., Tolstoy V.P. Synthesis of CoAl–LDH nanosheets and N-doped graphene nanocomposite via Successive Ionic Layer Deposition method and study of their electrocatalytic properties for hydrogen evolution in alkaline media. *J. Solid State Chem.*, 2019, **270**, P. 156–161.

[11] Huerta-Flores A.M., Torres-Martinez L.M., et al. Green synthesis of earth-abundant metal sulfides (FeS$_2$, CuS, and NiS$_2$) and their use as visible-light active photocatalysts for H$_2$ generation and dye removal. *J. Mater. Sci.: Mater. Electron.*, 2018, **29**, P. 11613–11626.

[12] Lukowski M.A., Daniel A.S., et al. Enhanced hydrogen evolution catalysis from chemically exfoliated metallic MoS$_2$ nanosheets. *J. Am. Chem. Soc.*, 2013, **135**, P. 10274–10277.

[13] Faber M.S., Dziedzic R., et al. High-performance electrocatalysis using metallic cobalt pyrite (CoS$_2$) micro- and nanostructures. *J. Am. Chem. Soc.*, 2014, **136**, P. 10053–10061.

[14] Yang X., Lu A.Y., et al. CoP nanosheet assembly grown on carbon cloth: a highly efficient electrocatalyst for hydrogen generation. *Nano Energy*, 2015, **15**, P. 634–641.

[15] Callejas J.F., McEnaney J.M., et al. Electrocatalytic and photocatalytic hydrogen production from acidic and neutral-pH aqueous solutions using iron phosphide nanoparticles. *ACS Nano*, 2014, **8**, P. 11101–11107.

[16] Liang Y., Liu Q., et al. Self-supported FeP nanorod arrays: a cost-effective 3D hydrogen evolution cathode with high catalytic activity. *ACS Catal.*, 2014, **4**, P. 4065–4069.

[17] Chen J., Zhou W., et al. Porous molybdenum carbide microspheres as efficient binder-free electrocatalysts for suspended hydrogen evolution reaction. *Int. J. Hydrogen Energy*, 2017, **42**, P. 6448–6454.

[18] Cao B., Veith G.M., et al. Mixed close-packed cobalt molybdenum nitrides as non-noble metal electrocatalysts for the hydrogen evolution reaction. *J. Am. Chem. Soc.*, 2013, **135**, P. 19186–19192.

[19] Kirillova S.A., Almjasheva O.V., Panchuk V.V., Semenov V.G. Solid-phase interaction in ZrO_2–Fe_2O_3 nanocrystalline system. *Nanosystems: Phys. Chem. Math.*, 2018, **9**, P. 763–769.

[20] Li J.S., Wang Y., et al. Coupled molybdenum carbide and reduced graphene oxide electrocatalysts for efficient hydrogen evolution. *Nat. Commun.*, 2016, **7**, 11204.

[21] Zvereva V.V., Popkov V.I. Synthesis of CeO_2–Fe_2O_3 nanocomposites via controllable oxidation of $CeFeO_3$ nanocrystals. *Ceramics International*, 2019, **45**, P. 1380–1384.

[22] Tran P.D., Nguyen M., et al. Copper molybdenum sulfide: a new efficient electrocatalyst for hydrogen production from water. *Energy Environ. Sci.*, 2012, **5**, P. 8912–8916.

[23] Yan Y., Xia B., Xu Z., Wang X. Recent development of molybdenum sulfides as advanced electrocatalysts for hydrogen evolution reaction. *ACS Catal.*, 2014, **4**, P. 1693–1705.

[24] Jaramillo T.F., Jorgensen K.P., et al. Identification of active edge sites for electrochemical H_2 evolution from MoS_2 nanocatalysts. *Science*, 2007, **317**, P. 100–102.

[25] Dasgupta A., Rajukumar L.P., et al. Covalent three-dimensional networks of graphene and carbon nanotubes: synthesis and environmental applications. *Nano Today*, 2017, **12**, P. 116–135.

[26] Kodintsev I., Reshanova K., Tolstoy V. Layer-by-layer synthesis of metal oxide (or hydroxide) – graphene nanocomposites. The synthesis of CuO nanorods – graphene nanocomposite. *AIP Conference Proceedings*, 2016, **1748**, 040005.

[27] Ehsan M.A., Naeem R., et al. Facile fabrication of CeO_2–TiO_2 thin films via solution-based CVD and their photoelectrochemical studies. *J. Mater. Sci.: Mater. Electron.*, 2018, **29**, P. 13209–13219.

[28] Popkov V.I., Tolstoy V.P., Omarov S.O., Nevedomskiy V.N. Enhancement of acidic-basic properties of silica by modification with CeO_2–Fe_2O_3 nanoparticles via successive ionic layer deposition. *Appl. Surf. Sci.*, 2019, **473**, P. 313–317.

[29] Bayram O., Simsek O., et al. Effect of the number of cycles on the optical and structural properties of Mn_3O_4 nanostructures obtained by SILAR technique. *J. Mater. Sci.: Mater. Electron.*, 2018, **29**, P. 10542–10549.

[30] Dmitriev D.S., Popkov V.I. Layer by layer synthesis of zinc-iron layered hydroxy sulfate for electrocatalytic hydrogen evolution from ethanol in alkali media. *Nanosystems: Phys. Chem. Math.*, 2019, **10**, P. 480–487.

[31] Lobinsky A.A., Tolstoy V.P., Kodinzev I.A. Electrocatalytic properties of gamma-NiOOH nanolayers, synthesized by successive ionic layer deposition, during the oxygen evolution reaction upon water splitting in the alkaline medium. *Nanosystems: Phys. Chem. Math.*, 2018, **9**, P. 669–675.

[32] Popkov V.I., Almjasheva O.V., et al. Crystallization behavior and morphological features of $YFeO_3$ nanocrystallites obtained by glycine-nitrate combustion. *Nanosystems: Phys. Chem. Math.*, 2015, **6**, P. 866–874.

[33] Popkov V.I., Almjasheva O.V. Formation mechanism of $YFeO_3$ nanoparticles under the hydrothermal conditions. *Nanosystems: Phys. Chem. Math.*, 2014, **5**, P. 703–708.

[34] Popkov V.I., Tolstoy V.P. Peroxide route to the synthesis of ultrafine CeO_2–Fe_2O_3 nanocomposite via successive ionic layer deposition. *Heliyon*, 2019, **5**, e01443.

[35] Shinagawa T., Garcia-Esparza A.T., Takanabe K. Insight on Tafel slopes from a microkinetic analysis of aqueous electrocatalysis for energy conversion. *Sci. Rep.*, 2015, **5**, 13801.

NANOSYSTEMS: PHYSICS, CHEMISTRY, MATHEMATICS, 2019, 10 (5), P. 579–584

In-situ conversion of rGO from graphene oxide based on solar mediated enhanced characterization properties

Subramani shanmugam, Sivanandan nanjan

Department of Electronics, PSG College of Arts and Science, Coimbatore- 641014, India
sai.subbu29@gmail.com, sivanandannanjan@gmail.com

DOI 10.17586/2220-8054-2019-10-5-579-584

A globally acknowledged green synthesis of reduced graphene oxide (rGO) from graphene oxide (GO) is presented in this paper. The graphene oxide powder was synthesized from Graphite powder by a modification of Hummer's method. The GO is exposed to focused sunlight to obtain reduced graphene oxide (rGO). The reduction of GO under solar light is an eco-friendly method to conventional method of rGO preparation. The mechanism of the reduction of GO by sunlight imperative to exfoliation was seen to be well defined. The rGO powder was characterized by X-ray Diffraction (XRD), Field-Emission Scanning Electron Microscopy (FESEM), Raman spectroscopy, Fourier-Transform Infrared Spectroscopy (FTIR) and High-Resolution Transmission Electron Microscopy (HRTEM). This eco-friendly method of synthesizing of rGO paves way for an alternative method of rGO nanosheets preparation and it can be effectively used for fabrication of various electronic devices.

Keywords: reduced graphene oxide, crystal structure, reduction, exfoliation, raman.

Received: 4 July 2019

Revised: 5 September 2019

1. Introduction

Graphene Oxide (GO) is being single-layered carbon atom in a hexagonal lattice has a combination of both aromatic (sp^2 hybridized C–C atoms) and aliphatic (sp^3 hybridized –OH, C–O–H, C=O, –COOH) groups [1–3]. Thus, it exhibits a wide range of striking properties like optical transmittance, electrical conduction, energy storage, medical diagnosis and treatment, electronic applications, etc. The properties of GO and its reduced form plays a vital role in the multi-disciplinary functionality of these materials. They possess high surface area to volume ratio, high tensile strength, good thermal conduction, tremendous electrical conduction and superb optical properties [4]. The single layer GO and rGO can be synthesized by several methods, such as mechanical exfoliation, electrochemical reactions, thermal treatment and [5], photocatalytic method of preparing of GO and rGO. The solar energy assisted route of synthesis has an advantage of enhancement in its performance, especially when used for energy storage devices and super capacitors. Currently, a metallic oxide in combination with rGO and carbon nanotubes (CNTs), enhances the network performance of the devices. Oxides of tin, zinc, and cobalt are coated on graphene to obtain the desired quality of electrical devices [6–9]. Here, the purest form of solar energy was used to reduce the GO into rGO and this product was thoroughly characterized.

2. Experimental

2.1. Materials and methods

GO was synthesized from graphite powder using a modification of Hummer's method [10]. The reduced GO was prepared by using a convex lens of 100 mm diameter to focus solar radiation [11]. Briefly, 1 g of GO was taken in a glass Petri dish and kept under focused solar radiation at 12 Noon. GO powder was exposed to the focused solar radiation for approximately 10 – 15 minutes. GO was exfoliated into rGO sheets. The power of focused sunlight ranged from 1.8 – 2.5 W and the temperature was about $\sim 300\ ^\circ$C [12]. GO was exfoliated into rGO sheets under this high temperature and power [13].

3. Result and discussion

3.1. XRD Analysis

The XRD pattern of synthesized GO/rGO shows diffraction with Cu Kα radiation ($\lambda = 1.54178$ Å) and depicted in Fig. 1 [14]. The GO/rGO exhibits a well-crystalline orthorhombic crystal structure (JCPDS card No. 89-8491).

The GO/rGO featured sharp diffraction peaks indicates that GO at 11.83, 42.78 corresponds to (001) and (100) peaks. The diffraction peaks of rGO at 10.30, 23.31 & 43.76 correspond to (001), (002) & (100) [15]. The diffraction

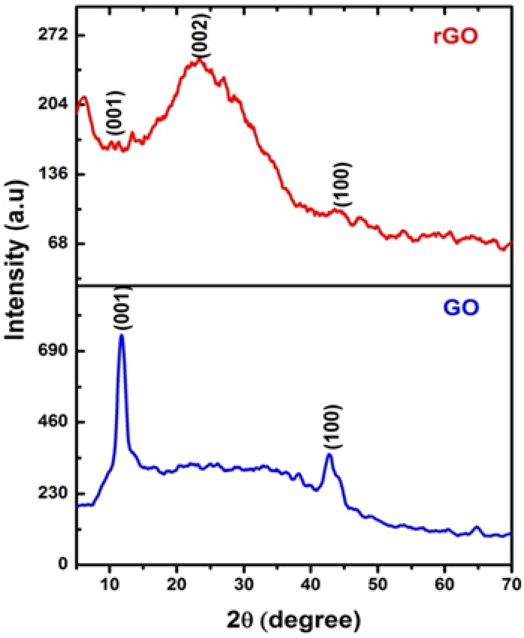

FIG. 1. X-ray diffraction pattern of GO and rGO nanosheets

plane of the hexagonal crystal structure has lattice constants of value, $a = 2.47$ and $c = 6.79$ Å. The crystalline size (D) of the GO/rGO was calculated using Scherrer's formula:

$$D = \frac{0.89\lambda}{\beta \cos\theta}, \tag{1}$$

where λ is the wavelength of the X-ray radiation, 2θ is the diffraction angle and β is the full width at half maximum (FWHM). Measured broadening of the GO/rGO with (001), (100) and 001),(002), (100) X-ray peaks offers average crystalline size about at 72.97, 14.03, and 19.59, 14.31, 21.23 nm for the GO/rGO, respectively [16].

3.2. FESEM/EDS

The morphology of GO/rGO nanosheets was observed using FESEM and shown in Fig. 2(a–b). The morphological feature clearly shows the formation of GO/rGO in 2D sheet-like pattern morphology in the prepared graphene materials similar to commercial materials. 2D wrinkled structure morphology of both GO and rGO sheets were observed to be fine micrometer in size. The rGO has a few broad and highly wrinkled layers with a regular shape and slanting size estimated in the range size of approximately 300 – 500 μm exclusively [17, 18].

The Energy Dispersive X-Ray Spectroscopy (EDS) analysis of the GO and rGO reveals that the atomic percentage of oxygen was considerably reduced in rGO than GO as expected. This is also confirmed by the increased ratio of C/O from 1.6684 to 2.0075.

3.3. HRTEM

Transmission electron microscopic (TEM) study was carried out to obtain the wide-ranging morphological information about the GO/rGO nanosheets and the respective HRTEM images were also showed in Fig. 3(a–d). The TEM image of GO/rGO confirms the nanosheets like morphology with their wrinkle shape with the face end (Fig. 3(a, b)). However, the TEM images of GO/rGO exhibits sheet-like shape with an average size of about 0.2 μm. In order to obtain that lattice fringes form in the plane (100) indicated, the d-spacing values in three different places are shown in Fig. 3(b). Inset images shows good conformity with TEM images [19].

A clear morphology of rGO was observed, as evidence that is shown in Fig. 3(c). The sheets of rGO obtained by the chemical reduction process possess a few layer forms, such as crumpled sheet-like morphology and the structure were further confirmed by TEM, as shown in Fig. 3(c, d). The uniform and wrinkled sheet-like morphology, as well as the micropores on sheet surface of rGO samples (Fig. 3(c)) were clearly observed. Also, it displays highly interconnected ultrathin silk-like morphology and wrinkled shape [20]. Moreover, the wrinkle of the layers folded over each other was clearly visible, suggesting that these wrinkles were occurred by the crumpling of graphene-like sheets. The results also show that the highly crumbled morphology can effectively prevent the aggregation of the sheets as

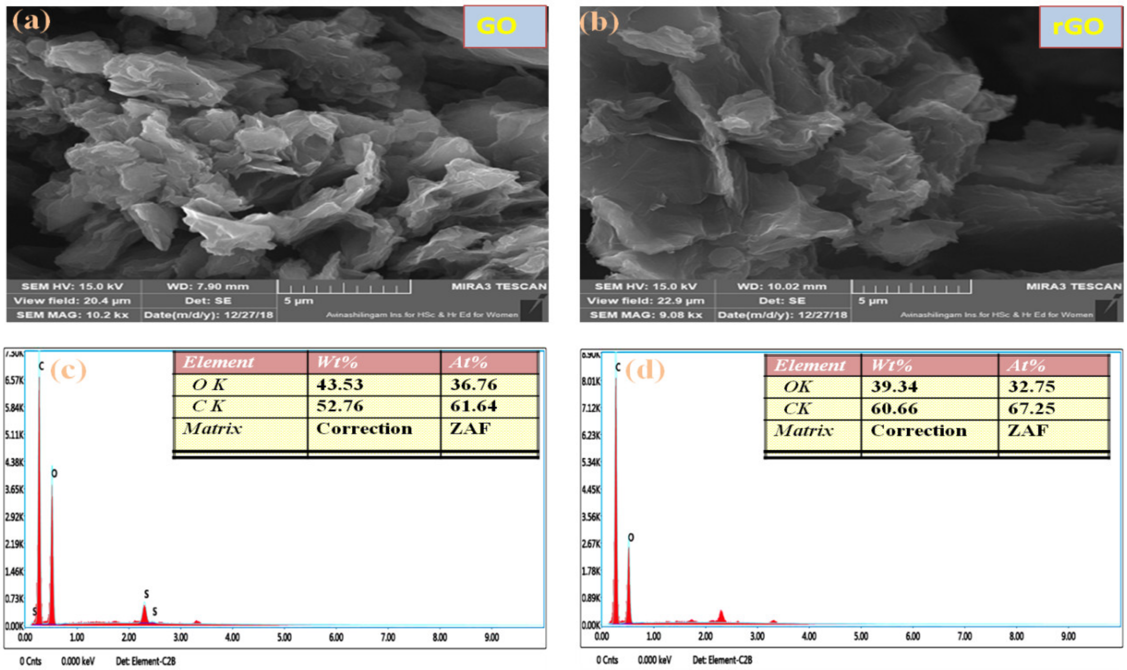

(c)

Element	Wt%	At%
O K	43.53	36.76
C K	52.76	61.64
Matrix	Correction	ZAF

(d)

Element	Wt%	At%
OK	39.34	32.75
CK	60.66	67.25
Matrix	Correction	ZAF

FIG. 2. FESEM surface morphology of GO and rGO nanosheets

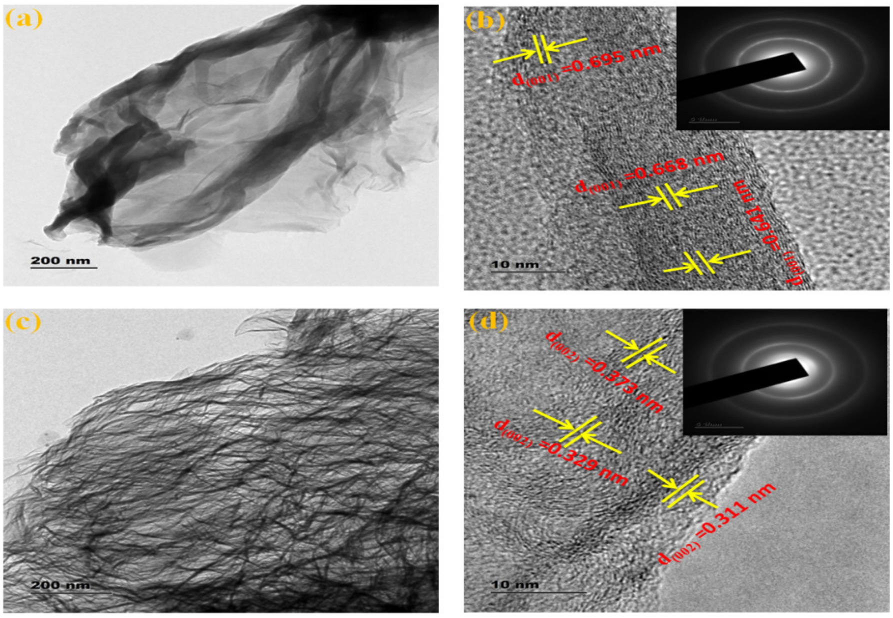

FIG. 3. HRTEM micrographs of GO and rGO nanosheets

shown in Fig. 3(d). The lattice fringes form was correlated with the reports in the plane about (002) as indicated in the d-spacing value. Inset image Fig. 3(d) clearly shows a well standard SAED pattern in two ring shape with a circle in the poly crystalline nature of the rGO [21]. The HRTEM result is in agreement with the XRD result in Fig. 2(d). These results conclude the morphology of the prepared GO/rGO [22].

3.4. Raman spectroscopy

The structure of GO/rGO was studied using Raman spectroscopy. The GO/rGO nanosheets exhibited a series of bands at 143, 493, 625, 687, 847, 1172, 1369, 1617, 1840, 1980, 2234 and 2336 cm^{-1}. All these bands were attributed to the fundamental vibration modes existing in graphene oxides. The reduction of GO and rGO sheets were further confirmed through Raman spectra as shown in Fig. 4. The Raman spectra of GO displays two characteristic Raman bands centered at 1369 and 1617 cm^{-1} were assigned to the well-known D and G bands, respectively [23].

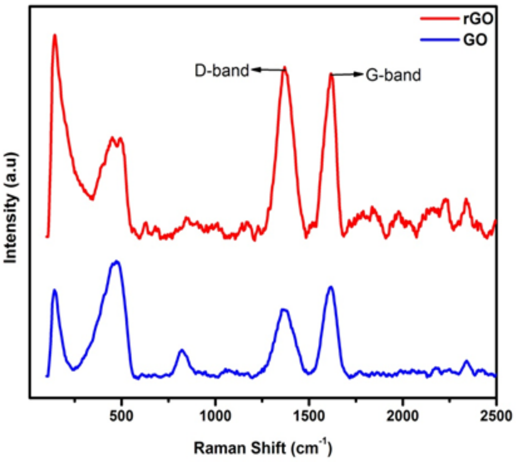

FIG. 4. Raman spectra of GO and rGO nanosheets

The D band ($\sim$ 1369 cm^{-1}) corresponds to disorder in the sp^2 carbon network, and the G band ($\sim$ 1617 cm^{-1}) is associated with the tangential vibrations of the sp^2 carbon atoms in the hexagonal planes. In general, the D band is known as an imperfect band that typically arises from the first order diffusion of sp^3 hybridized carbon atoms, while the G band is mainly reflects from the stretching vibration of sp^2 hybridized C=C bonds. Results show that there is a shift occurring in Raman peaks positions for pure graphene oxide, which confirms the bond formation between graphene layers of rGO. The ID/IG ratio of the D-band to the G-band is related to the disorderliness of the sp^2 domain, owing to the removal of the oxygen functional groups (Fig. 4) [24]. The ID/IG ratios for GO and rGO were found to be 0.750 and 1.030 respectively (Fig. 4).

3.5. FTIR spectrum

The major difference between the GO and rGO depicts the presence of specific functional groups like hydroxyl (–OH), carboxyl(C=O), epoxy (C–O–C) molecules attached to the main graphene layer [25]. These groups show the molecular vibrations of a specific characteristic frequency, when exposed to infrared radiation, as shown by the FTIR study in Fig 5.

The GO shows a sharp peak at 1040cm^{-1} (representing C–O–C), 1713 & 1607 cm^{-1} (corresponding to C=O) and a board peak around 3000 cm^{-1} (attributed to –OH groups) apart from oxygen base plane [26]. These have become less broadened with rGO samples due to the reduction in the concentration of vibrational groups.

3.6. PL Spectrum

The PL spectrum of GO nanosheets are depicted in Fig 6(a). The photoluminescence characterized by a broad peak between 600 – 900 nm was observed and the emission sharp peak was detected in GO at 750 nm. Fig. 6(b) shows PL spectra of rGO.

Three emission peaks was observed at 350, 435 and 524 nm, respectively, that are observed in rGO and it is attributed to the recombination of electron hole pairs in local state of sp^2 carbon cluster embedded in sp^3 matrix [27], in which are clearly known as GO is reduced to become rGO.

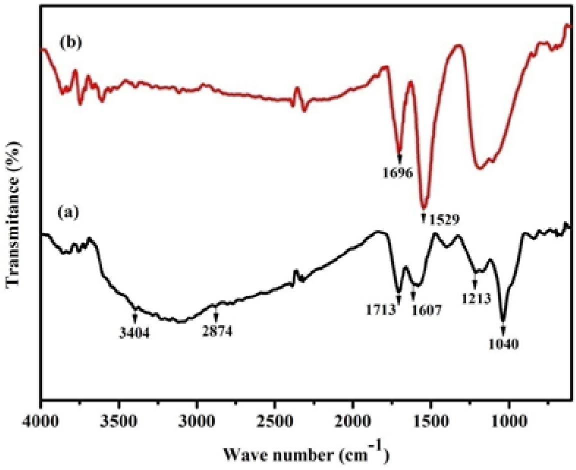

FIG. 5. FTIR spectra of (a) GO and (b) rGO nanosheets

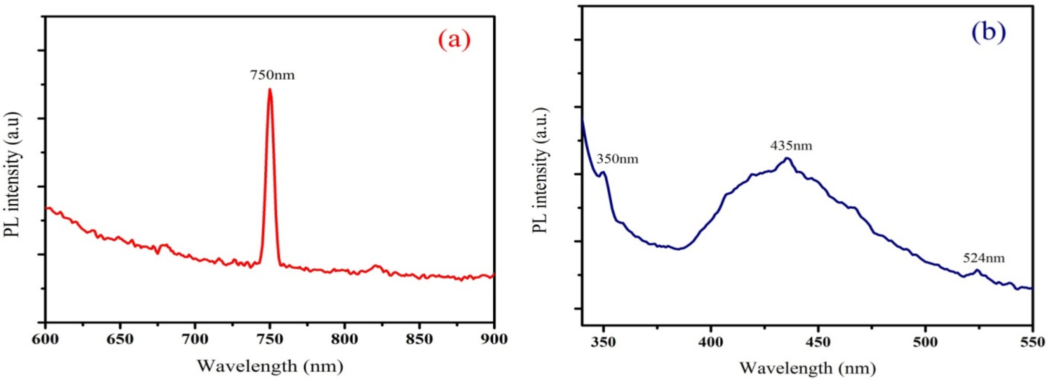

FIG. 6. PL spectrum of (a) GO and (b) rGO nanosheets

4. Conclusions

To summarize, we have successfully synthesized and characterized GO/rGO nanosheets. The crystalline structures of GO/rGO have been determined by XRD measurements. The morphological analysis shown by FESEM exhibits conspicuous wrinkled flakes. HRTEM images studies shows SAED patterns and nanosheets like structure in the plane with (002) orientation. The weight percentage of oxygen was reduced in rGO, as compared to GO which confirms the reduction and the formation of reduced graphene oxide. Raman spectra inferred that D/G value of GO 0.750 ($<$ 1) and rGO 1.030($>$ 1) respectively, which confirms the formation of GO and rGO. Thus, the shallow peaks of rGO observed in FTIR reveals the partial removal of oxygen-linked functional groups from the hexagonal carbon-carbon plane of GO. The PL spectra of GO/rGO peak at 750 and 435 nm shows red and blue shift. Design of hetero-junction photodiode fabrication could be a thought for future amelioration and future scope of this research work. Due to its simplicity, this eco-friendly method of synthesizing rGO paves the way for making enormous rGO supported devices with good characteristics.

References

[1] Anand K., Singh O., et al. Hydrogen sensor based on graphene/ZnO nanocomposite. *Sens. Actuators B*, 2014, *195*, P. 409–415.

[2] Ning G., Fan Z., et al. Gram-scale synthesis of nanomesh graphene with high surface area and its application in supercapacitor electrodes. *Chem. Commun.*, 2011, **47**, P. 5976–5978.

[3] Lee V., Whittaker L., Jaye C., Baroudi K.M. Large-area chemically modified graphene films: Elecrophoretic deposition and characterization by soft X-ray absorption spectroscopy. *Chem. Mater.*, 2009, **21** (16), P. 3905–3916.

[4] Veldevi T., Thileep Kumar K., et al. Synthesis of Hierarchical graphene-MnO_2 nanowire composites with enhanced specific capacitance. *Asian J. Chem.*, 2019, **31** (8), P. 1709–1718.

[5] Mahanandia P., Simon F., Heinrich G., Nanda K.K. An electrochemical method for the synthesis of few layer graphene sheets for high temperature applications. *Chem. Commun.*, 2014, **50** (35), P. 4613–4615.

[6] Zhou Y., Ma L., et al. Mono disperse MnO_2@$NiCo_2O_4$ core/shell nanospheres with highly opened structures as electrode materials for good-performance super capacitors. *Appl. Surf. Sci.*, 2018, **444**, P. 1–9

[7] Sahoo S., Shim J.J. Nanostructured 3D zinc cobaltite/nitrogen-doped reduced graphene oxide composite electrode for supercapacitor applications. *J. Ind. Eng. Chem.*, 2017, **54**, P. 205–217.

[8] Zhou X., Shen X., et al. Hollow Fluffy Co_3O_4 Cages as Efficient Electro active Materials for Super capacitors and Oxygen Evolution Reaction. *ACS Appl. Mater. Interface*, 2015, **7**, P. 20322–20331.

[9] Pawar S.A., Patil D.S., Shin J.C. Hexagonal sheets of Co_3O_4 and Co_3O_4–Ag for high-performance electrochemical super capacitors. *J. Ind. Eng. Chem.*, 2017, **54**, P. 162–173.

[10] Hummers W.S., Offeman R.E. Preparation of Graphitic oxide. *J. Am. Chem. Soc.*, 1958, **80** (6), P. 1339–1339.

[11] Aravind S.S.J., Eswaraiah V., Ramaprabhu S. Facile and simultaneous production of metal/metal oxide dispersed graphene nano composites by solar exfoliation. *J. Mater. Chem.*, 2011, **21**, P. 17094–17097.

[12] Mohandoss M., Gupta S.S., et al. Solar mediated reduction of graphene oxide. *RSC Adv.*, 2017, **7**, P. 957–963.

[13] Thangavel P., Kannan R., et al. Development of reduced graphene oxide (rGO)-isabgol nano composite dressings for enhanced vascularization and accelerated wound healing in normal and diabetic rats. *J. Coll. Inter. Sci.*, 2018, **517**, P. 251–264.

[14] Murugandi G., Saravanan M., et al. Barium borate nanorod decorated reduced graphene oxide for optical power limiting applications. *Opt. Mat.*, 2018, **75** (2018), P. 612–618.

[15] Chakraborty A., Agresti A., et al. Wet-Chemical Synthesis of ZnO Nanowires on Low Temperature Photo-Activated ZnO-rGO Composite Thin Film with Enhanced Photoconduction. *J. Materresbull.*, 2018, **47**, P. 5863–5869.

[16] Meng H., Yang W., et al. Cu_2O nanorods modified by reduced graphene oxide for NH_3 sensing at room temperature. *J. Mater. Chem. A*, 2015, **3**, P. 1174–1181.

[17] Babeela C., Sabari Girisun T.C. Advances on the fabrication process of Er^{3+}/Yb^{3+}: GeO_2–PbO pedestal waveguides for integrated photonics. *Opt. Mater.*, 2015, **49**, P. 190–200.

[18] SabariGirisun T.C., Madura Somayaji R., Priyadarshini N., Venugopal Rao S. Femto third order optical nonlinearity and optical limiting studies of (γ and β) Barium borate nanostructures. *Mater. Res. Bull.*, 2017, **87**, P. 102–108.

[19] Gao G., Wu H.B., et al. Growth of ultrathin $ZnCo_2O_4$ nanosheets on reduced graphene oxide with enhanced lithium storage properties. *Adv. Sci.*, 2015, **2**, 1400014.

[20] Roy M., Kusurkar T.S., et al. Graphene oxide from silk cocoon: a novel magnetic fluorophore for multi-photon imaging. *3Biotech.*, 2014, **4**, P. 67–75.

[21] Sun Z., Yan Z., et al. Growth of graphene from solid carbon sources. *Nature*, 2010, **468**, P. 549–552.

[22] Bo Z., Shuai X., et al. Green preparation of reduced graphene oxide for sensing and energy storage applications. *Sci.ReP.*, 2014, **4**, P. 4684.

[23] Liu H., Xu B., et al. Polyaniline nanofiber/large mesoporous carbon composite as electrode materials for super capacitors. *Appl. Surf. Sc.*, 2015, **332**, P. 40–46.

[24] Fan Z.J., Kai W., et al. Facile synthesis of graphene nanosheers via Fe reduction of exfoliated graphite oxide. *ACS nano*, 2011, **5** (1), P. 191–198.

[25] Sengupta I., Chakraborty S., et al. Thermal reduction of graphene oxide: How temperature influences purity. *J. Mater. Res.*, 2018, **33** (23), P. 4113–4122.

[26] Etacheri V., Yourey J.E., Bartlett B.M. Chemically bonded TiO_2-bronzenanosheet/reduced graphene oxide hybrid for high-power lithium ion batteries. *ACS nano*, 2014, **8** (2), P. 1491–1499.

[27] Zhu Y.W., Murali S., et al. Graphene and graphene oxide: synthesis, properties and applications. *Adv. Mater.*, 2010, **22**, P. 3906–3924.

NANOSYSTEMS: PHYSICS, CHEMISTRY, MATHEMATICS, 2019, 10 (5), P. 585–598

Hydrophobization of up-conversion luminescent films based on nanocellulose/MF$_2$:Ho particles (M = Sr, Ca) by acrylic resin

A. A. Luginina[1], S. V. Kuznetsov[1], V. V. Voronov[1], A. D. Yapryntsev[2], V. K. Ivanov[2], D. I. Petukhov[3], A. A. Lyapin[4], A. S. Ermakov[4], D. V. Pominova[1], E. V. Chernova[1], A. A. Pynenkov[4], K. N. Nishchev[4], P. P. Fedorov[1]

[1]Prokhorov General Physics Institute of the Russian Academy of Sciences, Vavilov str. 38, Moscow, 119991, Russia
[2]Kurnakov Institute of General and Inorganic Chemistry of the Russian Academy of Sciences,
Leninskii prosp. 31, Moscow, 119991, Russia
[3]Lomonosov Moscow State University, Chemical department, Leninskie Gory str. 1, Moscow, 119991, Russia
[4]Ogarev Mordovia State University, Bolshevistskaya str. 68, Saransk, 430005, Russia
ppfedorov@yandex.ru

DOI 10.17586/2220-8054-2019-10-5-585-598

Luminescent hydrophobic composite films based on nanocrystalline (CNC) and nanofibrillated (CNF) cellulose matrix with up-conversion MF$_2$:Ho (M = Ca, Sr) particles and acrylic resin (ACR) as a coating have been synthesized. Flexible, translucent composite films were obtained by molding from the CNC/CNF suspensions with up-conversion particles. ACR coating was applied to the composite film by spraying. Studies have shown that ACR coating with a layer thickness of 7 – 10 μm provides hydrophobic properties for the films, increasing the water contact angle up to $100 \pm 2^\circ$ with a simultaneous improvement in the luminescent properties. Transparency of CNC/CNF/MF$_2$:Ho-ACR films in the visible and near IR region improves by 20 – 25 % without compromising the flexibility and thermal stability. The manufactured water-resistant composite films can be utilized as potential photonics materials, in particular for visualization of near-IR laser radiation and luminescent labels.

Keywords: cellulose nanocrystals, cellulose nanofibrils, nanocomposites, hydrophobicity, acrylic resins, SrF$_2$:Ho, CaF$_2$:Ho, up-conversion luminescence films.

Received: 1 October 2019

Revised: 4 October 2019

1. Introduction

Luminescent composite materials based on a nanocellulose matrix have attracted much attention due to environmental problems [1, 2] and their promising for photonics [3–7], optoelectronics [8–11], and biomedicine [12, 13]. Luminescent nanocomposites with a nanocellulose matrix are light-weight, flexible, thin materials with sufficient mechanical strength. These nanocomposites can be used in a number of practical applications, including: miniature biosensors and chemosensors [12–20], photodetectors [21, 22], organic light-emitting diodes [23, 24], organic solar cells [25], anti-counterfeiting [26] and different photonics devices [27–29].

Cellulose is a widely-spread natural "green" environmentally friendly polysaccharide, which has an amorphous-crystalline structure. Cellulose nanocrystals (CNC) and cellulose nanofibrils (CNF) are synthesized from wood and other plant sources, which have nanoscale transverse sizes and lengths ranging from nanometers to micrometers [30–32]. The preparation and properties of CNF and CNC are described in detail in numerous review articles [33–36]. Nanocellulose is a unique platform for nanocomposites producing due to attractive properties such as renewability, affordability, low density, unique optical properties, excellent mechanical properties, biocompatibility, and biodegradability. The properties of CNC and CNF make them promising for smart photonic devices [7, 37]. Thin CNC films are one-dimensional photonic crystals [38–40]. Like CNC, the CNF can form optically transparent films [41, 42]. One of the most specific nanocellulose characteristics is the presence of three free hydroxyl groups in each monomer unit, which provide a chemically active surface. A large number of hydroxyl groups on the nanocellulose surface is responsible for its inherent hydrophilic nature and possibilities for their modifications [1, 3, 33, 36].

CNF and CNC can serve as a matrix for inorganic phosphors. So Miao et al. developed a simple method for highly-transparent luminescent nanopaper production with high heat resistance by grafting Eu, Sm, Tb lanthanide complexes onto TEMPO-oxidized CNF [43]. Chu with co-authors synthesized chiral nematic CNC luminescent films with YVO$_4$:Eu^{3+} nanoparticles [44]. Yb (III) doped carbon quantum dots (CQD) grafted oxidized nanofibrillated cellulose (Yb^{3+}-CQDs-ONFC) was proposed as novel anti-counterfeiting materials. The CQD serve as a visible emitter and antenna for the Yb^{3+} ions NIR emission sensitizing. As a result, Yb^{3+}-nanopaper fabricated from Yb^{3+}-CQDs grafted ONFC by amide condensation show in eight times higher NIR emission than Yb^{3+}-CQDs in solution with significant aggregation. Further, polystyrene as surface sizing was used to improve the water-resistant property in those nanopapers [45]. Nguyen with co-authors proposed to use nanocellulose as a matrix for up-conversion photonic films production with chiral nematic ordering containing $NaYF_4$: Yb,Er hexagonal nanorods [46]. Films have a low resistance to water due to the hydrophilic nature of the cellulose. The hydrophilic nature limits their using as luminescent composite materials based on CNF and CNC. Increase of hydrophobicity by surface modification is very attractive for manufacture of luminescent composite materials based on a nanocellulose matrix. The purpose of the modification is to change only the surface of the nanocellulose with preservation of the initial morphology of the nanocomposite material and the complex structure of internal hydroxyl groups.

This paper is devoted to the studies of hydrophobic composite luminescent nanocellulose films with up-conversion particles based on calcium and strontium fluorides doped with holmium for identify the hydrophobic agent influence on the change in the optical and luminescent properties of nanocomposite films.

2. Experimental section

2.1. Chemicals

Powdered bleached woodkraft cellulose (PCC-0.25 (PC) from Polycell, Vladimir, Russia), filter paper “Blue Ribbon” (FP), 98 % sulfuric acid, 18 % hydrochloric acid, double distilled water, acrylic varnish (KUDOKU-9002 from Elf Filling, Electrougli, Russia), regenerated cellulose dialysis tubing with 12 – 14 kDa molecular weight cut-off from Orange Scientific (Graignette Business Park, Braine-l’Alleud, Belgium), up-conversion $Ca_{0.92}Ho_{0.08}F_{2.08}$ and $Sr_{1-x}Ho_xF_{2+x}$ ($x = 0.08$, and 0.10) powders, which prepared by our proposed technique [47, 48] were used as starting materials.

2.2. Preparation techniques of cellulose nanocrystals and nanofibrills, and nanocellulose films

Initial PC cellulose samples were mixed with double distilled water (cellulose: H_2O = 1:10 g/g) in a beaker. The prepared suspension was placed in an ice bath. Concentrated sulfuric acid (cellulose: H_2SO_4 = 1:25 g/g) was added drop-wise to the cellulose suspensions under vigorous stirring until acid concentration reached about 65 wt%. The resulting suspension was placed in a water bath at 47 °C for 60 min under 350 rpm stirring. Hydrolysis was terminated by addition of 10-fold excess of cold double distilled water. The hydrolyzed suspension was washed with double distilled water and repeatedly centrifuged (Eppendorf 5804 centrifuge, 8000 rpm, 10 min). The supernatant was separated from the precipitate and then a new portion of water was added. After 4 – 5 centrifugation cycles, washing procedure was terminated at pH = 5. The resulting cellulose gel was dispersed in double distilled water and then placed into a dialysis bag and dialyzed for 7 days. After dialysis, the dispersion was sonicated for 15 min (UZG13-01/22 sonicator, 110 W, VNIITVCH) in an ice bath. The yield of CNC was about 30 %. The CNC content in the dispersion was determined gravimetrically. CNF was obtained by hydrolysis of FP with hydrochloric acid with followed by ultrasonic treatment. FP was preliminarily shredded into small pieces (2 × 2 mm). The aqueous suspension was prepared at FP:H_2O = 1:10 g/g. Hydrochloric acid (FP:HCl = 1:13 g/g) was added drop-wise to the suspension under vigorous stirring at 80 °C for 20 min. The hydrolysis was terminated by adding a large amount of cold double distilled water (10 times the volume of the suspension). Further, the suspension was washed with double distilled water and repeatedly centrifuged (10 min at 8000 rpm, an Eppendorf 5804 centrifuge). The supernatant was separated from the precipitate and then a new portion of water was added. After 4 – 5 centrifugation cycles, washing was terminated at pH 4.5 – 5.0. The resulting cellulose gel was dispersed in double distilled water and sonicated in an ice bath for 15 min, then placed into a dialysis bag and dialyzed for 7 days. After dialysis, the suspension was sonicated according to the above-mentioned procedure. pH value was reached 5.5. The yield of CNF was about 50 %. The CNF content in the dispersion was determined gravimetrically.The resulting CNC and CNF dispersions were stored in a refrigerator at a temperature < 5 °C.

The nanocellulose films were prepared by solution casting technique of CNC, CNF dispersion with concentration less 3 wt.% in polystyrene Petri dishes with followed drying at ambient temperature for 2 – 3 days. The film thickness was about 25 – 35 μm.

2.3. Preparation of nanocomposites films

$Ca_{0.92}Ho_{0.08}F_{2.08}$ and $Sr_{1-x}Ho_xF_{2+x}$ ($x = 0.08$ and 0.10) powders annealed at 750 °C were carefully ground in an agate mortar. The ground powders were dispersed in CNC or CNF colloidal solutions by sonication on an ice bath for 15 min. The colloidal suspensions were poured into polystyrene Petri dishes and dried under ambient conditions for 2 – 3 days. The air-dried composite films were further dried at 90 °C for 40 min to remove residual moisture, so that hydration would not affect the products’ morphology, physical and luminescent characteristics. The film thickness was about 25 – 45 μm. The nanocellulose content in the dried films varied from 45 to 90 wt%, while the Ho content in the dried films ranged from 1.00 to 6.71 wt% for SrF_2:Ho samples and from 2 to 8 wt.% for CaF_2: Ho samples. The composite films were designated as CNC:xHo, CNF:xHo, CNC/CNF:xHo, where x = Ho wt%.

2.4. Surface modification of nanocomposite films by acrylic resin

The hydrophobicity was reached by the simple procedure for applying a double-sided coating of KUDOKU-9002 acrylic varnish, which includes modified acrylic resin (ACR). Procedure consists of acrylic resin spraying from a balloon from 25 – 30 cm distance onto suspended composite films CNC:xHo, CNF:xHo, CNC/CNF:xHo. One to three thin layers were applied to each side of the film. The drying time between layers spraying was 5 – 10 minutes, then the next layer was applied. Dry to stick 20 – 30 minutes, but complete drying in air for 2 hours. The film thickness varied in the range of 45 – 75 μm, the thickness of the ACR layer was from 2.5 to 16 μm on each side. Designation of CNC composite films were CNC:xHo-zACR, CNF:xHo-zACR, CNC/CNF:xHo-zACR, where z is the number of layers deposited, from 1 to 3.

2.5. Characterization techniques and equipments

X-ray diffraction analysis was carried out on a Bruker D8 Advance diffractometer (Bruker AXS GmbH, Karlsruhe, Germany) using CuKα-radiation in the range 8 – 60 2θ with 0.02 2θ step. The diffraction peak at 22.7 2θ was used for crystallinity index (IC, %) calculation by Segal's method according to Eq. (1):

$$IC = \frac{I_{200} - I_{AM}}{I_{200}} \times 100, \tag{1}$$

where, I_{200} is the intensity of the $\langle 200 \rangle$ reflex at 22.70 2θ. I_{200} consist of both crystalline and amorphous phases. I_{AM} is the intensity at the minimum between the $\langle 200 \rangle$ and $\langle 110 \rangle$ peaks at 18.00 2θ.

The nanoparticle size distribution in aqueous dispersions was determined by dynamic light scattering (DLS) using a Photocor Complex DLS spectrometer equipped with He–Ne laser. The CNC and CNF dispersions were preliminarily diluted up to 0.01 wt% concentration and then sonicated for 5 min in an ice bath.

The degree of polymerization (DP) was measured by the viscosity method using diluted solutions of dry cellulose particles in Cadoxen (cadmium ethylenediamine) [49]. The polymerization degree was determined as the average of two independed measurements. The relative error was 4 % at $p = 0.95$.

Film thickness was measured using a micrometer (MKTS-25 0.001, Kalibron, Russia) at seven randomly selected locations on each film, and mean value was reported for each replication.

Water absorption test carried out for ACR film and without ACR layer nanocomposite films without ACR coatings were dried at 90 °C for 40 min and immersed in distilled water for 2 min. ACR coated nanocomposite films were immersed in distilled water for 2 min without drying. After immersed in doubly-distilled water, the samples were wet with FP to carefully remove excess water from the surface and weighed. Water adsorption % (WA) was calculated by the formula:

$$WA = \frac{W_{wet} - W_{dry}}{W_{dry}} \times 100, \tag{2}$$

where W_{dry} is the weight of the dried sample, W_{wet} is the weight of the wet sample after soaked in water for 2 min.

The microstructure of the particles in films was analyzed by scanning electron microscopy (SEM) using a NVision 40 microscope (Carl Zeiss NTS GmbH, Oberkochen, Germany) with simultaneous energy-dispersive spectroscopy (EDX) (X-Max detector, Oxford Instruments, Abingdon, UK).

Fourier transform infrared spectroscopy (FTIR) with ATR unit (Pike) was performed on a INFRALUM FT-08 spectrometer from 400 to 4000 cm^{-1}. The transmission spectra were recorded using a Cary 5000 spectrophotometer in the 250 –3000 nm range.

Thermal gravimetric analysis (TG) was performed from 25 to 800 °C with a 5 °C/min heating rate in air on the Netzsch TG 209 F1 Libra.

The contact angle was measured using the FTA1000 Drop Shape Instrument B Frame System. The test sample was placed on a horizontal holder. The water was applied to the surface of the test sample by a special microdosing syringe. The droplet volume was 100 μl. The image was recorded using a CCD detector of 640 × 480 pixels. Images were obtained 1 s after application of the droplets. The measurements were carried out at room temperature (24 ± 2 °C) and repeated 5 times on various fresh surfaces.

The up-conversion luminescence spectra were recorded with a Horiba FHR 1000 spectrophotometer with OL IS-670-LED integrating sphere (Gooch & Housego). A continuous solid-state LiYF$_4$:Tm laser was used as the excitation source for Ho^{3+} ions at 1912 nm. The beam diameter of incident laser radiation was 300 μm. The incident excitation power was 960 mW.

3. Results and discussion

3.1. Characterization of a hydrophobic agent (ACR)

Acrylic universal gloss varnish KU-9002 was chosen as a hydrophobic agent. It contains xylene, methyl acetate, butanol, propanol, and modified acrylic resin (ACR). ACR is ethylhexyl acrylate, methyl methacrylate and styrene copolymer. The varnish is transparent, colorless and insoluble in water. KU-9002 designed to create a protective coating for metal, wood, and plastic products. It allows the masking of surface defects without yellowing and provides resistance to mechanical stress and abrasion. ACR has excellent surface adhesion and high environmental resistance [50]. Hardening takes place quickly at room temperature. The first drying came unstuck is 20 – 30 minutes but complete drying in the air for 2 hours. ACR contains esters of acrylic and methacrylic acids, as well as a phenyl group. The phenyl group ACR can improve the water-resistance of the film after drying [51]. Negatively polarized oxygen atoms of the ACR ester group are able to form hydrogen bonds [52]. Hydrogen bonds with the hydroxyl groups of nanocellulose improve the bonding between the nanocellulose film and the ACR. It ensures the uniformity of the ACR film on the surface of the nanocellulose. Intra- and intermolecular hydrogen bonds play a decisive role in the formation of supramolecular structures that affect on the nanocellulose properties. As a result, cellulose chains are assembled into highly ordered structures [4]. A possible mechanism for the interaction of a nanocellulose film and ACR in composite materials is shown in Fig. 1.

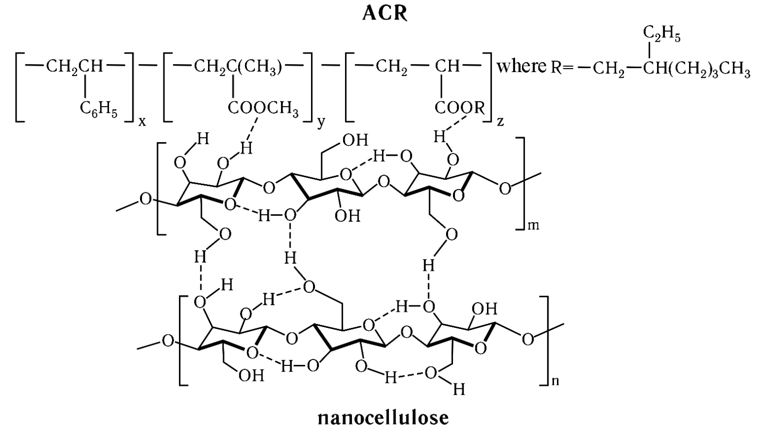

FIG. 1. Scheme of inter-surface hydrogen bonds between hydroxyl groups of nanocellulose and oxygen atoms of the ester group of ACR (ethylhexyl acrylate, methyl methacrylate and styrene copolymer)

3.2. Characterization of dispersions, nanocellulose films, and nanocomposite films CaF_2:Ho and SrF_2:Ho with up-conversion particles

The 1.55 – 2.50 wt.% CNC aqueous dispersions are transparent and stable colloidal solutions of nanocrystalline cellulose, which staying without coagulation during for more than four months. The stability of CNC dispersions is explained by the presence of negatively charged sulfate groups on the surface of the CNC and an increase in the surface charge of CNC particles. It leads to a more stable CNC dispersion due to electrostatic repulsion between sulfate groups. The presence of sulfur in CNC samples (0.71 wt.%) confirmed by EDX analysis (Table 1) as a result of esterification of cellulose hydroxyl groups by sulfate ions.

Aqueous CNF dispersions with a concentration of 0.94 – 2.07 wt.% with milky hue are stable for a month. After one month of aging, the dispersion begins to stratify. Mixed aqueous dispersions of CNC/CNF with a concentration of 1.24 – 2.28 wt.% are transparent and stable colloidal solutions without coagulation for three months.

The hydrodynamic particle radii for CNC and CNF dispersion show a polydisperse particle distribution. CNC and CNF form whiskers and nanofibrils, respectively. Most particles are 10 – 30 nm and 90 – 170 nm sizes, but a small portion are aggregated CNCs. As a result of hydrolysis, the CNC particle sizes are reduced one thousand-fold compared to the initial PC. CNF is characterized by the presence of three groups of particles corresponding to sizes 22 – 32 nm, 90 – 180 nm, and 500 – 1800 nm.

Samples for SEM analysis were prepared by applying a drop of 0.01 wt.% dilute aqueous dispersions nanocellulose on the single-crystal silicon substrate with followed by drying in air. The properties of the initial cellulose (PC and FP) are shown in Table 2. Rod-like particles with a width of about 15 – 25 nm and length of about 100 – 200 nm,

TABLE 1. EDX analysis of nanocellulose

Elements	at. %		wt. %	
	CNC	CNF	CNC	CNF
C	53.8 ± 0.2	56.2 ± 0.1	46.5	49.1
O	45.8 ± 0.2	43.8 ± 0.1	52.8	50.9
S	0.3 ± 0.1	—	0.7	—

as well as aggregates are determined on SEM images for CNC samples (Fig. 2(a)). Cellulose nanofibrils with a width of 20 – 35 nm and length of 200 – 1800 nm with a large aspect ratio (ratio of length to smallest transverse size) of 20 – 60 are determined on SEM images for CNF films (Fig. 2(b)), which confirms the production of nanofibrillated cellulose. Nanocellulose prepared from a mixed dispersion of CNC/CNF = 1/1 present on Fig. 2(c,d). Entangled CNF fibrils form a porous network with CNC evenly distributed inside the CNF.

TABLE 2. Properties of the initial and synthesized nanocellulose

Sample	Particle size (SEM), nm		Cellulose Type Structure	IC, %	DP	Decomposition temperature
	diameter	length				T_{onset}/T_{endset}, °C
PC	25 – 50 *	230 – 500 *	Iß	69.2	930	300/491
FP	25 – 50 *	200 – 1500 *	Iß	68.7	1112	300/486
CNC	15 – 25	100 – 200	Iß	86.2	105	157/567
CNF	22 – 35	200 – 1800	Iß	70.3	154	196/591
CNC/CNF	15 – 35	100 – 1800	Iß	71.6	147	186/567

* Particle sizes of PC and FP are expressed in microns [53].

Particle sizes determined using SEM are consistent with DLS results.

CNC and CNF showed different behaviors during the film formation process due to the different shapes and lengths. CNCs tend to form the ordered structure, which associated with the self-assembly of CNC during slow drying. CNC forms transparent but fragile films. At 0.94 wt.% CNF dispersion, the flexible but wrinkled film with a milky tint is formed with porous network. The non-transparent film is formed at 2.07 wt.% dispersion concentration. In our earlier study of nanocellulose films was shown [53], that a transparent and flexible film was synthesized from CNC/CNF = 1/1 mixed dispersions.

Changes in the supramolecular structure of cellulose during hydrolysis are characterized by X-ray diffraction of cast films, but the monoclinic crystal structure of $I\beta$ cellulose is preserved for all nanocellulose films (Fig. 3).

X-ray diffraction patterns of the CNC (Fig. 3(a)) samples revealed the $I\beta$ crystal structure [54]. The CNC samples are characterized by a significant increase in the crystallinity index compared to the initial cellulose (Table 2) due to optimized acid hydrolysis process. A smaller increase in IC for CNF is observed due to the partial destruction of the amorphous regions of cellulose (Table 2).

The degree of polymerization for cellulose materials after hydrolysis is significantly reduced, namely by 8-fold for CNC. Moreover, CNC has a degree of polymerization about 1.3-fold less than CNF.

The thermal degradation of the initial cellulose (PC and FB) and nanocellulose (CNC and CNF) showed obvious differences (Table 2) [53]. Degradation onset temperature (T_{onset}) in comparison to the initial cellulose was decreased by 100 and 140 °C for CNF and CNC, respectively. The decrease in thermal stability of CNC and CNF compared to the initial cellulose is probably associated with an increase of heat transfer rate due to an increase in surface area of smaller particle sizes. Also, it‘s probably due to the introduction of sulfate groups during acid hydrolysis. The lower temperatures of the T_{onset} (157 °C) for CNC compared to CNF/CNC (186 °C) are due to the higher content of sulfate

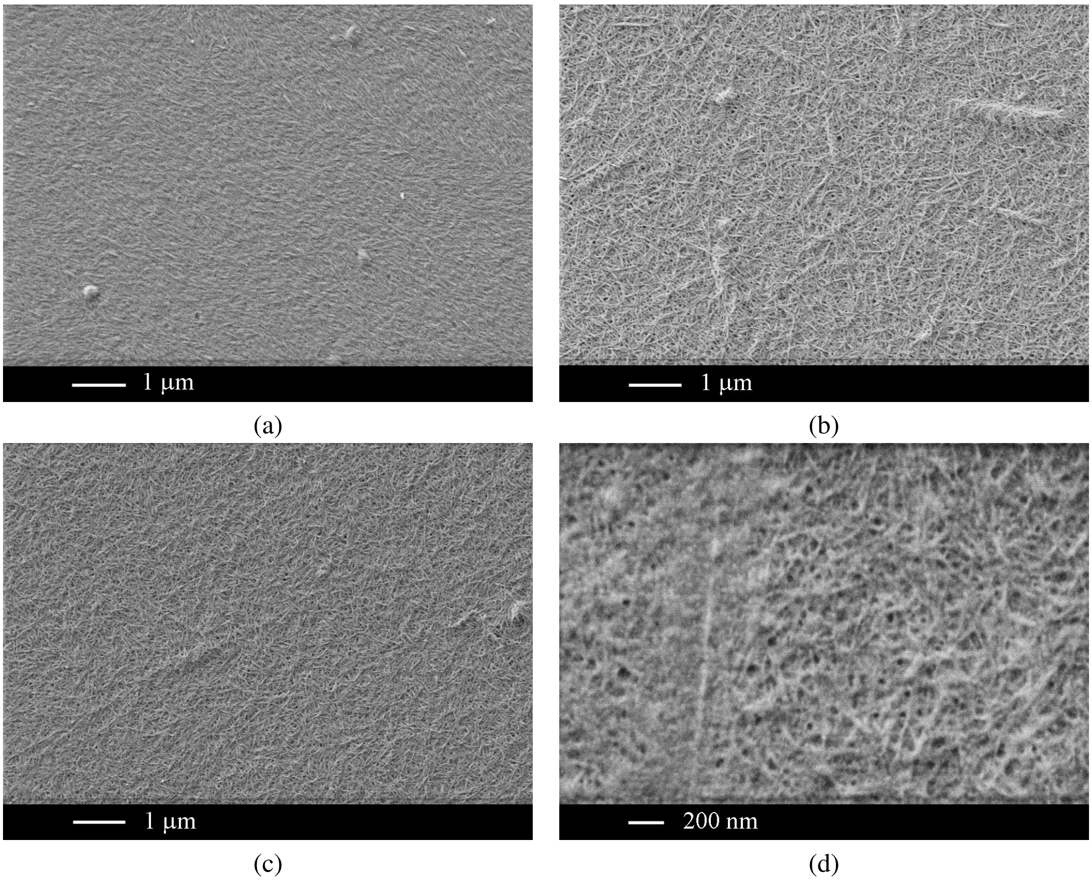

FIG. 2. SEM images of CNC and CNF: (a) CNC; (b) CNF; (c), (d) CNC/CNF

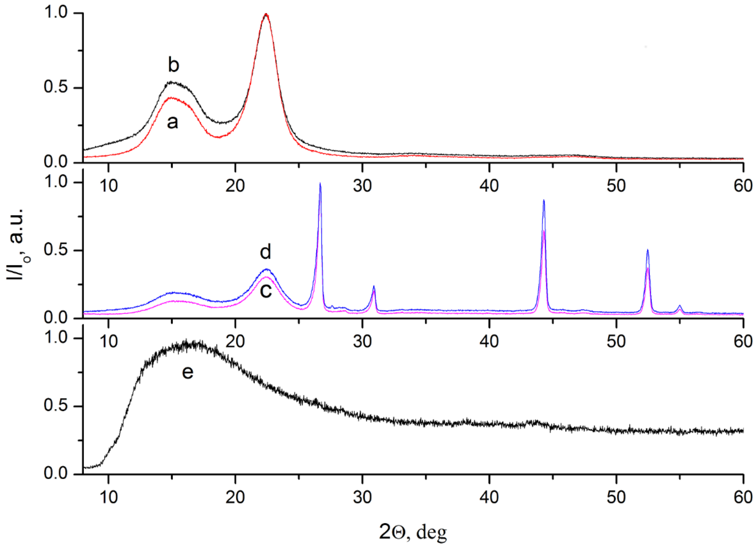

FIG. 3. X-ray pattern diffractions (a) CNC; (b) CNC-2ACR; (c) CNC: 5.5 Ho; (d) CNC: 5.5 Ho-1ACR; (e) ACR

groups in them, which is confirmed by EDX data. The total mass loss for all samples during thermal decomposition in the air is 100 %.

Finally, the morphology, particle size, the ratio of geometric parameters (sides), the degree of polymerization and the degree of crystallinity of nanocellulose are determined by preparation technique. Various mechanisms for the formation of CNC, CNF films affect their optical, thermal and mechanical properties.

Mixing CNC or CNC/CNF with $Ca_{0.92}Ho_{0.08}F_{2.08}$ particles, or $Sr_{0.92}Ho_{0.08}F_{2.08}$, or $Sr_{0.90}Ho_{0.10}F_{2.10}$ particles with the subsequent ultrasonic treatment result in good distribution of the filler in the nanocellulose matrix. The resulting dispersion is transparent and stable during the day with 0.28 – 1.57 wt.% content of up-conversion powders.

The X-ray diffraction pattern of the CNC: 5.5Ho (45.4 wt% $Sr_{0.90}Ho_{0.10}F_{2.10}$) composite film exhibit diffraction peaks characteristic of cellulose $I\beta$ and the crystalline fluorite phase $Sr_{0.90}Ho_{0.10}F_{2.10}$ with unit cell parameter $a = 5.7778(1)$ Å (Fig. 3(c)).

It means that the crystalline structure of cellulose does not change after dispersion since the positions of all reflexes are preserved but their intensity changes.

The thermal destruction of CNC: 4.4Ho composite film (36.4 wt.% $Sr_{0.90}Ho_{0.10}F_{2.10}$) begins in the air at 157 °C (Fig. 4(b)). The latter does not differ from the decomposition temperature of CNC film (Table 2). According to TG, the residue after heating up to 800 °C is 36.4 wt.%, which corresponds to the content of up-conversion powder in the composite film.

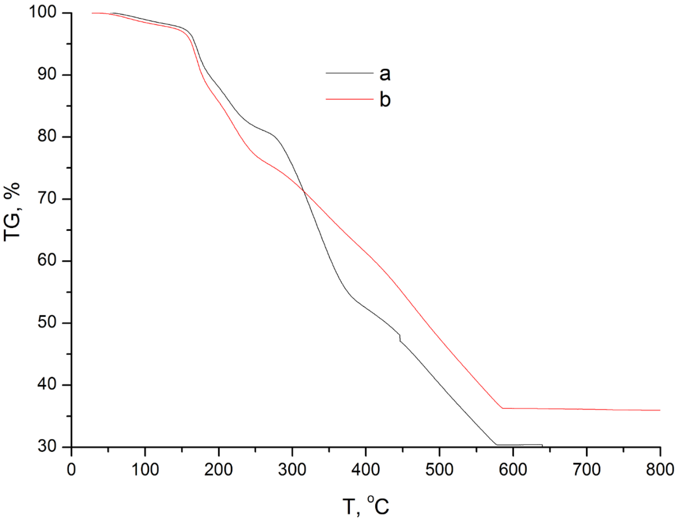

FIG. 4. TG measurements in the air at a heating rate of 5 °/min for films: (a) CNC: 4.4 Ho-1ACR; (b) CNC: 4.4 Ho

Scanning electron microscopy images of the surface and cleavage of composite films CNC/CNF: 4.6Ho (37.7 wt.% $Sr_{0.90}Ho_{0.10}F_{2.10}$) and CNC: 5.1Ho (34.8 wt.% $Ca_{0.92}Ho_{0.08}F_{2.08}$) analyzed in topographic contrast (Fig. 5(a, c, e, g)) and in the Z contrast (Fig. 5(b, d, f, h)).

CNC/CNF: 4.6Ho and CNC: 5.1Ho composite films have a uniform morphology and contain uniformly distributed up-conversion particles over the entire surface and volume (Fig. 5(c, d, f, h)). The SrF_2:Ho and CaF_2:Ho particle size varies between 50 – 200 nm. EDX analysis confirmed that the measured atomic ratio of Sr/Ho and Ca/Ho elements in composites is very close to that measured in $Sr_{0.90}Ho_{0.10}F_{2.10}$ and $Ca_{0.92}Ho_{0.08}F_{2.08}$ powders. Thus, the use of CNC or mixed CNC/CNF dispersions (1:1) allows to composite films producing with a uniform distribution of up-conversion particles without losses and changing of the crystal structure.

The thickness of composite films depends on the concentration and volume of CNC and CNC/CNF dispersions, as well as on the content of up-conversion particles in them. The optimal concentration of nanocellulose dispersions is 1.8 – 2.2 wt.% with the 0.9 – 1.3 wt.% content of up-conversion particles for preparation of composite films with a thickness of 35 – 50 μm. Such concentrations ensure the stability of the dispersions and the drying of the film in during two days.

3.3. Effect of ACR coating on the thermal, structural, optical, and luminescent properties of composite films

The thermal stability of a CNC: 4.4Ho-1ACR composite ACR coated films do not change in comparison to uncoated film (Fig. 4(a)). An increase in losses during annealing by 6.3 % in comparison to CNC: 4.4Ho film is

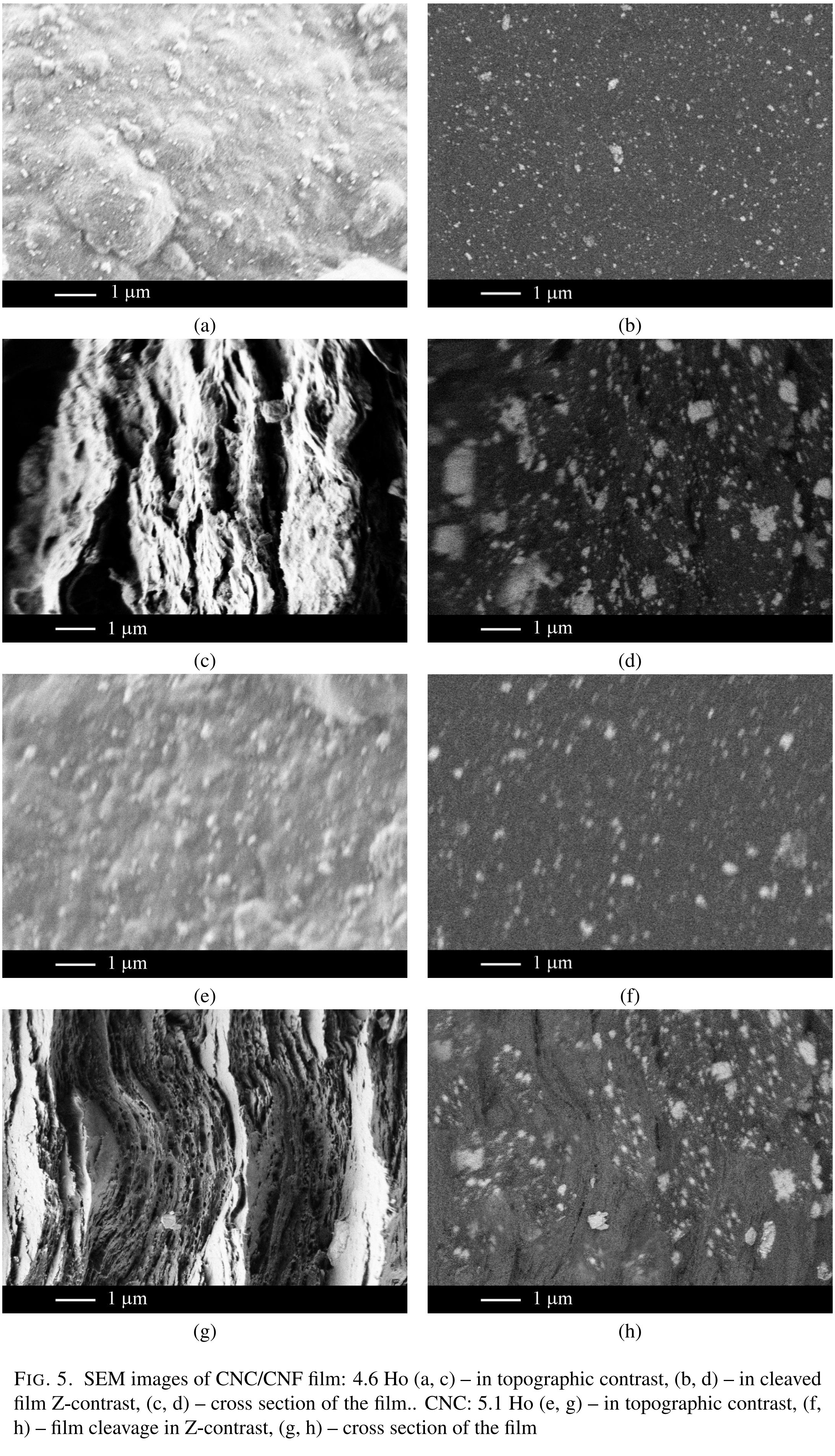

FIG. 5. SEM images of CNC/CNF film: 4.6 Ho (a, c) – in topographic contrast, (b, d) – in cleaved film Z-contrast, (c, d) – cross section of the film.. CNC: 5.1 Ho (e, g) – in topographic contrast, (f, h) – film cleavage in Z-contrast, (g, h) – cross section of the film

associated with the burnout of the ACR coating. It was found that the crystalline structure of nanocellulose does not change after applying the ACR coating since the positions of all reflections are preserved but intensity changes (Fig. 3(b,d)). An increase of the amorphous halo intensity is also noted, which can be explained by the amorphous nature of ACR coating. The X-ray diffraction pattern of the ACR film does not have clear reflections (Fig. 3(e)).

The IR spectrum of CNC films contains absorption bands about 2900 cm^{-1} (stretching modes of the CH and CH$_2$ groups), about 1430 cm^{-1} (symmetric deformation vibrations of the CH$_2$ group), 1000 – 1200 cm^{-1} (stretching vibrations of C–O–C and C–O bonds in the pyranose ring) (Fig. 6(a)). The CNC spectrum has a weak band at 1203 cm^{-1} (S = O), which confirms the introduction of a sulfate group into the cellulose structure during acid hydrolysis [55].

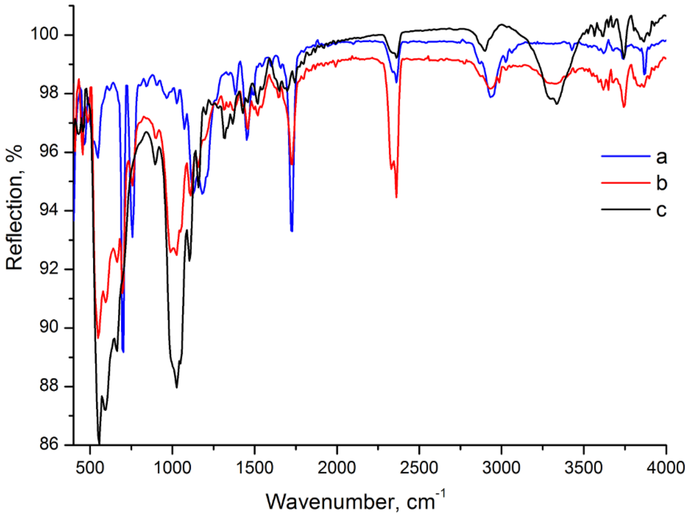

FIG. 6. IR spectra of (a) ACR, CNC-ACR (b), and (c) CNC films

The spectrum for CNC is characterized by a wide absorption band in the region 3284 – 3335 cm^{-1} (stretching modes of hydroxyl groups included in the hydrogen bond). In the IR spectrum of the ACR film, wide bands at 2868, 2933 and 2951 cm^{-1} are caused by aliphatic regions (C–H), such as CH$_2$ and CH$_3$ (Fig. 6(a)). Absorption spectrum contains band at 1725 cm^{-1} (stretching vibrations of the C=O ester group), at 1128 and 1183 cm^{-1} (stretching vibrations of C–O groups), and at 1452 and 1340 cm^{-1} (symmetric and asymmetric stretching vibrations of C–CH$_3$). The absorption band at 698 and 756 cm^{-1} are associated with the out-of-plane transverse vibrations of the phenyl ring and out-of-plane peak CH, respectively [56]. The shape of the complicated peak at 3273 – 3356 cm^{-1} for the CNC-ACR film becomes wider and shifts along compared to pure CNC. It can be explained by the formation of intersurface hydrogen bonds between CNC hydroxyl groups and oxygen atoms in ACR ester group. It confirmed by the shift of the bands of C–O groups to 1108 and 1157 cm^{-1} (Fig. 6).

A comparison of the transmittance spectra of the same composition films with ACR coating (Fig. 7(a, c, d)) and without coating (Fig. 7(b, e, f)) confirms that the transparency of films with ACR coating significantly (by 20 – 25 %) improves in the visible and near IR spectral regions.

Comparison of the SEM images of the CNC: 5.1Ho (34.8 wt.% Ca$_{0.92}$Ho$_{0.08}$F$_{2.08}$) surface without coating (Fig. 8(a)) and with ACR coating shows that the coating of the transparent acrylic resin provides good surface smoothness. ACR fills all of the irregularities of the composite films (Fig. 8(b)), which resulted in increase in the transparency of composite films with ACR coating. However, the uniformity of the coating depended on the thickness of the ACR layer. The triple-layer coating resulted in cracks on the film (Figs. 8(c, d)), which did not affect on the optical transmission but reduced the water-resistance of the films (Table 3).

Films of CNC/CNF: 4.6Ho (37.7 wt.% Sr$_{0.90}$Ho$_{0.10}$F$_{2.10}$) (Fig. 9(a)) and CNC/CNF: 4.6Ho-2ACR (Fig. 9(b)) are flexible, uniform, and wrinkle-free. The film without ACR is translucent, while the film with ACR is almost transparent.

The luminescence intensity of composite films with ACR coating (CNC/CNF: 8.4Ho-2ACR, CNC/CNF: 6.8Ho-2ACR) is higher than films without ACR coating (CNC/CNF: 8.4Ho (57.5 wt.% Ca$_{0.92}$Ho$_{0.08}$F$_{2.08}$), CNC/CNF: 6.8Ho (55.8 wt% Sr$_{0.90}$Ho$_{0.10}$F$_{2.10}$) with the same amount of holmium (Fig. 10). The ACR coating protects the nanocomposite film from atmospheric moisture and prevents luminescence quenching.

Finally, it was determined that the ACR coating improves the optical transmission and luminescent properties of up-conversion nanocomposite films based on nanocellulose.

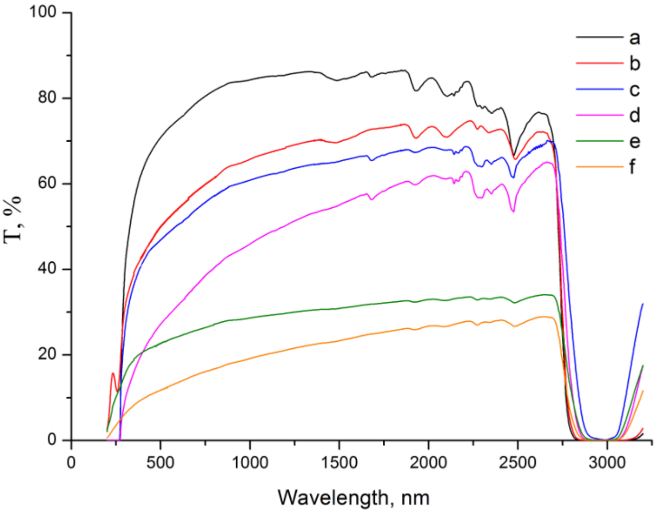

FIG. 7. Transmission spectra of films: a) CNC/CNF-2ACR; (b) CNC/CNF; (c) CNC: 5.4 Ho-2ACR; (d) CNC/CNF: 6.8 Ho-2ACR; (e) CNC: 5.4 Ho (54.5 wt.% $Sr_{0.92}Ho_{0.08}F_{2.08}$); (f) CNC/CNF: 6.8 Ho (55.8 wt.% $Sr_{0.90}Ho_{0.10}F_{2.10}$)

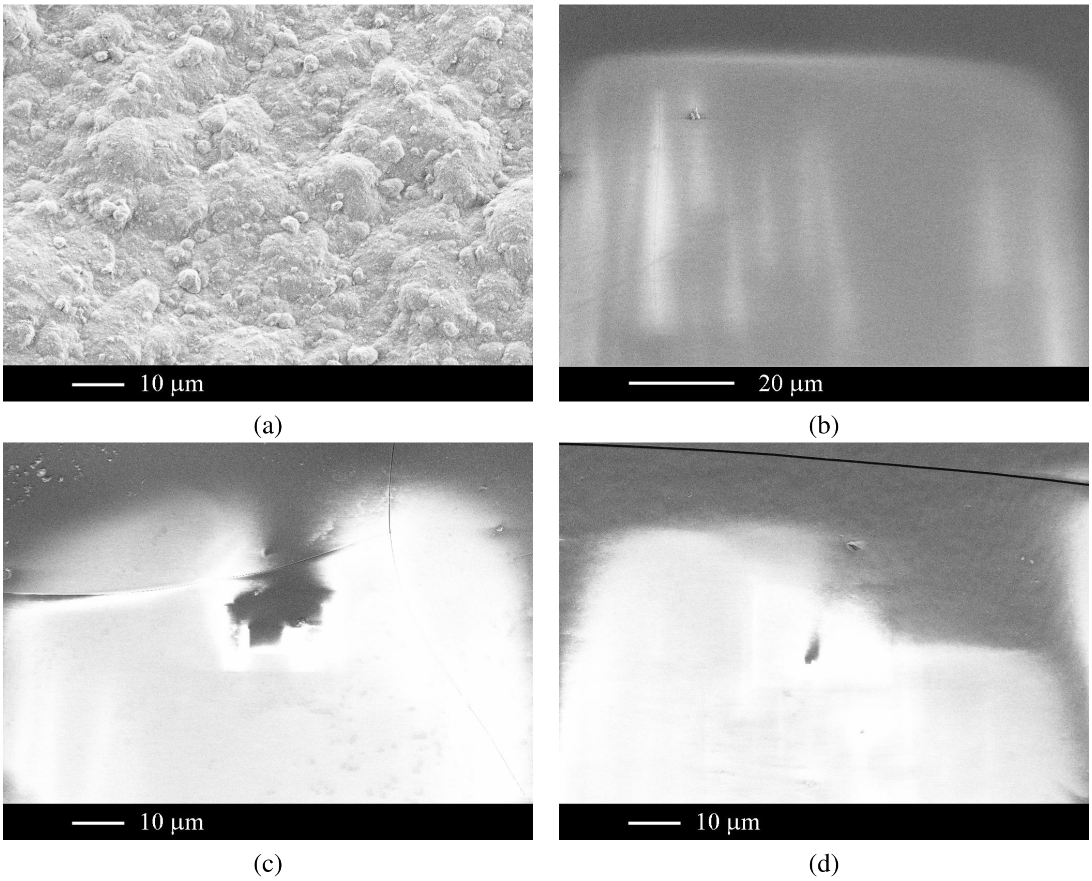

(a) (b)

(c) (d)

FIG. 8. SEM images of film surface: (a) CNC: 5.1 Ho; (b) CNC: 5.1 Ho-2ACR; (C, d) CNC: 5.1 Ho-3ACR

TABLE 3. Wetting angle and water adsorption of nanocomposite films with different number of applied acrylic resin layers

Film composition	Film thickness, μm	ACR, wt.%	WA, wt.%	Wetting angle
CNC/CNF: 4.6 Ho (37.7 wt.% $Sr_{0.90}Ho_{0.10}F_{2.10}$)	50 ± 2	—	46.8	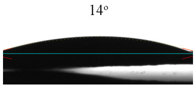
CNC/CNF: 4.6 Ho-1ACR (37.7 wt.% $Sr_{0.90}Ho_{0.10}F_{2.10}$)	59 ± 2	9.8	0	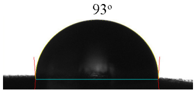
CNC: 5.1 Ho (57.5 wt.% $C_{0.92}Ho_{0.08}F_{2.08}$)	42 ± 2	—	53.0	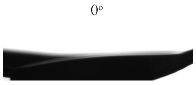
CNC: 5.1 Ho-2ACR (57.5 wt.% $C_{0.92}Ho_{0.08}F_{2.08}$)	58 ± 2	21.5	0	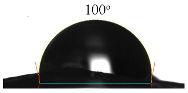
CNC: 5.1 Ho (57.5 wt.% $C_{0.92}Ho_{0.08}F_{2.08}$)	35 ± 2	—	53.3	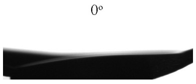
CNC: 5.1 Ho-3ACR (57.5 wt.% $C_{0.92}Ho_{0.08}F_{2.08}$)	65 ± 2	48.3	6.1	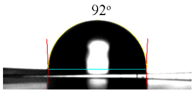

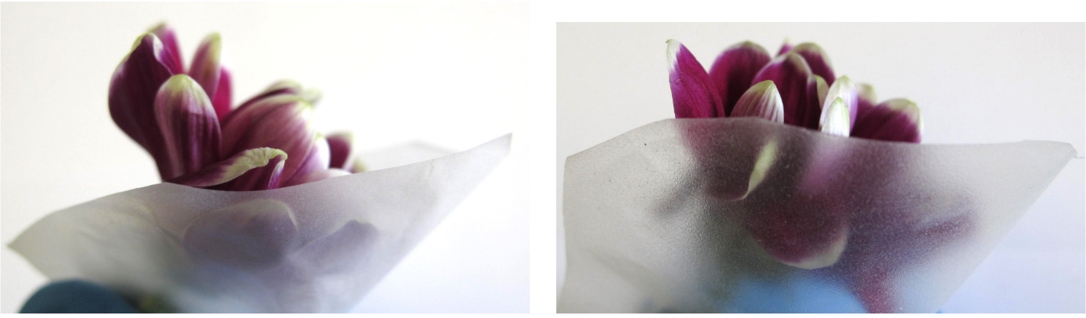
(a) (b)

FIG. 9. Film photos: (a) CNC/CNF: 4.6 Ho; (b) CNC/CNF: 4.6 Ho-2ACR

3.4. Effect of ACR coating thickness on the hydrophobic properties of composite films

The cleaved composite films with a different number of ACR coating layers demonstrate the strong adhesion of the ACR to the surface of the nanocellulose film (Fig. 11). This indicates a good interaction and compatibility of nanocellulose with ACR due to the presence of hydrogen bonds between the hydroxyl groups of CNC and oxygen atoms of ACR ester group, which is confirmed by IR spectra (Fig. 6). ACR layer thicknesses are 3 – 5 μm, 7 – 10 μm and 14 – 17 microns for single, double, and triple-layered coatings, respectively. Cracks appear in the ACR layer for the triple-layered coating (Fig. 11(d)), which are also visible on the film surface (Fig. 8(c, d)).

The use of ACR coatings provides an easy way to impart hydrophobic properties to nanocomposite films (Table 3).

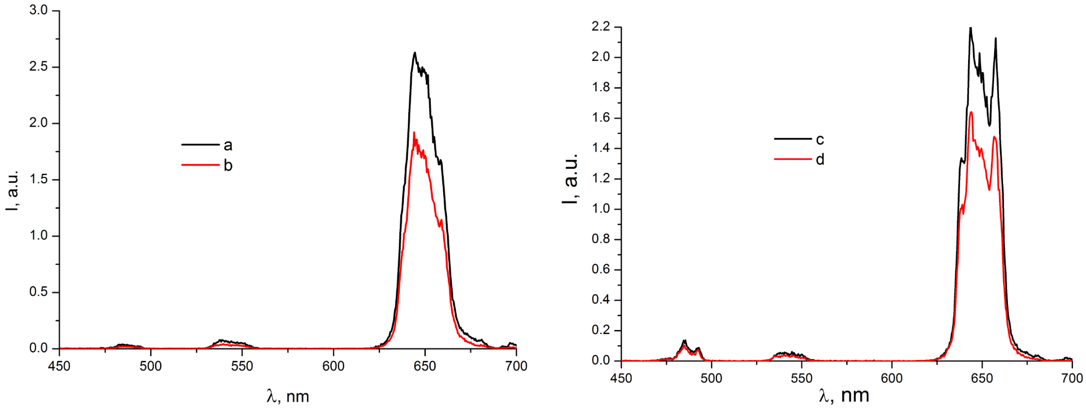

FIG. 10. Up-conversion luminescence spectra of composite films: (a) CNC/CNF: 8.4 Ho-2ACR; (b) CNC/CNF: 8.4 Ho; (c) CNC/CNF: 6.8 Ho-2ACR;(d) CNC/CNF: 6.8 Ho

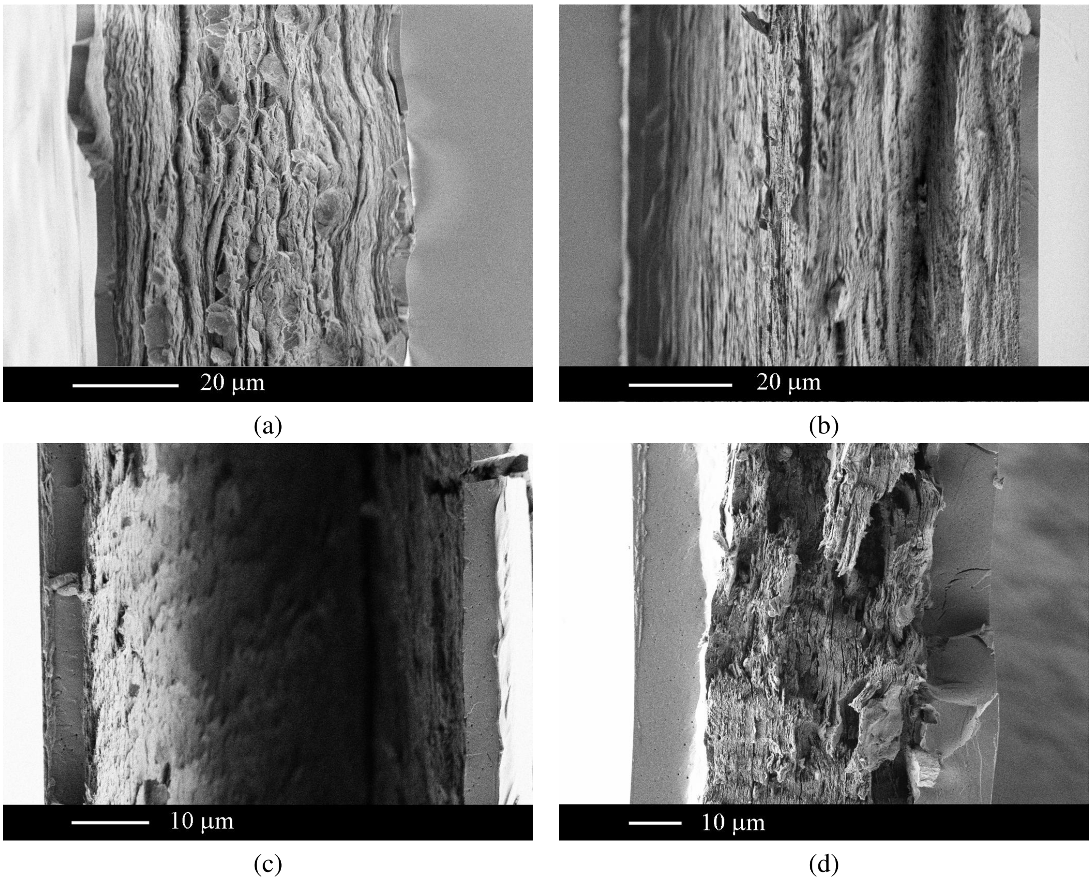

(a) (b) (c) (d)

FIG. 11. SEM image of cleaved films: (a) CNC/CNF: 4.6 Ho-1ACR; (b) CNC/CNF-1ACR; (c) CNC: 5.1 Ho-2ACR; (d) CNC: 5.1 Ho-3ACR

The ACR uncoated nanocomposite film is hydrophilic and easily wetted by water. Water adsorption and water contact angle of CNC/CNF: 4.6 Ho and CNC: 5.1Ho films are 47 and 53 %, and 15 and 0°, respectively. After a single-layer ACR coating, the film acquired hydrophobic properties. This was confirmed by the water contact angle (93°) and the absence of water adsorption. After a two-layer coating of the film, the water contact angle increased up to 100° without water adsorption. Three-layer coating demonstrate the water contact angle (92°), but the water adsorption of the film was 6 %. This behavior is associated with a presence of cracks in the thick ACR layer. Water penetrates into the composite film via cracks. Studies have shown that a two-layer ACR coating with a layer thickness of 7 – 10 μm provides good hydrophobic properties of up-conversion composite films with simultaneously improving transparency and luminescent properties.

4. Conclusions

By spraying a two-layer ACR coating with 7 – 10 μm thickness onto up-conversion CNC/CNF/MF_2:Ho composite films, the hydrophobic composite films with a water contact angle of $100\pm2^\circ$ and good water resistance were prepared. The water adsorption of up-conversion composite films after applying a two-layer ACR coating decreased from 53 to 0 %. The thickness effect of the ACR layer on the film water-resistance is established. After applying a three-layer ACR coating, the thickness of the ACR layer is approximately 14 – 17 μm with water adsorption increase. It associated with the presence of cracks in the ACR layer. Using TGA and X-ray diffraction, it was shown that the deposition of ACR coatings did not affect on the thermal stability of the films and the crystal structure of CNC, CNF, and up-conversion particles. SEM studies show strong adhesion of ACR to the surface of a nanocellulosic film. This indicates good adhesion and interaction of nanocellulose with ACR due to the presence of hydrogen bonds between hydroxyl groups in CNC/CNF and oxygen atoms of the ACR ester group. The transparent acrylic resin coating led to a smoother surface, which contributed to an increase in the transparency of composite films with ACR coating by 20 – 25 % in the visible and near-infrared spectral range with a simultaneous improvement in luminescent properties. Water-resistant, flexible, uniform, translucent up-conversion films with a thickness of 50 – 65 μm were prepared. These films can be used as a potential material for the photonics, as a luminescent label, luminescent detector, and in particular for imaging near-IR laser radiation, etc.

Acknowledgements

The study was funded by the Russian Foundation for Basic Research (RFBR 16-29-11784-ofi-m).

References

[1] Thomas B., Raj M.C., et al. Nanocellulose, a Versatile Green Platform: From Biosources to Materials and Their Applications. *Chem. Rev.*, 2018, **118** (24), P. 11575–11625.

[2] Eichhorn S.J., Rahatekar S.S., Vignolini S., Windle A.H. New horizons for cellulose nanotechnology. *Phil.Trans. R. Soc. A*, 2018, **376**, 20170200.

[3] Kontturi E., Laaksonen P., et al. Advanced Materials through Assembly of Nanocelluloses, *Adv. Mater.*, 2018, **30**, 1703779.

[4] Abitbol T., Rivkin A., et al. Nanocellulose, a tiny fiber with huge applications. *Curr. Opin. Biotechnol.*, 2016, **39**, P. 76–88.

[5] Jiang H., Zhou D., et al. Self-organized helical superstructure of photonic cellulose loaded with upconversion nanoparticles showing modulated luminescence. *RSC Advances*, 2016, **6**, P. 76231–76236.

[6] Xue B., Zhang Z., et al. Near-infrared emissive lanthanide hybridized nanobrillated cellulose nanopaper as ultraviolet lter. *Carbohydr. Polym.*, 2018, **186**, P. 176–183.

[7] Eichhorn S.J. Cellulose Nanofibres for Photonics. *Curr. Opin. Green and Sustainable Chemistry*, 2018, **12**, P. 1–7.

[8] Yu Z., Xu Z.,et al. Water-Resistant and Haze-Tunable Transparent Cellulose Nanopaper for Patterned Electroluminescence Devices. *Macromol. Mater. Eng.*, 2018, **306** (6) 1800142.

[9] Du X., Zhang Z., Liu W., Deng Y. Nanocellulose-based conductive materials and their emerging applications in energy devices – A review. *Nano Energy*, 2017, **35**, P. 299–320.

[10] Vicente A.T., Araujo A., et al. Multifunctional cellulose-paper for light harvesting and smart sensing applications. *J. Mater. Chem. C*, 2018, **6**, P. 3143–3181.

[11] Ha D., Fang Z., Zhitenev N.B. Paper in Electronic and Optoelectronic Devices. *Adv. Electron. Mater.*, 2018, **4** (5), 1700593.

[12] Seabra A.B., Bernardes J.S., et al. Cellulose nanocrystals as carriers in medicine and their toxicities: A review. *Carbohydr. Polym.*, 2018, **181**, P. 514–527.

[13] Yang J., Li J. Self-assembled cellulose materials for biomedicine: A review. *Carbohydr. Polym.*, 2018, **181**, P. 264–274.

[14] Morales-Narváez E., Golmohammadi H., et al. Nanopaper as an Optical Sensing Platform. *ACS Nano*, 2015, **9**, P. 7296–7305.

[15] Li M., Li X., Xiao H.N., James T.D. Fluorescence sensing with cellulose-based materials. *Chemistry Open*, 2017, **6**, P. 685–696.

[16] Golmohammadi H., Morales-Narváez E., Naghdi T., Merkoi A. Nanocellulose in Sensing and Biosensing. *Chem. Mater.*, 2017, **29**, P. 5426–5446.

[17] Zor E., Alpaydin S., et al. Photoluminescent nanopaper-based microcuvette for iodide detection in seawater. *Sens Actuators B Chem.* 2018, **254**, P. 1216–1224.

[18] Dong S., Roman M. Fluorescently Labeled Cellulose Nanocrystals for Bioimaging Applications. *J. Am. Chem. Soc.*, 2007, **129**, P. 13810–13811.

[19] Pouzesh M., Nekouei S., et al. Fabrication of stable copper nanoparticles embedded in nanocellulose film as a bionanocomposite plasmonic sensor and thereof for optical sensing of cyanide ion in water samples. *Cellulose*, 2019, **26** (8), P. 4945–4956.

[20] Guan Q., Song R., et al. Fluorescent CdTe-QD-encoded nanocellulose microspheres by green spraying method. *Cellulose*, 2018, **25** (12), P. 7017–7029.

[21] Yan C-Y., Fang Z-Q., et al. A tunable optoelectronic nanofibrillated cellulose/CdS quantum dot film with improved transmittance and strength. *Cellulose*, 2018, **25**, P. 2405–2417.

[22] Park J., Seo J-H., et al. Flexible and Transparent Organic Phototransistors on Biodegradable Cellulose Nanofibrillated Fiber Substrates. *Adv. Optical Mater.*, 2018, **6** (9), 1701140.

[23] Zhang Z., Zhang M., et al. Irreversible Solvatochromic Zn-Nanopaper Based on Zn(II) Terpyridine Assembly and Oxidized Nanofibrillated Cellulose. *ACS Sustainable Chem. Eng.*, 2018, **6**, 11614.

[24] Yang S., Xie Q., et al. Acetylation improves thermal stability and transmittance in FOLED substrates based on nanocellulose films. *RSC Adv.*, 2018, **8**, P. 3619–3625.

[25] You Y., Zhang H., et al. Preparation and properties of $Sr_2Si_5N_8$:Eu^{2+}-cellulose hybrid films for sunlight conversion. *Cellulose*, 2015, **22**, P. 3337–3345.

[26] Zhang L., Lyu S., Chen Z., Wang S. Fabrication Flexible and Luminescent Nanofibrillated Cellulose Films with Modified $SrAl_2O_4$: Eu, Dy Phosphors via Nanoscale Silica and Aminosilane. *Nanomaterials*, 2018, **8**, 352.

[27] Zhang L., Lyu S., et al. Dual-emitting film with cellulose nanocrystal-assisted carbon dots grafted $SrAl_2O_4$, Eu^{2+}, Dy^{3+} phosphors for temperature sensing. *Carbohydr. Polym.*, 2019, **206**, P. 767–777.

[28] Zor E. Silver nanoparticles-embedded nanopaper as a colorimetric chiral sensing platform. *Talanta*, 2018, **184**, P. 149–155.

[29] Querejeta-Fernández A., Chauve G., et al. Chiral Plasmonic Films Formed by Gold Nanorods and Cellulose Nanocrystals. *J. Am. Chem. Soc.*, 2014, **136**, P. 4788–4793.

[30] Klemm D., Heublein B., Fink H-P., Bohn A. Cellulose: fascinating biopolymer and sustainable raw material. *Angew Chem. Int. Edit.*, 2005, **44**, P. 3358–3393.

[31] Habibi Y., Lucia L.A., Rojas O.J. Cellulose nanocrystals: chemistry, self-assembly, and applications. *Chem. Rev.*, 2010, **110**, P. 3479–3500.

[32] Klemm D., Kramer F., et al. Nanocelluloses: a new family of nature-based materials: a review. *Angew Chem. Int. Edit.*, 2011, **50**, P. 5438–5466.

[33] Foster E.J., Moon R.J., et al. Current characterization methods for cellulose nanomaterials. *Chem. Soc. Rev.*, 2018, **47**, P. 2609–2679.

[34] Jonoobil M., Oladi R., et al. Different preparation methods and properties of nanostructured cellulose from various natural resources and residues: a review. *Cellulose*, 2015, **22**, P. 935–969.

[35] Mondal S. Preparation, properties and applications of nanocellulosic materials. *Carbohydr. Polym.*, 2017, **163**, P. 301–316.

[36] Kargarzadeh H., Mariano M., et al. Advances in cellulose nanomaterials. *Cellulose*, 2018, **25**, P. 2151–2189.

[37] Hamad W.Y. Cellulose Nanocrystals and Nanofibrils in Advanced Applications, in *Handbook of Nanocellulose and Cellulose Nanocomposites* (eds H. Kargarzadeh, I. Ahmad, S. Thomas and A. Dufresne), Wiley-VCH Verlag GmbH & Co. KGaA, Weinheim, Germany, 2017, P. 799–829.

[38] Wilts B.D., Dumanli A.G., et al. Chiral optics of helicoidal cellulose nanocrystal films. *APL Photonics*, 2017, **2**, 040801.

[39] Gray D.G. Recent advances in chiral nematic structure and iridescent color of cellulose nanocrystal films. *Nanomaterials*, 2016, **6**, 213.

[40] Surov O.V., Voronova M.I., Zakharov A.G. Functional materials based on nanocrystalline cellulose. *Russ. Chem. Rev.*, 2017, **86**, P. 907–933.

[41] Qing Y., Sabo R., et al. Self-assembled optically transparent cellulose nanofibril films: effect of nanofibril morphology and drying procedure. *Cellulose*, 2015, **22**, P. 1091–1102.

[42] Sun X. Wu Q., et al. Nanocellulose films with combined cellulose nanofibers and nanocrystals: tailored thermal, optical and mechanical properties. *Cellulose*, 2018, **25**, P. 1103–1115.

[43] Miao M., Zhao J., et al. Fast fabrication of transparent and multi-luminescent TEMPO-oxidized nanofibrillated cellulose nanopaper functionalized with lanthanide complexes. *J. Mater. Chem. C*, 2015, **3**, P. 2511–2517.

[44] Chu G., Wang X., et al. Chiral electronic transitions of YVO_4:Eu^{3+} nanoparticles in cellulose based photonic materials with circularly polarized excitation. *J. Mater. Chem. C*, 2015, **3**, P. 3384–3390.

[45] Nguyen T.D., Hamad W.Y., MacLachlan M.J. Near-IR sensitive up-converting nanostructured photonic cellulose films. *Adv. Opt. Mater.*, 2017, **5**, 1600514.

[46] Zhang Z., Chang H., et al. Near-infrared and visible dual emissive transparent nanopaper based on Yb(III)-carbon quantum dots grafted oxidized nanofibrillated cellulose for anti-counterfeiting applications. *Cellulose*, 2018, **25** (1), P. 377–389.

[47] Fedorov P.P., Luginina A.A., et al. Preparation of nanodispersed fluorite-type $Sr_{1-x}R_xF_{2+x}$ (R = Er, Yb, Ho) phases from citrate solutions. *J. Fluorine Chem.*, 2017, **194**, P. 8–15.

[48] Kuznetsov S.V., Proydakova V.Yu., et al. Synthesis and quantum yield investigations of the $Sr_{1-x-y}Pr_xYb_yF_{2+x+y}$ luminophores for photonics. *Nanosystems: Phys., Chem., Math.*, 2018, **9** (5), P. 663–668.

[49] Ioelovich M.Y. Study of cellulose interaction with concentrated solutions of sulfuric acid. *ISRN Chem. Eng.*, 2012, 4289741.

[50] Acrylic universal gloss varnish KU-9002. Technical Information Sheet. `URL: https://kudo-paint.ru/products/dekorativnaya-seriya/laki/lak-akrilovyj-universalnyj-glyantsevyj/`

[51] Song X., Yang S., et al. Transparent and Water-Resistant Composites Prepared from Acrylic Resins ABPE-10 and Acetylated Nanofibrillated Cellulose as Flexible Organic Light-Emitting Device Substrate. *Nanomaterials*, 2018, **8** (9), 648.

[52] Ternay A.L. *Contemporary Organic Chemistry*. W. B. Saunders Co, Philadelphia, 1976, 993 .

[53] Fedorov P.P., Luginina A.A., et al. Composite up-conversion luminescent films containing a nanocellulose and SrF_2:Ho particle. *Cellulose*, 2019, **26** (4), P. 2403–2423.

[54] Feng X., Meng X., et al. Extraction and preparation of cellulose nanocrystals from dealginate kelp residue: structures and morphological characterization. *Cellulose*, 2015, **22**, P. 1763–1772.

[55] Al-Dulaimi A.A., Wanrosli W. Isolation and Characterization of Nanocrystalline Cellulose from Totally Chlorine Free Oil Palm Empty Fruit Bunch Pulp. *J. Polym. Environ.*, 2017, **25**, P. 192–202.

[56] Slepchuk I., Semeshko O.Ya., Asaulyuk T.S., Saribekova Yu.G. Investigation of impact of rosslinking agents on characteristics of spatial net and properties of styrene-acrylic polymer films. *Izv. Vyssh. Uchebn. Zaved. Khim. Khim. Tekhnol.*, 2018, **61**(7), P. 68–76 (in Russian).

NANOSYSTEMS: PHYSICS, CHEMISTRY, MATHEMATICS, 2019, 10 (5), P. 599–599

Corrections to paper "A theoretical study of the propagation of light soliton produced by semiconductor quantum dots through optical fibers"

O. P. Swami, V. Kumar, B. Suthar, A. K. Nagar

Published in: NANOSYSTEMS: PHYSICS, CHEMISTRY, MATHEMATICS, 2019, 10(3), P. 273–281

1. Table 1 should be changed in following manner:

TABLE 1. Relation between the density of SQDs and FWHM of solitons

S.No.	Density of SQD (10^{11} cm^{-3})	FWHM (ps)
1.	2.63	6.18
2.	8.00	3.52
3.	22.88	2.06
4.	99.42	1.00

2. The heading of Fig. 3 should be modified as:

Fig. 3. Simulation of soliton generated by SQDs system with different densities of QDs. (a) $n_0 = 2.63 \times 10^{11}$ cm^{-3}; (b) $n_0 = 8.00 \times 10^{11}$ cm^{-3}; (c) $n_0 = 22.88 \times 10^{11}$ cm^{-3} and (d) $n_0 = 99.42 \times 10^{11}$ cm^{-3}.

3. Reference [3] requires a change such that:

S. D. Horta, et al. Study of the propagation of solitary waves produced by an assembly of quantum dots through optical fibers. A theoretical study. *J. Phys.: Conf. Ser.*, 2019, **1221**, P. 012020(1-6).

NANOSYSTEMS:

PHYSICS, CHEMISTRY, MATHEMATICS

INFORMATION FOR AUTHORS

The journal publishes research articles and reviews, and also short scientific papers (letters) which are unpublished and have not been accepted for publication in other magazines. Articles should be submitted in English. All articles are reviewed, then if necessary come back to the author to completion.

The journal is indexed in Web of Science Core Collection (Emerging Sources Citation Index), Chemical Abstract Service of the American Chemical Society, Zentralblatt MATH and in Russian Scientific Citation Index.

Author should submit the following materials:

1. Article file in English, containing article title, the initials and the surname of the authors, Institute (University), postal address, the electronic address, the summary, keywords, MSC or PACS index, article text, the list of references.
2. Files with illustrations, files with tables.
3. The covering letter in English containing the article information (article name, MSC or PACS index, keywords, the summary, the literature) and about all authors (the surname, names, the full name of places of work, the mailing address with the postal code, contact phone number with a city code, the electronic address).
4. The expert judgement on possibility of publication of the article in open press (for authors from Russia).

Authors can submit a paper and the corresponding files to the following addresses: nanojournal.ifmo@gmail.com, popov1955@gmail.com.

Text requirements

Articles should be prepared with using of text editors MS Word or LaTex (preferable). It is necessary to submit source file (LaTex) and a pdf copy. In the name of files the English alphabet is used. The recommended size of short communications (letters) is 4-6 pages, research articles– 6-15 pages, reviews – 30 pages.

Recommendations for text in MS Word:

Formulas should be written using Math Type. Figures and tables with captions should be inserted in the text. Additionally, authors present separate files for all figures and Word files of tables.

Recommendations for text in LaTex:

Please, use standard LaTex without macros and additional style files. The list of references should be included in the main LaTex file. Source LaTex file of the paper with the corresponding pdf file and files of figures should be submitted.

References in the article text are given in square brackets. The list of references should be prepared in accordance with the following samples:

[1] Surname N. *Book Title*. Nauka Publishing House, Saint Petersburg, 2000, 281 pp.
[2] Surname N., Surname N. Paper title. *Journal Name*, 2010, **1** (5), P. 17-23.
[3] Surname N., Surname N. Lecture title. In: Abstracts/Proceedings of the Conference, Place and Date, 2000, P. 17-23.
[4] Surname N., Surname N. Paper title, 2000, URL: http://books.ifmo.ru/ntv.
[5] Surname N., Surname N. Patent Name. Patent No. 11111, 2010, Bul. No. 33, 5 pp.
[6] Surname N., Surname N. Thesis Title. Thesis for full doctor degree in math. and physics, Saint Petersburg, 2000, 105 pp.

Requirements to illustrations

Illustrations should be submitted as separate black-and-white files. Formats of files – jpeg, eps, tiff.

NANOSYSTEMS:

PHYSICS, CHEMISTRY, MATHEMATICS

Журнал зарегистрирован
Федеральной службой по надзору в сфере связи, информационных технологий и массовых коммуникаций
(свидетельство ПИ № ФС 77 - 49048 от 22.03.2012 г.)
ISSN 2220-8054

Учредитель: федеральное государственное автономное образовательное учреждение высшего образования
«Санкт-Петербургский национальный исследовательский университет информационных технологий, механики и оптики»

Издатель: федеральное государственное автономное образовательное учреждение высшего образования
«Санкт-Петербургский национальный исследовательский университет информационных технологий, механики и оптики»

Отпечатано в Учреждении «Университетские телекоммуникации»
Адрес: 197101, Санкт-Петербург, Кронверкский пр., 49

Подписка на журнал НФХМ
На первое полугодие 2020 года подписка осуществляется через
ОАО Агентство «Роспечать»
Подписной индекс 57385 в каталоге «Издания органов научно-технической информации»